UNIVERSIDADE FEDERAL DE SÃO CARLOS - UFSCar
CENTRO DE CIÊNCIAS EXATAS E DE TECNOLOGIA

PROGRAMA DE PÓS-GRADUAÇÃO EM FÍSICA
DEPARTAMENTO DE FÍSICA

Importância dos Efeitos de Absorção no Espalhamento Elástico de Elétrons por Moléculas

JORGE RONAN FERRAZ

Orientador: Prof. Dr. Luiz Eugênio Machado

Tese apresentada ao programa de Pós-Graduação em Física da Universidade Federal de São Carlos (UFSCar) como parte dos requisitos para obtenção do título de **Doutor em Ciências**. Área de concentração: Física Atômica e Molecular.

São Carlos – SP
Março, 2017

UNIVERSIDADE FEDERAL DE SÃO CARLOS

Centro de Ciências Exatas e de Tecnologia
Programa de Pós-Graduação em Física

Folha de Aprovação

Assinaturas dos membros da comissão examinadora que avaliou e aprovou a Defesa de Tese de Doutorado do candidato Jorge Ronan Ferraz, realizada em 11/03/2017:

Prof. Dr. Luiz Eugenio Machado
UFSCar

Prof. Dr. Gabriel Luiz Cruz de Souza
UFMT

Profa. Dra. Maria das Graças Reis Martins
UFBA

Prof. Dr. Marco Aurélio Pinheiro Lima
UNICAMP

Prof. Dr. Manoel Gustavo Petrucelli Homem
UFSCar

AGRADECIMENTOS

Ao Prof. Dr. Luiz Eugênio Machado (orientador), com quem muito aprendi e cresci como pesquisador, pela constante orientação, pela GRANDE PACIÊNCIA com as minhas dificuldades e pela amizade.

Ao Prof. Dr. Antônio Sergio dos Santos (que pode ser considerado como meu co-orientador), por todas as discussões e sugestões.

Agradeço à minha esposa, Sarah, a minha grande amiga e sempre companheira em tudo e de quem muito me orgulho.

À minha mãe, Elisa, batalhadora, sempre disposta e com quem muito aprendi e aprendo.

Ao meu irmão-amigo, Juliano, sempre companheiro.

A minha sogra, Neuseli, que acompanhou toda a trajetória desde o mestrado, sempre disposta a ajudar e sempre preocupada com o com o bem-estar do casal.

Pelo apoio financeiro da CAPES, pelo apoio financeiro.

RESUMO

Neste trabalho investigamos a importância dos efeitos de absorção na dinâmica da interação elétron-molécula. Estes efeitos são simulados a partir de um potencial modelo óptico complexo, sendo a parte imaginária deste potencial correspondente a um potencial de absorção. Na solução numérica da equação de onda de espalhamento é utilizada técnica dos aproximantes de Padé, combinada à utilização do método de expansão em ondas parciais. Assim como a equação de onda de espalhamento, o potencial de interação e todas as matrizes relacionadas são expandidos sobre centro único, centro de massa da molécula, e com a parte angular escrita em termos das funções de simetria adaptadas $X_{lh}^{p\mu}$. A conhecida dificuldade de convergência destas expansões, para alvos com dipolo elétrico permanente, foi contornada em nossos estudos pela utilização de uma técnica de complementação baseada na Primeira Aproximação de Born. Foram realizados estudos de espalhamento de elétrons por oito moléculas: amônia, formaldeído, fluorometano, formamida, dimetil éter, dimetil sulfeto, pirimidina e acetona, todas com forte dipolo elétrico permanente. Foram calculadas seções de choque diferenciais (SCD), integrais (SCI) e de transferência de momento (SCTM) para o espalhamento elástico, bem como seções de choque total (SCT) e de absorção total (SCAT) para espalhamento de elétrons por todas as moléculas mencionadas acima. Os resultados obtidos foram comparados com resultados teóricos e experimentais disponíveis na literatura e, em geral, uma boa concordância é observada. Nossos resultados comprovam a importância dos efeitos de absorção para energias do elétron incidente na faixa entre 20 e 500 eV.

Palavras-chave: Física Molecular. Espalhamento de Elétrons. Seções de Choque. Absorção.

ABSTRACT

In this work we study the importance of absorption effects on the electron-molecule interaction dynamics. These effects are simulated by a complex optical model potential from which the imaginary part is an absorption potential. In the numerical solution of the scattering electron wave equation, Padé's approximant technique is used in association with the partial-wave expansion method. In our calculations, the scattering wave function, the interaction potential and all the related matrices are single-center expanded about the center of mass of the molecule, in terms of the angular symmetry-adapted functions $X_{lh}^{p\mu}$. The well-known convergence difficulty for polar targets is overcome in our studies by the use of a closure technique based on the First Born Approximation. We carry out studies on electron scattering by eight molecules: ammonia, formaldehyde, fluoromethane, formamide, dimethyl ether, dimethyl sulfide, pyrimidine, and acetone, all of them featuring a strong permanent electric dipole. We report elastic electron-molecule scattering differential (DCS), integral (ICS) and momentum transfer (MTCS) cross sections, as well as electron-molecule scattering total (TCS) and total absorption (TACS) cross sections for all the above-mentioned molecules. Our theoretical results are compared to experimental and other theoretical data available in the literature. Our results show the importance of absorption effects on electron-molecule scattering for incident electron energies in the (20-500) eV range.

Key-words: Molecular Physics. Elastic Scattering. Cross Section. Absorption.

SUMÁRIO

1 INTRODUÇÃO

Compostos orgânicos são relacionados com áreas importantes na saúde, na indústria, no meio ambiente, no transporte e, devido a isto, o número de pesquisas sobre eles tem crescido muito no meio científico nas últimas décadas. É estimado que o número de substâncias orgânicas pode chegar a mais de 10^{60} [1], entre naturais e sintéticas, encontradas por todo nosso planeta e no espaço interestelar. O aquecimento global, do qual os combustíveis fósseis são os principais vilões, tornou-se uma preocupação séria ao redor do mundo e a pesquisa por novas fontes de combustíveis e/ou novos processamentos, que sejam mais limpos e menos agressivos à natureza, tem sido intensa [2,3]. Mas combustíveis extraídos de fontes renováveis, como certos álcoois, também liberam vapores na atmosfera, mesmo que em menor quantidade, e as moléculas que constituem estes vapores estão expostas a colisões com partículas e radiações presentes no ambiente. Além disso, muitas das moléculas liberadas na atmosfera pela queima do combustível também são encontradas em meios interestelares [4]. Na área biológica, estudos mostram que danos causados a moléculas de DNA podem estar ligados a uma série de eventos secundários desencadeados a partir de um evento primário [5,6], a absorção de radiação, por esta razão dita danosa. Na indústria farmacêutica, a maioria dos medicamentos em uso tem como princípio ativo um composto orgânico [1] e, sendo assim, é de fundamental importância o conhecimento de a que grupos pertencem determinados componentes orgânicos, bem como sua formação e interação com outros grupos. Já nas indústrias siderúrgica e de novos materiais existe um grande interesse no aperfeiçoamento da modelagem de plasmas [7].

Estudos de colisões de partículas elementares com moléculas podem levar a um melhor entendimento da dinâmica dos processos físicos e químicos envolvidos nestas colisões. Há um número grande de modelos teóricos que simulam estas interações, em uma variedade de situações. Em colisões com moléculas de DNA, por exemplo, os cálculos são feitos separadamente para cada uma das moléculas que compõem a fita de DNA, mas a análise dos resultados é feita de forma integrada através de observações sobre todo o sistema. Já a validação dos resultados teóricos a partir de resultados experimentais diretos não é tão fácil, pois a reprodução em laboratório de tais colisões nem sempre é possível. Quando possíveis estas validações podem ser feitas a partir da comparação de resultados teóricos e experimentais de grandezas físicas como as seções de choque, dentre outras. É com esta motivação que é apresentada neste trabalho de doutorado uma investigação teórica sobre o

espalhamento de elétrons por moléculas orgânicas polares em um amplo alcance de energia do elétron incidente.

Cálculos teóricos de espalhamento de elétrons por átomos e moléculas são realizados por diversos grupos de pesquisas ao redor do mundo. Para a realização destes cálculos são utilizados diversos métodos, alguns baseados em princípios variacionais, como o Método Variacional Iterativo de Schwinger (ISVM), o Método Variacional Multicanal de Schwinger (SMC), o Método Variacional de Kohn e o Método da Matriz-*R*, outros baseados em métodos numéricos iterativos como o Método Algébrico-Linear (LAM), o Método das Frações Continuadas e o Método dos Aproximantes de Padé, além dos mais simples como o Método de Átomos Independentes (IAM), o Método de Átomos Independentes – Regra da Aditividade com Blindagem (IAM–SCAR), e o da Primeira Aproximação de Born (FBA), cujas aplicabilidades estão restritas às faixas de energias intermediárias e altas do elétron incidente. É usual definir como baixas as energias menores que o primeiro potencial de ionização do alvo, intermediárias as que vão daí a até alguns keV, e altas aquelas acima deste limite.

As várias implementações dos métodos citados acima podem ser classificadas, quanto ao número de canais[1] que podem ser incluídos no cálculo, em multicanais (SMC, LAM, Kohn e Matriz-*R*) ou monocanal (ISVM, Frações Continuadas, Aproximantes de Padé, FBA e as baseadas no IAM). Nestas últimas os acoplamentos entre o canal em estudo e os demais canais podem ser levados em conta aproximadamente, via a inclusão de potenciais modelo complexos que simulem estes acoplamentos, ou serem totalmente ignorados. No primeiro caso, os efeitos desta inclusão são chamados, genericamente, de efeitos de absorção.

A proposta desta tese de doutorado é uma extensão dos estudos, já iniciados no mestrado, sobre a relevância dos efeitos de absorção em espalhamento elástico de elétrons por moléculas. Os efeitos de absorção são simulados a partir de um potencial óptico complexo implementado pelo nosso grupo no pacote computacional monocanal EPolyScat-D, que é baseado no método de aproximantes de Padé [8]. Nosso grupo da UFSCar, até este momento, é um dos poucos que incluem efeitos de absorção a partir de um potencial óptico complexo neste tipo de estudos.

Uma das características do pacote EPolyScat-D é que ele nos permite realizar cálculos para espalhamento de elétrons por moléculas de simetria arbitrária exceto linear. Já o ISVM, por exemplo, que tem sido utilizado por várias décadas pelo nosso grupo, é restrito a cálculos

[1] Canal é cada um dos processos que pode vir a ocorrer numa colisão quântica, como uma excitação, uma ionização, um rearranjo, o próprio espalhamento elástico, entre outros.

de espalhamento de elétrons por moléculas e fotoionização molecular apenas para moléculas lineares, e não-lineares de simetria C_{2V} ou redutíveis a esta.

A parte imaginária do potencial óptico complexo, corresponde a um potencial de absorção. Em nossos cálculos, o potencial de absorção utilizado foi um potencial modelo proposto por nosso grupo em 2007 e conhecido na literatura como SQFSM [9] (do inglês *scaled quasi-free scattering model*) e que é um aperfeiçoamento da versão 3 do QFSM [10] (*quasi-free scattering model*) discutido na seção 4.4.

O potencial óptico foi utilizado na solução numérica da equação de Lippmann-Schwinger para a obtenção das funções de onda do elétron do contínuo e das amplitudes de espalhamento, usadas no cálculo das correspondentes seções de choque. As funções de onda, assim como o potencial de interação, e todas as matrizes relacionadas, são expandidas em ondas parciais sobre um único centro, usualmente o centro de massa (CM) da molécula. Para moléculas alvo não lineares de baixa simetria e com muitos centros atômicos estas expansões normalmente demandam grande esforço computacional. No pacote EPolyScat-D, o uso das funções de simetria adaptadas $X_{lh}^{p\mu}$, como conjunto base da parte angular (como discutido na seção 2.3), possibilita uma considerável redução desta demanda.

As soluções numéricas para a funções radiais são obtidas pela técnica dos aproximantes de Padé [8], $[N/N]$, enquanto que a conhecida dificuldade de convergência destas expansões em ondas parciais, para moléculas com forte dipolo elétrico permanente, é contornada em nossos estudos pela utilização da técnica de complementação utilizando a Primeira Aproximação de Born.

Nossos resultados evidenciam a importância da inclusão dos efeitos de absorção no estudo das colisões elásticas de elétrons por moléculas, na faixa de energias intermediárias. De um modo geral, tais efeitos são associados à perda de fluxo de elétrons espalhados elasticamente devido à abertura de processos inelásticos que competem com o processo elástico e surgem sempre que a energia do elétron incidente for suficiente para excitar eletronicamente o alvo, mas a sua relevância para o processo elástico depende do alvo em estudo e da energia do elétron incidente.

Neste trabalho estudamos o espalhamento de elétrons por oito moléculas, a maioria compostos orgânicos polares com forte dipolo elétrico permanente, a saber: amônia (NH_3) [11], formaldeído (CH_2O) [12], fluorometano ou fluoreto de metila (CH_3F) [13], formamida (NH_2CHO) [11], dimetil éter (CH_3OCH_3) [14], dimetil sulfeto (CH_3SCH_3) [15], pirimidina ou 1,3-diazine ($C_4H_4N_2$) [12] e acetona (CH_3COCH_3) [16]. O intervalo de energia do elétron

incidente é bastante amplo, incluindo energias baixas e intermediárias. Embora efeitos de absorção só ocorram para energias acima do primeiro limiar de excitação molecular, em muitos casos estendemos nossos cálculos a energias abaixo deste limiar, porque é nesta faixa que normalmente são observadas possíveis ressonâncias e em que detalhes mais sensíveis do modelo teórico podem ser testados. A boa concordância, em termos gerais, observada entre nossos resultados e dados da literatura nesta faixa de energia pode ser entendida como uma afirmação da confiabilidade de nossos estudos. Por outro lado, sabe-se que a contribuição dos processos de excitação eletrônica aos efeitos de absorção é relativamente menos importante que a dos processos de ionização molecular. Em termos de valores típicos, a predominância dos processos de ionização pode ser estimada em 70% para energias desde o primeiro limiar de ionização até cerca de 20 ou 30 eV e pode chegar a próximo de 100% para energias em torno de 100 a 200 eV [18]. Nossos cálculos mostram que a inclusão do potencial de absorção não altera os valores das diversas seções de choque para energias até cerca de 12 a 15 eV, e a partir destas energias os efeitos de absorção tornam-se mais significativos, levando a uma redução sistemática dos valores de seções de choque diferenciais elásticas (em comparação aos obtidos sem a inclusão de tais efeitos), redução esta que cresce com a energia até a faixa entre 100 e 200 eV, e que pode chegar, para determinados ângulos de espalhamento, a cerca de 50%, sendo normalmente decrescente para energias acima destas.

Em nosso trabalho foram calculadas seções de choque diferenciais (SCD), seções de choque integrais (SCI) e seções de choque de transferência de momento (SCTM) para o espalhamento elástico, bem como seções de choque total (SCT) e seções de choque total de absorção (SCTA) para todas as moléculas em estudo.

Esta tese está organizada como se segue: no segundo capítulo discutimos a metodologia utilizada para a descrição das funções de onda de espalhamento e a obtenção das seções de choque e no terceiro discutimos a técnica de correção de Born para a complementação da convergência da expansão em ondas parciais da amplitude de espalhamento bem como a técnica de expansão da SCD em termos das seções de choque de excitação rotacional. No quarto capítulo discutimos os vários potenciais de interação elétron-alvo considerados neste trabalho. O quinto capítulo apresenta uma série de detalhes acerca dos cálculos efetuados. Nossos resultados são apresentados no capítulo seis, onde também fazemos a discussão e análise dos mesmos e, finalmente, no sétimo capítulo apresentamos nossas conclusões e perspectivas.

2 FUNÇÃO DE ONDA DE ESPALHAMENTO E SEÇÕES DE CHOQUE

Quando se procura uma solução numérica da equação de Schrödinger para o problema de espalhamento elétron-molécula, para o qual a função de onda do elétron de espalhamento não é de quadrado integrável, mas satisfaz a condições assintóticas específicas, é útil reescrevermos a equação de Schrödinger numa forma de equação integral em que a condição assintótica já esteja incorporada à equação. A equação resultante é a chamada equação de Lippmann-Schwinger (LS). No que se segue serão feitas as discussões da descrição das funções de onda de espalhamento assim como da obtenção da amplitude de espalhamento e consequentemente das diversas seções de choque.

2.1 Equação de Lippmann-Schwinger e Amplitude de Espalhamento

A equação de Schrödinger independente do tempo para um elétron no campo de um potencial local $V(\vec{r})$ é dada por

$$\left(\nabla^2_{(\vec{r})} + k^2 - U(\vec{r})\right)\psi(\vec{r}) = 0, \tag{1}$$

onde o valor *k* do momento linear do elétron se relaciona à sua energia *E* pela relação usual $E = \hbar^2 k^2 / 2m$ e *U*, chamado de potencial reduzido, é dado por $U(\vec{r}) = 2mV(\vec{r})/\hbar^2$. Utilizando unidades atômicas (*a.u.*), $\hbar = e = m_e = 1$, temos $k^2 = 2E$ e $U(\vec{r}) = 2V(\vec{r})$.

Para um potencial $U(\vec{r})$ que tende a zero mais rápido que 1/*r* para $r \to \infty$, a função de onda $\psi(\vec{r})$ deve satisfazer à conhecida condição assintótica

$$\psi^{(+)}_{\vec{k}_i}(\vec{r}) \underset{r\to\infty}{\to} A\left(e^{i\vec{k}_i\cdot\vec{r}} + f(\theta,\phi)\frac{e^{ikr}}{r}\right). \tag{2}$$

Nesta equação, *A* é uma constante arbitrária, $\vec{k}_i$ é o momento linear do elétron incidente, $k = |\vec{k}_i|$, e $f(\theta,\phi)$ é a amplitude de espalhamento, que depende apenas de *k* e da direção de propagação do elétron de espalhamento, definida pelos ângulos (θ,ϕ). O índice superior (+) denota o fato de que a função $\psi^{(+)}_{\vec{k}_i}(\vec{r})$ é uma onda *outgoing*, já que o termo e^{ikr}/r corresponde a uma onda esférica cujo pacote de ondas, em energia ou momento linear, se propaga "para fora" do centro espalhador.

Podemos reescrever a eq. (1) na forma de uma equação integral que englobe a condição assintótica da eq. (2). Neste procedimento obtemos a equação de LS dada por

$$\psi_{\vec{k}_i}^{(+)}(\vec{r}) = \Phi_{\vec{k}}(\vec{r}) + \int G_0^{(+)}(\vec{r},\vec{r}')U(\vec{r}')\psi_{\vec{k}_i}^{(+)}(\vec{r}')d\vec{r}', \tag{3}$$

onde $\Phi_{\vec{k}}(\vec{r}) = (2\pi)^{-3/2} e^{i\vec{k}\cdot\vec{r}}$ é uma onda plana de momento linear $\vec{k}$ e $G_0^{(+)}$ é a função de Green para uma partícula livre com condição assintótica *outgoing*, que satisfaz a equação $\left(\nabla^2_{(\vec{r})} + k^2\right) G_0^{(+)}(\vec{r},\vec{r}') = \delta(\vec{r}-\vec{r}')$. Mostra-se [19, 20] que $G_0^{(+)}$ é dada por

$$G_0^{(+)}(\vec{r},\vec{r}') = -\frac{1}{4\pi}\frac{e^{ik|\vec{r}-\vec{r}'|}}{|\vec{r}-\vec{r}'|}. \tag{4}$$

Desta forma a função de onda do elétron incidente pode ser escrita, na região assintótica, como

$$\psi_{\vec{k}_i}^{(+)}(\vec{r}) \underset{r\to\infty}{\longrightarrow} (2\pi)^{-3/2} e^{i\vec{k}_i\cdot\vec{r}} + \frac{e^{ikr}}{r}\left[-\frac{1}{4\pi}\int e^{-i\vec{k}_f\cdot\vec{r}'}U(\vec{r}')\psi_{\vec{k}_i}^{(+)}(\vec{r}')d\vec{r}'\right], \tag{5}$$

onde $\vec{k}_f = k\hat{r}$. Comparando as eqs. (2) e (5) obtemos a forma integral para a amplitude de espalhamento, a saber:

$$f(\theta,\phi) = -\frac{(2\pi)^{3/2}}{4\pi}\int e^{-i\vec{k}_f\cdot\vec{r}}U(\vec{r})\psi_{\vec{k}_i}^{(+)}(\vec{r})d\vec{r} = -2\pi^2\left\langle \Phi_{\vec{k}_f}\middle|U\middle|\psi_{\vec{k}_i}^{(+)}\right\rangle. \tag{6}$$

Definindo-se o elemento de matriz de transição T_{fi} por

$$T_{fi} = \left\langle \Phi_{\vec{k}_f}\middle|U\middle|\psi_{\vec{k}_i}^{(+)}\right\rangle, \tag{7}$$

pode-se escrever a amplitude de espalhamento como

$$f\left(\hat{k}_f,\hat{k}_i\right) = -2\pi^2 T_{fi}. \tag{8}$$

Concluímos esta seção lembrando que toda a formulação acima pode ser estendida para o caso de interações não-locais, para as quais o operador da interação *V* é não-diagonal na representação das coordenadas [18].

2.2 Potencial Óptico

Como citado no capítulo 1 - Introdução, nas investigações teóricas sobre espalhamento de elétrons por moléculas, nosso grupo tem adotado o enfoque monocanal. Assim, podemos aplicar o formalismo da seção anterior. Nossos cálculos incluem a solução numérica da equação de LS de forma rigorosa, via um procedimento iterativo. Para isso, escolhe-se um potencial que descreva, o mais adequadamente possível, todas as interações inerentes ao processo de colisão elétron-molécula. O potencial que descreve todas estas interações

dinâmicas para este processo é um potencial óptico complexo, que pode ser escrito como [18, 19]:

$$V_{opt} = V_{SEP} + iV_{abs}, \tag{9}$$

onde V_{SEP} é formado pelos potenciais estático V_{st}, de troca V_{ex} e de correlação-polarização V_{CP}

$$V_{SEP} = V_{st} + V_{ex} + V_{CP}\ , \tag{10}$$

e o V_{abs} é um potencial de absorção. Os potenciais, V_{SEP} e V_{abs}, serão discutidos mais detalhadamente no Capítulo 4 – Potenciais de Interação. No presente trabalho adotamos para V_{CP} o potencial modelo de correlação-polarização de Perdew e Zunger [20] e para V_{abs} o potencial modelo SQFSM de Lee *et al.* [9]. A opção por um procedimento iterativo está relacionada à natureza não-local do potencial de troca. Seguindo o procedimento de Souza *et al.* [21] escreve-se o potencial óptico como uma soma

$$V_{opt} = V_1 + V_2 \tag{11}$$

com

$$V_1 = V_{st} + V_{ex}^{(loc)} + V_{CP} \tag{12}$$

e

$$V_2 = V_{ex} - V_{ex}^{(loc)} + iV_{abs}, \tag{13}$$

onde V_1 é um potencial local e $V_{ex}^{(loc)}$ é o potencial modelo de troca local de Hara [22] obtido pelo uso da aproximação do gás de elétrons livres.

Esta separação do potencial óptico tem sua motivação no formalismo *two potential* [18]. As eq. (11) - (13) também podem ser escritas em termos do potencial óptico reduzido, $U_{opt} = 2V_{opt}$, como em [21], de forma que a matriz T_{fi}, pode ser reescrita como uma soma de duas partes

$$T_{fi} = \left\langle \Phi_{\vec{k}_f} \middle| U_{opt} \middle| \psi_{\vec{k}_i}^{(+)} \right\rangle = \left\langle \Phi_{\vec{k}_f} \middle| U_1 + U_2 \middle| \psi_{\vec{k}_i}^{(+)} \right\rangle \tag{14}$$

ou

$$T_{fi} = T_1 + T_2 . \tag{15}$$

Pode-se mostrar [18] que, para colisões diretas (que não envolvem rearranjos)

$$T_1 = \left\langle \Phi_{\vec{k}_f} \middle| U_1 \middle| \psi_1^{(+)} \right\rangle \tag{16}$$

e

$$T_2 = \left\langle \psi_{\vec{k}_f}^{(-)} \middle| U_2 \middle| \psi_1^{(+)} \right\rangle . \quad (17)$$

Nas eqs. (16) e (17), as funções $\psi_1^{(+)}$ são as soluções da equação de LS para o elétron de espalhamento em um potencial U_1 com condições assintóticas *outgoing*.

Partindo de um potencial local conhecido (U_1) as funções $\psi_1^{(\pm)}$ podem ser obtidas numericamente e de posse destas, pode-se então iniciar um procedimento iterativo similar ao da série de Born. Este procedimento iterativo baseia-se no fato de que a cada passo *n*, funções de onda de espalhamento $\psi_n^{(\pm)}$ são obtidas a partir da eq. de LS:

$$\psi_{\vec{k},n}^{(\pm)}(\vec{r}) = \psi_{\vec{k},1}^{(\pm)}(\vec{r}) + \int G_1^{(\pm)}(\vec{r},\vec{r}\,') U_2(\vec{r}\,') \psi_{\vec{k},n-1}^{(\pm)}(\vec{r}) d\vec{r}\,' \quad (n = 2,3,\ldots) \quad (18)$$

onde $G_1^{(\pm)}$ é o operador de Green relacionado à onda distorcida pela presença do potencial de interação U_1, tal que

$$\left(\nabla^2 + k^2 - U_1\right) G_1^{(\pm)}(\vec{r},\vec{r}\,') = \delta(\vec{r},\vec{r}\,') . \quad (19)$$

Este procedimento pode ser repetido até que a convergência das funções de onda seja alcançada, quando $T_n' \approx T_{n-1}'$, onde T_n' é a matriz T_{fi} das eqs. (14-17) com $\psi_{\vec{k}_f}^{(-)}$ substituído por $\psi_{\vec{k},n}^{(-)}$, dentro de um critério de convergência pré-estabelecido (discutido no Capítulo 5 - detalhes computacionais) e neste caso, toma-se $\psi_{\vec{k}_i}^{(\pm)} = \psi_{\vec{k},n}^{(\pm)}$. A obtenção das funções $\psi_{k_i}^{(\pm)}$ e $\psi_1^{(\pm)}$ é feita em termos de ondas parciais, como discutido na próxima seção e a equação de LS é resolvida numericamente usando a técnica dos aproximantes de Padé [8]. A convergência da série é, em geral rápida, tipicamente até a 10ª iteração, para as moléculas em estudo [11, 12, 13, 14, 15 e 16].

2.3 Método de ondas parciais

O primeiro passo para a solução numérica da equação de LS, eq. (3) ou (18), é a expansão da função de onda de espalhamento $\psi_{\vec{k}_i}^{(+)}(\vec{r})$ em ondas parciais. Como se sabe, o conjunto dos harmônicos esféricos constitui uma base e as funções de onda de espalhamento podem sempre ser escritas na forma [18, 23]:

$$\psi_{\vec{k}_i}^{(+)}(\vec{r}) = \sum_{l=0}^{\infty} \sum_{l'=0}^{\infty} \sum_{m=-l}^{l} \sum_{m'=-l'}^{l'} c_{lml'm'}(k) R_{lml'm'}(k,r) Y_{lm}(\hat{r}) Y_{l'm'}^{*}(\hat{k}_i) . \quad (20)$$

Utilizando esta expansão, nossa procura por $\psi_{\vec{k}_i}^{(+)}$ se reduz à determinação das funções radiais $R_{lm}(k,r)$ e dos coeficientes $c_{lm}(k)$. O conjunto-base dos harmônicos esféricos, usado na eq. (20), pode ser substituído pelo conjunto-base das funções de simetria adaptadas, $X_{lh}^{p\mu}(\theta,\phi)$. Estas funções são combinações lineares dos harmônicos esféricos adequadas à simetria da molécula em estudo, e seu uso em lugar dos harmônicos esféricos conduz em geral a uma grande economia no tempo computacional. O índice *p* representa uma das representações irredutíveis (RI) do grupo pontual a que pertence a molécula, o índice μ é uma componente desta RI, *l* é o número quântico de momento angular e o índice *h* distingue entre duas diferentes bases da mesma RI correspondentes ao mesmo *l*. As funções de simetria adaptadas são definidas pela relação [24]:

$$X_{lh}^{p\mu}(\hat{r}) = \sum_{m=-l}^{l} b_{lhm}^{p\mu} Y_{lm}(\hat{r}). \tag{21}$$

Os coeficientes $b_{lhm}^{p\mu}$ correspondem aos elementos da matriz da transformação unitária entre as duas bases e podem ser obtidos algebricamente para cada grupo de ponto. As funções $X_{lh}^{p\mu}$ satisfazem a relação de ortogonalidade e os coeficientes $b_{lhm}^{p\mu}$ a certas relações de soma [24]. Usando esta nova base a eq. (20) pode ser escrita como

$$\psi_{\vec{k}_i}^{(+)}(\vec{r}) = \sum_{p\mu} \sum_{lhl'h'} c_{lhl'h'}(k) R_{lhl'h'}(k,r) X_{lh}^{p\mu}(\hat{r}) X_{l'h'}^{p\mu *}(\hat{k}_i). \tag{22}$$

Expansões semelhantes à da eq. (22) também podem ser feitas para a função de onda ψ_1, para as ondas planas $\Phi_{\vec{k}_f}$ e $\Phi_{\vec{k}_i}$, e para o potencial reduzido U_{opt}. Como consequência, a matriz T_{fi} definida pela eq. (14) resulta expandida em ondas parciais, na forma:

$$T_{fi} = \frac{1}{k} \sum_{p\mu} \sum_{lhl'h'} i^{l-l'} T_{ll'hh'}^{p\mu} X_{lh}^{p\mu}(\hat{k}_f) X_{l'h'}^{p\mu *}(\hat{k}_i), \tag{23}$$

onde $T_{ll'hh'}^{p\mu}$ é obtido pela inserção dessas expansões na eq. (14).

2.4 Seções de Choque

Os cálculos sobre a eq. (23) são efetuados nas coordenadas do sistema do alvo SA (ou *body-frame* - BF)[2] devendo ser passados para o sistema de laboratório SL (ou *lab-frame* - LF)[3] onde as medidas experimentais são realizadas. Esta transformação é feita usando a relação [24]:

$$Y_l^m(\hat{k}) = \sum_{m'} D^l_{m'm}(\alpha,\beta,\gamma) Y_l^{m'}(\hat{k}'), \tag{24}$$

onde $\hat{k}'$ denota a direção do momento linear do elétron de espalhamento no SL, $D^l_{m'm}$ são as matrizes de rotação de Wigner [25] e α, β, γ são os ângulos de Euler [25] que relacionam os dois sistemas de coordenadas. Desta forma, a amplitude de espalhamento no referencial do laboratório é dada por:

$$f^{SL} = -2\pi^2 T^{SL}_{\vec{k}_f,\vec{k}_i} \tag{25}$$

onde $f^{SL} = f^{SL}(\hat{k}'_f, \hat{k}'_i, \alpha\beta\gamma)$ depende dos ângulos de Euler. Considerando-se alvos em fase gasosa, a orientação da molécula em relação ao SL é randômica e neste caso deve-se tomar a média sobre todas as orientações possíveis. Assim a SCD no SL é calculada como

$$\left(\frac{d\sigma}{d\Omega}\right)_{Lab} = \frac{1}{8\pi^2}\int \left| f^{SL}(\hat{k}'_f, \hat{k}'_i, \alpha\beta\gamma)\right|^2 d\hat{R} = \frac{\pi^2}{2}\int \left|T^{SL}_{\vec{k}'_f,\vec{k}'_i}(\alpha\beta\gamma)\right|^2 d\hat{R} \tag{26}$$

com $d\hat{R} = d\alpha sen\beta d\beta d\gamma$.

A SCI é obtida integrando-se as SCD para todos os ângulos de espalhamento

$$\sigma_I = \int \frac{d\sigma}{d\Omega} d\Omega, \qquad \text{com} \quad d\Omega = sen\theta d\theta d\varphi . \tag{27}$$

A equação (26) é a desejada relação entre o comportamento assintótico da função de onda e a SCD. Esta relação é de fundamental importância uma vez que liga o valor teórico da amplitude de espalhamento à quantidade experimental $d\sigma / d\Omega$.

A SCTM é definida em termos de uma SCD com simetria azimutal, pela seguinte integral [26]

$$\sigma_{SCTM} = \int (1-\cos\theta)\frac{d\sigma}{d\Omega} d\Omega, \qquad \text{com} \quad d\Omega = sen\theta d\theta d\varphi \tag{28}$$

onde o termo $(1-\cos\theta)$, que multiplica a SCD, está relacionado à fração do momento transferido pela partícula incidente. A obtenção da eq. (28) é discutida no APÊNDICE B.

---

[2] Usualmente se escolhe o eixo-z do SA na direção do eixo principal de simetria do alvo.
[3] Usualmente se escolhe o eixo-z do SL na direção do feixe de elétrons incidentes.

2.5 Teorema Óptico

O cálculo da SCD numa dada direção está relacionado com o fluxo de partículas naquela direção. Este fluxo de partículas é descrito pela densidade de corrente de probabilidade $\vec{j}$,

$$\vec{j} = \frac{\hbar}{2mi}\left\{\psi^*(\vec{\nabla}\psi) - (\vec{\nabla}\psi^*)\psi\right\} \tag{29}$$

que satisfaz à conhecida equação da continuidade, dada por

$$\vec{\nabla}\cdot\vec{j} + \frac{\partial\rho}{\partial t} = 0\,. \tag{30}$$

Se ρ não variar no tempo (estado estacionário) a eq. (30) se reduz a

$$\vec{\nabla}\cdot\vec{j} = 0\,. \tag{31}$$

Esta relação, que expressa a conservação do fluxo na ausência de sorvedouro ou absorção de partículas, pode ser integrada sobre o volume de uma esfera arbitrária. Pela aplicação do teorema da divergência, a integral de superfície da componente radial de $\vec{j}$ é escrita como

$$r^2\int \vec{j}\cdot\hat{r}d\Omega = 0. \tag{32}$$

Tomando $r\to\infty$ e usando a forma assintótica da função de onda [eq. (2)] na eq. (32), mostra-se [18] que

$$\sigma_{tot} = \frac{4\pi}{k}\,\mathrm{Im}\,f_{el}(\theta=0), \tag{33}$$

onde a amplitude de espalhamento f_{el} é dada pela equação

$$f_{el}(k,\theta) = \frac{1}{2ik}\sum_{l=0}^{\infty}(2l+1)\left[S_l(k)-1\right] \tag{34}$$

com

$$S_l(k) = e^{2i\delta_l(k)}\,, \tag{35}$$

onde $S_l(k)$ é a matriz espalhamento *S* e $\delta_l(k)$ é um *phase shift* real. A partir da eq. (34) a seção de choque total elástica é dada por

$$\sigma_{tot}^{el} = \frac{4\pi}{k^2}\sum_{l=0}^{\infty}(2l+1)sen_2\delta_l(k)\,. \tag{36}$$

A dedução da eq. (33) e (36) pressupõe espalhamento por potenciais, portanto processos não elásticos não são permitidos.

Generalizando a eq. (34) para o caso onde processos não elásticos são permitidos, a matriz-*S* deve ser escrita a partir de um *phase shift* complexo

$$\delta_l(k) = \mathrm{Re}\,\delta_l(k) + i\,\mathrm{Im}\,\delta_l(k)\,, \tag{37}$$

e desta forma a matriz-*S* passa a ser escrita como

$$S_l(k) = \eta_l(k) e^{2i\,\mathrm{Re}\,\delta_l(k)} \tag{38}$$

com

$$\eta_l(k) = e^{-2i\,\mathrm{Im}\,\delta_l(k)} \tag{39}$$

onde η_l representa um de fator de absorção com a seguinte condição

$$0 \le \eta_l(k) \le 1 \qquad \text{e} \qquad \mathrm{Im}\,\delta_l(k) \ge 0\,. \tag{40}$$

Assim, o cálculo da amplitude de espalhamento, a partir de um *phase shift* complexo é dado por

$$f_{el}(k,\theta) = \frac{1}{2ik}\sum_{l=0}^{\infty}(2l+1)\left[\eta_l(k) e^{2i\,\mathrm{Re}\,\delta_l(k)} - 1\right]P_l(\cos\theta) \tag{41}$$

e a seção de choque total elástica é dada por

$$\sigma_{tot}^{el} = \frac{4\pi}{k^2}\sum_{l=0}^{\infty}(2l+1)\left|\eta_l(k) e^{2i\,\mathrm{Re}\,\delta_l(k)} - 1\right|^2\,. \tag{42}$$

A análise da função de onda de espalhamento, que leva em conta o *phase shift* complexo, também deve conter na região de $r \to \infty$ as mesmas condições assintóticas da eq. (2). Esta equação é dada por [18]

$$\psi_{\vec{k}_i}^{(+)}(k,\vec{r}) \underset{r\to\infty}{\to} A(k)\sum_{l=0}^{\infty}(2l+1)\frac{i}{2kr}\left[(-1)^l e^{-ikr} - S_l(k) e^{ikr}\right]P_l(\cos\theta) \tag{43}$$

Tomando a eq. (43) na eq. (29), mostra-se [18] que a densidade de corrente de probabilidade $\vec{j}$ correspondente a função de onda (43) é

$$\vec{j}\cdot\hat{r} = A^* A \frac{k\hbar}{m}\frac{1}{r^2}\left[\left|C_{out}(k,\theta)\right|^2 - \left|C_{inc}(k,\theta)\right|^2\right] \tag{44}$$

com

$$C_{inc}(k,\theta) = -\frac{1}{2ir}\sum_{l=0}^{\infty}(-1)^l(2l+1)P_l(\cos\theta) \tag{45}$$

e

$$C_{out}(k,\theta) = -\frac{1}{2ir}\sum_{l=0}^{\infty}(2l+1)S_l(k)P_l(\cos\theta)\,, \tag{46}$$

e desta forma, a seção de choque total na qual leva os processos não elásticos é dado por

$$\sigma_{tot}^{reação} = -\frac{1}{\vec{j}_{inc}\cdot\hat{k}_i} r^2 \int \vec{j}\cdot\hat{r}d\Omega \tag{47}$$

na qual resulta em

$$\sigma_{tot}^{reação} = \frac{\pi}{k^2}\sum_{l=0}^{\infty}(2l+1)\left[1-\eta^2{}_l(k)\right], \tag{48}$$

onde $\sigma_{tot}^{reação}$ é a seção de choque total de reação e $\vec{j}_{inc}\cdot\hat{k}_i$ é o fluxo através de uma área normal ao vetor de onda incidente dado por [18]

$$\vec{j}_{inc}\cdot\hat{k}_i = A^* A\frac{k\hbar}{m}. \tag{49}$$

Desta forma a seção de choque total que inclui ambos os processos (elástico e não elásticos) é dado por

$$\sigma_{tot} = \sigma_{tot}^{el} + \sigma_{tot}^{reação}. \tag{50}$$

ou

$$\sigma_{tot} = \frac{2\pi}{k^2}\sum_{l=0}^{\infty}(2l+1)\left[1-\eta_l(k)\cos(2\,\mathrm{Re}\,\delta_l(k))\right], \tag{51}$$

Obtendo a parte imaginária da eq. (41) para $(\theta=0)$, dada por

$$\mathrm{Im}\, f_{(\theta=0)}^{el}(k,\theta) = \frac{1}{2k}\sum_{l=0}^{\infty}(2l+1)\left[1-\eta_l(k)\cos(2\,\mathrm{Re}\,\delta_l(k)\right] \tag{52}$$

ou

$$\mathrm{Im}\, f_{(\theta=0)}^{el}(k,\theta) = \frac{k}{4\pi}\left\{\frac{2\pi}{k^2}\sum_{l=0}^{\infty}(2l+1)\left[1-\eta_l(k)\cos(2\,\mathrm{Re}\,\delta_l(k)\right]\right\}, \tag{53}$$

notemos que o teorema óptico pode ser generalizado, a partir da eq. (51), ao escrever

$$\sigma_{tot} = \frac{4\pi}{k}\mathrm{Im}\, f_{el}(\theta=0). \tag{54}$$

Obtido a SCT podemos obter a SCTA, na qual indica a intensidade de fluxo das partículas espalhadas por todos os canais inelásticos, a partir da diferença entre a SCT e a SCI dada pela equação

$$\sigma_{SCTA} = \sigma_{SCT} - \sigma_I\ , \tag{55}$$

3 TÉCNICAS DE COMPLEMENTAÇÃO DE BORN

3.1 Complementação de Born

É bem conhecida a dificuldade de convergência das expansões em ondas parciais da função de onda $\psi_{\vec{k}_i}^{(+)}$ e da matriz de transição T_{fi} para espalhamento de elétrons por alvos com dipolo elétrico permanente, cujo potencial é de longo alcance. Em muitos cálculos deve-se incluir na expansão um número muito grande, da ordem de centenas, de componentes de ondas parciais para garantir a convergência e isto nem sempre é possível por limitações computacionais. Nestes casos é comum a utilização da técnica de complementação de Born para incluir, de uma maneira menos custosa computacionalmente, as contribuições das componentes de ondas parciais mais elevadas. A técnica se baseia no fato de que as componentes da função de onda correspondentes a valores elevados do número quântico l descrevem elétrons que interagem apenas com a parte de longo alcance do potencial, *i.e.*, o potencial do dipolo permanente. Nesta região o potencial é suficientemente fraco para validar a utilização da Primeira Aproximação de Born (PAB). Num primeiro passo usa-se a PAB, para o cálculo da amplitude de espalhamento, pelo potencial dipolar:

$$f^{B_1} = -2\pi^2 \left\langle \Phi_{\vec{k}_f} \left| U_{dipolo} \right| \Phi_{\vec{k}_i} \right\rangle \tag{56}$$

onde

$$U_{dipolo}(\vec{r}) = \frac{-D}{r^2}\cos\theta = \frac{-D}{r^2}\left(\frac{4\pi}{3}\right)^{1/2} Y_{10}(\hat{r}), \tag{57}$$

e o cálculo de f^{B_1} é feito analiticamente.

Por outro lado, as funções de ondas planas $\Phi_{\vec{k}_i}$ e $\Phi_{\vec{k}_f}$ podem ser expandidas em ondas parciais, em termos das funções esféricas de Bessel $j_l(kr)$ e das funções de simetria adaptadas $X_{lh}^{p\mu}$. Nesse procedimento a matriz-T na aproximação de Born, $T_{fi}^{B_1}$, pode ser escrita como

$$T_{fi}^{B_1} = \frac{-2}{\pi} \sum_{p\mu} \sum_{l_i h_i l_f h_f} i^{l_i - l_f} T_{l_i h_i l_f h_f}^{B_1, p\mu} X_{l_f h_f}^{p\mu *}(\hat{k}_i) X_{l_f h_f}^{p\mu}(\hat{k}_f) \tag{58}$$

com

$$T_{l_i h_i l_f h_f}^{B_1,p\mu} = \left(\frac{4\pi}{3}\right)^{1/2} \sum_{m_i m_f} b^{p\mu *}_{l_f h_f m_f} b^{p\mu}_{l_i h_i m_i} \left\langle j_{l_f}(kr) \left| \frac{D}{r^2} \right| j_{l_i}(kr) \right\rangle \left\langle Y^{p\mu *}_{l_f m_f}(\hat{r}) \middle| Y_{10}(\hat{r}) \middle| Y^{p\mu}_{l_i m_i}(\hat{r}) \right\rangle \quad (59)$$

e a amplitude de espalhamento para a primeira aproximação de Born $f^{B_1} = -2\pi^2 T_{fi}^{B_1}$, expandida em ondas parciais resulta em

$$f^{B_1} = 4\pi \sum_{l_i h_i l_f h_f}^{p\mu} i^{l_i - l_f} T_{l_i h_i l_f h_f}^{B_1,p\mu} X^{p\mu *}_{l_f h_f}(\hat{k}_i) X^{p\mu}_{l_f h_f}(\hat{k}_f). \quad (60)$$

Como o programa EPolyScat-D já realizou de forma rigorosa os calculados para a amplitude de espalhamento até um *lmax* especificado no input, devemos assim extrair da eq. (60) todos os termos até o *lmax* utilizando pelo programa EPolyScat-D, a fim de não haver duplicidade destes termos. Os termos extraídos da f^{B_1} são especificados como:

$$f_{L_i L_f}^{B_1} = 4\pi \sum_{l_i h_i l_f h_f h}^{p\mu} i^{l_i - l_f} T_{l_i h_i l_f h_f h}^{B_1,p\mu} X^{p\mu *}_{l_f h_f}(\hat{k}_i) X^{p\mu}_{l_f h_f}(\hat{k}_f). \quad (61)$$

onde o par (L_i, L_f), de valores máximos de l_i e l_f, são todos os termos calculados, na primeira aproximação de Born, até um *lmax* calculado pelo EPolyScat-D. Desta forma a amplitude completa é dada por

$$f = f^{B_1} + f^{EpolyScat-D} - f_{L_i L_f}^{B_1}. \quad (62)$$

3.2 Expansão da SCD em termos das seções de choque de excitação rotacional

Toda a discussão feita até agora para a obtenção da amplitude de espalhamento para o cálculo da seção de choque foi feita na aproximação de núcleos fixos. Levando em conta o movimento rotacional da molécula podemos obter a SCD, em termos das seções de choque de excitação rotacional, na aproximação dos núcleos girantes adiabaticamente [27] (ARN, do inglês *adiabatic rotating nuclei approximation*).

Uma molécula pode ser considerada como um rotor rígido de momento de inércia I podendo ser classificado como: rotor esférico (quando apresenta $I_{XX} = I_{YY} = I_{ZZ}$), rotor simétrico ($I_{XX} = I_{YY} \neq I_{ZZ}$) e rotor assimétrico ($I_{XX} \neq I_{YY} \neq I_{ZZ}$). Para as moléculas estudadas nesta tese, temos as que são consideradas como pião simétrico (nome devido a geometria e ao grupo de simetria a qual cada molécula pertence): amônia [11] e fluorometano [13], e as consideradas como pião assimétrico: formaldeído [12], dimetil éter [14], dimetil sulfeto [15], pirimidina [12], acetona [16] e formamida [11].

O movimento de rotação de uma molécula poliatômica arbitrária é descrito pela função de onda do pião assimétrico $\psi_{J\tau M}$, dada por [24]

$$\psi_{J\tau M}(\Omega) = \sum_{K=-J}^{J} a_{KM}^{J\tau}\, \phi_{JKM}(\Omega), \tag{63}$$

onde os coeficientes $a_{KM}^{J\tau}$ podem ser obtidos pela diagonalização do Hamiltoniano do rotor rígido e ϕ_{JKM} são as autofunções do pião simétrico, dadas por [24]

$$\phi_{JKM}(\Omega) = \left(\frac{2J+1}{8\pi^2}\right)^{\frac{1}{2}} D_{KM}^{J*}(\Omega), \tag{64}$$

onde J é número quântico do operador momento angular rotacional, K e M são números quânticos das projeções deste operador ao longo dos eixos de quantização BF e LF, τ $(-J \le \tau \le J)$ indica as diferentes energias de excitação rotacional e $D_{KM}^{J}(\Omega)$ são as matrizes rotacionais de Wigner, eq. (24), que satisfazem à seguinte relação de ortogonalidade [25]:

$$\frac{1}{8\pi^2}\int D_{mm_1}^{l}(\alpha,\beta,\gamma) D_{m'm_1'}^{l'*}(\alpha,\beta,\gamma) d\Omega = \delta_{mm'}\delta_{m_1m_1'}\delta_{JJ'}\frac{1}{2J+1} \tag{65}$$

Para os números quânticos rotacionais J, τ e M iguais a zero, o valor da $\psi_{J\tau M}$ [eq. (63)] é $\psi_{000} = \left(8\pi^2\right)^{-1/2}$ [ψ_{000} é a função de onda do estado fundamental rotacional da molécula].

A SCD (obtida após uma média sobre as orientações da molécula definidas pelos ângulos de Euler [25]) dada pela eq. (26)

$$\frac{d\sigma}{d\Omega} = \frac{1}{8\pi^2}\int \left| f^{SL}(\hat{r}, \alpha\beta\gamma)\right|^2 d\alpha sen\beta d\gamma \tag{66}$$

é equivalente a escrever como

$$\frac{d\sigma}{d\Omega} = \left\langle \psi_{000} \left| f^{SL} f^{SL*} \right| \psi_{000} \right\rangle. \tag{67}$$

Usando uma relação de fechamento dos estados rotacionais, o membro direito da eq. (67) pode ser desenvolvido como [26]

$$\frac{d\sigma}{d\Omega} = \sum_{J\tau M} \left\langle \psi_{000} \left| f^{SL} \right| \psi_{J\tau M} \right\rangle \left\langle \psi_{J\tau M} \left| f^{SL*} \right| \psi_{000} \right\rangle \quad \text{ou} \quad \frac{d\sigma}{d\Omega} = \sum_{J\tau M} \left| \left\langle \psi_{000} \left| f^{SL} \right| \psi_{J\tau M} \right\rangle \right|^2 \tag{68}$$

e, desta forma, a SCD para a excitação rotacional de um nível inicial J para um nível final J' é dada, na ARN [27], por

$$\frac{d\sigma}{d\Omega}\left(J\tau \to J'\tau'\right) = \frac{1}{(2J+1)}\frac{k_{J'\tau'}}{k_{J\tau}} \sum_{M=-J}^{J} \sum_{M'=-J'}^{J'} \left| f_{J\tau M \to J'\tau' M'} \right|^2 \tag{69}$$

onde $k_{J'\tau'}$ e $k_{J\tau}$ são os momentos lineares final e inicial do elétron de espalhamento, respectivamente e $f_{J\tau M\to J'\tau' M'}$ é a amplitude de espalhamento de excitação rotacional relacionada com as autofunções rotacionais do alvo por [26]

$$f_{J\tau M\to J'\tau' M'} = \left\langle \psi_{J'\tau' M'}(\Omega)\middle| f^{SL}\middle|\psi_{J\tau M}(\Omega)\right\rangle \tag{70}$$

onde f^{SL} é a amplitude de espalhamento no SL, eq. (25).

Da eq. (68), vemos que a SCD em termos das seções de choque de excitação rotacional para espalhamento elétron-molécula é calculada através de uma soma para as transições $00\to J\tau$, isto é;

$$\frac{d\sigma}{d\Omega} = \sum_{J\tau}(2J+1)\frac{k_0}{k_{J\tau}}\frac{d\sigma}{d\Omega}(00\to J\tau). \tag{71}$$

Dentre as várias transições rotacionais incluídas na soma da eq. (71) as únicas para as quais a correção de Born deve ser feita são as transições $(J=0,\tau=0\to J'=1,\tau'=0,\pm 1)$.

4 POTENCIAIS DE INTERAÇÃO

Neste capítulo discutiremos a forma dos potenciais de interação para o cálculo de espalhamento. Os potenciais V_{st} e V_{ex}, descritos a seguir (seções 4.1 e 4.2), são determinados de forma exata a partir da função de onda do estado fundamental do alvo, obtida de um cálculo via método do campo auto-consistente (SCF) ao nível da aproximação de Hartree-Fock (HF). Para o potencial de correlação-polarização V_{CP} adotamos o modelo proposto por Perdew e Zunger [20] descrito na seção 4.3. Da mesma forma, para o potencial de absorção V_{abs} adotamos o modelo SQFSM [9] proposto por nosso grupo, que foi obtido como um aperfeiçoamento do modelo QFSM3 de Staszewska *et al.* [10]; ambos são discutidos na seção 4.4.

4.1 Potencial estático V_{st}

O potencial estático V_{st} representa a interação coulombiana média entre os elétrons do alvo e o elétron do contínuo (interação repulsiva) e a atração entre o elétron do contínuo e os núcleos do alvo, podendo ser escrito como

$$V_{st}(\vec{r}) = -\frac{1}{4\pi\varepsilon_0}\sum_{\alpha=1}^{M}\frac{Ze^2}{r_\alpha} + \frac{1}{4\pi\varepsilon_0}\int\frac{\rho(\vec{r})}{|\vec{r}-\vec{r}'|}d\vec{r}'\,. \tag{72}$$

O primeiro termo do lado direito da eq. (72), descreve as interações do elétron do contínuo com os M núcleos do alvo de coordenada $\vec{r}_\alpha$ e o segundo termo a interação eletrostática entre o elétron do continuo com os N elétrons do alvo.

Na descrição HF [28], a densidade de carga ρ é escrita como:

$$\rho(\vec{r}) = \sum_{i=1}^{N} n_i \left|\varphi_i(\vec{r})\right|^2 \tag{73}$$

onde N é o número de orbitais ocupados do alvo, n_i é o número de ocupação de cada orbital e $\varphi_i(\vec{r})$, com (i = 1, n), representa cada um desses orbitais do alvo.

Usando a bem conhecida expansão em termos dos polinômios de Legendre:

$$\frac{1}{|\vec{r}-\vec{r}'|} = \sum_{l=0}^{\infty}\frac{r_<^{\,l}}{r_>^{\,l+1}}P_l(\cos\theta) \tag{74}$$

o segundo termo do potencial estático pode ser expandido como

$$\frac{1}{4\pi\varepsilon_0}\int\sum_{l=0}^{\infty}\frac{r_<^l}{r_>^{l+1}}P_l(\cos\theta)\rho(\vec{r}')d\vec{r}'. \tag{75}$$

Nas eqs. (75) e (75), $r_<(r_>)$ é o menor (maior) entre *r* e *r´*. As integrações radial e angulares podem ser separadas utilizando-se a expansão em ondas parciais da densidade de carga e o teorema da adição para a expansão de $P_l(\cos\theta)$.

4.2 Potencial de troca V_{ex}

O potencial de troca sentido pelo elétron de espalhamento $\psi_{\vec{k}_i}^{(+)}(\vec{r})$ pode ser escrito como:

$$V_{ex}\psi_{\vec{k}_i}^{(+)}(\vec{r})=\frac{1}{4\pi\varepsilon_0}\left(\sum_i^N n_i\int\frac{\varphi_i^*(\vec{r})\psi_{\vec{k}_i}^{(+)}(\vec{r})}{|\vec{r}-\vec{r}'|}d\vec{r}'\right)\varphi_i(\vec{r}). \tag{76}$$

Este potencial surge devido à função de onda eletrônica ser escrita na forma de um determinante de Slater [28], assegurando a propriedade de antissimetria por troca de elétrons. O potencial V_{ex} exato é obtido a partir do mesmo processo iterativo utilizado na obtenção da função de onda $\psi_{k_i}^{(\pm)}$, eq. (18). Adota-se como aproximação inicial para o potencial de troca, o potencial modelo conhecido como FEGE (*free electron gas exchange*) de Hara [22], que é baseado na aproximação do gás de elétrons livres e tem a forma:

$$V_{ex}^{(loc)}(\vec{r})=-\frac{2}{\pi}k_F F(\eta) \tag{77}$$

onde

$$F(\eta)=\frac{1}{2}+\frac{1-\eta^2}{4\eta}\ln\left|\frac{1+\eta}{1-\eta}\right| \tag{78}$$

e

$$\eta=\frac{k}{k_F}. \tag{79}$$

Nesta última equação, *k* é o momento linear do elétron incidente e k_F é o momento de Fermi,

$$k_F=[3\pi^2\rho(\vec{r})]^{\frac{1}{3}}. \tag{80}$$

Com este potencial de troca local o pacote Polyangd calcula a função de espalhamento ψ_1^+, eq. (16) e (17). O processo iterativo é então iniciado substituindo-se $\psi_{k_i}^+$ por ψ_1^+ na eq. (76)

acima e recalculando-se a função de espalhamento com este potencial de troca modificado. Este procedimento é repetido até a convergência, utilizando-se um algoritmo baseado nos aproximantes de Padé [8]. Note-se que a obtenção da $\psi_{k_i}^{(+)}$ e de V_{ex} é feita simultaneamente.

4.3 Potencial de correlação-polarização

Embora o termo polarização remeta à interação do elétron de espalhamento com o dipolo elétrico molecular a grandes distâncias entre eles esta interação continua existindo à medida que esta distância diminui. Quando o elétron incidente penetra no ambiente molecular esta interação passa a representar uma correlação entre ele e os elétrons e núcleos do alvo. É usual referir-se então a um potencial de correlação-polarização que é a composição do potencial de correlação V_c para regiões internas e o potencial de polarização V_p para regiões externas ao alvo. O potencial de polarização adotado é tomado em sua forma assintótica. Para moléculas com simetria C_{2v} (dentre as moléculas em estudo no presente trabalho, formaldeído [12], dimetil éter [14], dimetil sulfeto [15], pirimidina [12] e acetona [16] pertencem a este grupo de simetria) a forma assintótica do potencial de polarização é dada por [24]:

$$V_P(\vec{r})_{r\to\infty} \sim -\frac{1}{2r^4}[\alpha_0 + \alpha_2\sqrt{\frac{4\pi}{5}}X_{20}^{A1}(\theta,\varphi) + \alpha_{22}\sqrt{\frac{4\pi}{15}}X_{22}^{A1}(\theta,\varphi)]. \qquad (81)$$

Na equação acima α_0 é a conhecida componente esférica da polarizabilidade molecular e α_2 e α_{22} são componentes devida à anisotropia da distribuição da carga molecular. Estas componentes são obtidas a partir dos termos diagonais do tensor polarizabilidade pelas relações:

$$\alpha_0 = \frac{\alpha_{zz}+\alpha_{xx}+\alpha_{yy}}{3}; \qquad \alpha_2 = \frac{2\alpha_{zz}-\alpha_{xx}-\alpha_{yy}}{3}; \qquad \alpha_{22} = \frac{1}{12}\left(\alpha_{xx}-\alpha_{yy}\right).$$

Para moléculas com simetria C_{3v} (neste trabalho, amônia [11] e fluorometano [13]) $\alpha_{22} = 0$ já que $\alpha_{xx} = \alpha_{yy}$. Por outro lado, para a moléculas com simetria C_S de interesse no presente trabalho, formamida [11], os termos não-diagonais do tensor polarizabilidade são muito menores que os da diagonal principal (cerca de 26 vezes menor) [29] e quando desprezados a eq. (81) é válida também para estas moléculas.

À medida que o elétron se aproxima do alvo, o potencial V_P vai gradualmente se tornando um potencial de correlação. Há na literatura várias propostas para a obtenção de uma

forma local deste potencial, a maioria delas baseadas no modelo do gás de elétrons livres – FEG. Nosso grupo adota a forma proposta por Perdew e Zunger [20]:

$$V_C(\vec{r}) = \begin{cases} [0.0311\ln r_s - 0.0584 + 0.00133 r_s \ln r_s - 0.0084 r_s]H(1-r_s) & r_s < 1 \\ \left[\dfrac{\gamma(1+\frac{7}{6}\beta_1\sqrt{r_s}+\frac{4}{3}\beta_2 r_s)}{\left(1+\beta_1\sqrt{r_s}+\beta_2 r_s\right)^2}\right] H(r_s - 1) & r_s \geq 1 \end{cases} \tag{82}$$

onde $\gamma = -0.1423$, $\beta_1 = 1.0529$, $\beta_2 = 0.3334$. *H(x)* é a usual função degrau de Heaviside,

$$H(x) = \begin{cases} 0 & x < 0 \\ 1 & x \geq 0 \end{cases}$$

e r_s é o raio eletrônico de Fermi na aproximação de gás de elétrons livres dado por

$$r_s = \left[\frac{3}{4\pi\rho(\vec{r})}\right]^{1/3}. \tag{83}$$

Seguindo a prescrição de Padial e Norcross [30], os pontos de transição contínua ("*matching*") entre estes dois regimes são definidos como o primeiro ponto de cruzamento das funções radiais de cada um dos potenciais, para cada componente da expansão em ondas parciais de ambos V_c e V_p.

4.4 Potencial de absorção

Historicamente, potenciais efetivos que incluem potenciais de absorção são chamados de potenciais ópticos, pela sua relação com o modelo óptico que, ao tratar o alvo como uma esfera opaca, faz uma analogia à absorção de radiação eletromagnética por um meio material [31]. Assim, as ondas representadas pela partícula incidente poderiam ser parcialmente absorvidas e parcialmente refletidas, ou seja, a partícula pode ser refletida ou transmitida, de modo que podemos associar ao alvo um respectivo índice de refração.

Potenciais efetivos de absorção para espalhamento de elétrons por moléculas têm sido obtidos, usualmente, com base em resultados empíricos. Baseando-se no modelo de McCarthy *et al.* [32] e usando aproximações baseadas no modelo de espalhamento quase-livre (QFSM), Staszewska *et al.* [33] obtiveram um potencial de absorção não empírico. Num artigo subsequente Staszewska *et al.* [34, 10] introduziram duas versões empíricas de seu modelo de potencial que foram referidas como QFSM2 [34] e QFSM3 [10]. Em diversas aplicações, verificou-se que QFSM3 [10] fornecia seções de choque em melhor acordo com os dados

experimentais quando comparadas tanto à versão não empírica [33] quanto ao QFSM2 [34]. Nosso grupo usou o modelo QFSM3 em estudos de colisões de elétrons com diversas moléculas e radicais [35-38], num largo espectro de energias do elétron incidente (tipicamente 20-1000 eV). Nestes estudos mostrou-se que o modelo de potencial óptico QFSM3 fornece resultados bastante precisos da SCD elástica, da SCI e da SCTM mas, por outro lado, os resultados mostraram que os valores da SCT calculados para elétrons incidentes com altas energias são sistematicamente subestimados pelo modelo QFSM3. Esta discordância claramente indicava a necessidade de um aperfeiçoamento deste modelo de potencial. Num artigo publicado em 2007 [9], nosso grupo propôs um aperfeiçoamento do modelo QFSM3 que objetivava corrigir deficiências deste modelo para as regiões onde a densidade eletrônica tinha valores muito altos ou muito baixos. Especificamente, nosso grupo propôs a aplicação de um fator de escala, F_s ao potencial QFSM3, na forma

$$V_{abs} = F_s V_{abs}^{(v3)}, \tag{84}$$

onde $V_{abs}^{(v3)}$ é o potencial de absorção de Staszewska *et al.* [10] na versão QFSM3 e F_s é dada por [9]

$$F_s = 1.0 + Mkr_s - N(kr_s)^{-1}. \tag{85}$$

O segundo e o terceiro termos da eq. (85) estão relacionados com a correção para as regiões de baixa e alta densidade eletrônica, respectivamente e r_s é o raio eletrônico de Fermi na aproximação de gás de elétrons livres dado pela eq. (83). Foi encontrado que para uma variedade de alvos atômicos e moleculares a SCT ficava em melhor acordo com os dados experimentais tomando-se valores de M = 0.12 e N = 2.2 (ajustados convenientemente) [9]. Isto levava há um acréscimo ou um decréscimo deste potencial $V_{abs}^{(v3)}$ fazendo o ajuste teórico sobre o experimental.

A expressão dada aos potenciais empíricos QFSM2 [34] e QFSM3 [10] tem a mesma forma, dada por

$$V_{abs}^{(v2,v3)} = -\rho(\vec{r})\left(\frac{T_L}{2}\right)^{1/2}\left(\frac{8\pi}{5k^2}k_F^{-3}\right)H\left(k^2-\alpha-\beta+k_F^2\right)(A+B+C), \tag{86}$$

sendo H a função de Heaviside e diferenciando apenas pelos valores das parametrizações α e β, tomados como

$$\alpha = \beta = k_F^2 + \Delta - 2V_{SEP} \tag{87}$$

para o modelo QFSM2 e

$$\alpha = k_F^2 + 4\Delta - 2I - V_{SEP} \tag{88}$$

e

$$\beta = k_F^2 + 2(I - \Delta) - V_{SEP}\,, \tag{89}$$

para o modelo QFSM3. Os outros termos da eq. (86) são definidos abaixo

$$T_L = \frac{k^2}{2} - V_{SEP} \tag{90}$$

$$A = \frac{5k_F^3}{\alpha - k_F^2} \tag{91}$$

$$B = -\frac{k_F^3\left[5\left(k^2 - \beta\right) + 2k_F^2\right]}{\left(k^2 - \beta\right)^2} \tag{92}$$

$$C = 2\frac{\left(\alpha + \beta - k^2\right)^{5/2}}{\left(k^2 - \beta\right)^2} H\left(\alpha + \beta - k^2\right) \tag{93}$$

Nas eqs. (90-93) acima, k é o momento linear do elétron incidente em unidades atômicas, k_F é o momento de Fermi do alvo e V_{SEP} é o potencial estático-troca-correlação-polarização. Nas eqs. (87-89), Δ é a energia média de excitação, e I é a energia de ionização (ou potencial de ionização da camada mais externa) do alvo. Vários estudos publicados por nosso grupo, [9, 21, 39, 40, 41, 42], mostram que a adoção de nosso modelo (daqui em diante denominado SQFSM, modelo de espalhamento quase livre escalonado) leva a valores da SCT em muito melhor concordância com resultados experimentais e teóricos disponíveis na literatura que os obtidos pelo QFSM3. As Figs. (1) e (2), que mostra a SCD obtida para o espalhamento de e^--SO_2 [42], são um bom exemplo que pode ser dado para visualizar o efeito do potencial de absorção (SQFSM) sobre o espalhamento elástico.

Nossos resultados obtidos para energias de 100 e 200 eV são comparados com resultados experimentais e teóricos de outros autores. Observa-se que as curvas de linha cheia (resultados teóricos calculados pelo ISVM com a inclusão do potencial de absorção SQFSM [42]) concordam muito bem com os resultados experimentais de Machado *et al*. [42], enquanto que as curvas de linha pontilhada, também calculadas utilizando o programa ISVM sem levar em conta tais efeitos [42], superestimam a SCD em praticamente todos os ângulos de espalhamento.

Fig. (1) - SCD para o espalhamento elástico e^--SO_2 à energia de 100 eV.

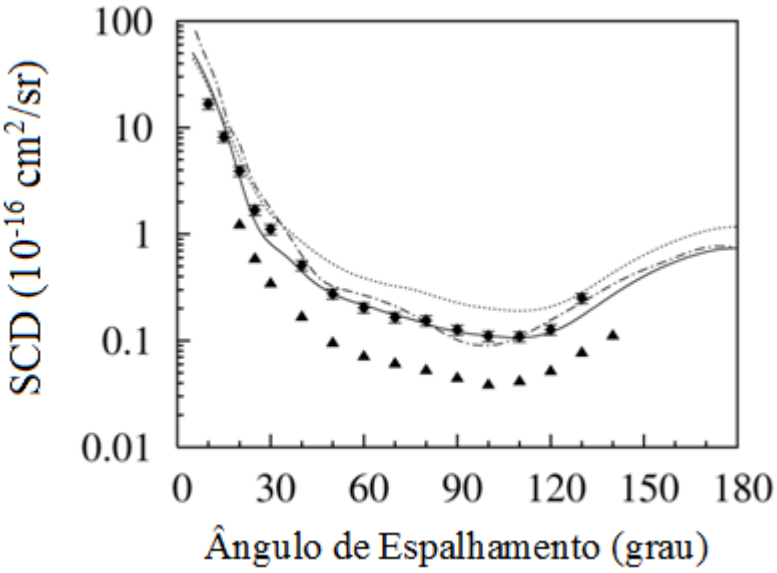

Fonte: Linha cheia - resultados teóricos calculados pelo ISVM com a inclusão do potencial de absorção SQFSM [42]; linha pontilhada – resultados teóricos calculados pelo ISVM sem a inclusão do potencial de absorção SQFSM [42]; traço ponto – resultados teóricos de Raj e Tomar [43]; triângulos cheios – resultados experimentais de Orient *et al*. [44]; e círculos fechados - resultados experimentais Machado *et al*. [42].

Fig. (2) - SCD para o espalhamento elástico e^--SO_2 à energia de 200 eV.

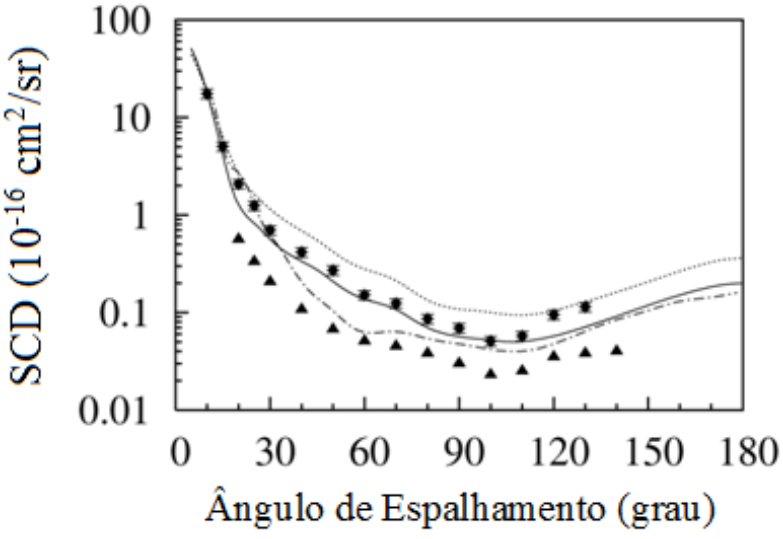

Fonte: O mesmo da Fig. (1).

5 DETALHES COMPUTACIONAIS

O EPolyScat-D é um pacote computacional direcionado à resolução numérica da equação de LS de forma iterativa usando a técnica dos aproximantes de Padé [8], para alvos de simetria arbitrária exceto linear. Ele faz uso das funções de onda para o estado fundamental de uma molécula, no nível HF-SCF [28], obtidas a partir dos programas de estrutura eletrônica GAMESS [45] ou GAUSSIAN [46], os quais utilizam bases de funções Gaussianas cartesianas. O programa também faz uso das componentes de polarizabilidade, α_{xx}, α_{yy} e α_{zz}, (também calculadas no GAMESS ou GAUSSIAN) para obter a forma assintótica do potencial de polarização-correlação. Em nossos cálculos com o EPolyScat-D, as expansões em ondas parciais dos orbitais moleculares, da função de onda do elétron de espalhamento e dos elementos de matriz-*T* incluem valores de *l* e *h* até 30. Já para a expansão do potencial óptico, estes valores vão até 60.

O critério de convergência da função de onda de espalhamento $\psi_{\vec{k},n}^{(-)}$, onde toma-se $\psi_{\vec{k}_i}^{(\pm)} = \psi_{\vec{k},n}^{(\pm)}$ na matriz-T_{fi}, (eq. 14), está relacionado com a matriz-*K*. A matriz-*K* se relaciona com matriz-T_{fi} pela seguinte relação

$$K_{fi} = \frac{T_{fi}}{1 - iT_{fi}}, \tag{94}$$

e a convergência acontece quando a diferença de valores de qualquer elementos da matriz-*K*, para duas iterações consecutivas, for menor ou igual a $1\text{x}10^{-6}$.

A partir da matriz T_{fi}, as seções de choque sem correção de Born são obtidas usando o programa *edcs*. Já o programa *rotedcs* é utilizado para o cálculo da correção de Born das seções de choque de excitações rotacionais. Em ambos os, as expansões dos elementos de matriz-T_{fi} podem ser truncadas em valores menores ou iguais aos utilizados anteriormente no cálculo com o EPolyScat-D. Em nossos cálculos para energias acima de 15 eV mantivemos os valores máximos de *l* e *h* iguais a 30, enquanto que para energias abaixo ou igual a 15 eV usamos valores de *l* e *h* menores (normalmente em torno de $l = 10$ e $h = 10$) (os critérios para a escolha desta truncagem são discutidos no Capítulo 6 – resultados e discussão). O programa *rotedcs* utiliza as energias das transições rotacionais para as quais a correção de Born deve ser feita $\left(J = 0, \tau = 0 \rightarrow J' = 1, \tau' = 0, \pm 1\right)$. Em nossos cálculos essas energias foram calculadas usando o programa *roteigen* a partir dos valores das constantes rotacionais A, B e C obtidas da literatura [29, 47].

6 RESULTADOS E DISCUSSÃO

A discussão dos resultados será feita de modo a dar uma visão geral dos mesmos, tendo em vista os artigos publicados com base neste trabalho de tese para o espalhamento elétron-molécula.

Alguns resultados, disponíveis nos artigos sobre as moléculas em estudo, serão colocados nesta tese, juntamente com resultados teóricos e experimentais disponíveis na literatura, a fim de complementar a discussão. Também, como uma forma de auxiliar a discussão, um conjunto de informações teóricas e experimentais está anexado em quadros no APÊNDICE A, para todas as moléculas em estudo neste trabalho, apresentadas em ordem crescente ao número de átomos que compõem cada molécula, e no APÊNDICE C, estão anexados todos os artigos, para as moléculas em estudo neste trabalho, em ordem de publicação.

Os resultados obtidos por meio do pacote computacional EPolyScat-D, para todas as energias de interesse neste trabalho, são corrigidos pela correção de Born para o dipolo elétrico. Resultados com os efeitos de absorção são apresentados para energias do elétron incidente iguais ou acima de 20 eV. Como citado antes, os efeitos de absorção aparecem a partir de energias do elétron incidente acima do limiar de excitação, mas são significativos somente para energias acima do primeiro potencial de ionização [17].

De fato, como dito anteriormente, nossos cálculos mostram que a inclusão do potencial de absorção não altera significativamente os valores das diversas seções de choque para energias abaixo de 20 eV, mostrando que não há uma perda significativa de fluxo no canal elástico. Por outro lado, os estudos na região de energias baixas são importantes devido à observação de possíveis ressonâncias. Nesta faixa de energia, em geral, existem resultados teóricos e experimentais disponíveis na literatura, que serão comparados com os resultados obtidos no presente trabalho.

Ao analisar as SCD de espalhamento elástico, para energias de 20 eV ou maiores de todas as moléculas em estudo neste trabalho, vemos que a curva que inclui o potencial de absorção fica consistentemente abaixo da curva sem os efeitos de absorção, mostrando uma perda de fluxo no canal elástico. Esta perda de fluxo do canal elástico faz com que os resultados com os efeitos de absorção fiquem em melhor concordância com resultados experimentais. A importância de tais efeitos fica evidente nas Figs. (3a) e (3b) [figuras (2a) e (3a) da Ref. 13].

Fig. 3 - SCD elástica para espalhamento e^--CH_3F à energia de 30 eV (a) e 100 eV (b).

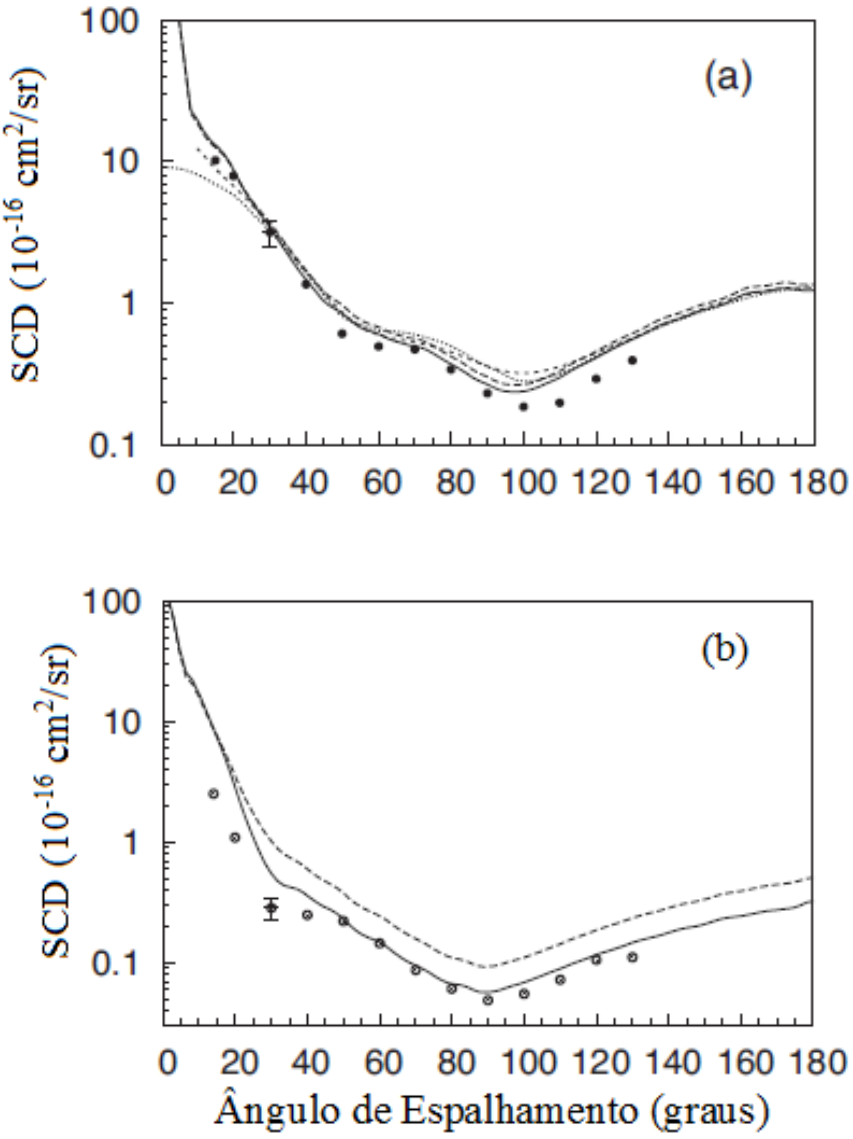

Fonte: Linha cheia – resultados teóricos de Ferraz *et al.* [13] calculados com a inclusão do potencial de absorção; linha tracejada – resultados teóricos de Ferraz *et al.* [13] calculados sem a inclusão do potencial de absorção; linha pontilhada – resultados teóricos de Natalense *et al.* [48]; linha traço curto - resultados teóricos de Varella *et al.* [49]; círculos fechados - resultados experimentais de Varella *et al.* [49]; Círculos abertos - dados experimentais de Tanaka *et al.* [50].

Como se pode ver, a influência dos canais inelásticos no espalhamento elástico tende a crescer [21, 41] com a energia do elétron incidente até energias tipicamente da ordem de 100 a 200 *eV*, Fig. (4a) [figura (3b) da Ref. 13].

Fig. 4 - SCD elástica para espalhamento e^--CH_3F à energia de 200 eV (a) e 500 eV (b).

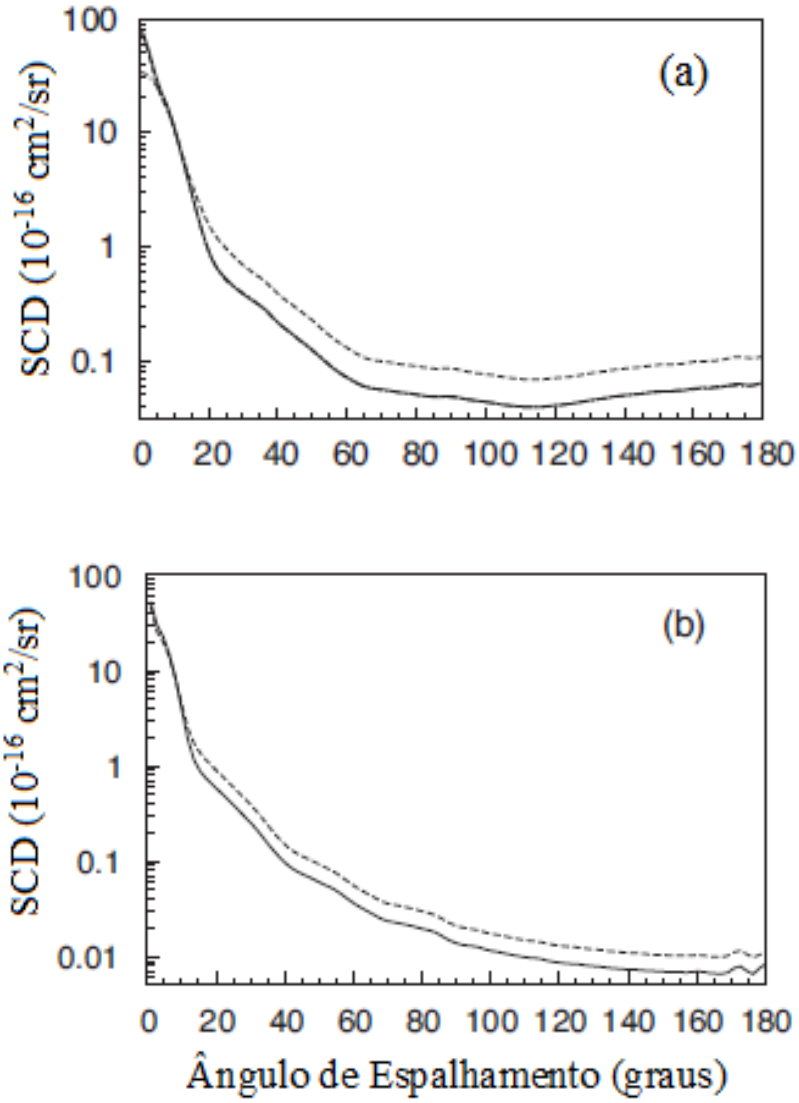

Fonte: Linha cheia, resultados teóricos de Ferraz *et al.* [13] calculados com a inclusão do potencial de absorção; linha tracejada, resultados teóricos de Ferraz *et al.* [13] calculados sem a inclusão do potencial de absorção.

Com o aumento da energia para o elétron incidente a influência dos canais inelásticos tende a diminuir, ver Fig. (4b) [figura (4b) da Ref. 13] e Fig. (5a) [figura (5a) da Ref. 14], possivelmente como consequência do menor tempo de interação elétron-molécula. Ainda na região de altas energias, usualmente 300 eV ou maiores, oscilações de pequenas amplitudes são observadas nas curvas das SCD em ângulos entre 150º a 180º, ver Fig. (4b) e Fig. (5b)

[figura (5b) da Ref. 14]. Mais pronunciadas em algumas moléculas do que em outras, estas oscilações são espúrias (não correspondem à realidade física) e são decorrentes da não convergência das funções de onda. Esta convergência só pode ser alcançada, em muitos casos, com a inclusão um número extremamente grande de componentes na expansão em ondas parciais das funções de onda de espalhamento.

Fig. 5 - SCD elástica para espalhamento e^--CH_3OCH_3 à energia de 500 eV (a) e 1000 eV (b).

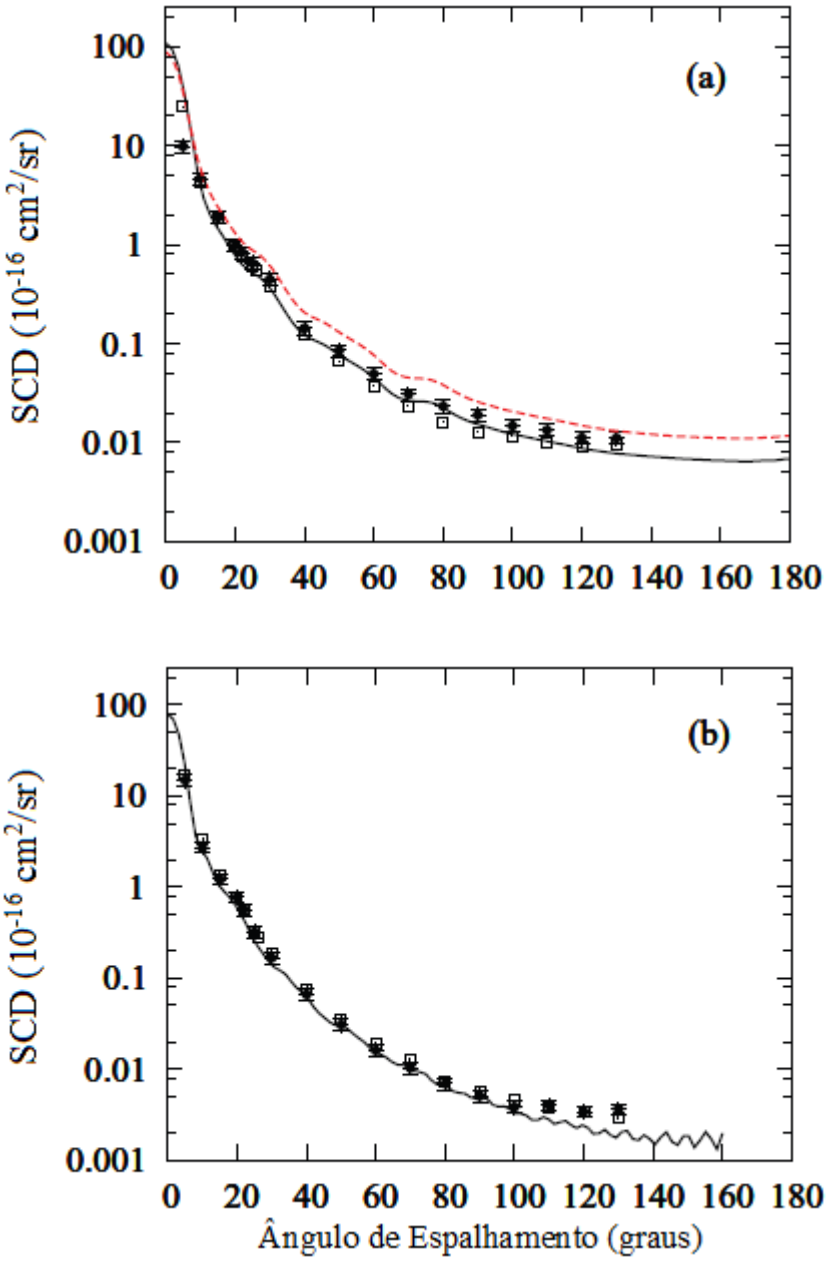

Fonte: Linha cheia, resultados teóricos de Sugohara *et al.* [14] com a inclusão do potencial de absorção; linha tracejada, resultados teóricos de Sugohara *et al.* [14] calculados sem a inclusão do potencial de absorção; círculos cheios, resultados experimentais de Sugohara *et al.* [14] para dimetil éter; quadrados abertos, dados experimentais para etanol de Lee *et al.* [52].

Para energia em torno de 60 eV a curva de SCD elástica, para todas as moléculas estudadas neste trabalho [11, 12, 13, 14, 15 e 16], observa-se um mínimo mais pronunciado entre os ângulos de 80º e 100º e volta a crescer suavemente para ângulos até 180º. Para energias acima de 150 eV este mínimo fica atenuado ou desaparece e a curva da SCD elástica diminui consistentemente para ângulos até 180º, refletindo uma menor probabilidade de o elétron ser retroespalhado. A discussão pode ser visualizada nas Fig. (3a) e (3b), Fig. (4a) e (4b) e Fig. (5a) e (5b).

A discussão feita acima também pode ser observada para os resultados de espalhamento de e^--NH_2CHO, Fig. (6) [figura (7) da Ref. 11]. Os nossos resultados com os efeitos de absorção estão sendo comparados com os resultados experimentais de Maljkovic *et al.* [51]. Novamente pode ser observado uma boa concordância entre os nossos resultados teóricos com os resultados experimentais.

Fig. 6 - SCD elástica para espalhamento e^--NH_2CHO à energia de 100 eV (a), 150 eV (b), 200 eV (c) e 300 eV (d).

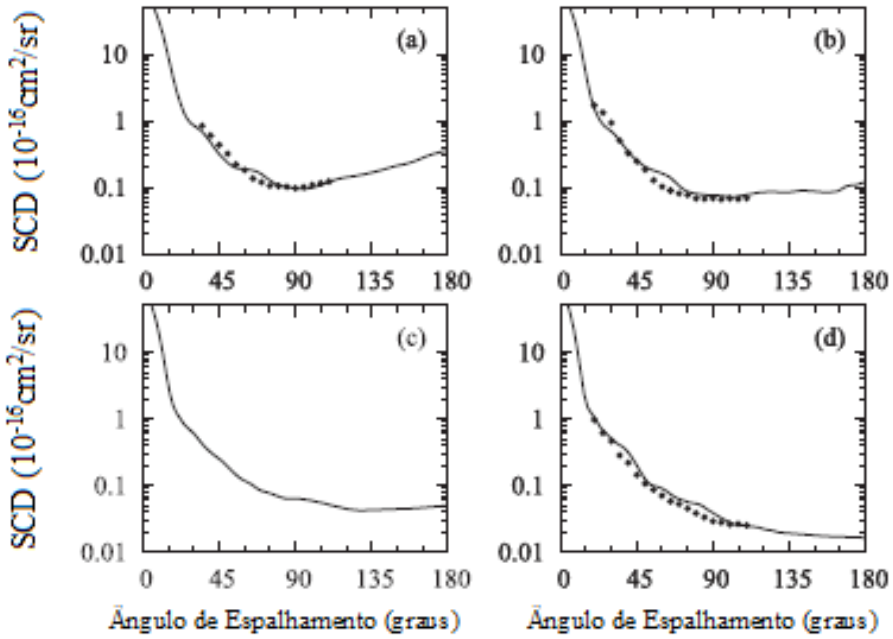

Fonte: Linha cheia, resultados teóricos de Homem *et al.* [11] com a inclusão do potencial de absorção; círculos cheios, resultados experimentais de Maljkovic *et al.* [51].

A importância do potencial de absorção sobre o espalhamento elástico também pode ser visualizada nos resultados das SCD para o espalhamento de e^--CH_3SCH_3 [15], Fig. (7a) e (7b) [figuras (4a) e (4b) da Ref. 15], por concordar muito bem com os nossos resultados experimentais para todas as energias exibidas no artigo. Neste mesmo artigo também foi

realizado pelo nosso grupo cálculos de SCD com a inclusão do potencial de absorção no IAM. Os resultados obtidos pelo IAM com a implementação do potencial de absorção se mostraram muito bons quando comparados com os resultados teóricos (obtidos com o EpolyScat-D) e experimentais do nosso grupo para energias acima de 300 eV, Fig. (7a) e (7b), e para energias abaixo destas a SCD apresenta resultados coerentes, mas que ficam acima dos resultados teóricos e experimentais.

Fig. 7 - SCD elástica para espalhamento e^{-}-CH_3SCH_3 à energia de 400 eV (a) e 500 eV (b).

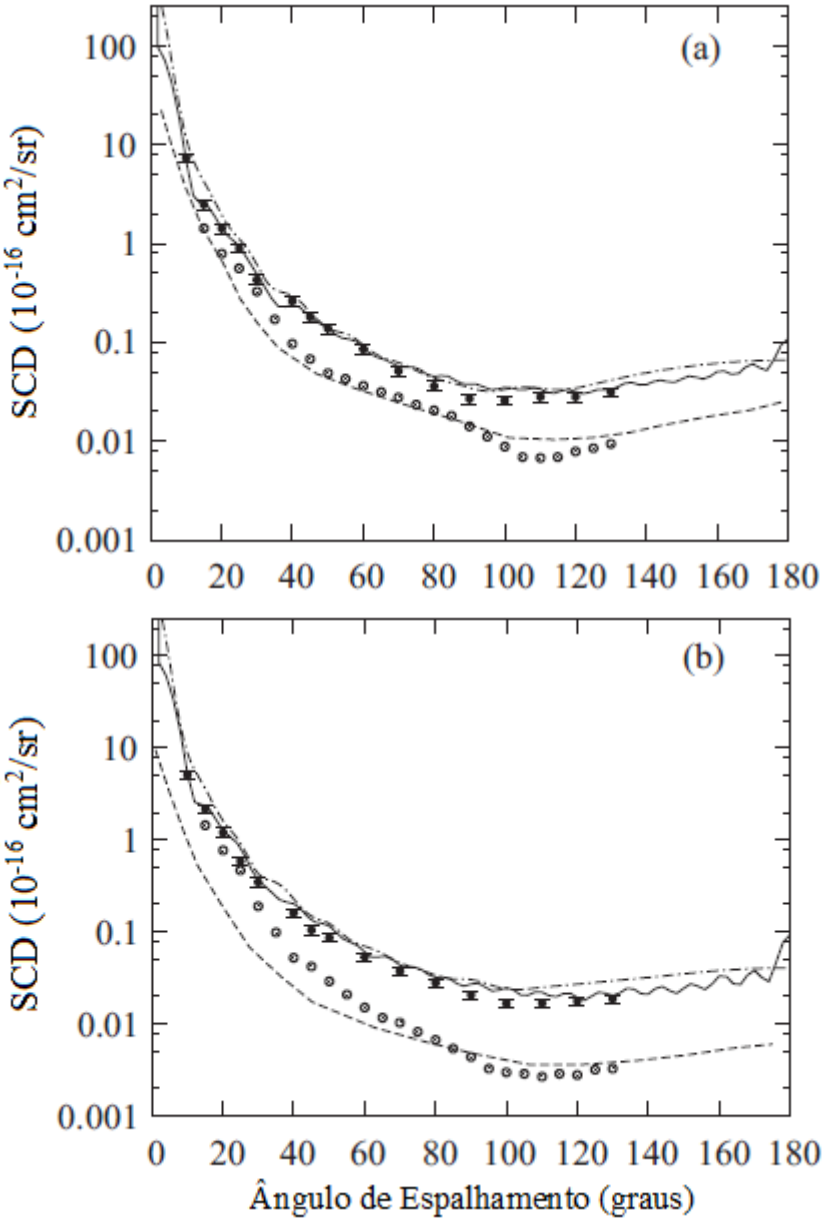

Fonte: Linha cheia, resultados teóricos de Homem *et al.* [15] com a inclusão do potencial de absorção; linha traço ponto, resultados teóricos de Homem *et al.* [15] usando o IAM; linha tracejada, resultados do IAM de Rao *et al.* [53]; círculos cheios com barra de erros – resultados experimentais de Homem *et al.* [15]; círculos abertos, medidas de Rao *et al.* [53].

Os resultados para a SCD no IAM são obtidos a partir da equação [54]

$$\left(\frac{d\sigma}{d\Omega}\right)_{Lab} = I_S + I_{SS} \tag{95}$$

onde

$$I_S = \sum_i^{N_a} \left| f_i(k,\theta) \right|^2 \tag{96}$$

e

$$I_{SS} = 2\,\mathrm{Re}\left\{ \sum_i^{N_a} f_i^*(k,\theta) f_j(k,\theta) \frac{sen\left(qR_{ij}\right)}{qR_{ij}} \right\} \quad . \tag{97}$$

Nas equações acima, I_S está relacionado ao espalhamento simples pelos potenciais atômicos e I_{SS} aos termos de interferência entre os átomos que constituem a molécula.

Devido ao dipolo elétrico permanente, presente em todas as moléculas em estudo neste trabalho, observa-se que as curvas das SCD obtidas pelo EPolyScat-D para todas as energias crescem fortemente na região de ângulos pequenos. Este comportamento é relacionado à conhecida divergência da SCD no ângulo de 0º para o espalhamento de elétrons por um dipolo elétrico puntual com posição e orientação fixas, comportamento que não é observado em moléculas apolares [55, 56]. Devido ao forte dipolo elétrico do alvo, o elétron incidente continua sendo espalhado por este potencial, mesmo a grandes distâncias, e é nesta região de ângulos pequenos que o tratamento da técnica de complementação utilizando a primeira aproximação de Born tem sua maior contribuição. Novamente, sem técnicas do tipo correção de Born, a convergência só poderia ser atingida com o uso um número extremamente grande de termos na expansão das funções de onda de espalhamento.

É interessante notar que vários resultados teóricos de SCD de espalhamento elétron-molécula a baixas energias, disponíveis na literatura, mostram oscilações de natureza não física, que ocorrem em alguns casos em todo o domínio angular, em outros apenas na região de ângulos pequenos (onde o efeito de dipolo elétrico é mais pronunciado), enquanto que nossos cálculos com a correção de Born fornecem curvas suaves, mesmo quando nossos dados obtidos sem esta correção mostram tais oscilações, ver Fig. (8) [figura (1) da Ref. 11].

Fig. 8 - SCD elástica para espalhamento e^--NH_3 à energia de 1 eV (a), 2 eV (b), 5 eV (c) e 7.5 eV (d).

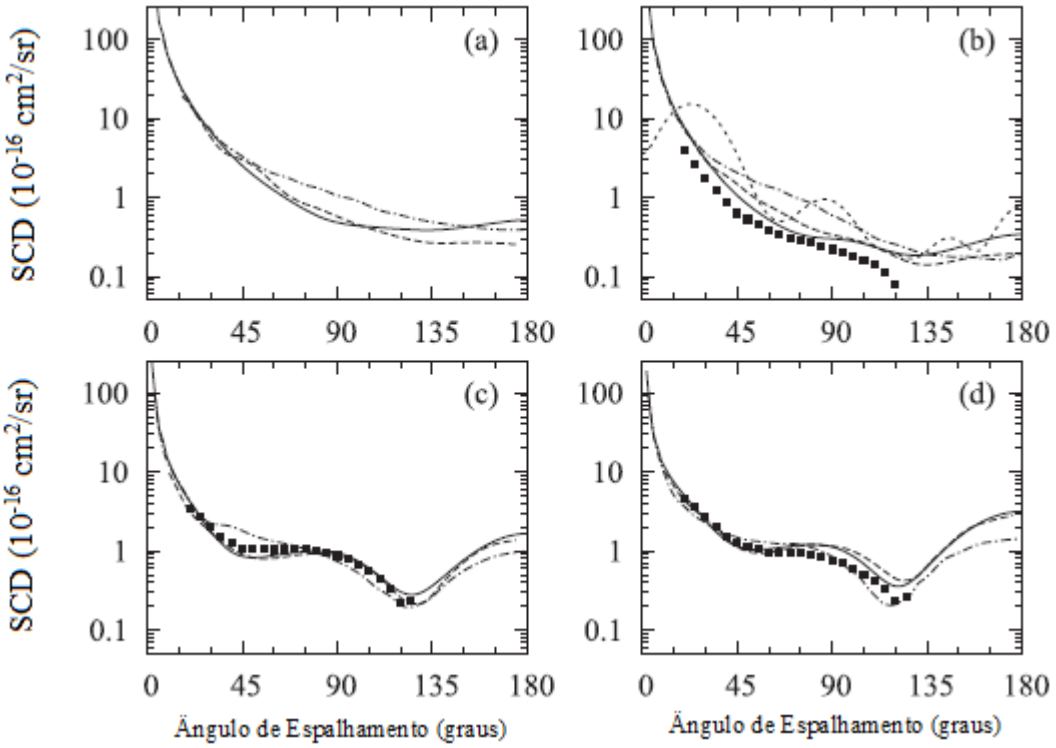

Fonte: Linha cheia, resultados teóricos de Homem *et al.* [11] com correção de Born; linha tracejada, resultados teóricos de Rescigno *et al.* [57]; linha traço ponto, resultados teóricos de Munjal e Baluja [58]; linha traço curto, resultados teóricos de Homem *et al.* [11] sem o procedimento de correção de Born; quadrados cheios, resultados experimentais de Alle *et al.* [59].

Esta discrepância entre os resultados deve estar relacionada com as formas propostas para a correção de Born por diferentes autores. Por exemplo, os resultados para espalhamento de e^--CH_2O por parte de Kaur e Balluja [60], Fig. (9a) e (9b) [figuras (1a) e (2a) da Ref. 12], para energias de 1 e 10 eV respectivamente, mostram oscilações ao longo de toda a curva. Tais oscilações podem ter sido causadas pela forma como é feita a correção de Born. No caso desses autores, a correção feita não é sobre a amplitude de espalhamento, como é feita em nosso grupo, mas diretamente sobre a seção de choque. A correção feita nesta aproximação, que é dada por

$$\frac{d\sigma}{d\Omega} = \frac{d\sigma^B}{d\Omega} + \sum_L (A_L - A_L^B) P_L(\cos\theta), \tag{98}$$

não leva em conta termos de interferências entre as componentes da expansão em onda parcial.

Fig. 9 - SCD para o espalhamento elástico e^--CH_2O à energia de 1 eV (a) e 10 eV (b)

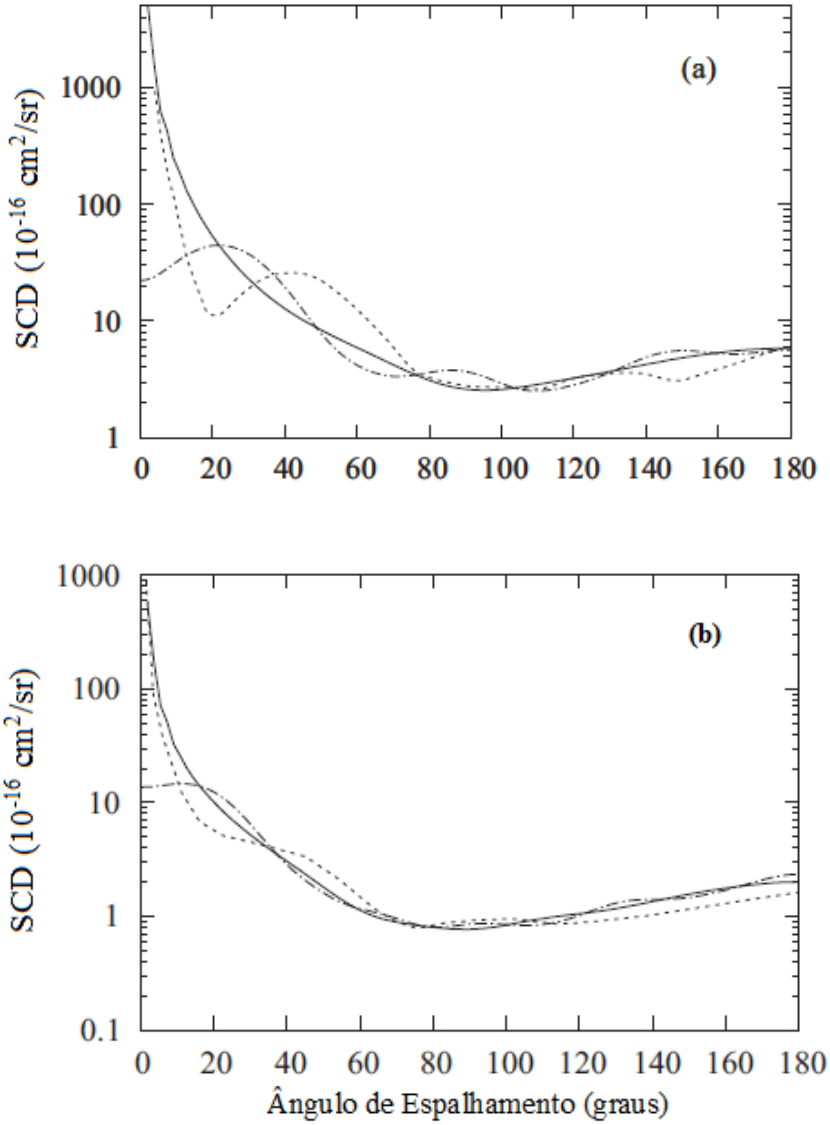

Fonte: Linha cheia, resultados teóricos de Ferraz *et al.* [12] calculados com a correção de Born; linha traço ponto, resultados teóricos de Ferraz *et al.* [12] calculados sem a correção de Born; linha pontilhada, resultados de Kaur e Baluja [60] usando o método da matriz-*R*.

Ainda nas Fig. (9a) e (9b) pode-se observar que quando a correção de Born é aplicada, os valores das SCD para ângulos próximos de 0º tomam valores muito grandes, que é um comportamento esperado para moléculas polares e que não é observado em cálculos sem a correção. Este comportamento também pode ser observado nos resultados para a molécula de pirimidina [12], Fig. (10a) e (10b) [figuras (8a) e (8b) da Ref. 12], e na Fig. (8b).

Fig. 10 - SCD para o espalhamento elástico e^--$C_4H_4N_2$ à energia de 10 eV (a) e 15 eV (b).

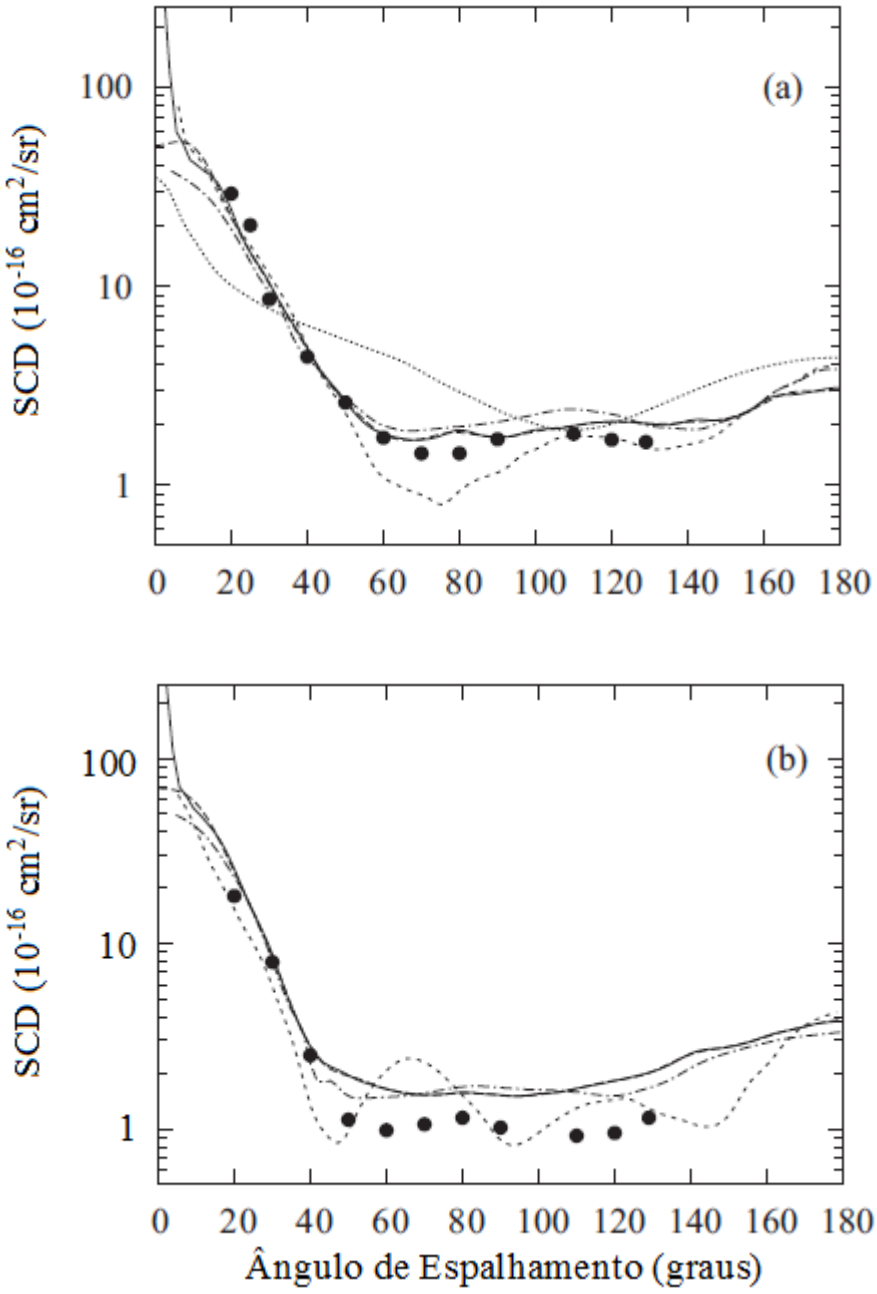

Fonte: Linha cheia, resultados teóricos de Ferraz *et al.* [12] com a correção de Born; linha tracejada, resultados teóricos de Ferraz *et al.* [12] sem a correção de Born; linha traço curto, resultados de Masín *et al.* [61] usando o método da matriz-*R;* linha traço ponto, resultados de Palihawadana *et al.* [62] calculados no SMC; linha pontilhada, resultados de Palihawadana *et al.* [62] calculados no IAM-SCAR; círculos cheios, resultados experimentais de Palihawadana *et al.* [62].

Com relação a estas oscilações das SCD a baixas energias, há ainda outro ponto interessante a mencionar. Em alguns trabalhos do nosso grupo, mas não pertencentes ao trabalho desta tese, verificou-se que tais oscilações podem aparecer mesmo quando a correção

de Born é aplicada. Por exemplo, nas Fig. (11a) e (11b) [figuras (6a) e (6b) da Ref. 14], mostramos SCD para o espalhamento elástico de elétrons por moléculas de dimetil éter e de etanol, a energias de 2 e 5 eV, respectivamente, onde oscilações não físicas são claramente observadas para as SCD de espalhamento elétron-etanol.

Fig. 11 - SCD para o espalhamento elástico e^--CH_3OCH_3 à energia de 2 eV (a) e 5 eV (b).

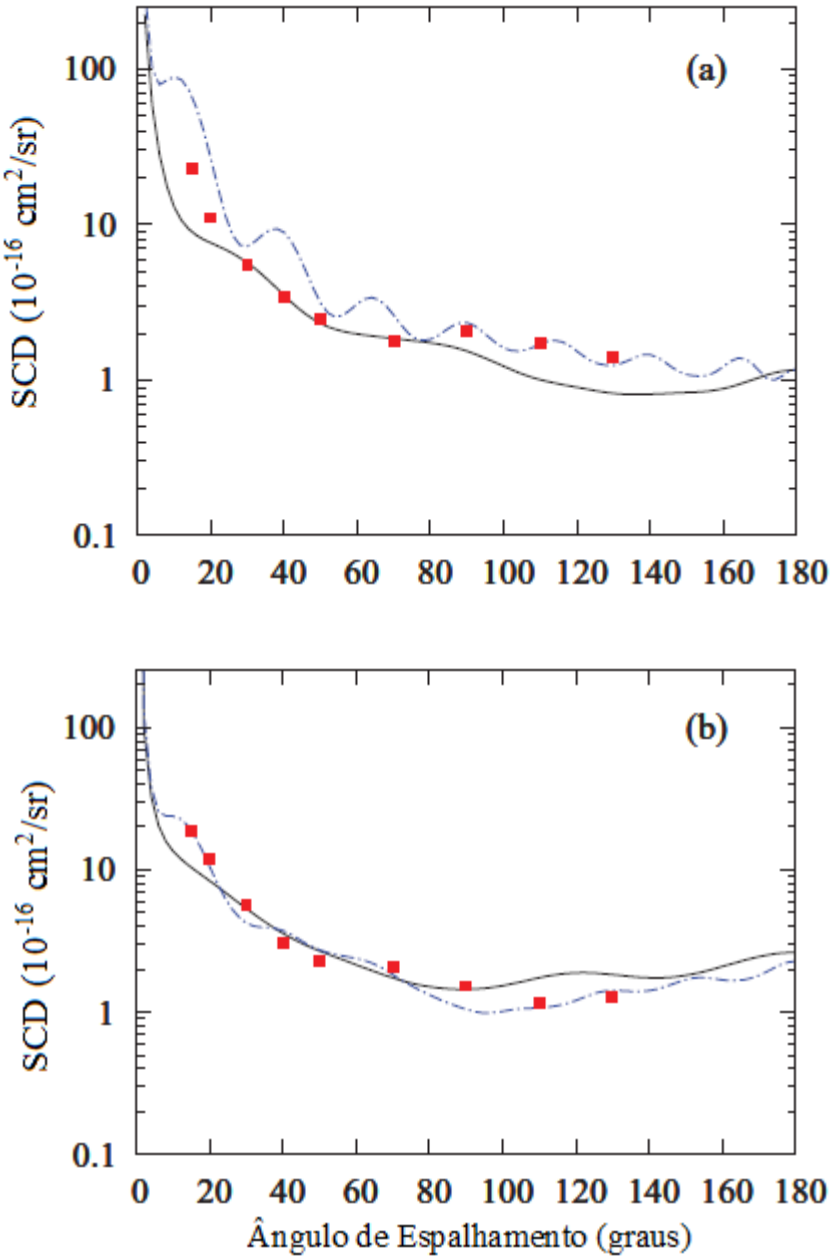

Fonte: Linha cheia, resultados teóricos de Sugohara *et al.* [14] calculados com a correção de Born; linha traço ponto, resultados de Lee *et al.* [52] para etanol com a correção de Born; quadrados cheios, resultados experimentais de Khakoo *et al.* [63] para etanol.

Quando oscilações deste tipo são observadas, mesmo após a correção de Born ter sido aplicada sobre a amplitude de espalhamento, dizemos que não há um *matching*, uma correspondência entre a matriz-T^{poly} calculada no EPolyScat-D até um valor de corte l_{max} especificado no cálculo e a matriz-T^{B_1} calculada na Primeira Aproximação de Born a partir de (l_{max} *+1*). Este problema, observado não apenas para a molécula de etanol, mas também para outras moléculas polares, poderia ser resolvido se o *matching* ocorresse a l_{max} maiores na expansão da função de onda de espalhamento calculada pelo pacote EPolyScat-D. Todavia, este procedimento nem sempre é viável devido à grande demanda computacional. Pode-se nestes casos recorrer a um procedimento numérico de suavização da SCD que remova as oscilações não físicas, mantendo-se os valores médios, que são fisicamente corretos. De qualquer modo estas dificuldades desaparecem para energias em torno ou maiores que 20 eV mostrando que acima deste limite há uma correspondência entre as matrizes-T^{poly} do pacote EPolyScat-D e as da correção de Born, matriz-T^{B_1}.

Ainda em relação aos estudos do espalhamento elástico elétron- dimetil éter [14], resultados bastante interessantes são observados quando se comparam as SCD das moléculas de dimetil éter e etanol. A comparação de nossas SCD para dimetil éter e as de Lee *et. al*. [52] para etanol com os resultados das SCD experimentais de Khakoo *et al.* [63] para etanol mostram uma grande similaridade em energias intermediárias, a partir de 15 eV, Fig. (12a) e (12b) [figuras (7b) e (8a) da Ref. 14]. Considerando que ambas as moléculas pertencem a grupos funcionais distintos, com propriedades químicas e físicas diferentes, nossos estudos parecem indicar que em energias intermediárias é mais relevante a interação do elétron de espalhamento com o conjunto de átomos que compõem os isômeros, do que com o alvo molecular como um todo. Deve-se lembrar, entretanto, que o mesmo não acontece para energias abaixo do limiar de excitação [figura (6a) e (6b) da Ref. 14], pois nesta região, como o elétron não tem grande poder de penetração, o processo de espalhamento passa a ser dominado por potenciais do tipo dipolo induzido e permanente e em menor escala dos demais multipolos.

Fig. 12 - SCD para o espalhamento elástico e^--CH_3OCH_3 à energia de 15 eV (a) e 20eV (b).

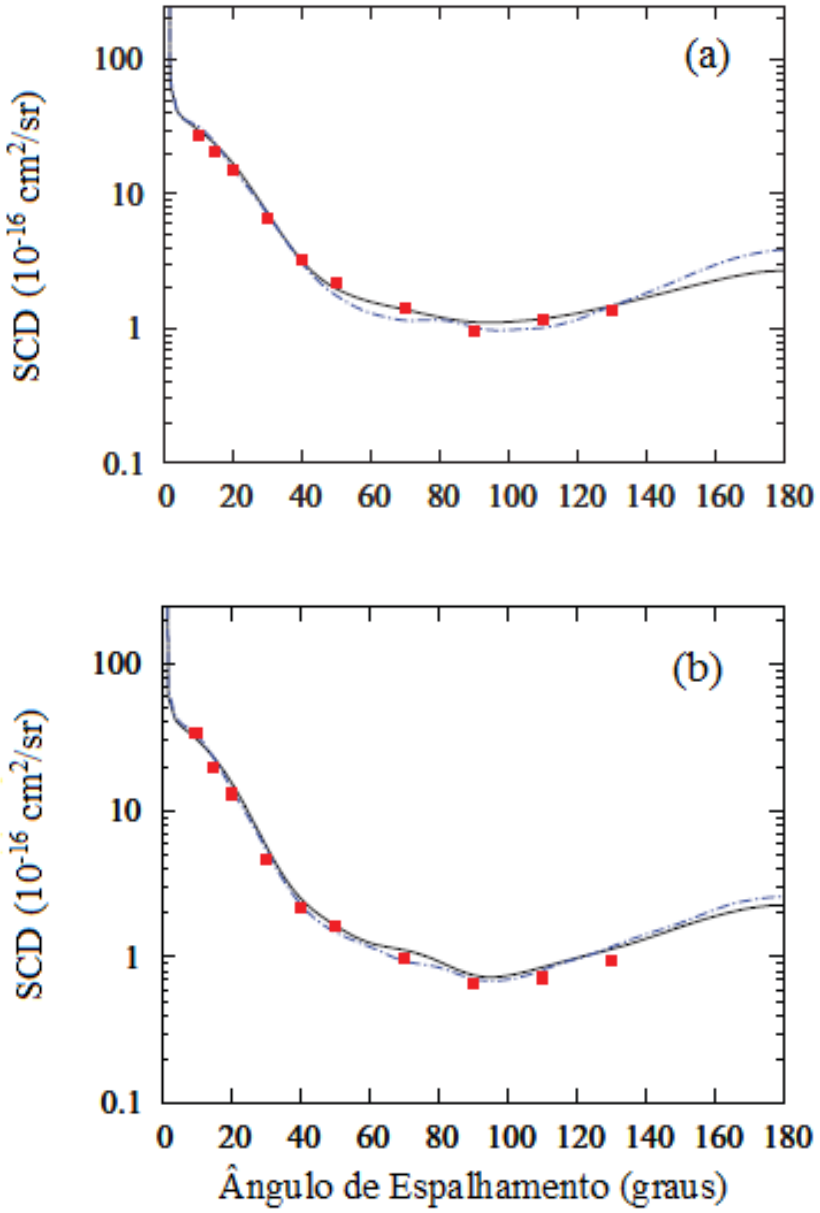

Fonte: Linha cheia, resultados teóricos de Sugohara *et al.* [14] calculados com a correção de Born; linha traço ponto, resultados de Lee *et al.* [52] para etanol com a correção de Born; quadrados cheios, resultados experimentais de Khakoo *et al.* [63] para etanol.

As Fig. (13a) e (13b) mostram nossos resultados de SCT e SCI, para a molécula de formaldeído [12] – estendida a faixa de energia do elétron incidente de 0,2 eV a 500 eV e para a molécula de fluorometano [13] – estendida a faixa de energia de elétron incidente de 2 eV a 500 eV, respectivamente. Como esperado, observa-se uma sobreposição das curvas para energias abaixo de 15 eV mostrando a predominância do canal elástico sobre os demais canais nesta região. Também como esperado, para energias acima deste limite a SCT é maior do que a SCI pois esta última só leva em conta o espalhamento elástico enquanto a SCT leva em

conta todos os canais. Tal comportamento foi verificado em todos os cálculos de espalhamento de elétrons pelas moléculas estudadas no presente trabalho.

Fig. 13 – (a) Sobreposição dos resultados da SCT e da SCI para o espalhamento elástico e^--CH_2O e (b) sobreposição dos resultados da SCT e da SCI para o espalhamento elástico e^--CH_3F.

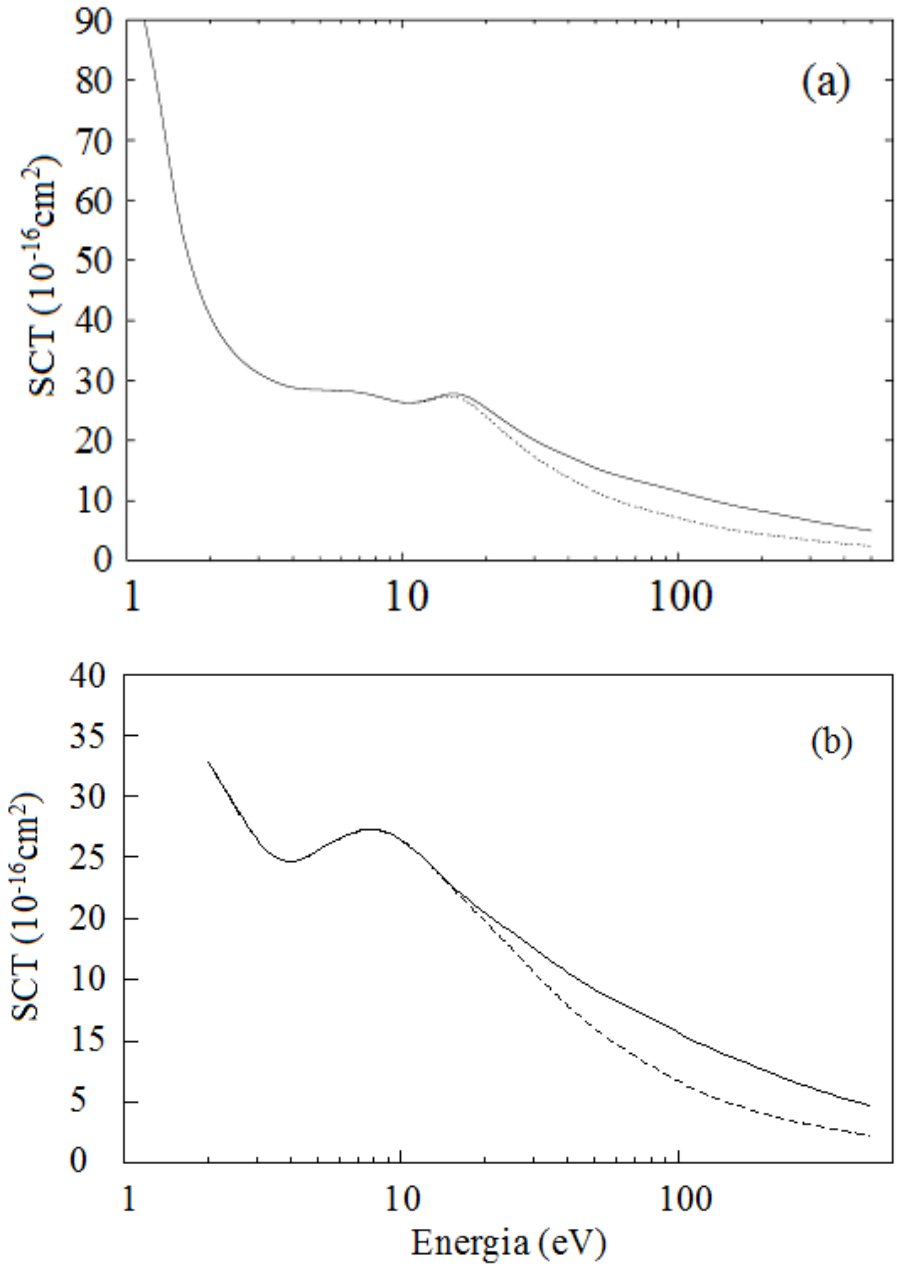

Fonte: Linha cheia, resultados teóricos de Ferraz *et al.* [12] (a) e [13] (b) da SCT calculado a partir do Teorema Óptico, eq. (34); linha pontilhada - resultados teóricos de Ferraz *et al.* [12] da SCI para CH_2O e linha tracejada, resultados teóricos de Ferraz *et al.* [13] da SCI para CH_3F, calculadas a partir da eq. (27).

Em todos os nossos cálculos, os valores da SCT foram obtidos a partir do teorema óptico, eq. (34), que leva em conta todos os efeitos de absorção que possam ocorrer dentro do ambiente molecular, enquanto que os valores de SCI elástica foram obtidos pela eq. (27). Para moléculas polares, a SCI elástica é determinada predominantemente pelos valores de SCD a pequenos ângulos de espalhamento (de 0º a ~15º) já que, devido à aplicação da correção de Born, os valores da SCD para estes ângulos podem chegar a ser da ordem de 100 ou até 1000 vezes maiores que os dos outros ângulos.

Análises de SCI a baixas energias são de muito interesse já que é nesta região que é mais frequente a ocorrência de ressonâncias. Uma ressonância é um estado do sistema elétron-molécula em que o elétron incidente é temporariamente preso na região do alvo, gerando um estado iônico de curto tempo de vida que produz uma variação aguda da seção de choque numa faixa estreita de energias, que caracteriza a localização (em energia) da ressonância. Ressonâncias são classificadas de acordo com o mecanismo pelo qual o projétil é capturado pelo alvo e podem ser do tipo *ressonância de forma* ou *ressonância de Feshbach*. No primeiro caso o mecanismo responsável pela captura da partícula incidente resulta da combinação do potencial do alvo neutro com a barreira centrífuga – barreira de momento angular, $l(l+1)/r^2$, que é uma parcela do potencial efetivo U_{eff} da equação de Schrödinger para as componentes da expansão em onda parciais, dada por [18]

$$U_{eff} = U(r) + \frac{l(l+1)}{r^2}. \tag{99}$$

A barreira centrifuga é repulsiva e fica mais alta a medida que l aumenta, tornando a contribuição do potencial espalhador cada vez menor. A Fig. (14) mostra a variação do potencial efetivo U_{eff} para um poço quadrado profundo. A análise mostra que quanto maior for o l mais difícil fica para a partícula incidente sentir o potencial espalhador. Para $l=0$ na eq. (99), a partícula vê apenas o poço; quando $l>0$ a partícula enxerga um potencial efetivo que se modifica mostrando a seguinte situação: se a partícula estiver com energia E_1, ela sente o potencial efetivo e é espalhada, caso a partícula se encontra com uma energia E_2, esta sente o potencial repulsivo da barreira centrifuga podendo tunelar e ser capturada pela molécula e se desprender depois de um determinado tempo, gerando assim um estado virtual - não genuinamente ligado [18].

Fig. 14 - Potencial efetivo atuando na equação radial para $u_l(k,r) = rR_l(k,r)$ [18].

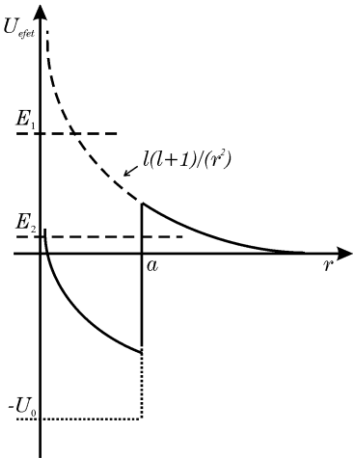

Fonte: Joachain [18]. Linha sólida, corresponde ao potencial efetivo eq. (99); linha tracejada, corresponde a barreira de potencial centrifuga $l(l+1)/r^2$; linha pontilhada, corresponde ao poço de potencial; a é a largura do poço e E é a energia da partícula incidente.

Ressonâncias de forma podem ocorrer mesmo quando a descrição do processo de colisão é feita via potenciais efetivos, como no caso deste trabalho. Por outro lado, segundo Varella [64], "ressonâncias de Feshbach ocorrem quando existe um estado do íon (composto e^--alvo) com energia muito próxima à de algum estado excitado da molécula isolada, denominado estado pai. Assim, quando a energia de impacto for pouco mais baixa que a energia de excitação do estado pai, o estado do íon poderá ser formado através de uma excitação virtual. Uma vez formado, o estado do íon tende a decair para o estado pai, pela ejeção de um elétron. No entanto, como isso não é permitido pela conservação de energia, o decaimento envolverá a ejeção de um elétron e a desexcitação da molécula, fazendo com que o tempo de colisão possa superar 10^{-13} segundos".

Nas Fig. (15a) e (15c) são mostrados os resultados de SCI obtidos para o espalhamento elástico de elétrons pelas moléculas de dimetil éter [14] e acetona [16], respectivamente. Nas Fig. (15b) e (15d) são mostrados os resultados obtidos para a SCTM para as mesmas moléculas. O intervalo de energias do elétron incidente é de 1 a 1000 eV para a molécula de dimetil éter e de 1 a 500 eV para a molécula de acetona.

Fig. 15 - (a) SCI e (b) SCTM para o espalhamento elástico e^--CH_3OCH_3 e figuras (c) SCI e (d) SCTM para o espalhamento elástico e^--CH_3COCH_3.

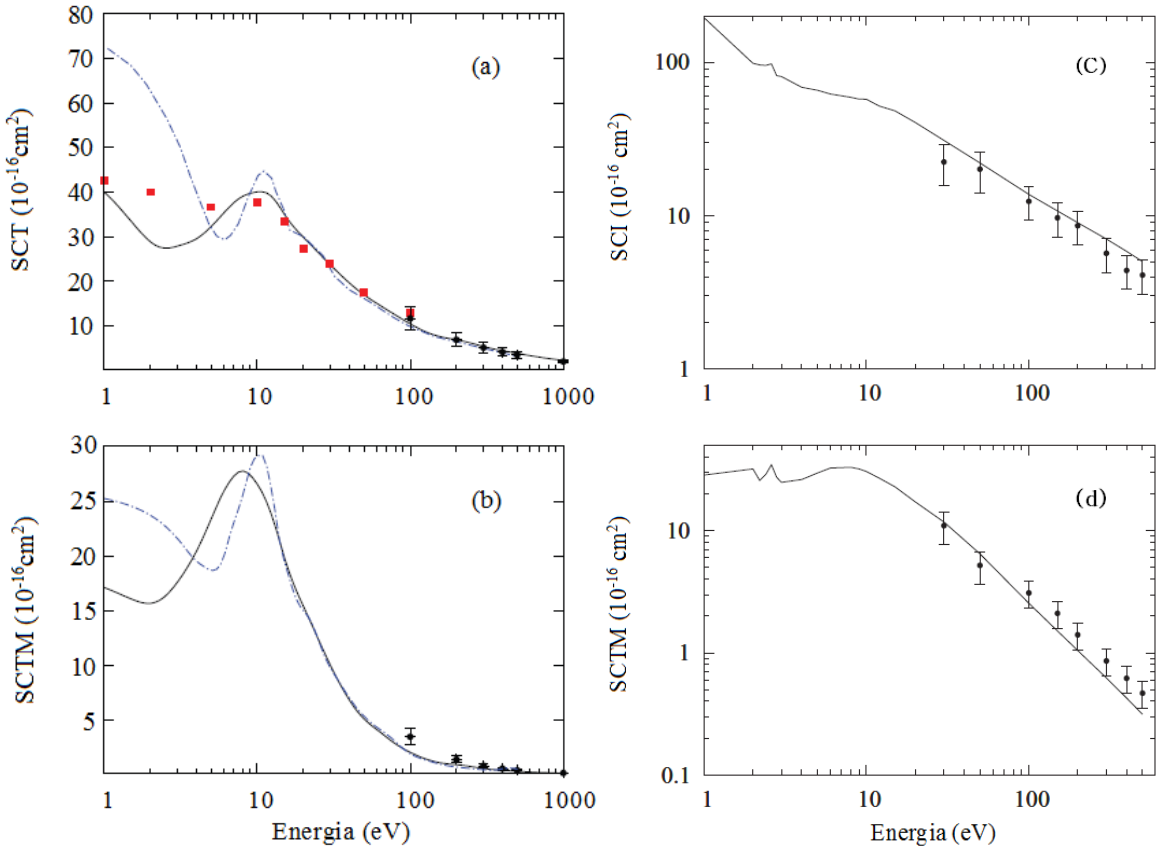

Fonte: Linha cheia, resultados teóricos de Sugohara *et al.* [14] e de Homem *et al.* [16] calculados com a correção de Born; linha traço ponto, resultados de Lee *et al.* [52] para etanol com a correção de Born; quadrados cheios, resultados experimentais de Khakoo *et al.* [63] para etanol; círculos cheios, resultados experimentais de Sugohara *et al.* [14] e de Homem *et al.* [16].

Os máximos observados nas SCI, associados à presença da ressonância, aparecem mais pronunciados em cálculos de SCTM, já que a forte contribuição das SCD nas direções próximas à direção do feixe incidente na integral, que define a SCTM [eq. (28)], é fortemente reduzida pelo fator $(1-\cos\theta)$ que multiplica a SCD naquela integral.

A estrutura observada em torno de 10 eV nos resultados da SCTM dos isômeros dimetil éter e etanol também é observada, com pouco menos intensidade, nos resultados para

a SCI na mesma região de energia. Já a estrutura observada na SCTM para a molécula de acetona, em torno de 8 eV, é muito mais atenuada na SCI devido a grande contribuição das SCD em ângulos pequenos. Já para a molécula de formaldeído a estrutura observada na SCTM é bem discreta na SCI, Fig. (16a) e (16b) [figuras (5a) e (5b) da Ref. 12]. Isto mostra a importância da SCTM na análise de possíveis ressonâncias.

Fig. 16 - (a) SCI e (b) SCTM para o espalhamento elástico e^--CH_2O estendida a faixa de energia do elétron incidente de 0.2 a 500 eV.

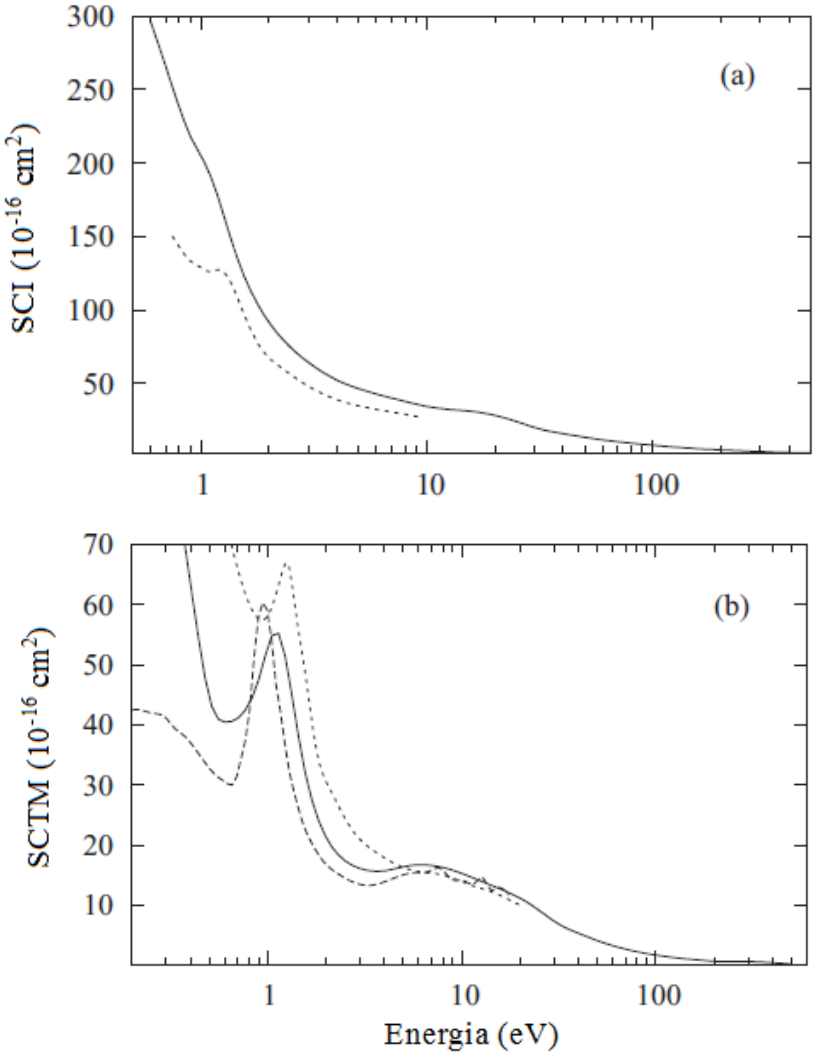

Fonte: Linha cheia, resultados teóricos de Ferraz *et al.* [12] calculados com a correção de Born; linha pontilhada, resultados de Kaur e Baluja [60] usando o método da matriz-*R* com a correção de Born; linha tracejada, resultados de Freitas *et al.* [65].

A partir dos diferentes canais do contínuo, ou seja, para as diferentes simetrias da função de onda do elétron de espalhamento, teoricamente podemos localizar em qual (ais) contínuo (os) a ressonância é representada na SCI. Para o caso da molécula de formaldeído [12] a ressonância, que também é avaliada por Kaur e Baluja [60], corresponde ao contínuo B_1, Fig. (17c).

Fig. 17 - Canais parciais da SCI para espalhamento elástico e^--CH_2O:
(a) simetria A_1; (b) simetria A_2; (c) simetria B_1; (d) simetria B_2.

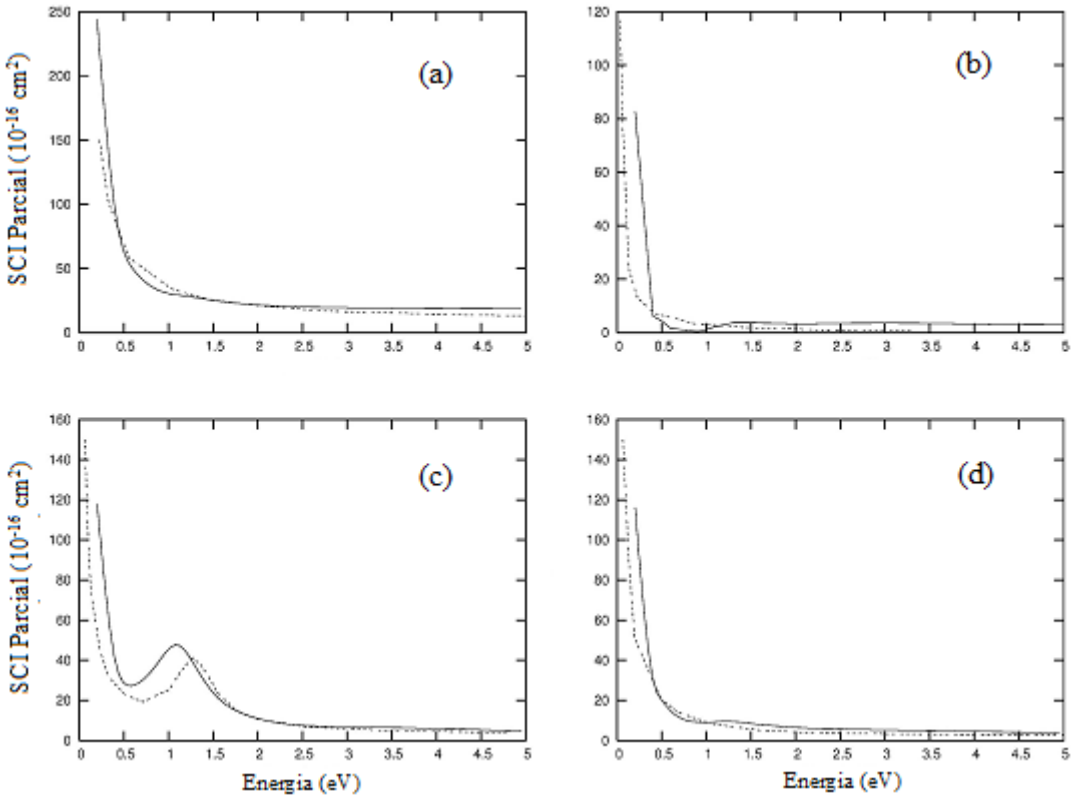

Fonte: Linha cheia, resultados teóricos de Ferraz *et al.* [12] usando o EPolyScat-D; linha pontilhada, resultados de Kaur e Baluja [60] usando o método da matriz-*R*.

A ressonância na SCI do espalhamento elástico e^--CH_3OCH_3 localizada a 10 eV e já vista na Fig. 15(a), é aqui analisada em termos das contribuições de todos os canais parciais na Fig. 18(a), [figura (10) da Ref. 14]. Nota-se que a referida ressonância é resultante da combinação de estruturas presentes nos vários canais de simetria. Já para a SCI do espalhamento elástico de elétron por moléculas de acetona Fig (15c) [figura (6a) da Ref. 16] são observadas três ressonâncias que correspondem à contribuição do contínuo B_2 para a ressonância a 2.6 eV, à soma das contribuições dos contínuos B_1 e A_2 para a ressonância (muito fraca) a 8 eV e à contribuição do contínuo A_1 para a ressonância observada em 10 eV, como se pode ver na Fig. 18(b).

Fig. 18 – (a) Canais parciais de SCI para o espalhamento elástico e^--CH_3OCH_3 para energias de 1 a 30eV e (b) canais parciais da SCI para o espalhamento elástico e^--CH_3COCH_3 para energias de 1 a 20 eV.

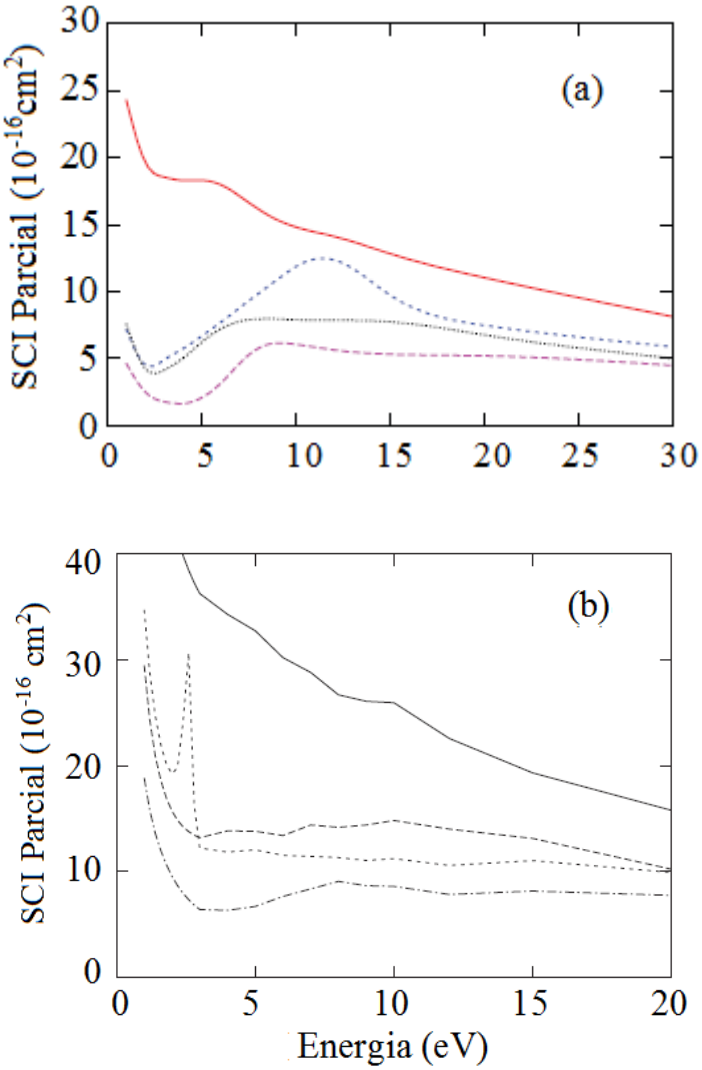

Fonte: Fig. 16a, resultados teóricos de Sugohara *et al.* [14]. Linha cheia, resultados para simetria A_1; traço longo, simetria A_2; traço curto, canal B_1; curva pontilhada, canal B_2. Fig. 16b**,** resultados teóricos de Homem *et al.* [16]. Linha cheia, resultados para simetria A_1; traço ponto, simetria A_2; traço longo, canal B_1; traço curto, canal B_2.

As Fig. (19a) e (19b) mostram resultados para a SCTA obtidos a partir da diferença da SCT pela SCI, eq. (29), e indicam a intensidade de fluxo das partículas espalhadas por todos os canais inelásticos. Nestas figuras observa-se que os valores da SCTA crescem com a energia chegando a um máximo em torno de 90 eV e diminuem a energias maiores. Na Fig. (19a) [figura (6b) da Ref. 12] nossos resultados para a SCTA estão sendo comparados com as seções de choque de ionização total (SCIT) de Kim e Irikura [66], calculados a partir do modelo BEB (*binary-encounter Bethe model*). Observa-se no gráfico que os resultados de Kim e Irikura ficam constantemente abaixo de nossos valores em todo o intervalo de energia.

Este é um comportamento esperado, já que a SCIT considera apenas os canais de ionização. Na Fig. (19b) [figura (6b) da Ref. 13] nossos resultados para CH_3F mostram-se coerentes quando comparados com os resultados teóricos e experimentais para SCIT de Vallance *et al.* [67], já os resultados experimentais para SCIT de Beran e Kevan [68] superestimam nossos resultados em todo o intervalo de energia calculados por eles, assim como os resultados teóricos para SCTA de Joshipura e Vinodkumar [69].

Fig. 19 – (a) SCTA para o espalhamento e^--CH_2O e (b) SCTA para o espalhamento e^--CH_3F.

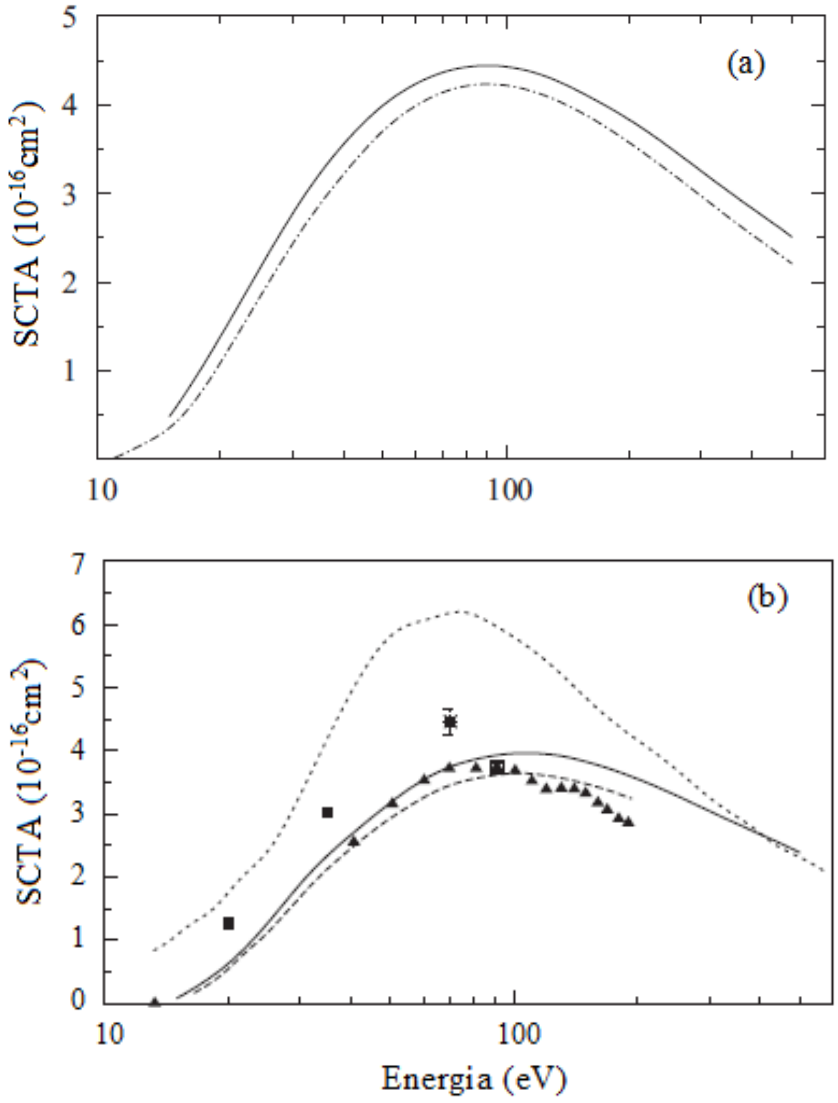

Fonte: Linha cheia, resultados teóricos de Ferraz *et al.* [12, 13] calculados com a inclusão do potencial de absorção; linha traço ponto, SCIT para o espalhamento de e^--CH_2O calculadas por Kim e Irikura [66] usando o método do encontro binário de Bethe (BEB); linha pontilhada, resultados teóricos de Joshipura e Vinodkumar [69]; linha tracejada, resultados teóricos de SCIT BEB de Vallance *et al.* [67]; quadrados cheios, resultados experimentais de Beran e Kevan [68]; triângulos cheios, resultados experimentais de Vallance *et al.* [67].

7 CONCLUSÕES E PERSPECTIVAS

Neste trabalho foram realizados estudos sobre os efeitos de absorção no espalhamento de elétrons por moléculas polares no alcance de energia para o elétron incidente de 0.2 a 500 eV. Devido à característica polar das moléculas envolvidas, a técnica de complementação de Born foi utilizada para descrever as componentes de ondas parciais mais altas na expansão da função de onda de espalhamento. Já os efeitos de absorção foram simulados sobre o canal elástico, no processo de espalhamento elétron-molécula, a partir de um modelo de potencial ótico complexo proposto pelo nosso grupo e conhecido na literatura como SQFSM.

Os estudos mostraram que o pacote computacional EPolyScat-D foi capaz de fornecer resultados de SCD, SCI, SCTM, SCT e SCTA em boa concordância com outros resultados experimentais e teóricos disponíveis na literatura, principalmente em energias intermediárias, que é exatamente a faixa de energias de interesse de nosso grupo. Isto pode ser entendido como uma afirmação da confiabilidade de nossos estudos e que, podem ser estendidos a espalhamento de elétrons por moléculas maiores e por aglomerados. Dentre outros, estudos sobre alvos como por exemplo, citosina, uracil e timina, que são complexos formados a partir da molécula de pirimidina e que tem em suas estruturas ligações com radicais e com ligações duplas de oxigênio, são de nossos interesses imediatos.

Por outo lado, a realização de estudos para moléculas com grande grau de complexidade pode ocasionar dificuldades devido à elevada demanda computacional. Vários estudos recentes mostram que para energias acima de 200 eV, métodos mais simples, como IAM, são capazes de fornecer resultados bastantes confiáveis. Nesta linha de pesquisa temos como perspectiva para um trabalho futuro o estudo de Espalhamento Múltiplo por Potenciais Atômicos, um aperfeiçoamento do método IA que introduz a interação entre os centros espalhadores. Este método deverá fornecer resultados mais precisos da SCD na faixa superior das energias intermediárias que os obtidos pelo IAM. O método também usará o mesmo modelo de potencial ótico complexo utilizado pelo EPolyScat-D e os efeitos de absorção também serão simulados sobre o canal de espalhamento elástico. Além disso, devido à menor demanda computacional, ele permitirá a utilização de um grande número de componentes de ondas parciais na expansão das amplitudes de espalhamento atômicas.

REFÊRENCIAS BIBLIOGRÁFICAS

[1] Burke, Antony. Química Orgânica: Sempre Presente!: Universidade de Évora – Departamento de Química. Disponível em: <http://home.uevora.pt/%7Eueline/quimica_para_todos/quimica_organica_sempre-presente.pdf>. Acesso em: 27 jan. 2017.

[2] Verbeek, R.; Smokers, R. T. M.; Kadijk. G.; Hensema, A.; Passier, G. L. M.; Rabé, E. L. M.; Kampman, B.; Riemersma, I. J. Verbeek, R. and Van der Weide, J. **Impact of biofuels on air pollutant emissions from road vehicles - TNO report MON-RPT-33-DTS-2008-01737.** Delft: TNO Science and Industry, 2008.

[3] Verbeek, R. and Van der Weide, J., Global Assessment of Dimethyl-Ether: Comparison with Other Fuels. **SAE Technical Paper 971607**, p.1-14, 1997.

[4] Peeters, Z.; Rodgers, S. D.; Charnley, S. B.; Schriver-Mazzuoli, L.; Schriver, A.; Keane, J. V. and Ehrenfreund, P. Astrochemistry of dimethyl ether. **Astronomy & Astrophysics**, v.445, n.1, p.197-204, 2006.

[5] Boudaïffa, B.; Cloutier, P.; Hunting, D.; Huels, M. A. and Sanche, L. Resonant Formation of DNA Strand Breaks by Low-Energy (3 to 20 eV) Electrons. **Science**, v.287, p.1658-1660, 2000.

[6] Sanches, L. **Eur. Phys. J. D**., v.35, n.367, 2005.

[7] Morgan, W. L. Electron Collision Data for Plasma Chemistry Modeling. **Adv. At. Mol. Opt. Phys.**, v.43, p.79-110, 2000.

[8] Gianturco F.A.; Lucchese R.R.; and Sanna N. On the scattering of low-energy electrons by sulphur hexafluoride. ***J. Chem. Phys.***, v.102, n.14, p.5743-5751, 1995.

[9] Lee M.T.; Iga I.; Machado L.E.; Brescansin L.M.; y Castro E.A.; Sanches I.P. and de Souza G.L.C. Improvement on the complex optical potential for electron collisions with atoms and molecules. **J. Electron Spectrosc. Rel. Phenom.**, v.155, p.14-20, 2007.

[10] Staszewska G.; Schwenke D. W.; and Truhlar D. G. Investigation of the shape of the imaginary party of the aptical-madel potencial for elecron scattering by rares gases. **Phys. Rev. A**, v.29, n.6, p.3078-3091, 1984.

[11] Homem, M. G. P.; Iga, I.; de Souza, G. L. C.; Zanelato, A. I.; Machado, L. E.; Ferraz J. R.; dos Santos, A. S.; Brescansin, L. M.; Lucchese, R. R. e Lee, M. T. Electron collisions with ammonia and formamide in the low- and intermediate-energy ranges. **Phys. Rev. A**, v.90, p.062704/1-0627049/9, 2014.

[12] Ferraz, J. R.; dos Santos, A. S.; de Souza, G. L. C.; Zanelato, A. I.; Alves, T. R. M.; Lee, M. T.; Brescansin, L. M.; Lucchese, R. R. e Machado, L. E. Cross sections for electron scattering by formaldehyde and pyrimidine in the low- and intermediate-energy ranges. **Phys. Rev. A,** v.87, p.032717/1-032717/10, 2013.

[13] Ferraz, J. R.; dos Santos, A. S.; de Souza, G. L. C.; Lee, M. T.; Brescansin, L. M.; Lucchese, R. R. e Machado L.E. Cross sections for electron scattering by methylfluoride (CH_3F) in the low and intermediate-energy ranges. **J. Electron Spectrosc. Rel. Phenom.**, v.193, p.16-20, 2014.

[14] Sugohara, R. T.; Homem, M. G. P.; Iga, I.; de Souza, G. L. C.; Machado, L. E.; Ferraz, J. R.; dos Santos, A. S.; Brescansin, L. M.; Lucchese, R. R. e Lee, M. T. Cross sections for electron collisions with dimethyl ether. **Phys. Rev. A**, v.88, p.022709/1-022709/9, 2013.

[15] Homem, M. G. P.; Iga, I.; Ferraz, J. R.; de Souza, G. L. C.; dos Santos, A. S.; Machado, L. E.; Brescansin L. M.; Lucchese, R. R. e Lee, M. T. Theoretical and experimental investigation of electron collisions with dimethyl sulfide. **Phys. Rev. A**, v.91, p.012713/1-012713/7, 2015.

[16] Homem, M. G. P.; Iga, I.; da Silva, L. A.; Ferraz, J. R.; Machado, L. E.; de Souza, G. L. C.; da Mata, V. A. S.; Brescansin, L. M.; Lucchese, R. R. e Lee, M. T. Theoretical and experimental investigation of electron collisions with acetone. **Phys. Rev. A**, v.92, p.032711/1-032711/8, 2015.

[17] Joshipura, K. N.; Vinodkumar, M. and Patel, U. M. Electron impact total cross sections of CH_x, NH_x and OH radicals *vis-à-vis* their parent molecules. **J. Phys. B: At. Mol. Opt. Phys.**, v.34, p.509-519, 2001.

[18] Joachain, C. J. **Quantum Collision Theory.** Amsterdam: North-Holland, 1975.

[19] Bransden, B. H. and Joachain, C. J. **Physics of Atoms and Molecules.** New York: Longman Scientific & Technical, 1983.

[20] Perdew, J. P. and Zunger, A. Self-interaction correction to density-functional approximations for many-electron systems. **Phys. Rev. B**, v.23, p.10, 5048-5079, 1981.

[21] de Souza, G. L. C.; Lee, M. T.; Sanches, I. P.; Rawat, P.; Iga, I.; dos Santos, A. S.; Machado, L. E.; Sugohara, R. T.; Brescansin, L. M.; Homem, M. G. P. and Lucchese, R. R. Cross sections for electron scattering by propane in the low- and intermediate-energy ranges. **Phys. Rev. A**, v.82, p.012709/1-012709/8, 2010.

[22] Hara, S. Scattering of slow electrons by hydrogen molecules. **J. Phys. Soc. Japan**, v.22, n.3, p.710-718, 1967.

[23] Fliflet, A. W. and Mckoy, V. Distorted-wave-approximation for excitation of the $b^3\sum_u^+$ and $B^1\sum_u^+$ states of H_2 by low-energy-electron impact. **Phys. Rev. A**, v.21, n.6, p.1863-1875, 1980.

[24] Burke, P. G.; Chandra, N. and Gianturco, F. A. Electron-molecule interactions IV. Scattering by polyatomic molecules. **J. Phys. B: Atom. Molec. Phys.**, v.5, p.2212-2224, 1972.

[25] Edmonds, A. R. **Angular Momentum in Quantum Mechanics.** 2.ed., Princeton: Princeton University Press, 1960.

[26] de Souza, G. L. C.; y Castro, E. A.; Machado, L. E.; Brescansin, L. M.; Iga, I. and Lee, M. T. Theoretical study on electron collisions with SiF and SiF_2 radicals in the low- and intermediate-energy range. **Phys. Rev. A**, v.76, p.042706/1-042706/9, 2007.

[27] Chase, D. M. Adiabatic Approximation for Scattering Processes. **Phys. Rev.**, v.104, n.3, p.838-842, 1956.

[28] Levine, I. N. **Quantum Chemistry.** 4.ed. Englewood Cliffs: Prentice Hall, 1991.

[29] NIST. National Institute of Standards and Technology. Disponível em: <http://cccbdb.nist.gov/expdatax.asp>. Acesso em: 27 jan. 2017

[30] Padial, N. T. and Norcross, D. W. Parameter-free model of the correlation-polarization potential for electron-molecule collisions. **Phys. Rev. A**, v.29, n.4, p.1742-1748, 1984.

[31] Souza, M. A. M. Modelo Óptico das Reações Nucleares: Determinação fenomenológica e analítica do Potencial Óptico. **Lat. Am. J. Phys. Educ.**, v.4, n.1, p.251-257, 2010.

[32] McCarthy, I. E.; Noble, C. J.; Phillips, A. and Turnbull, A. D. Optical model for electron scattering from inert gases. **Phys. Rev. A**, v.15, n.6, p.2173-2185, 1977.

[33] Staszewska, G.; Schwenke, D. W.; Thirumalai, D. and Truhlar, D. G. Non-empirical model for the imaginary part of the optical potential for electron scattering. **J. Phys. B**, v.16, p.L281-L287, 1983.

[34] Staszewska, G.; Schwenke, D. W.; Thirumalai, D. and Truhlar D. G. Quasifree-scattering model for the imaginary part of the optical potential for electron scattering. **J. Phys. Rev. A**, v.28, n.5, p.2740-2751, 1983.

[35] Iga, I.; Lee, M. T.; Homem, M. G. P.; Machado, L. E. and Brescansin, L. M. Elastic cross sections for e^--CH4 collisions at intermediate energies. **Phys. Rev. A**, v.61, p.022708/1-022708/8, 2000.

[36] Lee, M. T.; Iga, I.; Brescansin, L. M.; Machado, L. E. and Machado, F. B. C. Theoretical studies on electron-carbon monoxide collisions in the low and intermediete energy range. **J. Mol. Struct. (Theochem)**, v.585, p.181-187, 2002.

[37] Brescansin, L. M.; Rawat, P.; Iga, I.; Homem, M. G. P.; Lee, M. T. and Machado, L. E. Elastic and absorption cross sections for electron scattering by ethylene in the intermediate energy range. **J. Phys. B: At. Mol. Opt. Phys.**, v.37, p.471–483, 2004.

[38] Lee, M. T.; Iga, I.; Machado, L. E.; Brescansin, L. M.; y Castro, E. A. and de Souza, G. L. C. Theoretical study of electron collisions with the CF_2 radical. **Phys. Rev. A**, v.74, p.052716/1-052716/7, 2006.

[39] Cho, H.; Park, Y. S.; y Castro, E. A.; de Souza, G. L. C.; Iga, I.; Machado, L. E.; Brescansin, L. M. and Lee, M. T. A comparative experimental–theoretical study on elastic electron scattering by methane. **J. Phys. B: At. Mol. Opt. Phys.**, v.41, p.045203/1-045203/7, 2008.

[40] Lee, M. T.; Iga, I.; Machado, L. E. and Brescansin, L. M. Theoretical investigation of electron collisions with sulfur monoxide in the low- and intermediate-energy range. **Phys. Rev. A**, v.80, p.022706/1-022706/8, 2009.

[41] Brescansin, L. M.; Iga, I.; Machado, L. E.; Michelin, S. E. and Lee, M. T. Cross sections for electron scattering by carbon disulfide in the low- and intermediate-energy range. **Phys. Rev. A**, v.81, p.012709/1-012709/6, 2010.

[42] Machado, L. E.; Sugohara, R. T.; dos Santos, A. S.; Lee, M. T.; Iga, I.; de Souza, G. L. C.; Homem, M. G. P.; Michelin, S. E. and Brescansin, L. M. Absorption effects in electron–sulfur-dioxide collisions. **Phys. Rev. A**, v.84, p.032709/1-032709/9, 2011.

[43] Raj, D. and Tomar, S. Electron scattering by triatomics: SO_2, CS_2 and OCS at intermediate energies. **J. Phys. B: At. Mol. Opt. Phys.**, v.30, p.1989–1999, 1997.

[44] Orient, O. J.; Iga, I. and Srivastava, S. K. Elastic scattering of electrons from SO_2. **J. Chem. Phys.**, v.77, n.7, p.3523-3526, 1982.

[45] Schmidt, M. W.; Baldridge, K. K.; Boatz, J. A.; Elbert, S. T.; Gordon, M. S.; Jensen, J. H.; Koseki, S.; Matsunaga, N.; Nguyen, K. A.; Su, S.; Windus, T. L.; Dupuis, M. and Montgomery, J. A. **J. Comput. Chem.** v.14, p.1347, 1993.

[46] Frisch, M. J.; Trucks, G. W.; Schlegel, H. B.; Scuseria, G. E.; Robb, M. A.; Cheese-man, J. R.; Montgomery Jr., J. A.; Vreven, T.; Kudin, K. N.; Burant, J. C.; Millam, J. M.; S.S.Iyengar, J. Tomasi, V. Barone, B. Mennucci, M. Cossi, G. Scalmani, N. Rega, G.A.Petersson, H. Nakatsuji, M. Hada, M. Ehara, K. Toyota, R. Fukuda, J. Hasegawa,M. Ishida, T. Nakajima, Y. Honda, O. Kitao, H. Nakai, M. Klene, X. Li, J.E. Knox, H.P.Hratchian, J.B. Cross, V. Bakken, C. Adamo, J. Jaramillo, R. Gomperts, R.E. Strat-mann, O. Yazyev, A.J. Austin, R. Cammi, C. Pomelli, J.W. Ochterski, P.Y. Ayala, K.Morokuma, G.A. Voth, P. Salvador, J.J. Dannenberg, V.G. Zakrzewski, S. Dapprich,A.D. Daniels, M.C. Strain, O. Farkas, D.K. Malick, A.D. Rabuck, K. Raghavachari,J.B. Foresman, J.V. Ortiz, Q. Cui, A.G. Baboul, S. Clifford, J. Cioslowski, B.B. Ste-fanov, G. Liu, A. Liashenko, P. Piskorz, I. Komaromi, R.L. Martin, D.J. Fox, T. Keith,M.A. Al-Laham, C.Y. Peng, A. Nanayakkara, M. Challacombe, P.M.W. Gill, B. John-son, W. Chen, M.W. Wong, C. Gonzalez, J.A. Pople, Gaussian 03, Revision C. 02, Gaussian Inc., Wallingford, CT, 2004.

[47] Herzberg G. **Molecular Spectra and Molecular Structure III. Electronic Spectra and Electronic Structure of Polyatomic Molecules.** New York, NY (USA): Van Nostrand Reinhold Co., 1966.

[48] Natalense, A. P. P.; Bettega, M. H. F.; Ferreira, L. G. and Lima, M. A. P. Halogenation effects in electron scattering from CHF_3, CH_2F_2, CH_3F, HCl_3, CH_2Cl_2, CH_3Cl, $CFCl_3$, CF_2Cl_2, and CF_3Cl. **Phys. Rev. A**, v.59, n.1, p.879-881, 1999.

[49] Varella, M. T. N.; Winstead, C.; McKoy, V.; Kitajima, M. and Tanaka, H. Low-energy electron scattering by CH_3F, CH_2F_2, CHF_3, and CF_4. **Phys. Rev. A**, v.65, n.2, p.022702/1-022702/17, 2002.

[50] Tanaka, H.; Masai, T.; Kimura, M.; Nishimura, T. and Itikawa, Y. Fluorination effects in electron scatterings from CH_4, CH_3F_1, CH_2F_2, CH_1F_3, and CF_4. **Phys. Rev. A**, v.56, n.5, p.R3338-R3341, 1997.

[51] Maljkovic, J. B.; Blanco, F.; García, G. and Milosavljevic, A. R. Elastic electron scattering from formamide molecule. **Nuclear Instruments and Methods in Physics Research B**, v.279, p124, 2012.

[52] Lee, M. T.; de Souza, G. L. C.; Machado, L. E.; Brescansin, L. M.; dos Santos, A. S.; Lucchese, R. R.; Sugohara, R. T.; Homem, M. G. P.; Sanches, I. P. and Iga, I. Electron scattering by methanol and ethanol: A joint theoretical-experimental investigation; **Journal of Chemical Phys.**, v.136, p.114311/1-114311/7, 2012.

[53] Rao, K. C.; Bhushan, K. G.; Mukund, R.; Gadkari, S. C. and Yakhmi, J. V. Elastic scattering of electrons from dimethylsulfide and dimethylsulfoxide. **Phys. Rev. A**, v.79, n.6, p.062714/1-062714/8, 2009.

[54] Hayashi, S. and Kuchitsu, K. Elastic scattering of electrons by molecules at intermediate energies. Calculation of double scattering effects in N_2 and P_4. **Chemical Physics Letters**, v.41, n.3, p.575-579, 1976.

[55] Rawat, P.; Homem, M. G. P.; Sugohara, R. T.; Sanches, I. P.; Iga, I.; de Souza, G. L. C.; dos Santos, A. S.; Lucchese, R. R.; Machad,o L. E.; Brescansin, L .M. and Lee, M. T. Cross sections for electron scattering by ethane in the low and intermediate energy ranges. **J. Phys. B. At. Mol. Opt. Phys.**, v.43, p.225202/1-225202/8, 2010.

[56] de Souza, G. L. C.; dos Santos, A. S.; Lucchese, R. R.; Machado, L. E.; Brescansin, L. M.; Manini, H. V.; Iga, I. and Lee, M. T. Theoretical investigation on electron scattering by benzene in the intermediate-energy range. **Chemical Physics**, v.393, p.19–24, 2012.

[57] Rescigno, T. N.; Lengsfield, B. H.; McCurdy, C. W. and Parker, S. D. Ab initio description of polarization in low-energy electron collisions with polar molecules: Application to electron- NH_3 scattering. **Phys. Rev. A**, v.45, n.11, p.7800-7809, 1992.

[58] Munjal, H. and Baluja, K. L. Electron-impact study of PH_3: an *R*-matrix approach. **J. Phys. B**, 40, v.10, p.1713-1718, 2007.

[59] Alle, D. T.; Gulley, R. J.; Buckman, S. J. and Brunger, M. J. Elastic scattering of low-energy electrons from ammonia. **J. Phys. B**, v.25, n.7, p.1533-1542, 1992.

[60] Kaur. S. and Baluja, K. L. Electron-impact study of formaldehyde using the *R*-matrix method. **J. Phys. B**, v.38, n.21, p.3917-3933, 2005.

[61] Masín, Z.; Gorfinkiel, J. D.; Jones, D. B.; Bellm, S. M. and Brunger, M. J. Elastic and inelastic cross sections for low-energy electron collisions with pyrimidine. **J. Chem. Phys.**, v.136, n.14, p.144310/1-144310/10, 2012.

[62] Palihawadana, P.; Sullivan, J.; Brunger, M.; Winstead, C.; McKoy, V.; Garcia, G.; Blanco, F. and Buckman, S. Low-energy elastic electron interactions with pyrimidine. **Phys. Rev. A**, v.84, p.062702/1-062702/8, 2011.

[63] Khakoo, M. A.; Blumer, J.; Keane, K.; Campbell, C.; Silva, H.; Lopes, M. C. A.; Winstead, C.; McKoy, V.; da Costa, R. F.; Ferreira, L. G.; Lima, M. A. P. and Bettega, M. H. F. Low-energy electron scattering from methanol and ethanol. **Phys. Rev. A**, v.77, n.4, p.042705/1-042705/10, 2008.

[64] Varella, M. T. N. O Método Multicanal de Schwinger Aplicado ao Espalhamento de Elétrons I: Aspectos Formais. **Revista Physicae**, v.1, p.45-53, 2000.

[65] Freitas, T. C.; Lima, M. A. P.; Canuto, S. and Bettega, M. H. F. Electron collisions with the CH_2O-H_2O complex. **Phys. Rev. A**, v.80, n.6, p.062710/1-062710/4, 2009.

[66] Kim, Y. K. and Irikura, K. K. Proc. 2nd Int. Conf. on Atom. Molec. Data and Their Applications, ed. by K.A. Berrington and K.L. Bell, AIP Conf. Proc. (AIP, New York, NY), v.543, p.220, 2000. Disponível em: <https://www.nist.gov/pml/electron-impact-cross-sections-ionization-and-excitation-database>. Acesso em: 10 fev. 2017.

[67] Vallance, C.; Harris, S. A.; Hudson, J. E. and Harland P. W. Absolute electron impact ionization cross sections for CH_3X, where X=H, F, Cl, Br, and I. **J. Phys. B**, v.30, n.10, p.2465-2475, 1997.

[68] Beran, J. A. and Kevan, L. Molecular electron ionization cross sections at 70 eV. **J. Phys. Chem.**, v.73, n.11, p.3866-3876, 1969.

[69] Joshipura, K. N. and Vinodkumar, M. Various total cross-sections for electron impact on C_2H_2, C_2H_4 and CH_3X (X = CH_3, OH, F, NH_2). **Eur. Phys. J. D.**, v.5, n.2, p.229-235, 1999.

[70] Roy Dennington, Todd Keith and John Millam. GaussView, Version 5, **Semichem Inc.**, Shawnee Mission KS, 2009.

[71] Dunning Jr, T. H. **J. Chem. Phys.**, v.53, p.2823, 1970.

[72] Shoolery, J. N. and Sharbaugh, A. H. Some Molecular Dipole Moments Determined by Microwave Spectroscopy. **Phys. Rev.**, v.82, p.95, 1951.

[73] Bettega, M. H. F. Collisions of low-energy electrons with formamide. **Phys. Rev. A**, v.81, p.062717/1-062717/5, 2010.

[74] Blackman, G. L.; Brown, R. D. and Burden, F. R. The microwave spectrum, dipole moment, and nuclear quadrupole coupling constants of pyrimidine. **J. Mol. Spectrosc.**, v.35, n.3, p.444-454, 1970.

APÊNDICE A – Propriedades Moleculares

Serão apresentadas neste apêndice a fórmula e estrutura molecular das moléculas em estudo neste trabalho assim como o grupo ponto (grupo de simetria) a qual pertencem. Também será apresentado o conjunto de base Gaussiana, utilizada no programa GAMESS [45] ou no programa GAUSSIAN [46], para a obtenção da função de onda para o estado fundamental da molécula, para cada molécula em estudo neste trabalho (informação que também está disponível no artigo referente à molécula) a partir da geometria molecular experimental [29].

Algumas das propriedades obtidas no programa GAMESS ou no programa GAUSSIAN, para cada molécula em estudo, tais como: o momento de dipolo elétrico (apresentadas em unidades atômicas - *a.u*[4]) e a polarizabilidade α_0 juntamente com suas componentes α_{xx}, α_{yy} e α_{zz} [apresentadas em unidades atômicas de - a_0^3][5] estão disponíveis em quadros a seguir, além de informações experimentais disponíveis na literatura. Para melhor organização desta tese e direcionamento da leitura as informações abaixo, referentes as moléculas, estão apresentadas em ordem crescente ao número de átomos que compõem cada molécula.

A fórmula estrutural para cada molécula em estudo, apresentadas abaixo, é de domínio público e podem ser encontradas em livros didáticos ou na internet. Devido a simplicidade destas estruturas, estas foram feitas pelo autor no aplicativo Paint (Windows).

[4] Fator de conversão - *a.u.* - Debye (2,5414).

[5] Fator de conversão - a_0^3 - Å^3 (6,7567).

Amônia - NH_3

O grupo ponto a qual a molécula de amônia pertence é o C_{3V}. A função de onda no HF-SCF para o estado fundamental da molécula de amônia foi obtida usando um conjunto base de funções gaussianas aug-cc-pVTZ (6*d*, 10*f*) no programa GAUSSIAN [46] na geometria molecular experimental [29].

Fig. 20 – (a) Fórmula estrutural e (b) configuração espacial da molécula de amônia.

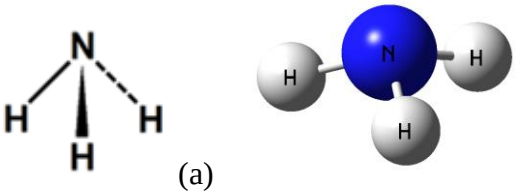

(a) (b)

Fonte: (a) elaborado pelo autor, (b) modelo virtual desenvolvido no GaussView [70]

Quadro 1 – Propriedades físicas da molécula de amônia.

	Dipolo elétrico *(a.u)*	$\alpha_0\ (a_0^3)$	$\alpha_{xx}\ (a_0^3)$	$\alpha_{yy}\ (a_0^3)$	$\alpha_{zz}\ (a_0^3)$
GAMESS	0.5777	12.473	12.31	12.31	12.80
Exp.	0.5784 [29]	14.192 [29]			

Fonte: Elaborado pelo autor.

Formaldeído – CH_2O

A molécula de formaldeído pertencente ao grupo ponto C_{2v}. A função de onda no HF-SCF para o estado fundamental da molécula de formaldeído foi obtida usando um conjunto base de funções Gaussianas cartesianas de Dunning [71]. Para o átomo de carbono, o conjunto base [9s5p/5s3p] foi aumentada em três funções *s* (α = 0.0473, 0.0125 e 0.0045), quatro funções *p* (α = 0.0825, 0.365, 0.125 e 0.0035) e três funções *d* (α = 0.756, 0.15 e 0.0375). Para o átomo de oxigênio, o conjunto base [9s5p/3s3p] foi aumentada em três funções *s* (α = 0.0473, 0.0125 e 0.0045), quatro funções *p* (α = 0.0825, 0.365, 0.125 e 0.0035) e três funções d (α = 0.756, 0.15 e 0.0375) e para o para o átomo de hidrogênio, o conjunto base [4s4p/2s1p] foi aumentada em três funções *p* (α = 0.3, 0.012 e 0.04). As funções aumentadas para todos os átomos são funções não contraídas (primitivas). Na geometria de equilíbrio experimental $R_{(O-C)} = 2.286 a.u.$ e $R_{(C-H)} = 2.082 a.u.$

Fig. 21 – (a) fórmula estrutural e (b) configuração espacial da molécula de formaldeído.

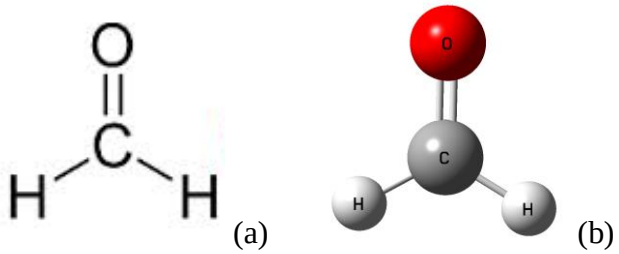

(a) (b)

Fonte: (a) elaborado pelo autor, (b) modelo virtual desenvolvido no GaussView [70]

Quadro 2 – Propriedades físicas da molécula de formaldeído.

	Dipolo elétrico *(a.u)*	$\alpha_0\,(a_0^3)$	$\alpha_{xx}\,(a_0^3)$	$\alpha_{yy}\,(a_0^3)$	$\alpha_{zz}\,(a_0^3)$
GAMESS	1,1214	16.5531	16.2486	12.3329	21.0778
Exp.	0.9207 [72]	18.69 [29]			

Fonte: Elaborado pelo autor.

Fluorometano (Fluoreto de Metila) – CH_3F

A molécula de fluorometano pertence ao grupo ponto C_{3V}. A função de onda no HF-SCF para o estado fundamental da molécula de fluorometano foi obtida usando um conjunto base de funções gaussianas aug-cc-pVTZ do programa GAUSSIAN [46] na geometria molecular experimental [29].

Fig. 22 – (a) fórmula estrutural e (b) configuração espacial da molécula de fluorometano.

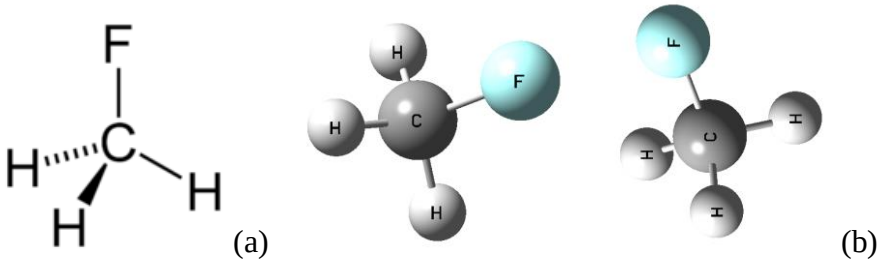

Fonte: (a) elaborado pelo autor, (b) modelo virtual desenvolvido no GaussView [70]

Quadro 3 – Propriedades físicas da molécula de fluorometano.

	Dipolo elétrico *(a.u)*	$\alpha_0\ (a_0^3)$	$\alpha_{xx}\ (a_0^3)$	$\alpha_{yy}\ (a_0^3)$	$\alpha_{zz}\ (a_0^3)$
GAUSSIAN	0.8042	15.54	15.23	15.23	16.16
Exp.	0.7279 [72]	17.14 [29]			

Fonte: Elaborado pelo autor.

Formamida – NH_2CHO

O grupo ponto a qual a molécula de formamida pertence é o C_S. A função de onda no HF-SCF para o estado fundamental da molécula de formamida foi obtida usando um conjunto base de funções gaussianas cartesianas DZV (double-zeta valence) do programa GAMESS [45] na geometria molecular experimental [29].

Fig. 23 – (a) fórmula estrutural e (b) configuração espacial da molécula de formamida.

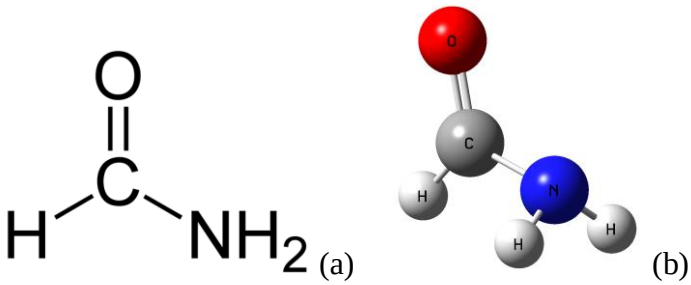

Fonte: (a) elaborado pelo autor, (b) modelo virtual desenvolvido no GaussView [70]

Quadro 4 – Propriedades físicas da molécula de formamida.

	Dipolo elétrico *(a.u)*	$\alpha_0\ (a_0^3)$	$\alpha_{xx}\ (a_0^3)$	$\alpha_{yy}\ (a_0^3)$	$\alpha_{zz}\ (a_0^3)$
GAMESS	1.6715	17.85	24.970	19.21	9.37
Exp.	1.6841 [73] 1.4676 [29]	27.53 [29]			

Fonte: Elaborado pelo autor.

Dimetil éter – CH_3OCH_3

O grupo ponto a qual a molécula de dimetil éter pertence é o C_{2v}. A função de onda no HF-SCF para o estado fundamental da molécula de dimetil éter foi obtida usando um conjunto base de funções gaussianas cartesianas TZV (triple-zeta valence) do programa GAMESS [45] aumentadas de duas funções *d* não contraídas no átomo de oxigênio ($\alpha = 2.56$ e $\alpha = 0.64$) e em cada átomo de carbono ($\alpha = 1.44$ e $\alpha = 0.36$) na geometria molecular experimental [29].

Fig. 24 – (a) fórmula estrutural e (b) configuração espacial da molécula de dimetil éter.

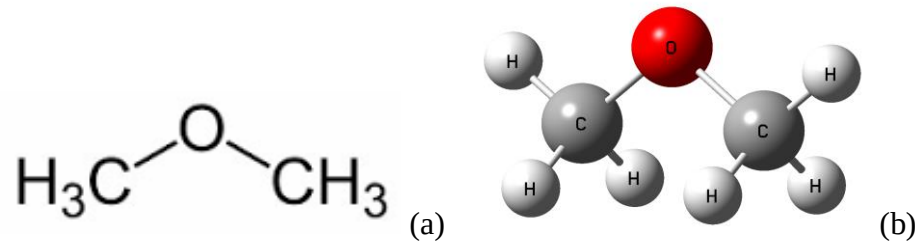

Fonte: (a) elaborado pelo autor, (b) modelo virtual desenvolvido no GaussView [70]

Quadro 6 – Propriedades físicas da molécula de dimetil éter.

	Dipolo elétrico *(a.u)*	$\alpha_0\ (a_0^3)$	$\alpha_{xx}\ (a_0^3)$	$\alpha_{yy}\ (a_0^3)$	$\alpha_{zz}\ (a_0^3)$
GAMESS	0.5619	31.323	28.810	36.036	29.122
Exp.	0.5115 [29]	34.82 [29]			

Fonte: Elaborado pelo autor.

Dimetil Sulfeto – CH_3SCH_3

O grupo ponto a qual a molécula de dimetil sulfeto pertence é o $C_{2V.}$ A função de onda no HF-SCF para o estado fundamental da molécula de dimetil sulfeto foi obtida usando um conjunto base gaussiana cartesianas TZV (triple-zeta valence) do programa GAMESS [45] aumentadas de três funções Gaussianas Cartesianas *d* primitivas no átomo de sulfeto ($\alpha = 2.168$, $\alpha = 0.542$ e $\alpha = 0.1355$) e em cada átomo de carbono ($\alpha = 2.88$, $\alpha = 0.72$ e $\alpha = 0.18$) na geometria molecular experimental [29].

Fig. 25 – (a) fórmula estrutural e (b) configuração espacial da molécula de dimetil sulfeto.

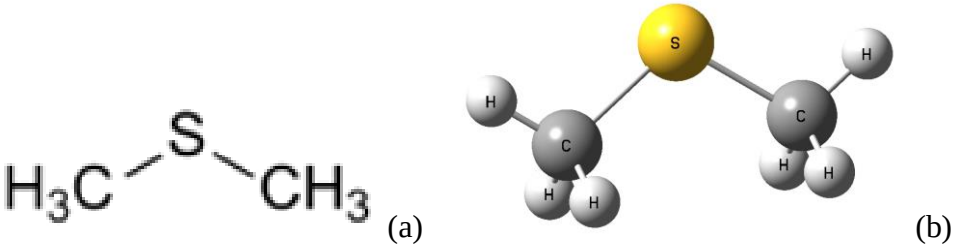

Fonte: (a) elaborado pelo autor, (b) modelo virtual desenvolvido no GaussView [70]

Quadro 7 – Propriedades físicas da molécula de dimetil dulfeto.

	Dipolo elétrico *(a.u)*	$\alpha_0\,(a_0^3)$	$\alpha_{xx}\,(a_0^3)$	$\alpha_{yy}\,(a_0^3)$	$\alpha_{zz}\,(a_0^3)$
GAMESS	0.6758	49.72	53.06	52.09	44.02
Exp.	0.5902 [29]	50.95 [29]			

Fonte: Elaborado pelo autor.

Pirimidina - $C_4H_4N_2$

A moléculas de pirimidina pertencente ao grupo ponto C_{2v}. A função de onda no HF-SCF para o estado fundamental da molécula de pirimidina foi obtida usando um conjunto base de funções gaussianas cartesianas TZVDP (triple-zeta valence plus d-Polarization) contraída, enquanto que, a polarizabilidade α_0 juntamente com suas componentes α_{xx}, α_{yy} e α_{zz} foram obtidos, também na aproximação HF-SCF, na base gaussiana aug-cc-pVDZ. Ambos os cálculos foram realizados no código de química quântica GAMESS [45] na geometria molecular experimental [29].

Fig. 26 – (a) fórmula estrutural e (b) configuração espacial da molécula de pirimidina.

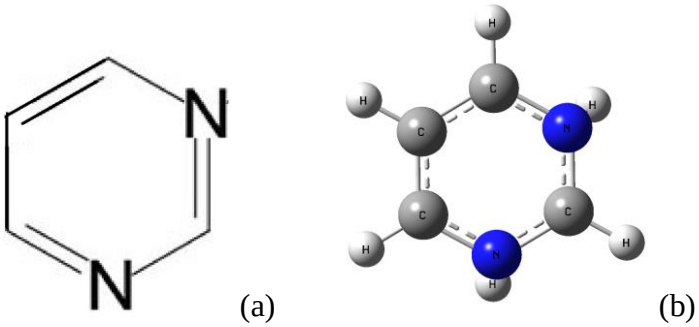

Fonte: (a) elaborado pelo autor, (b) modelo virtual desenvolvido no GaussView [70]

Quadro 8 – Propriedades físicas da molécula de pirimidina.

	Dipolo elétrico *(a.u)*	$\alpha_0\,(a_0^3)$	$\alpha_{xx}\,(a_0^3)$	$\alpha_{yy}\,(a_0^3)$	$\alpha_{zz}\,(a_0^3)$
GAMESS	0.9385 *u.a.*	45.553	22.54	55.06	59.06
Exp.	0.9184 *u.a.* [74]				

Fonte: Elaborado pelo autor.

Acetona - CH_3COCH_3

A molécula de acetona pertence ao grupo ponto $C_{2V.}$ A função de onda no HF-SCF para o estado fundamental da molécula de acetona foi obtida usando um conjunto base de funções gaussianas cartesianas TZV (triple-zeta valence) do pacote GAMESS [45] aumentadas de duas funções Gaussianas Cartesianas *d* primitivas no átomo de oxigênio ($\alpha = 2.56$ e $\alpha = 0{,}64$) e em cada átomo de carbono ($\alpha = 1{,}44$ e $\alpha = 0{,}36$) na geometria molecular experimental [29].

Fig. 27 – (a) fórmula estrutural e (b) configuração espacial da molécula de acetona.

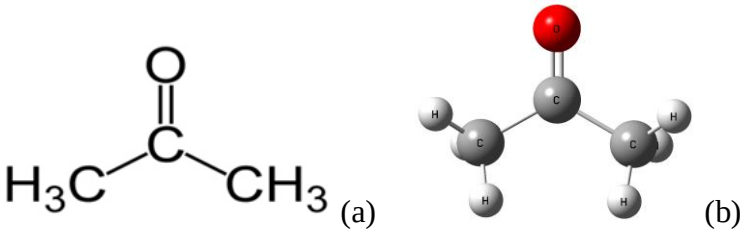

Fonte: (a) elaborado pelo autor, (b) modelo virtual desenvolvido no GaussView [70]

Quadro 9 – Propriedades físicas da molécula de acetona.

	Dipolo elétrico *(a.u)*	$\alpha_{0\,(}\,a_0^3)$	$\alpha_{xx\,(}\,a_0^3)$	$\alpha_{yy\,(}\,a_0^3)$	$\alpha_{zz\,(}\,a_0^3)$
GAMESS	1.2623	38.56	31.98	41.10	42.60
Exp.	1.1332 [29]	41.14 [29]			

Fonte: Elaborado pelo autor.

APÊNDICE B – Seção de Choque de Transferência de Momento

A SCTM é uma seção de choque útil para descrever o momento médio transferido a partir de uma partícula quando colide com um alvo. A SCTM é definida em termos de uma SCD com simetria azimutal, onde o termo $(1-\cos\theta)$ que multiplica a SCD está relacionado à fração do momento perdido pela partícula incidente, e é dada por

$$\sigma_{SCTM} = \int (1-\cos\theta)\frac{d\sigma}{d\Omega}d\Omega, \qquad \text{com} \quad d\Omega = sen\,\theta d\theta d\varphi \tag{78}$$

O fator $(1-\cos\theta)$ surge como segue: o momento da partícula incidente ao longo do eixo *z* pode ser descrito como um vetor momento $\vec{p}_{inc} = q\hat{z}$. A partícula espalhada terá momento $\vec{p}_{out} = q\cos\theta\hat{z} + qsen\,\theta\cos\phi\hat{x} + qsen\,\theta sen\,\phi\hat{y}$. Por conservação do momento, a molécula adquire momento $\Delta\vec{p} = \vec{p}_{out} - \vec{p}_{inc} = q(1-\cos\theta)\hat{z} - qsen\,\theta\cos\phi\hat{x} - qsen\,\theta sen\,\phi\hat{y}$, e assumindo simetria azimutal, em relação ao alvo, então as componentes radiais *x* e *y* do momento transferido terão uma média zero. Assim, a média de transferência de momento será apenas $q(1-\cos\theta)\hat{z}$. Se fizermos a média total sobre todos os ângulos possíveis de dispersão, obtemos

$$\Delta\vec{p}_{média} = \langle\Delta\vec{p}\rangle_{\Omega} = q\hat{z}\frac{\int(1-\cos\theta)\dfrac{d\sigma(\theta)}{d\Omega}d\Omega}{\int\dfrac{d\sigma}{d\Omega}d\Omega} \qquad \text{ou} \qquad \Delta\vec{p}_{média} = q\hat{z}\frac{\sigma_{TM}}{\sigma_{Tot}} \tag{79}$$

onde esta última equação pode ser analisada como uma probabilidade. Portanto, para uma dada seção de choque total, não é necessário calcular novas integrais para cada momento possível, a fim de determinar o momento médio transferido para um alvo, necessita-se apenas da σ_{SCTM}.

APÊNDICE C – Artigos publicados

Neste apêndice estão anexados todos os artigos para as moléculas em estudo neste trabalho, nos quais o autor da presente tese teve participação. Os artigos serão apresentados em ordem cronológica de publicação: Seções de choque para espalhamento de elétrons por moléculas de formaldeído e pirimidina em energias baixas e intermediarias [12], Seções de choque para colisões de elétrons com moléculas de dimetil éter [14], Seções de choque para espalhamento de elétrons por moléculas de fluorometano (CH_3F) em energias baixas e intermediarias [13], Colisões de elétrons como moléculas de amônia e formamida em energias baixas e intermediarias [11], Investigação teórica e experimental de colisões de elétrons com moléculas de dimetil sulfeto [15] e Investigação teórica e experimental de colisões de elétrons com moléculas de acetona [16].

Cross sections for electron scattering by formaldehyde and pyrimidine in the low- and intermediate-energy ranges

J. R. Ferraz,[1] A. S. dos Santos,[1] G. L. C. de Souza,[2] A. I. Zanelato,[2] T. R. M. Alves,[2] M.-T. Lee,[3] L. M. Brescansin,[4] R. R. Lucchese,[5] and L. E. Machado[1]

[1]*Departamento de Física, UFSCar, 13565-905 São Carlos, São Paulo, Brazil*
[2]*Instituto de Ciências Exatas e Tecnologia, UFAM, 69100-000 Itacoatiara, Amazonas, Brazil*
[3]*Departamento de Química, UFSCar, 13565-905 São Carlos, São Paulo, Brazil*
[4]*Instituto de Física "Gleb Wataghin", UNICAMP, 13083-970 Campinas, São Paulo, Brazil*
[5]*Department of Chemistry, Texas A & M University, College Station, Texas 7784-3255, USA*

(Received 19 December 2012; published 25 March 2013)

We report a theoretical study on electron scattering by two strongly polar molecules, namely, formaldehyde (CH_2O) and pyrimidine ($C_4H_4N_2$), in the low- and intermediate-energy ranges. Calculated elastic differential, integral, and momentum-transfer cross sections, as well as total (elastic + inelastic) and total absorption cross sections, are reported for impact energies ranging from 0.2 to 500 eV. A complex optical potential is used to represent the electron-molecule interaction dynamics, whereas a single-center-expansion method associated with the Padé approximant technique is used to solve the scattering equations. Our calculated results are compared with experimental results and other theoretical data available in the literature. Generally good agreement is seen in these comparisons.

DOI: 10.1103/PhysRevA.87.032717 PACS number(s): 34.80.Bm

I. INTRODUCTION

Recently, electron scattering from small organic molecules has been a subject of increasing interest, both theoretically and experimentally. The interest in such studies resides mainly in many applications of these species. For instance, cross sections of electron scattering by those molecules are important for understanding and modeling plasmas [1], to elucidate some mechanisms of astrophysical phenomena [2], and to control plasma processing in industry [3]. In particular, alcohols and biodiesels are currently used as renewable energy sources replacing the traditional fossil fuels. Such uses could lead to the increase of vapor concentration of these fuels in the atmosphere in the near future. Therefore, the investigation of electron interaction with them may help in the understanding of energy and material balances in combustion plasmas, as well as in the understanding of their chemistry in terrestrial atmosphere.

Moreover, radiation damage in biomolecular systems has been the subject of extensive research in the past few years. This interest is mainly due to the fact that significant damage can be caused in DNA via interaction with low-energy electrons, leading either to direct single- and double-strand breaks [4] or to the formation of free radicals, which can then chemically react with DNA, also leading to strand breaks. Ionizing radiation is widely used in medicine as a probe in radiodiagnostic examinations and as a genotoxic agent in radiotherapy. The major part of the energy deposited by ionizing radiation in condensed matter can lead to the production of abundant secondary electrons. In order to better understand the physical and chemical processes responsible for DNA damage, absolute-cross-section data of electron impact on DNA and its constituents are needed.

Many molecules of interest such as alcohols, biodiesels, and the constituents of the bases and backbone of DNA are strongly polar, which makes the measurement of their differential cross sections (DCS) at small scattering angles highly unreliable. In this sense, the development of theoretical methods is important in order to amend this problem. With this motivation in mind, in this work we present a theoretical investigation of electron scattering by two highly polar molecules, namely, formaldehyde (CH_2O) and pyrimidine ($C_4H_4N_2$), in a wide incident energy range.

Probably because formaldehyde is one of the simplest polar organic molecules, the first investigations of e^--CH_2O collisions were performed back in the 1970s. For instance, earlier electronic spectroscopic studies on CH_2O include those by Weiss *et al.* [5] and Chutjian [6]. Both studies used the crossed-beam technique and several electronic transitions in this compound were observed. Using the electron-transmission technique, Burrow and Michejda [7] observed pronounced Feshbach resonances at energies above 6 eV in their relative total cross sections (TCS). These authors also reported the occurrence of resonances in the 0.5–3.0 eV impact energy range. Lately, Benoit and Abouaf [8] reported vibrational excitations in e^--CH_2O collisions in the 0.4–2.6 eV energy range. These authors have confirmed the existence of a strong shape resonance at around 1 eV. Also, Van Veen *et al.* [9] measured the excitation function for the ($n \rightarrow \pi^*$) transition by using the trapped-electron method. Nevertheless, to our knowledge, there are no absolute-cross-section measurements for e^--CH_2O scattering reported in the literature.

On the theoretical side, both elastic and inelastic e^--CH_2O collisions in the low-energy range were investigated by Rescigno *et al.* [10,11] and Schneider *et al.* [12] using the complex Kohn variational method. In their work, Rescigno *et al.* [10] identified a $^2B_1$ shape resonance at about the same energy region previously observed by Benoit and Abouaf [8]. This resonance was also studied by Mahalakshmi and Mishra [13] using the propagator technique. In 2001, Sobrinho *et al.* [14] reported DCS and momentum-transfer cross sections (MTCS) for elastic scattering, as well as for the two lowest electronic transitions in formaldehyde in the 16–80 eV energy range by using the iterative Schwinger variational method (ISVM). Kaur and Baluja [15] reported

DCS, MTCS, and integral cross sections (ICS) for e^--CH_2O collisions in an eight-state multichannel calculation using the R-matrix method in the 0.1–20 eV range. Freitas *et al.* [16] also reported DCS and MTCS for elastic electron scattering by both formaldehyde and the binary CH_20-H_2O complex at several different geometries using the Schwinger multichannel method (SMC). More recently, TCS for e^--CH_2O scattering were calculated by Zecca *et al.* [17] using the independent atom model–screened additivity rule (IAM-SCAR) method for incident energies varying from 1 to 10 000 eV. In the same paper, DCS and MTCS for elastic e^+-CH_2O collisions calculated using the SMC were also reported. Also very recently, TCS for e^--CH_2O scattering in the 0.01–2000 eV energy range were calculated by Vinodkumar *et al.* [18] using a combination of the R-matrix method and the spherical complex optical potential (SCOP) method.

In contrast to formaldehyde, only recently have investigations on electron-pyrimidine collisions started appearing in the literature. This interest derives mainly from the possible radiation damage of DNA. Pyrimidine is a heterocyclic, aromatic organic compound containing two nitrogen atoms at positions 1 and 3 of the six-member ring. Due to the similarity of its ring structure to three of the five nucleobases, namely, cytosine ($C_4H_5N_3O$), thymine ($C_5H_6N_2O_2$), and uracil ($C_4H_4N_2O_2$), it is considered a model molecule for studies of electron interactions with DNA and RNA bases. Recently, e^--$C_4H_4N_2$ collisions have been intensively investigated both theoretically and experimentally. For instance, DCS and ICS for elastic scattering by pyrimidine were measured by Palihawadana *et al.* [19] in the 3–50 eV energy range and also by Maljković *et al.* [20] in the 50–300 eV range. Vibrational and electronic excitation cross sections for electron impact on condensed pyrimidine were determined by Levesque *et al.* [21]. DCS and ICS for low-energy electron-impact excitation of the unresolved combinations of the $2\,^3B_2 + 2\,^1A_1$ and $3\,^1A_1 + 2\,^1B_2$ electronic states of pyrimidine were reported by Jones *et al.* [22] at 15 and 30 eV incident energies. ICS for inelastic e^--$C_4H_4N_2$ collisions were recently measured by Mašín *et al.* [23] in the 15–50 eV range.

Theoretically, DCS and ICS for elastic e^--$C_4H_4N_2$ collisions were calculated by Palihawadana *et al.* [19] in the 0.1–50 eV energy range using both the SMC and IAM-SCAR methods. In their SMC ICS, calculated without including dipole correction, three strong resonances were identified. The peaks located at 0.38 and 4.6 eV are due to shape resonances occurring in $^2B_1$ symmetry, while the peak located at 0.63 eV is associated with a resonance of $^2A_2$ symmetry. Also, DCS and ICS up to 15 eV were calculated by Mašín *et al.* [23] using the R-matrix method. Two theoretical frameworks, namely, the static-exchange-polarization (SEP) and the close-coupling (CC) approximations, were used in their calculations. Resonances similar to those of Palihawadana *et al.* [19] were also seen in their calculated ICS. In their SEP model, these resonances were located at 0.21 eV for $^2A_2$ symmetry and at 0.68 and 5.15 eV for $^2B_1$ symmetry. Moreover, the IAM-SCAR method was also used by Maljković *et al.* [20] to calculate DCS and ICS in the 50–300 eV range and by Zecca *et al.* [24] to calculated TCS in the 1–10 000 eV range.

At energies above the ionization threshold, a number of inelastic scattering channels such as electronic excitation and ionization of the target are open, leading to a reduction in the electronic flux of the elastic scattering channel. Such effects (known as absorption effects) are difficult to account for in scattering calculations in an *ab initio* approach. Therefore, several semiempirical model absorption potentials have been proposed and applied within the single-channel framework [25,26]. Among them, the scaled quasi-free-scattering model (SQFSM), which is an improvement of the quasi-free-scattering model version 3 (QFSM3) of Staszewska *et al.* [27], was proposed by our group a few years ago [28,29]. In general, DCS, ICS, and MTCS calculated using the SQFSM for elastic electron-molecule scattering do not differ significantly from those computed using the QFSM3. However, for a variety of atomic and molecular targets [29–31], the agreement between the TCS and total absorption cross sections (TACS) calculated with the SQFSM and the corresponding experimental data is significantly better than the agreement with their QFSM3 counterparts. This improvement was confirmed by a recent benchmark study of Staszewska *et al.* [32] for electron-atom collisions. In the present work, the SQFSM absorption potential, combined with the static-exchange-correlation-polarization contribution, is applied to describe the dynamics of electron collisions with formaldehyde and pyrimidine. Particularly, for incident energies above 50 eV, the introduction of absorption effects in the collision dynamics should significantly reduce the magnitude of the DCS at intermediate and large scattering angles.

The organization of this paper is as follows: In Sec. II, the theory is briefly described. In Sec. III, some details of the calculations for each target are presented and our calculated results are compared with the experimental data available in the literature, as well as with other existing theoretical data. A brief conclusion is also summarized in this section.

II. THEORY

In the present study, a complex optical potential given by

$$V_{\rm opt} = V_{\rm st} + V_{\rm ex} + V_{\rm cp} + i\,V_{\rm ab} \tag{1}$$

is used to represent the e^--molecule interaction dynamics. In the above equation, $V_{\rm st}$ and $V_{\rm ex}$ are the static and the exchange components, respectively; $V_{\rm cp}$ is the correlation-polarization contribution; and $V_{\rm ab}$ is an absorption potential. Using this potential, the scattering problem is solved using the numerical solution of the Lippmann-Schwinger (LS) integral equation within the single-center-expansion close-coupling framework and further corrected using the Padé approximant technique. The basic theory of this method has already been presented elsewhere [31] and is only briefly outlined here.

The procedure starts by using the two-potential formalism to write the reduced complex optical potential $U_{\rm opt} = 2V_{\rm opt}$ as a sum:

$$U_{\rm opt} = U_1 + U_2, \tag{2}$$

where

$$U_1 = U_{\rm st} + U_{\rm ex}^{\rm loc} + U_{\rm cp} \tag{3}$$

and

$$U_2 = U_{\rm ex} - U_{\rm ex}^{\rm loc} + i\,U_{\rm ab}. \tag{4}$$

In the present work, U_{st} and U_{ex} are derived exactly from a near-Hartree-Fock self-consistent-field (SCF) target wave function, whereas U_{cp} is obtained in the framework of the free-electron-gas model, derived from a parameter-free local density, as prescribed by Padial and Norcross [33]. The Hara free-electron-gas-exchange potential [34] is used to generate the local-exchange potential U_{ex}^{loc}. U_{ab} is the reduced SQFSM absorption potential of Lee *et al*. [28].

The T matrix can then be written as

$$T_{fi} = T_1 + T_2, \tag{5}$$

where

$$T_1 = \langle \chi(\vec{k}_f)|U_1|\psi_1^+(\vec{k}_i)\rangle \tag{6}$$

and

$$T_2 = \langle \psi_1^-(\vec{k}_f)|U_2|\psi^+(\vec{k}_i)\rangle. \tag{7}$$

In Eq. (6), χ is the unperturbed plane wave function and ψ_1 is the numerical solution of the Schrödinger equation for the U_1 potential:

$$(\nabla^2 + k^2 - U_1)\psi_1^{\pm}(\vec{r}) = 0. \tag{8}$$

Next, T_2 is evaluated by using the Padé approximant technique in an iterative procedure similar to that developed by Lucchese and McKoy [35] for linear molecules. The $[N/N]$ Padé approximant for T_2 is given as [36]

$$T_2[N/N] = -\sum_{i,j=1,N-1} \langle \psi_1^-|U_2|\phi^{(i)+}\rangle (D^{-1})_{ij} \langle \phi^{(j)-}|U_2|\psi_1^+\rangle, \tag{9}$$

where

$$D_{ij} = \langle \phi^{(i)-}|U_2 - U_2 G_1^+ U_2|\phi^{(j)+}\rangle \tag{10}$$

and ϕ is given as

$$\phi^{(i)\pm} = (G_1^{\pm}U_2)^i \psi_1^{\pm}, \tag{11}$$

where $\phi^{(0)} = \psi_1$ and $G_1^{\pm}$ is a distorted-wave Green's function which satisfies the following condition:

$$(\nabla^2 + k^2 - U_1)G_1^{\pm}(\vec{r},\vec{r}') = \delta(\vec{r},\vec{r}'). \tag{12}$$

The superscripts $-$ and $+$ in the above equations denote the incoming- and outgoing-boundary conditions of the scattering waves, respectively. In our calculations, both the scattering wave function and the interaction potential are single-center expanded in terms of the symmetry-adapted functions [37] as has been done, for example, in Ref. [31].

It is known that for targets with considerable permanent dipole moments, partial-wave expansions converge slowly due to the long-range nature of the dipole interaction potential. In order to overcome this difficulty, a Born-closure formula is used to account for the contribution of higher partial-wave components to the scattering amplitudes. The procedure used is the same as that used in some of our previous studies [38–40].

Briefly, the vibronically elastic DCS is calculated within the adiabatic-nuclei-rotation framework:

$$\frac{d\sigma}{d\Omega} = \sum_{J'\tau'} \frac{d\sigma}{d\Omega}(J=0,\tau=0 \longrightarrow J'\tau'), \tag{13}$$

where

$$\frac{d\sigma}{d\Omega}(J\tau \longrightarrow J'\tau') = \frac{1}{(2J+1)}\frac{k}{k_0}\sum_{M=-J}^{J}\sum_{M'=-J'}^{J'} \times |f_{J\tau M \longrightarrow J'\tau' M'}|^2 \tag{14}$$

and

$$f_{J\tau M \longrightarrow J'\tau' M'} = \langle \Psi_{J'\tau' M'}(\Omega) \mid f^{LF} \mid \Psi_{J\tau M}(\Omega)\rangle. \tag{15}$$

In the above equation, $\Psi_{J\tau M}(\Omega)$ are eigenfunctions of an asymmetric-top rotor and f^{LF} is the electronic part of the laboratory-frame (LF) scattering amplitude which can be related to the corresponding body-frame (BF) T matrix by an usual frame transformation [41]. The Born-closure-corrected T matrix which accounts for the contribution of higher partial-wave components to the scattering amplitude is written as

$$T = T^B + \frac{1}{k}\sum_{p\mu lhl'h'}^{LL'} i^{l-l'}\left(T^{p\mu}_{k,lh;l'h'} - T^{p\mu^B}_{k,lh;l'h'}\right) \times X^{p\mu}_{lh}(\hat{k}) X^{p\mu^*}_{l'h'}(\hat{k}_0), \tag{16}$$

where $X^{p\mu}_{lh}(\hat{k})$ are the symmetry-adapted functions [37] which are expanded in terms of the usual spherical harmonics as follows,

$$X^{p\mu}_{lh}(\hat{r}) = \sum_m b^{p\mu}_{lhm} Y_{lm}(\hat{r}), \tag{17}$$

and T^B is the complete point-dipole first-Born-approximation (FBA) T matrix, $T^{p\mu}_{k,lh;l'h'}$ are the partial-wave T-matrix elements calculated via the Padé approximant technique, and $T^{p\mu^B}_{k,lh;l'h'}$ are the corresponding partial-wave point-dipole FBA T-matrix elements, given by

$$T^{p\mu^B}_{k,lh;l'h'} = -\frac{D}{L}\left[\frac{(L+h)(L-h)}{(2L+1)(2L-1)}\right]^{\frac{1}{2}}, \tag{18}$$

where D is the target electric dipole moment and $L = l'$ when $l' = l+1$ and $L = l$ when $l' = l-1$.

Moreover, the TCS for electron-molecule scattering are obtained using the optical theorem:

$$\sigma_{tot} = \frac{4\pi}{k}\mathrm{Im}[f(\theta = 0^\circ)]. \tag{19}$$

III. COMPUTATIONAL DETAILS AND RESULTS

A. Formaldehyde

The Hartree-Fock (HF) SCF wave function for ground-state formaldehyde was obtained using the standard contracted Gaussian functions of Dunning [42], specifically, a $[9s5p/5s3p]$ basis set augmented by three s (α = 0.0473, 0.0125, and 0.0045), four p (α = 0.0825, 0.365, 0.125, and 0.0035), and three d (α = 0.756, 0.15, and 0.0375) uncontracted functions for the carbon center; a $[9s5p/3s3p]$ basis set augmented by three s (α = 0.05, 0.02, and 0.005), one p (α = 0.04), and three d (α = 1.7, 0.85, and 0.34) uncontracted functions for the oxygen center; and a $[4s4p/2s1p]$ basis set augmented by three p (α = 0.3, 0.012, and 0.04) uncontracted functions for the hydrogen centers. At the experimental equilibrium geometry of $R_{(O\text{-}C)} = 2.286$ a.u. and

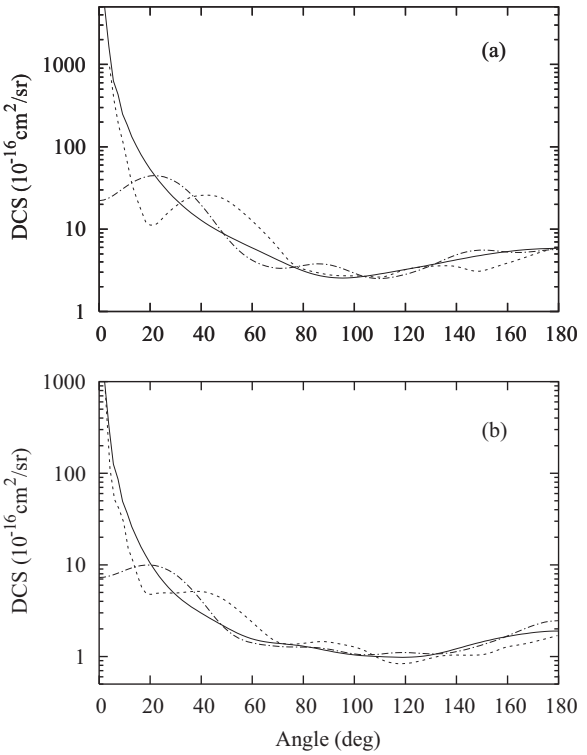

FIG. 1. DCS for elastic e^--CH_2O scattering at (a) 1 eV and (b) 5 eV. Solid line, present results calculated with the Born-dipole correction; dotted-dashed line, present results calculated without the Born-dipole correction; short-dashed line, calculated R-matrix data of Kaur and Baluja [15].

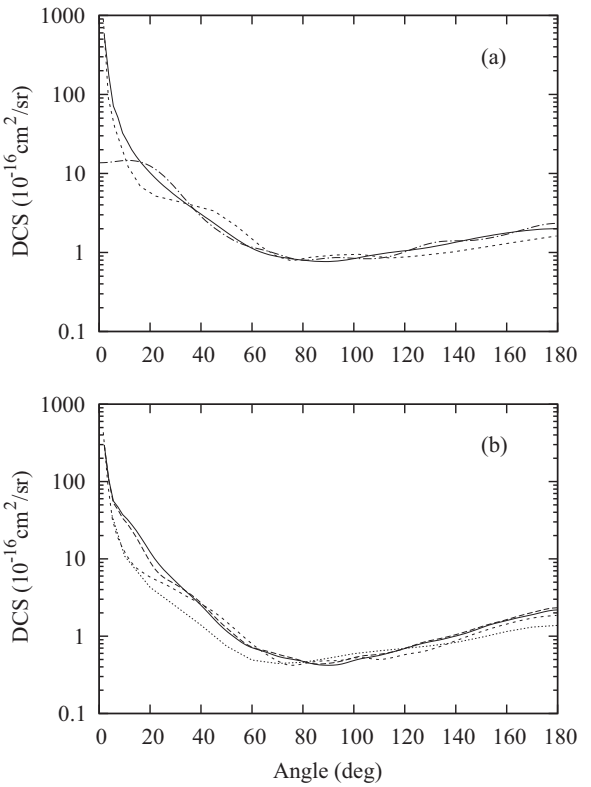

FIG. 2. DCS for elastic e^--CH_2O scattering at (a) 10 eV and (b) 20 eV. Symbols are the same as those in Fig. 1 with the addition of the following: dashed-line, present Born-corrected DCS calculated without inclusion of absorption effects; dotted line, calculated ISVM data of Sobrinho *et al.* [14].

$R_{(C\text{-}H)} = 2.082$ a.u. this basis set gives an SCF energy of $-113.910\ 11$ a.u. and a permanent dipole moment of 2.85 D, in reasonable agreement with the experimental value of 2.34 D [43]. The calculated dipole polarizabilities $\alpha_{xx} = 16.2486$ a.u., $\alpha_{yy} = 12.3328$ a.u., and $\alpha_{zz} = 21.0777$ a.u. were used to obtain the asymptotic form of V_{cp}. For incident energies of 15 eV and below, the absorption effects are negligible and therefore are not taken into account in the calculations.

In our study, all the single-center expansions were truncated at $l_c = 8$, 18, and 25 at incident energies lower than 15 eV, between 15 and 100 eV, and above 100 eV, respectively. All calculated cross sections were converged within five iterations.

In Figs. 1–4 we show our theoretical DCS, calculated with the Born-dipole correction, for elastic e^--CH_2O scattering in the 1–300 eV energy range, and also those calculated without the Born-dipole correction at 1, 5, and 10 eV. The theoretical results of Kaur and Baluja [15] obtained using the R-matrix method and those of Sobrinho *et al.* [14] using the ISVM [44], are shown at energies for which comparisons are possible. Unfortunately, to our knowledge, no experimental results for this target are available in the literature.

In Figs. 1 and 2, our DCS calculated without the Born correction show some oscillations, specially at 1 and 5 eV. They also present a falloff behavior at scattering angles near the forward direction, which is unphysical for polar targets. On the other hand, the DCS calculated with Born corrections are much smoother and are also forwardly peaked, as expected. Although the Born-corrected R-matrix DCS of Kaur and

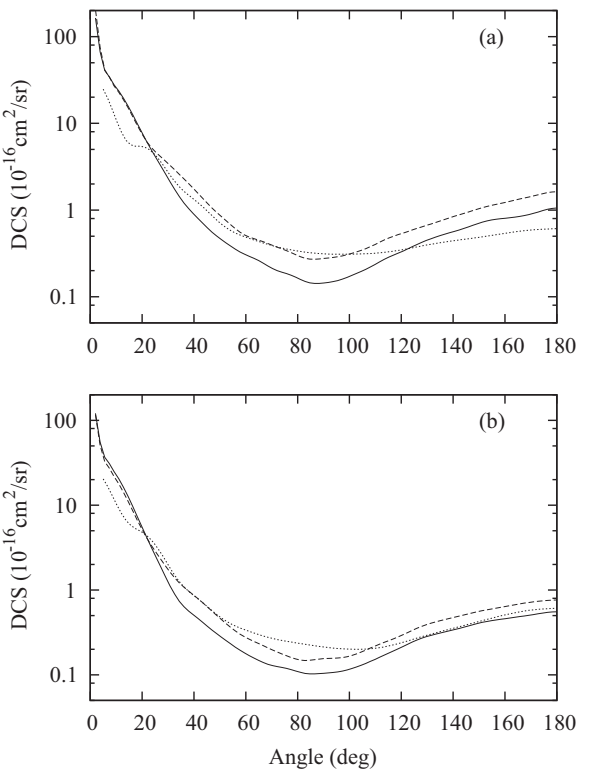

FIG. 3. DCS for elastic e^--CH_2O scattering at (a) 40 eV and (b) 60 eV. Symbols are the same as those in Fig. 2.

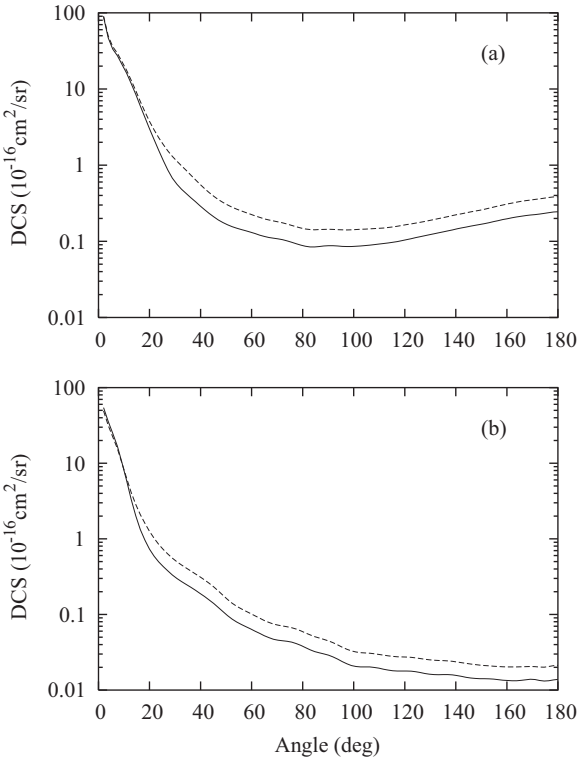

FIG. 4. DCS for elastic e^--CH_2O scattering at (a) 100 eV and (b) 300 eV. Symbols are the same as those in Fig. 2.

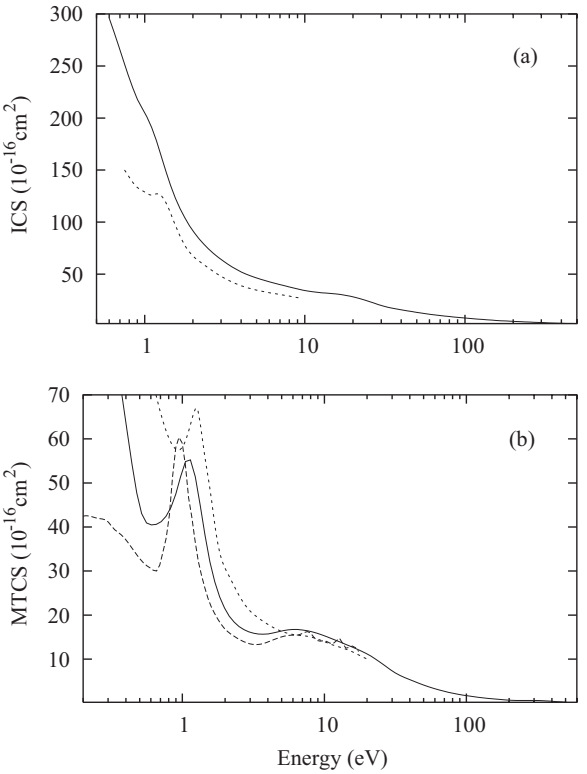

FIG. 5. (a) ICS and (b) MTCS for elastic e^--CH_2O scattering. Solid line, present theoretical results calculated with the Born-dipole correction; short-dashed line, calculated R-matrix data of Kaur and Baluja [15]; dashed line, SMC results of Freitas *et al.* [16].

Baluja [15] present the correct forward-direction behavior, some oscillations are still seen in their results. These observed oscillations may be due to the fact that the dipole-Born correction made by them was not on the scattering amplitudes but directly on the cross sections, which is given as

$$\frac{d\sigma}{d\Omega} = \frac{d\sigma^B}{d\Omega} + \sum_L \left(A_L - A_L^B\right) P_L(\cos\theta). \qquad (20)$$

Using this approximation, interference terms between the low-L and high-L partial-wave components are omitted.

At 20 eV, the ISVM DCS of Sobrinho *et al.* [14] calculated at the SEP level of approximation and our calculated data without accounting for absorption effects are also shown. A reasonable agreement among all the theoretical data is seen and also that the absorption effects are still not relevant at this energy.

In Figs. 3 and 4 we compare our DCS, calculated with and without the inclusion of absorption effects, in the 40–300 eV energy range. At 40 and 60 eV the results of Sobrinho *et al.* [14] obtained using the ISVM at the SEP approximation level are also included for comparison. For all energies in this range, the influence of the inelastic scattering channels on elastic collisions is evident: the DCS calculated including absorption effects lie well below those calculated without including them; the loss of electron flux in the elastic channel is a consequence of the open inelastic channels. The SEP data of Sobrinho *et al.* [14] agree with our results calculated without including absorption effects in the intermediate angular range.

In Figs. 5(a) and 5(b) we show our calculated ICS and MTCS, respectively, for elastic e^--CH_2O scattering in the 0.2–500 eV energy range, along with those of Kaur and Baluja [15] calculated using the R-matrix method and the SMC MTCS of Freitas *et al.* [16] calculated at the C_{2v} group and at the SEP level of approximation. Again, our calculated data for energies of 20 eV and above include absorption effects. Both our ICS and MTCS exhibit a resonancelike feature at around 1 eV. This feature is better characterized in the MTCS and is identified as a shape resonance in the B_1 partial scattering channel. This resonance was also identified by Kaur and Baluja [15] and by Freitas *et al.* [16], but was slightly shifted in energy. Although there are no experimental ICS and/or MTCS for this target to compare with calculations, experimental evidence of the existence of this resonance is given by Benoit and Abouaf [8] who observed the occurrence of a resonance near 1 eV in their measured energy-dependent fixed-angle (90°) vibrational excitation DCS, which is due to the occupation of the first empty $2b_1$ orbital by the scattering electron. The partial-channel ICS from our calculation have confirmed this assignment. Quantitatively, our ICS lie systematically above those of Kaur and Baluja [15] in the overlapped energy range. The difference between the two sets of ICS decreases with energy. In contrast, the MTCS calculated by Kaur and Baluja [15] are larger than ours at energies below 5 eV. On the other hand, our MTCS agree fairly well with the SMC data of Freitas *et al.* [16] at energies above 0.8 eV.

In Figs. 6(a) and 6(b) we present our TCS and TACS, respectively, calculated at incident energies up to 500 eV, along with the R-matrix TCS of Kaur and Baluja [15], the TCS of Zecca *et al.* [17] calculated using the IAM-SCAR, and the TCS of Vinodkumar *et al.* [18] calculated using the R-matrix

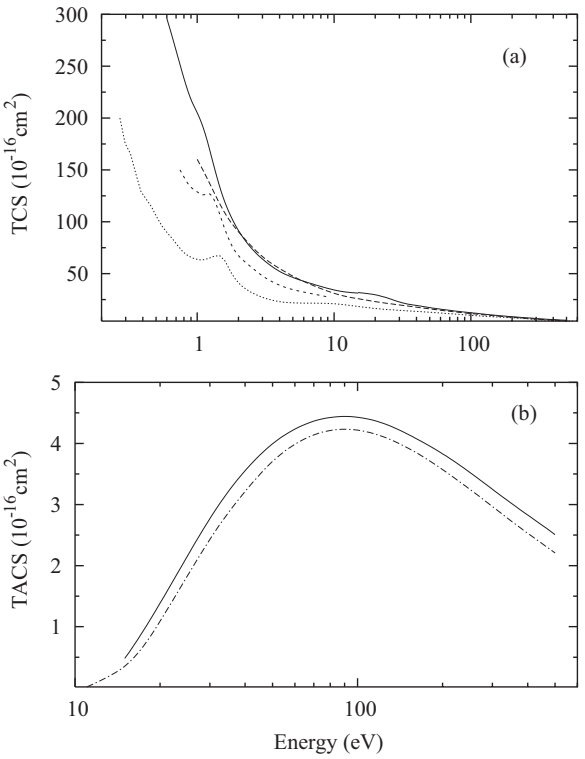

FIG. 6. (a) TCS and (b) TACS for e^--CH_2O scattering. Solid line, present theoretical results calculated including absorption effects; short-dashed line, calculated *R*-matrix data of Kaur and Baluja [15]; dashed line, calculated IAM-SCAR data of Zecca *et al.* [17]; dotted line, calculated SCOP data of Vinodkumar *et al.* [18]; dotted-dashed line, calculated BEB TICS of Kim and Irikura [45].

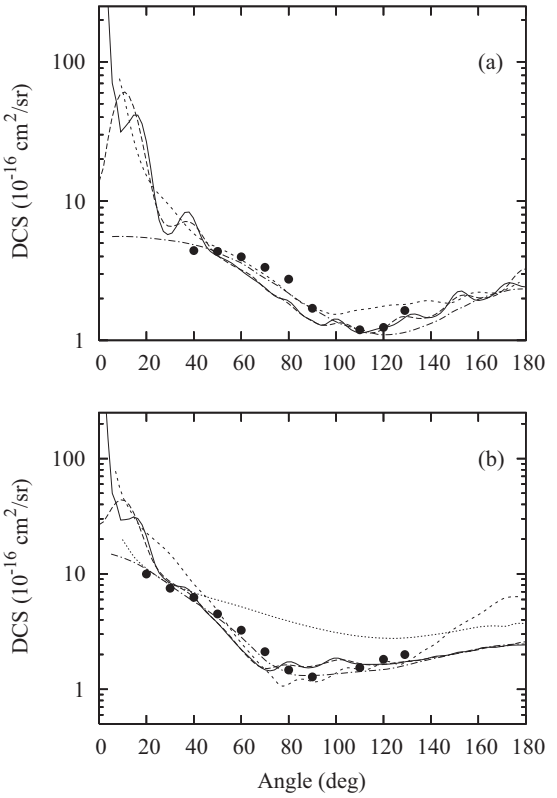

FIG. 7. DCS for elastic e^--$C_4H_4N_2$ scattering at (a) 3 eV and (b) 6 eV. Solid line, present results calculated with the Born-dipole correction; dashed line, present results calculated without the Born-dipole correction; short-dashed line, calculated *R*-matrix data of Mašín *et al.* [23]; dotted-dashed line, calculated SMC data of Palihawadana *et al.* [19]; dotted line, calculated IAM-SCAR data of Palihawadana *et al.* [19]; solid circles, experimental data of Palihawadana *et al.* [19].

approach for incident energies up to 20 eV and using the SCOP approximation above 20 eV. In Fig. 6(b) we compare our TACS with the total ionization cross sections (TICS) of Kim and Irikura [45], calculated using the binary-encounter Bethe (BEB) model. In general, all calculated TCS present similar qualitative energy-dependent behavior. However, the IAM-SCAR TCS of Zecca *et al.* [17] do not show the $^1B_1$ resonance feature at around 1 eV. In the entire energy range, the magnitudes of the TCS of Vinodkumar *et al.* [18] are significantly smaller than all other calculated results. The lack of the Born-type correction for the dipole interaction is probably the origin of this discrepancy. On the other hand, the IAM-SCAR data of Zecca *et al.* [17] are in good agreement with our calculated TCS at energies above 2 eV. In Fig. 6(b) one can notice a very good qualitative and quantitative agreement between our present TACS and the BEB TICS of Kim and Irikura [45]. The fact that their results are slightly below ours is expected since only ionization processes are taken into account in TICS calculations, whereas all inelastic processes are included in the SQFSM absorption potentials.

B. Pyrimidine

The SCF wave functions of the ground-state pyrimidine used in the generation of the e^--target potential were calculated at the HF SCF level. The calculations were performed using the quantum chemistry code GAMESS [46] with an Triple-Zeta Valence plus d-Polarization (TZVDP) contracted Gaussian basis set. The calculation was performed at the C_{2v} point group using the optimized equilibrium geometry taken from the literature [47]. The calculated SCF total energy is −262.767 36 a.u., slightly lower than the HF results of −262.75 a.u. calculated by Mašín *et al.* [23]. Our calculated permanent dipole moment is 2.385 D, in good agreement with the experimental value of 2.334 ± 0.01 D [48]. Moreover, the theoretical dipole polarizabilities $\alpha_{xx} = 22.54$ a.u., $\alpha_{yy} = 55.06$ a.u., and $\alpha_{zz} = 59.06$ a.u. were used for the generation of the asymptotic form of V_{cp}. These values, calculated within the HF framework using an aug-cc-pVDZ basis, were also taken from the database of the NIST website [47].

In the present study, the single-center expansions of bound and scattering wave functions, as well as the interaction potentials and all related matrices were truncated at $l_c = 25$ in the entire incident energy range covered herein. All the calculated cross sections were converged within seven iterations.

In Figs. 7 and 8 we show our theoretical DCS, calculated both with and without the Born-dipole correction, for elastic e^--$C_4H_4N_2$ scattering in the 3–15 eV range. As in formaldehyde, the absorption effects were neglected in this energy range. In addition, the experimental data of Palihawadana *et al.* [19], as well as the calculated DCS using both the SMC

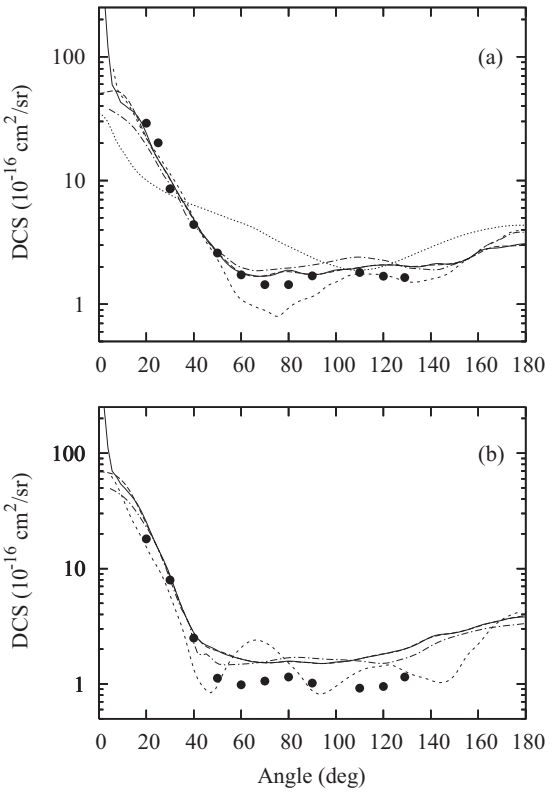

FIG. 8. DCS for elastic e^--$C_4H_4N_2$ scattering at (a) 10 eV and (b) 15 eV. Symbols are the same as those in Fig. 1.

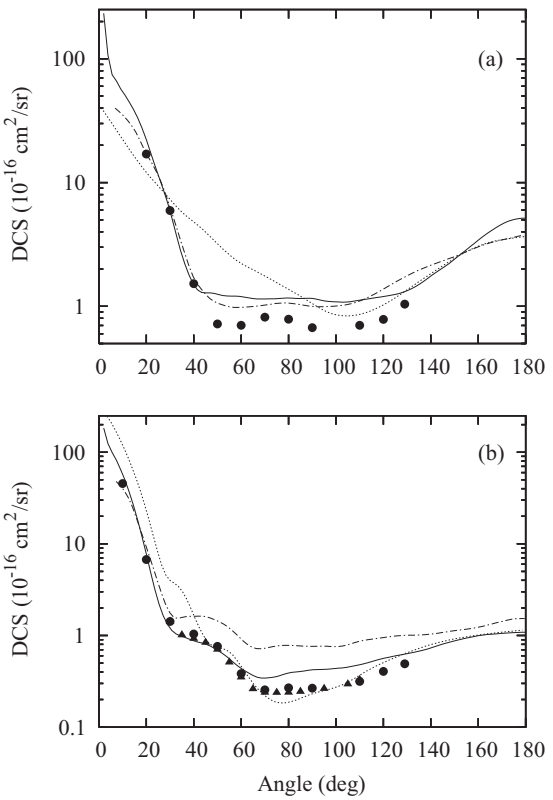

FIG. 9. DCS for elastic e^--$C_4H_4N_2$ scattering at (a) 20 eV and (b) 50 eV. Symbols are the same as those in Fig. 1 with the addition of the following: dotted line, calculated IAM-SCAR data of Maljković *et al*. [20]; solid circles, experimental data of Maljković *et al*. [20].

and IAM-SCAR of Palihawadana *et al*. [19], and the *R*-matrix DCS of Mašín *et al*. [23] in the CC framework are also shown for comparison. At 3 and 6 eV, our dipole-corrected DCS still retain some oscillations. This behavior was also observed for other polar targets such as methanol and ethanol [40,49] and could possibly be a limitation of the point-dipole Born-correction procedure. However, the calculated DCS becomes smoother with increasing incident energies. Quantitatively, since the measured data of Palihawadana *et al*. [19] started at 20°, our theoretical results both with and without the Born correction are in fairly good agreement with their measured data. In this energy range, the theoretical DCS calculated using the SMC are in generally good agreement with our Born-corrected data, except at scattering angles near the forward direction. Again, the lack of the Born-dipole correction in their data is the origin of this discrepancy. The comparison of our data with the CC DCS of Mašín *et al*. [23] also shows reasonably good agreement. As expected, the IAM-SCAR data at 6 and 10 eV strongly disagree with all the theoretical results, as well as with the experimental data.

In Figs. 9 and 10, we present the theoretical results of Born-dipole-corrected DCS in the 20–300 eV energy range. In this range, our calculations were performed including absorption effects via the SQFSM approach. The experimental results of Palihawadana *et al*. [19] up to 50 eV and those of Maljković *et al*. [20] in the 50–300 eV range along with the theoretical data calculated using the SMC [19] and IAM-SCAR [19,20] are also shown for comparison. At 20 eV, our calculated data are still in good agreement with the SMC DCS obtained at the SEP level of approximation, which indicates

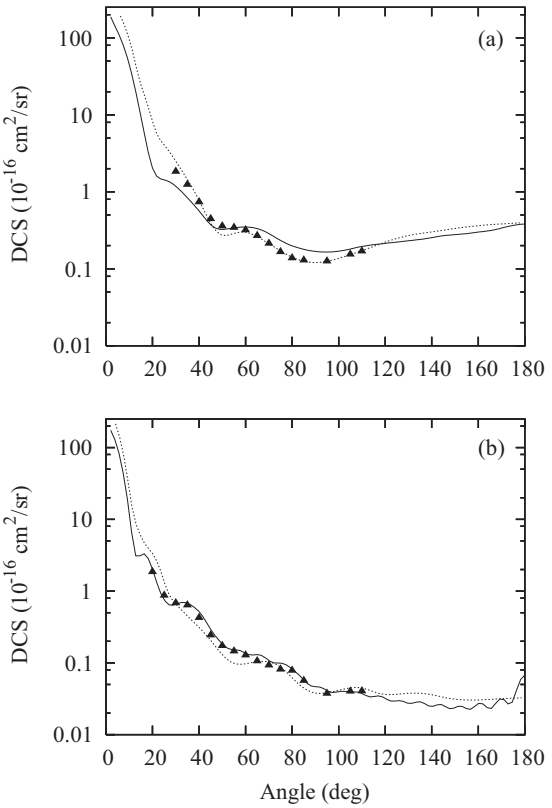

FIG. 10. DCS for elastic e^--$C_4H_4N_2$ scattering at (a) 100 eV and (b) 300 eV. Symbols are the same as those in Fig. 9.

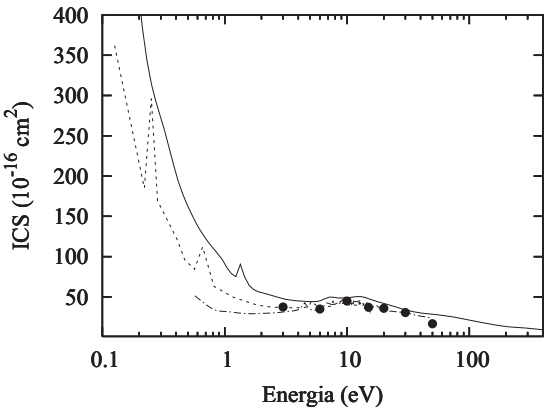

FIG. 11. ICS for elastic e^--$C_4H_4N_2$ scattering. Solid line, present theoretical results; short-dashed line, calculated CC data of Mašín *et al*. [23]; dotted-dashed line, calculated SMC data of Palihawadana *et al*. [19]; solid circles, experimental data of Palihawadana *et al*. [19]. All the calculations were performed without the Born-dipole correction.

that absorption is not yet significant even for this larger target. Again, the IAM-SCAR DCS are significantly different from our data. The comparison of our DCS with the experimental data shows a good qualitative agreement. Quantitatively, good agreement is also seen at angles up to 40°. Above this angle, our calculation overestimates the measured data. At 50 eV, the SMC DCS calculated without accounting for absorption effects lie significantly above our data at intermediate and large scattering angles, which clearly indicates the significant influence of such effects. At this energy, there is a reasonably good agreement between our calculated results and the two sets of experimental data [19,20]. Also, there is a significant improvement in the agreement between the IAM-SCAR data and our data. In the 100–300 eV range, there is a generally good agreement between our calculated results and the experimental and IAM-SCAR data of Maljković *et al*. [20].

In Fig. 11 we show our ICS calculated without the Born-dipole correction for elastic e^--$C_4H_4N_2$, in comparison with the corresponding data obtained by SMC [19] and by the *R*-matrix method at the SEP level of approximation [23]. The experimental results of Palihawadana *et al*. [19] in the 3–50 eV energy range are also presented. At energies above 3 eV, there is a good agreement among the calculated data and the experimental ICS. However, at energies near threshold, the three sets of theoretical ICS are different from each other, with our calculated data lying well above the others. Moreover, the ICS of Mašín *et al*. [23] calculated at the SEP level of approximation show two very sharp resonances centered at 0.21 eV ($^2A_2$) and 0.63 eV ($^2B_1$), respectively, and one broad resonance located at 5.15 eV ($^2B_1$). These resonances were also identified by Winstead and McKoy [50] but in a different order, namely, $^2B_1$, $^2A_2$, and $^2B_1$. In our calculation we have identified one sharp resonance located at 1.4 eV and another broad resonance located at about 7.5 eV. The partial-channel analysis of our ICS showed that both resonances are of $^2B_1$ symmetry and are probably the same as those identified by Mašín *et al*. [23], but shifted to higher incident energies, probably due to the different treatment of the polarization effects.

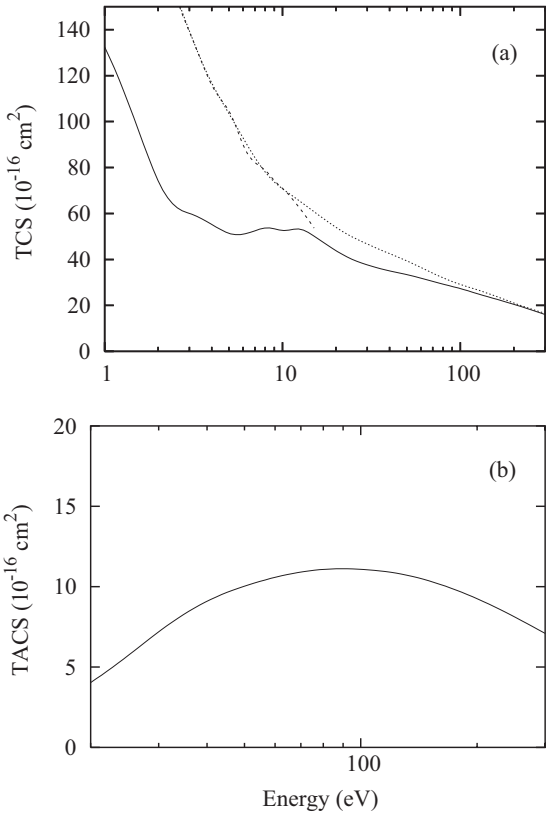

FIG. 12. (a) TCS and (b) TACS for e^--$C_4H_4N_2$ scattering. Solid line, present theoretical results calculated including absorption effects; short-dashed line, calculated SEP results of Mašín *et al*. [23] with the Born-dipole correction; dotted line, calculated IAM-SCAR data of Zecca *et al*. [24].

In Fig. 12(a) we present our TCS calculated with the Born-dipole correction at incident energies up to 300 eV. The ICS calculated with the *R*-matrix method with the SEP + Born-dipole correction [23] and the TCS obtained using the SCAR + rotational excitation of Zecca *et al*. [24] are also shown for comparison. Unfortunately, there are no reported experimental TCS in the literature. At low energies, both the *R*-matrix ICS and SCAR TCS lie well above our results. This discrepancy is probably due to the different ways of performing the dipole correction. In our calculation, this correction is made on the scattering amplitudes, whereas in SCAR and *R*-matrix calculations it is made directly on the cross sections. However, there is a good agreement between the SCAR TCS and our results for energies above 50 eV. In Fig. 12(b), we present our calculated results for TACS. Unfortunately, there are no experimental or calculated data to compare with.

IV. CONCLUDING REMARKS

In the present work, we report a theoretical study on e^--CH_2O and e^--$C_4H_4N_2$ scatterings in the low- and intermediate-energy ranges. These targets are both strongly polar. Due to this characteristic, DCS at near the forward direction are sharply peaked. Also, the ICS and TCS at very low incident energies are strongly enhanced. Our method was able to provide DCS in reasonably good agreement with

other theoretical results and experimental data available in the literature. Particularly for CH_2O, our calculations were able to predict a $^2B_1$ shape resonance located at around 1.0 eV, in agreement with previous calculations [10,15,16]. Experimental evidence of this resonance was observed by Benoit and Abouaf [8]. Also for $C_4H_4N_2$, our calculations have identified two $^2B_1$ shape resonances located at about 1.4 and 7.5 eV, respectively. These resonances are probably the same as those observed by Mašín *et al*. [23], although slightly shifted to higher incident energies. Nevertheless, the $^2A_2$ shape resonance identified by them located at 0.21 eV was not observed in the present study. Different ways to compute the correlation-polarization potential may be the reason for this discrepancy.

At energies above 30 eV, absorption effects become relevant. Therefore, the DCS calculated accounting for such effects lie below those obtained without them, particularly at intermediate and large scattering angles. In general, DCS and ICS including absorption effects are in better agreement with the experimental data available in the literature. Due to the lack of experimental and/or theoretical studies for e^--CH_2O scattering, mainly in the intermediate-energy region, we hope that the present study may stimulate further investigation on this target.

ACKNOWLEDGMENTS

This research was partially supported by the Brazilian agencies CNPq and FAPESP.

[1] R. K. Janev, in *Atomic and Plasma-Material Interaction Processes in Controlled Thermonuclear Fusion*, edited by R. K. Janev and H. W. Drawin (Elsevier, Amsterdam, 1993), p. 27.
[2] J. J. Perry, Y. H. Kim, J. L. Fox, and H. S. Porter, J. Geophys. Res. **104**, 16541 (1999).
[3] W. L. Morgan, Adv. At. Mol. Opt. Phys. **43**, 79 (2000).
[4] B. Boudaiffa, P. Cloutier, D. Hunting, M. A. Huels, and L. Sanche, Science **287**, 1658 (2000).
[5] M. J. Weiss, C. E. Kuyatt, and S. Mielczarek, J. Chem. Phys. **54**, 4147 (1971).
[6] A. Chutjian, J. Chem. Phys. **61**, 4279 (1974).
[7] P. D. Burrow and J. A. Michejda, Chem. Phys. Lett. **42**, 223 (1976).
[8] C. Benoit and R. Abouaf, Chem. Phys. Lett. **123**, 134 (1986).
[9] E. H. Van Veen, W. L. Van Dijk, and H. H. Brongersma, Chem. Phys. **16**, 337 (1976).
[10] T. N. Rescigno, C. W. McCurdy, and B. I. Schneider, Phys. Rev. Lett. **63**, 248 (1989).
[11] T. N. Rescigno, B. H. Lengsfield, and C. W. McCurdy, Phys. Rev. A **41**, 2462 (1990).
[12] B. I. Schneider, T. N. Rescigno, and C. W. McCurdy, Phys. Rev. A **42**, 3132 (1990).
[13] S. Mahalakshmi and M. K. Mishra, Chem. Phys. Lett. **296**, 43 (1998).
[14] A. A. Sobrinho, L. E. Machado, S. E. Michelin, M.-T. Lee, and L. M. Brescansin, J. Mol. Struct. (THEOCHEM) **539**, 65 (2001).
[15] S. Kaur and K. L. Baluja, J. Phys. B **38**, 3917 (2005).
[16] T. C. Freitas, M. A. P. Lima, S. Canuto, and M. H. F. Bettega, Phys. Rev. A **80**, 062710 (2009).
[17] A. Zecca, E. Trainotti, L. Chiari, G. García, F. Blanco, M. H. F. Bettega, M. T. do N. Varella, M. A. P. Lima, and M. J. Brunger, J. Phys. B **44**, 195202 (2011).
[18] M. Vinodkumar, H. Bhutadia, B. Antony, and N. Mason, Phys. Rev. A **84**, 052701 (2011).
[19] P. Palihawadana, J. Sullivan, M. Brunger, C. Winstead, V. McKoy, G. Garcia, F. Blanco, and S. Buckman, Phys. Rev. A **84**, 062702 (2011).
[20] J. B. Maljković, A. R. Milosavljević, F. Blanco, D. Šević, G. García, and B. P. Marinković, Phys. Rev. A **79**, 052706 (2009).
[21] P. L. Levesque, M. Michaud, and L. Sanche, J. Chem. Phys. **122**, 094701 (2005).
[22] D. B. Jones, S. M. Bellm, P. Limão-Vieira, and M. J. Brunger, Chem. Phys. Lett. **535**, 30 (2012).
[23] Z. Mašín, J. D. Gorfinkiel, D. B. Jones, S. M. Bellm, and M. J. Brunger, J. Chem. Phys. **136**, 144310 (2012).
[24] A. Zecca, L. Chiari, G. García, F. Blanco, E. Trainotti, and M. J. Brunger, J. Phys. B **43**, 215204 (2010).
[25] G. Staszewska, D. W. Schwenke, and D. G. Truhlar, Phys. Rev. A **29**, 3078 (1984).
[26] F. Blanco and G. García, Phys. Lett. A **255**, 147 (1999).
[27] G. Staszewska, D. W. Schwenke, D. Thirumalai, and D. G. Truhlar, Phys. Rev. A **28**, 2740 (1983).
[28] M.-T. Lee, I. Iga, L. E. Machado, L. M. Brescansin, E. A. y Castro, I. P. Sanches, and G. L. C. de Souza, J. Electron Spectrosc. Relat. Phenom. **155**, 14 (2007).
[29] E. A. y Castro, G. L. C. de Souza, I. Iga, L. E. Machado, L. M. Brescansin, and M.-T. Lee, J. Electron Spectrosc. Relat. Phenom. **159**, 30 (2007); **159**, 012709 (2010).
[30] P. Rawat, M. G. P. Homem, R. T. Sugohara, I. P. Sanches, I. Iga, G. L. C. de Souza, A. S. dos Santos, R. R. Lucchese, L. E. Machado, L. M. Brescansin, and M.-T. Lee, J. Phys. B **43**, 225202 (2010).
[31] G. L. C. de Souza, M.-T. Lee, I. P. Sanches, P. Rawat, I. Iga, A. S. dos Santos, L. E. Machado, R. T. Sugohara, L. M. Brescansin, M. G. P. Homem, and R. R. Lucchese, Phys. Rev. A **82**, 012709 (2010).
[32] G. Staszewska, P. Staszewski, and K. Zebrowski, J. Electron Spectrosc. Rel. Phenom. **168**, 40 (2008).
[33] N. T. Padial and D. W. Norcross, Phys. Rev. A **29**, 1742 (1984).
[34] S. Hara, J. Phys. Soc. Jpn. **22**, 710 (1967).
[35] R. R. Lucchese and V. McKoy, Phys. Rev. A **28**, 1382 (1983).
[36] F. A. Gianturco, R. R. Lucchese, and N. Sanna, J. Chem. Phys. **102**, 5743 (1995).
[37] P. G. Burke, N. Chandra, and F. A. Gianturco, J. Phys. B **5**, 2212 (1972).
[38] L. E. Machado, L. M. Brescansin, I. Iga, and M.-T. Lee, Eur. Phys. J. D **33**, 193 (2005).
[39] L. M. Brescansin, L. E. Machado, M.-T. Lee, H. Cho, and Y. S. Park, J. Phys. B **41**, 185201 (2008).
[40] M.-T. Lee, G. L. C. de Souza, L. E. Machado, L. M. Brescansin, A. S. dos Santos, R. R. Lucchese, R. T. Sugohara, M. G. P. Homem, I. P. Sanches, and I. Iga, J. Chem. Phys. **136**, 114311 (2012).

[41] M. E. Rose *Elementary Theory of Angular Momentum* (Wiley, New York, 1957).
[42] T. H. Dunning, Jr., J. Chem. Phys **53**, 2823 (1970).
[43] J. N. Shoolery and A. H. Sharbaugh, Phys. Rev. **82**, 95 (1951).
[44] R. R. Lucchese, G. Raseev, and V. McKoy, Phys. Rev. A **25**, 2572 (1982).
[45] Y.-K. Kim and K. K. Irikura, in *Proceedings of the Second International Conference on Atomic and Molecular Data and Their Applications*, edited by K. A. Berrington and K. L. Bell, AIP Conference Proceedings, Vol. 53 (AIP, New York, NY, 2000), p. 220. Data available at http://physics.nist.gov/PhysRefData/Ionization.
[46] M. W. Schmidt *et al*., J. Comput. Chem. **14**, 1347 (1993).
[47] http://cccbdb.nist.gov.
[48] G. L. Blackman, R. D. Brown, and F. R. Burden, J. Mol. Spectrosc. **35**, 444 (1970).
[49] M. A. Khakoo, J. Blumer, K. Keane, C. Campbell, H. Silva, M. C. A. Lopes, C. Winstead, V. McKoy, R. F. da Costa, L. G. Ferreira, M. A. P. Lima, and M. H. F. Bettega, Phys. Rev. A **77**, 042705 (2008).
[50] C. Winstead and V. McKoy, J. Chem. Phys. **125**, 174304 (2006).

Cross sections for electron collisions with dimethyl ether

R. T. Sugohara,[1] M. G. P. Homem,[2] I. Iga,[2] G. L. C. de Souza,[3] L. E. Machado,[4] J. R. Ferraz,[4] A. S. dos Santos,[4] L. M. Brescansin,[5] R. R. Lucchese,[6] and M. T. Lee[2]

[1]*IFSP-Campus Itapetininga, 18202-000 Itapetininga, São Paulo, Brazil*
[2]*Departamento de Química, UFSCar, 13565-905 São Carlos, São Paulo, Brazil*
[3]*Departamento de Química, UFMT, 78060-900 Cuiabá, MT, Brazil*
[4]*Departamento de Física, UFSCar, 13565-905 São Carlos, São Paulo, Brazil*
[5]*Instituto de Física "Gleb Wataghin," UNICAMP, 13083-970 Campinas, São Paulo, Brazil*
[6]*Department of Chemistry, Texas A&M University, College Station, Texas 77843-3255, USA*

(Received 19 June 2013; published 26 August 2013)

We report a joint theoretical-experimental investigation of electron collision with dimethyl ether (DME) in the low- and intermediate-energy ranges. Experimental absolute differential, integral, and momentum-transfer cross sections for elastic e^--DME scattering are reported in the 100–1000 eV energy range. Our measurements were performed using a crossed electron-beam–molecular-beam geometry. The angular distribution of the scattered electrons was converted to absolute cross section using the relative flow technique. Theoretically, elastic differential, integral, and momentum-transfer cross sections, as well as the grand-total and total absorption cross sections for electron collision with DME are calculated in the 1–1000 eV energy range. A single-center-expansion technique combined with the Padé approximant method is used in our calculations. A comparison between the present experimental and theoretical data shows very good agreement. Moreover, comparison with theoretical and experimental data for e^--ethanol (an isomer of DME) scattering shows interesting isomeric effects.

DOI: 10.1103/PhysRevA.88.022709 PACS number(s): 34.80.Bm

I. INTRODUCTION

Recently, global warming has become one of the most serious public concerns around the world. The continuous elevation of sea level due to the melting of glaciers and polar ice caps, as well as global climate changes, constitute a threat to the future of humanity. The indiscriminate use of fossil fuels has been pointed out as the main cause of such effects. The search for renewable energy sources is expected to minimize or delay such effects and therefore has become a top-priority governmental project for most countries. Small alcohols such as methanol and ethanol are good candidates for this purpose. Particularly, ethanol can be produced in large scale by the fermentation of biomaterials such as sugar cane and corn. Carbon dioxide is captured during the growth of these plants and thus reduces the effects of global warming.

In addition, dimethyl ether (DME) constitutes an interesting substitute for fossil fuels. DME can be produced either by extraction from jatropha seeds [1] or via chemical processes such as dehydration of methanol [2]. This compound is potentially an environmentally friendly alternative fuel for diesel engines due to its high cetane number and its overall low-sooting and low-polluting properties [2,3].

In general, the use of such biofuels requires the optimization of combustion processes in engines. The interaction of these molecules with electrons is important since it is what initiates the combustion in most engines [4]. In this regard, values of absolute cross sections of electron-fuel molecule collisions are key quantities to understand the ignition mechanisms.

From the astrochemical point of view, DME is one of the largest organic molecules in the interstellar medium and is highly abundant in star-forming regions [5]. Therefore, cross sections of e^--DME interaction could be useful to understand the evolutionary cycle and chemical pathways in such an environment; however, to the best of our knowledge, absolute electron elastic differential cross-section (DCS) measurements for oxygen-containing organic molecules are very scarce. Particularly for DME, such physical quantities have not been reported in the literature.

Recently, a number of experimental and theoretical investigations of isomeric effects for electron scattering by molecules were reported [6–9]. In those studies, remarkable similarities between the electron-scattering cross sections are observed for isomeric targets, particularly at intermediate incident energies. In general, the isomers previously studied belong to the same chemical functional groups and have similar physical and chemical properties. DME and ethanol are also isomers but belong to different organic functional groups. Thus, quite different chemical and physical properties of these compounds are observed. For instance, at room temperature and under atmospheric pressure, ethanol is a liquid, whereas DME is a gas. The strong hydrogen-bond formation between the hydroxyl groups in ethanol is the cause of its higher boiling temperature. Moreover, the strong hydrogen bonding between the hydroxyl groups can lead to the formation of small molecular clusters in gaseous ethanol, such as dimers and tetramers. It is expected that the cross sections for electron scattering from molecular clusters would certainly be significantly different from those of monomeric ethanol. Therefore, the comparison of absolute cross sections for electron scattering from ethanol and DME is interesting since it can show evidence of the formation or lack of clusters in gaseous ethanol. In this work, we present a joint theoretical-experimental study of electron scattering from DME in the low- and intermediate-energy ranges. Specifically, experimental absolute values of the DCS for electrons elastically scattered from this target are determined using the relative flow technique (RFT) [10–12] and reported in the 100–1000 eV range. Integral (ICS) and momentum-transfer cross sections (MTCS) are also derived

via direct numerical integration of the experimental DCS, measured in the 5°–130° angular range, and extrapolated to forward and backward directions. Theoretically, DCS, ICS, MTCS, and grand-total (TCS) and total absorption cross sections (TACS) are also reported in the 1–1000 eV energy range. The present study constitutes an attempt to partially fulfill the lack of both theoretical and experimental results for e^--DME collisions.

The organization of this paper is as follows: In Sec. II, we present some details of our experimental procedure. In Sec. III, details of the calculations are briefly described. In Sec. IV, our measured results are compared with the present calculated results, as well as with existing experimental and theoretical data for ethanol. Some conclusive remarks are also present in Sec. IV.

II. EXPERIMENT

Details of our experimental setup and procedure have already been presented in some of our previous works [13,14] and thus will only be briefly described here. The relative angular distribution of the scattered electrons at a given incident electron energy is measured using a crossed electron-beam–molecular-beam geometry. The scattered electrons are energy filtered by a retarding-field energy selector with a resolution of about 1.5 eV. This resolution allows the separation of inelastically scattered electrons resulting from electronic excitation, since the lowest excitation threshold of DME is 6.59 eV [15]. Nevertheless, it is unable to distinguish those from vibrational excitation processes. Therefore, our measured DCS are indeed vibrationally summed. The sample of DME used in the measurement is from Sigma-Aldrich Co. and has purity of 99%. This purity is constantly checked using a quadrupole mass spectrometer. During the measurements, the working pressure in the vacuum chamber is around 5×10^{-7} torr.

The recorded scattering intensities are converted into absolute elastic DCS using the RFT [10–12]. Accordingly, the DCS for a gas under determination (x) can be related with known DCS of a secondary standard (std) as

$$\left(\frac{d\sigma}{d\Omega}\right)_x = \left(\frac{d\sigma}{d\Omega}\right)_{std} \frac{I_x}{I_{std}} \frac{R_{std}}{R_x} \left(\frac{M_{std}}{M_x}\right)^{\frac{1}{2}}, \quad (1)$$

where I is the scattered electron intensity, R is the relative flow rate, and M is the molecular weight. The application of RFT requires precise measurements of R for both gases, x and std. Due to the polar nature of DME, there is a possibility that the injected vapors are adsorbed on the inner surfaces of the gas manifold, which may lead to errors in the precise R determination and, consequently, in the absolute calibration of DCS. In order to prevent such errors, we have recently developed a systematic procedure [16] for accurate relative flow-rate determination of gases and vapors. Details of such application were already described in our previous studies for methanol [17] and ethanol [18], and are not repeated in this paper.

TABLE I. Experimental DCS (in 10^{-16} cm^2/sr), ICS, and MTCS (in 10^{-16} cm^2) for elastic e^--DME scattering. The number in the parentheses (n) means 10^n.

Angle	E (eV)					
(deg)	100	200	300	400	500	1000
5		1.67(1)	2.53(1)	2.06(1)	9.83(0)	1.50(1)
6	5.91(1)					
8	3.73(1)					
10	2.31(1)	1.19(1)	9.30(0)	6.52(0)	4.62(0)	2.74(0)
12	1.57(1)					
14	9.26(0)					
15	7.84(0)	4.13(0)	2.93(0)	2.35(0)	1.87(0)	1.22(0)
16	6.58(0)					
20	3.21(0)	1.82(0)	1.40(0)	1.23(0)	9.78(−1)	7.78(−1)
22		1.47(0)	1.19(0)	9.93(−1)	8.31(−1)	5.66(−1)
25	1.73(0)	1.07(0)	8.82(−1)	7.45(−1)	6.50(−1)	3.20(−1)
30	1.12(0)	7.13(−1)	6.08(−1)	5.41(−1)	4.46(−1)	1.66(−1)
40	5.42(−1)	3.56(−1)	3.15(−1)	1.97(−1)	1.43(−1)	6.62(−2)
50	3.03(−1)	1.86(−1)	1.16(−1)	1.01(−1)	8.59(−2)	3.07(−2)
60	1.87(−1)	9.24(−2)	8.49(−2)	6.74(−2)	4.94(−2)	1.61(−2)
70	1.20(−1)	7.06(−2)	6.10(−2)	4.08(−2)	3.08(−2)	1.03(−2)
80	8.24(−2)	6.40(−2)	4.43(−2)	2.88(−2)	2.33(−2)	6.88(−3)
90	7.16(−2)	5.63(−2)	3.56(−2)	2.51(−2)	1.90(−2)	5.03(−3)
100	9.20(−2)	5.05(−2)	3.29(−2)	1.93(−2)	1.48(−2)	3.83(−3)
110	1.11(−1)	4.73(−2)	3.39(−2)	1.84(−2)	1.34(−2)	3.96(−3)
120	1.28(−1)	5.06(−2)	3.12(−2)	1.85(−2)	1.12(−2)	3.38(−3)
125	1.68(−1)					
130		6.09(−2)	3.04(−2)	1.83(−2)	1.11(−2)	3.63(−3)
ICS	1.16(1)	6.84(0)	5.06(0)	4.08(0)	3.44(0)	1.97(0)
MTCS	3.44(0)	1.37(0)	7.85(−1)	5.22(−1)	3.78(−1)	1.31(−1)

In the present study, Ar and N_2 are used as secondary standards. Absolute DCS of Jansen *et al.* [19] in the 100–1000 eV energy range are used to normalize our data. Details of the analysis of experimental uncertainties have also been given elsewhere [13]. They are estimated briefly as follows. Uncertainties of random nature such as pressure fluctuations, electron-beam current readings, background scattering, etc. are estimated to be less than 2%. These contributions combined with the estimated statistical errors give an overall uncertainty of 4% in the relative DCS for each gas. Also, the experimental uncertainty associated with the normalization procedure is estimated to be 5.7%. These errors combined with the quoted errors [19] in the absolute DCS of the secondary standard provide an overall experimental uncertainty of 11% in our absolute DCS. Absolute DCS were determined in the 5°–130° angular range. In order to obtain ICS and MTCS, a manual extrapolation procedure was adopted to estimate DCS at scattering angles out of the angular range covered experimentally. The overall uncertainties on ICS and MTCS are estimated to be 22%.

III. THEORY AND NUMERICAL PROCEDURE

In the present study, the single-center-expansion technique is used to treat the electron-target scattering problem. For that, the collision dynamics is described by using a complex optical potential given by

$$V_{\text{opt}} = V_{\text{st}} + V_{\text{ex}} + V_{\text{cp}} + iV_{\text{ab}}, \tag{2}$$

where V_{st} and V_{ex} are the static and the exchange components, respectively, and V_{cp} is the correlation-polarization contribution. In addition, V_{ab} is an absorption potential which describes the reduction of the flux of elastically scattered electrons due to the opening of inelastic-scattering channels. Using this optical potential, the many-body nature of the electron-molecule interaction is reduced to a one-particle single-channel scattering problem and therefore can be solved exactly using the numerical solution of the close-coupling Lippmann-Schwinger (LS) integral equation. In the recent past, this method was successfully applied by our group to treat electron collisions with ethane, propane, and pyrimidine [20–22]. In this work, we extend its application to DME. The details of this method were already given elsewhere [20,21,23] and thus will only be outlined here.

Basically, the reduced optical potential $U_{\text{opt}} = 2V_{\text{opt}}$ is described as a sum of two components:

$$U_{\text{opt}} = U_1 + U_2, \tag{3}$$

with

$$U_1 = U_{\text{st}} + U_{\text{ex}}^{\text{loc}} + U_{\text{cp}} \tag{4}$$

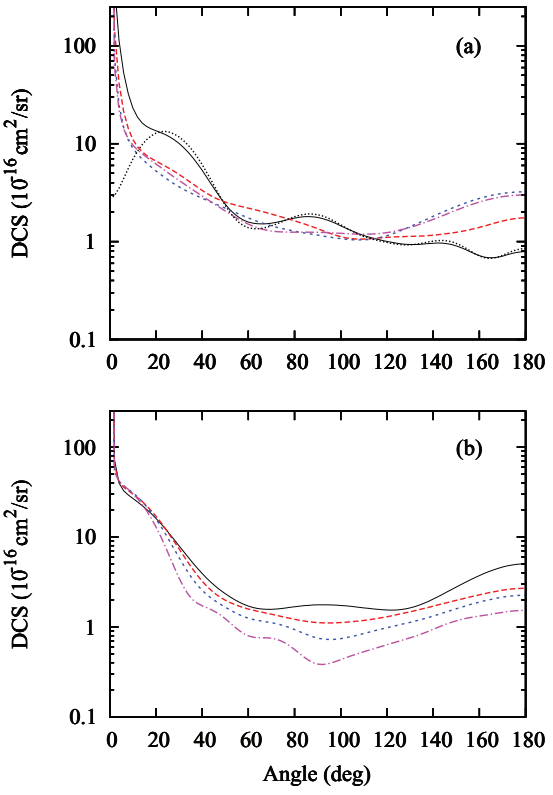

FIG. 1. (Color online) Present calculated dipole-Born-corrected DCS for elastic e^--DME scattering at (a) 1 eV (full black curve), 3 eV (long-dashed red curve), 6 eV (short-dashed blue curve), 8 eV (dash-dotted purple curve), and 1 eV (dotted black curve) calculated without Born correction; and at (b) 10 eV (full black curve), 15 eV (long-dashed red curve), 20 eV (short-dashed blue curve), and 30 eV (dot-dashed purple curve).

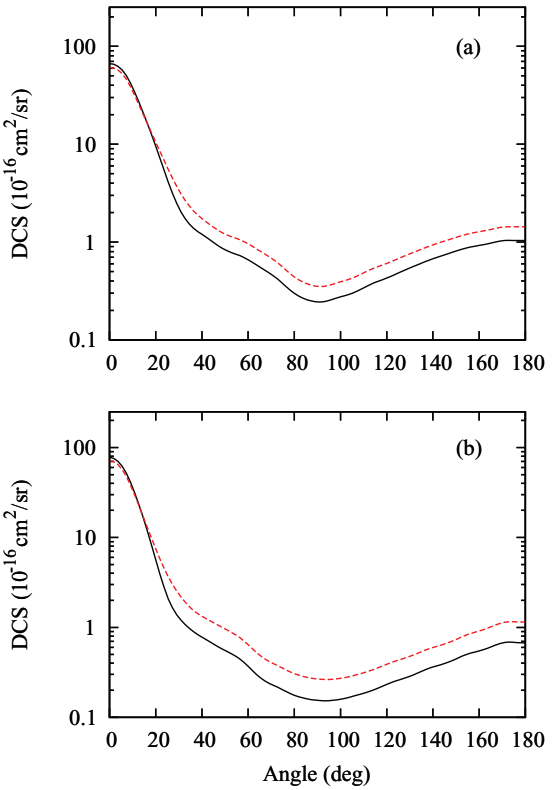

FIG. 2. (Color online) Present calculated dipole-Born-corrected DCS for elastic e^--DME scattering at (a) 40 eV and (b) 60 eV. Full black curves show the calculated data including absorption effects; long-dashed red curves show the calculated data without absorption effects.

and

$$U_2 = U_{\rm ex} - U_{\rm ex}^{\rm loc} + iU_{\rm ab}, \tag{5}$$

where $U_{\rm ex}^{\rm loc}$ is a reduced local exchange potential. According to the two-potential formalism, the full transition T matrix, given as

$$T_{\rm fi} = \langle \phi(\vec{k}_f)|U_{\rm opt}|\psi^+(\vec{k}_i)\rangle, \tag{6}$$

is also composed of two parts:

$$T_{\rm fi} = T_1 + T_2, \tag{7}$$

where

$$T_1 = \langle \phi(\vec{k}_f)|U_1|\psi_1^+(\vec{k}_i)\rangle \tag{8}$$

and

$$T_2 = \langle \psi_1^-(\vec{k}_f)|U_2|\psi^+(\vec{k}_i)\rangle. \tag{9}$$

In Eqs. (6) and (8), ϕ is the unperturbed plane-wave function, k is the magnitude of the electron linear momentum, and ψ_1 is the solution of the LS equation for potential U_1. Further, T_2 can be obtained iteratively using the $[N/N]$ Padé approximant technique [23],

$$T_2[N/N] = -\sum_{i,j=1,N-1} \langle \psi_1^-|U_2|\phi^{(i)+}\rangle \times (D^{-1})_{ij} \langle \phi^{(j)-}|U_2|\psi_1^+\rangle, \tag{10}$$

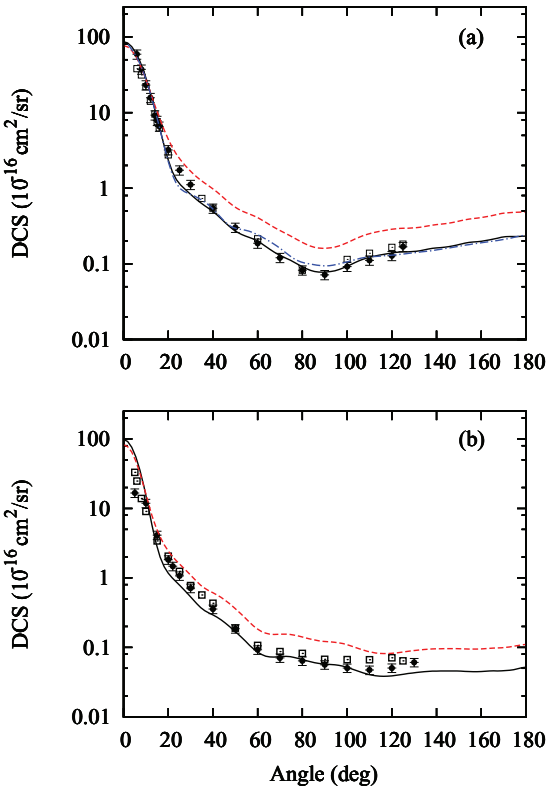

FIG. 3. (Color online) DCS for elastic e^--DME scattering at (a) 100 eV and (b) 200 eV. Full black curves: present calculated dipole-Born-corrected data including absorption effects; long-dashed red curves: calculated data without absorption effects; full black circles with error bars: present experimental data for DME; open squares: experimental data for ethanol [18]; and dot-dashed blue curve: calculated DCS for ethanol [18].

where

$$D_{ij} = \langle \phi^{(i)-}|U_2 - U_2 G_1^+ U_2|\phi^{(j)+}\rangle, \tag{11}$$

and G_1 is the distorted-wave Green's function, which satisfies the following condition:

$$(\nabla^2 + k^2 - U_1)G_1^{\pm}(\vec{r},\vec{r}') = \delta(\vec{r},\vec{r}'). \tag{12}$$

The superscripts $-$ and $+$ appearing in the above equations denote the incoming- and outgoing-boundary conditions of the scattering waves, respectively. In our calculation, the truncation parameter N is iteratively increased until convergence is achieved. The converged body-frame (BF) T matrix (or, equivalently, the BF scattering amplitude f) can then be expressed in the laboratory frame (LF) by a usual frame transformation. Additionally, the TCS for electron-molecule scattering are obtained using the optical theorem,

$$\sigma_{\rm tot} = \frac{4\pi}{k}{\rm Im}[f(\theta = 0^\circ)]. \tag{13}$$

In the present work, $U_{\rm st}$ and $U_{\rm ex}$ are derived exactly from a near-Hartree-Fock self-consistent-field (HF-SCF) target wave function, whereas $U_{\rm cp}$ is obtained in the framework of the free-electron-gas model, derived from a parameter-free local density, as prescribed by Padial and Norcross [24], and the absorption potential $U_{\rm ab}$ in Eq. (5) is the reduced scaled quasifree scattering model (SQFSM) absorption potential of Lee *et al.* [25] which is an improvement of version 3 of the

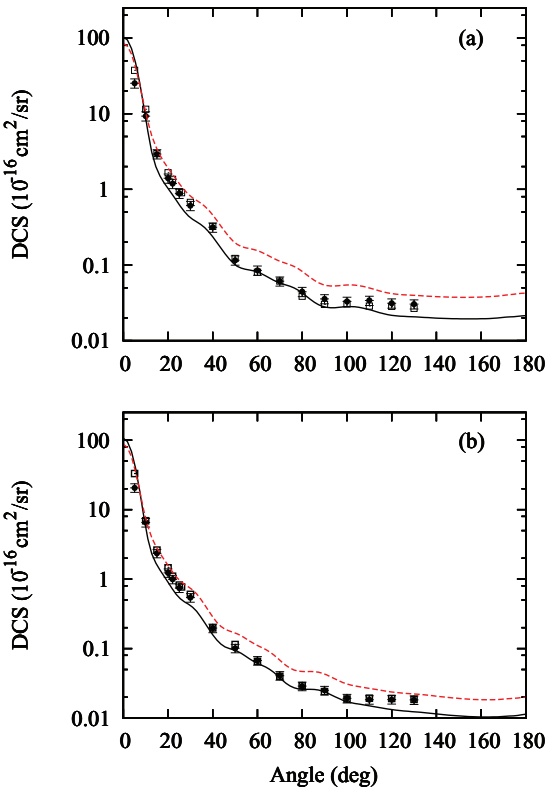

FIG. 4. (Color online) DCS for elastic e^--DME scattering at (a) 300 eV and (b) 400 eV. Full black curves: present calculated dipole-Born-corrected data including absorption effects; long-dashed red curves: calculated data without absorption effects; full black circles with error bars: present experimental data for DME; and open squares: experimental data for ethanol [18].

model absorption potential originally proposed by Staszewska *et al*. [26]. The Hara free-electron-gas-exchange potential [27] is used to generate the local exchange potential $U_{\rm ex}^{\rm loc}$. The HF-SCF target wave function is obtained using the triple-ζ-valence (TZV) basis of the GAMESS package [28] augmented by two uncontracted d Cartesian Gaussian functions on the oxygen atom ($\alpha = 2.56$ and 0.64) and on each carbon atom ($\alpha = 1.44$ and 0.36). The calculation is done at the experimental ground-state molecular geometry of DME [29]. The calculated electric dipole moment is 1.428 D, in good agreement with the experimental value of 1.30 D [29]. Moreover, the asymptotic form of $U_{\rm cp}$ is generated using the present calculated dipole polarizabilities. The obtained values are $\alpha_{xx} = 28.810$, $\alpha_{yy} = 36.036$, and $\alpha_{zz} = 29.122$ a.u., resulting in an averaged dipole polarizability of $\alpha_0 = 31.323$ a.u., in good agreement with the experimental value of 34.82 a.u. [29]. In our calculation, the wave functions and the interaction potentials, as well as the related matrices, are single-center expanded about the center of mass of the molecule in terms of the well-known symmetry-adapted functions $X_{\rm lh}^{p\mu}$ [30]. The truncation parameters used in these expansions are $l_c = 35$ and $h_c = 35$ for all bound and continuum orbitals, as well as for the T-matrix elements. The calculated cross sections were converged with $N = 7$. Since DME is a polar system, the partial-wave expansions converge slowly due to the long-range nature of the dipole interaction potential. In order to overcome this difficulty, a Born-closure formula is used to account for the contribution of higher partial-wave components to the scattering amplitudes. The procedure used is the same as in some of our previous studies [18,31,32].

IV. RESULTS AND DISCUSSION

The present experimental data of DCS, ICS, and MTCS, obtained in the 100–1000 eV energy range, are presented in Table I.

At some selected incident energies, results of DCS are also plotted. For instance, in Figs. 1 and 2, theoretical dipole-Born-corrected DCS for elastic electron scattering by DME in the 1–60 eV incident energy range are presented. Particularly in Fig. 1(a), DCS obtained without dipole-Born correction at 1 eV are also shown. It is seen that all dipole-Born-corrected DCS are strongly forward peaked, which is due to the long-range dipole interaction between the scattering electron and a polar target. In contrast, such forward-peaked behavior is not seen in the DCS calculated without such correction. At energies below 20 eV, the absorption effects are small, therefore DCS calculated with and without accounting for such effects are practically the same. Nevertheless, at energies above 30 eV, inelastic-scattering processes become relevant and thus affect significantly the elastic-scattering processes. Such influences are clearly seen in Fig. 2, where DCS at 40 and 60 eV calculated both with and without including the absorption effects are

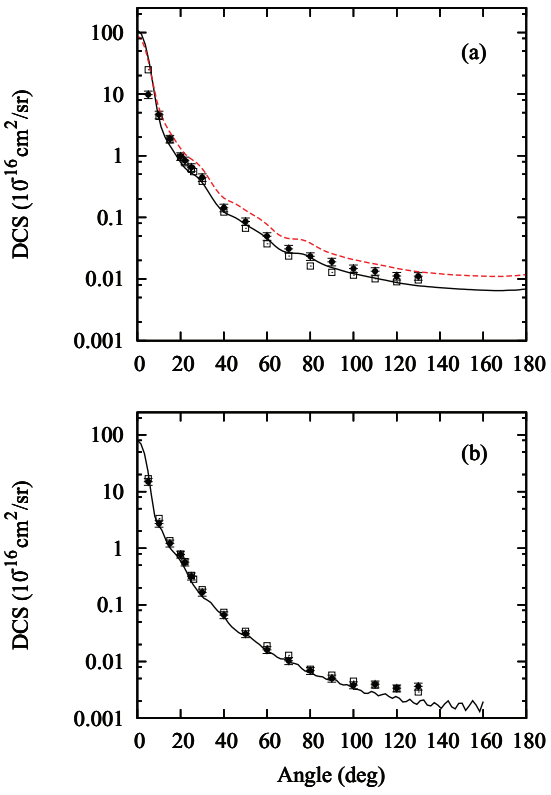

FIG. 5. (Color online) DCS for elastic e^--DME scattering at (a) 500 eV and (b) 1000 eV. Full black curves: present calculated dipole-Born-corrected data including absorption effects; long-dashed red curves: calculated data without absorption effects; full black circles with error bars: present experimental data for DME; and open squares: experimental data for ethanol [18].

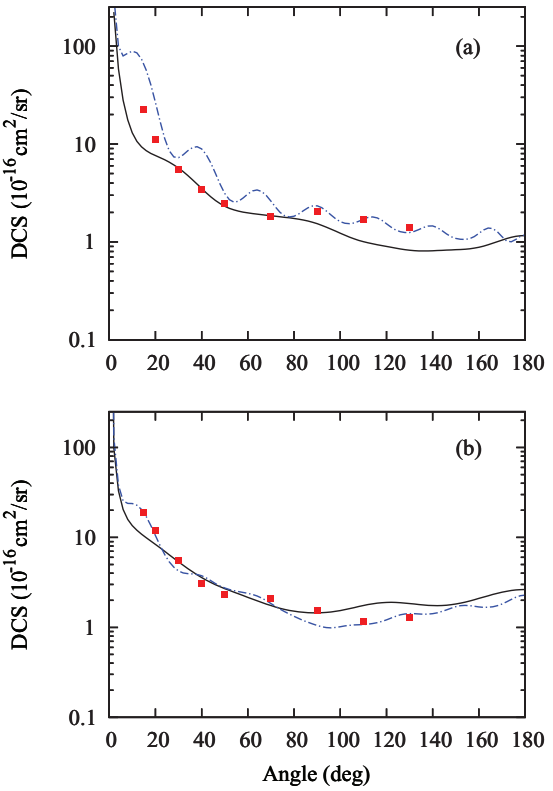

FIG. 6. (Color online) Present calculated dipole-Born-corrected DCS for elastic e^--DME scattering at (a) 2 eV and (b) 5 eV. Full black curves: calculated data including absorption effects; full red squares: experimental DCS of Khakoo *et al*. [33] for ethanol; and dot-dashed blue curve: calculated data of Lee *et al*. [18] for ethanol.

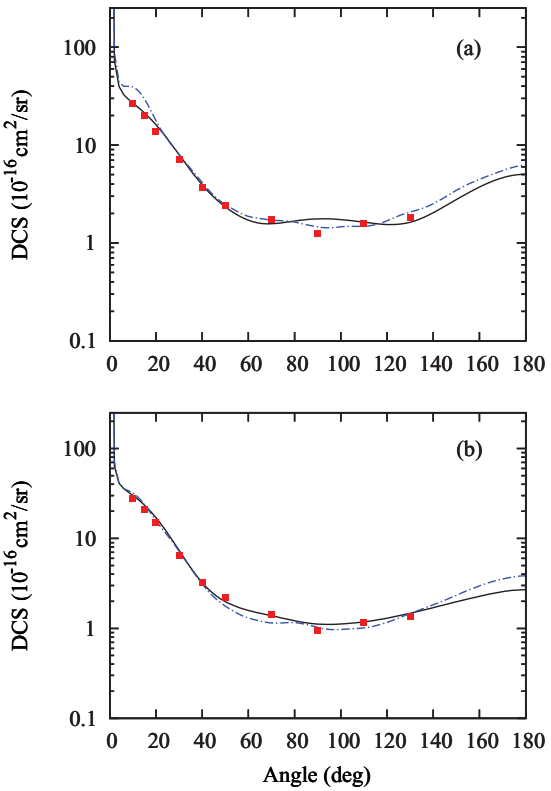

FIG. 7. (Color online) Present calculated dipole-Born-corrected DCS for elastic e^--DME scattering at (a) 10 eV and (b) 15 eV. Full black curves: calculated data including absorption effects; full red squares: experimental DCS of Khakoo *et al.* [33] for ethanol; and dot-dashed blue curve: calculated data of Lee *et al.* [18] for ethanol.

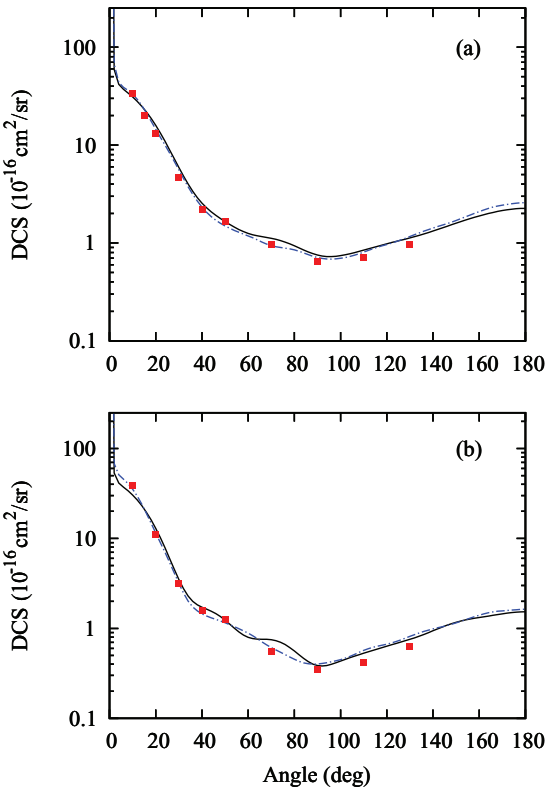

FIG. 8. (Color online) Present calculated dipole-Born-corrected DCS for elastic e^--DME scattering at (a) 20 eV and (b) 30 eV. Full black curves: calculated data including absorption effects; full red squares: experimental DCS of Khakoo *et al.* [33] for ethanol; and dot-dashed blue curve: calculated data of Lee *et al.* [18] for ethanol.

presented. It is shown that the DCS without absorption effects lie significantly above those calculated including these effects. Unfortunately, there are no experimental data or other theoretical results for elastic e^--DME scattering in this energy range to compare with.

In Figs. 3–5, present measured DCS are compared with the dipole-Born-corrected DCS calculated with the inclusion of absorption effects for energies ranging from 100–1000 eV. DCS calculated without such effects in the 100–500 eV range are also shown for comparison. Moreover, with the purpose of investigating the isomeric effects between DME and ethanol in mind, experimental results [18] for elastic e^--ethanol scattering in this energy range are also plotted. In these figures, a good agreement, both qualitatively and quantitatively, is seen between our theoretical data calculated including absorption effects and present measured data at all incident energies where comparisons are made. In general, the theoretical data calculated without such effects overestimate the experimental data, mainly at intermediate and large scattering angles. Moreover, it is seen that the similarity between the present measured DCS for DME and those measured for ethanol [18] is remarkable at all incident energies covered herein. Particularly for 100 eV, we also compare the theoretical DCS for elastic e^--DME and e^--ethanol [18] scatterings, both calculated with absorption effects. Again, the two sets of theoretical data are almost identical. Considering that DME and ethanol belong to two different organic chemical functional groups with very distinct physical and chemical properties, such similarity in elastic electron scattering for these targets is, in fact, very interesting. Although some previous investigations reported in the literature [6,8,9] also showed similarities between the DCS of electron scattering by isomers, the targets involved presented very similar physical and chemical properties. Therefore, our study seems to indicate that the interaction of the scattering electron with the constituent atoms, instead of the molecular character of the target itself, is more relevant in electron-molecule collisions.

In order to better understand the underlying physics involved in electron scattering by isomers, in Figs. 6–8 we also compare the theoretical DCS for elastic e^--DME and e^--ethanol [18] scatterings in the 2–30 eV energy range, along with the measured data of Khakoo *et al.* [33] for e^--ethanol scattering. It is clearly seen that at very low incident energies (2 and 5 eV), there are, in fact, significant differences between the calculated DCS of these two isomers. Specifically, the DCS of ethanol are significantly larger at small scattering angles, due to its larger dipole moment (1.69 D). Also, the unphysical oscillations in the DCS of ethanol at these energies are due to the stronger e^--ethanol dipole interaction. They were not appropriately corrected by the Born-closure method. Nevertheless, such differences decrease with increasing incident energies. For instance, at 20 eV, the calculated DCS for these two targets are very similar. From this comparison, one concludes that due to the low

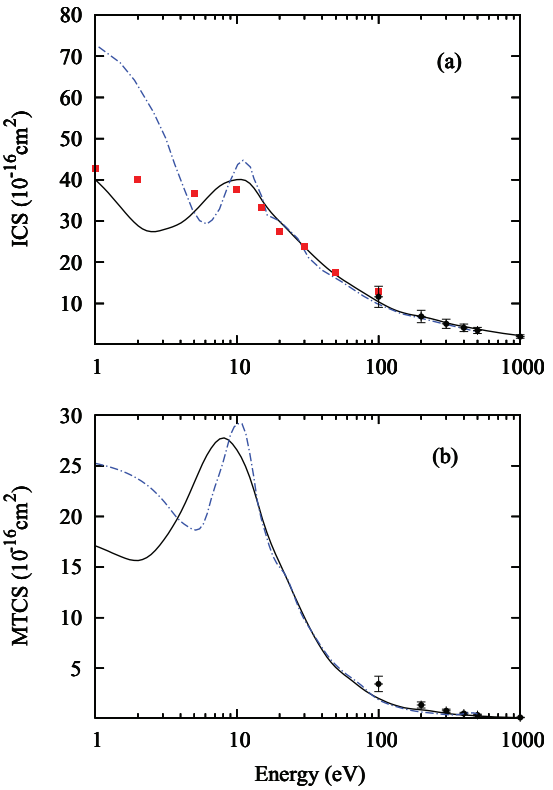

FIG. 9. (Color online) (a) ICS and (b) MTCS for elastic e^--DME scattering in the 1–1000 eV range. Full black curve: present dipole-Born-corrected results; dot-dashed blue curve: calculated results of Lee *et al*. [18] for ethanol; full black circles with error bars: present experimental data for DME; and full red squares: experimental DCS of Khakoo *et al*. [33] for ethanol.

penetration power of the low-energy electrons, only long-range potentials that resulted from permanent and induced dipole, and quadrupole types of interaction, are important. Such properties are determined by the molecular character of the target leading to significant differences seen in the DCS of DME and ethanol. With increasing incident energies, the scattering electrons penetrate deeper inside the target and, in such cases, the interaction with the constituent atoms becomes more important, implying a remarkable similarity of the DCS. The isomeric effects between the DME and ethanol, revealed by the similarity seen in their experimental DCS, have also indirectly confirmed that the formation of dimers of ethanol is negligible, since the DCS of electron scattering by monomer or dimer targets should be very different.

Figures 9(a) and 9(b) show our theoretical ICS and MTCS, respectively, for elastic electron scattering by DME in the 1–1000 eV energy range, which are compared with the corresponding data for ethanol [18]. Present measured ICS and MTCS for DME in the 100–1000 eV energy range and measured ICS of ethanol [33] in the 1–100 eV energy range are also presented for comparison. Again, the isomeric effects are present in these cross sections. At very low energies (up to 5 eV), the ICS and MTCS of ethanol are larger than those of DME, due to its larger dipole moment. Also, the resonance feature seen in the ICS and MTCS of DME and ethanol appears at about the same energy region, although the resonance of DME is much broader than that of ethanol. The partial cross-section analysis (see Fig. 10) shows that this broad resonancelike enhancement in ICS and MTCS is, in fact, constituted by several individual resonances extending in an energy region from 7 eV ($^2A_1$) to 12 eV ($^2B_2$). At energies above 10 eV, both the ICS and MTCS of DME are very similar to the corresponding data of ethanol, showing again strong isomeric effects. A comparison between the present calculated and experimental data of ICS and MTCS in the 100–1000 eV energy range shows very good agreement.

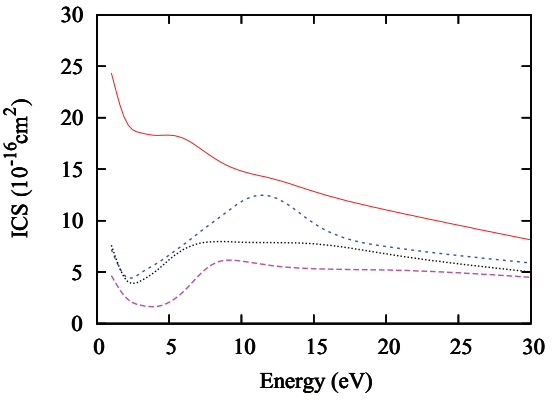

FIG. 10. (Color online) Partial-channel ICS for elastic e^--DME scattering in the 1–30 eV range. Full red curve: results for k^2A_1 symmetry; long-dashed purple curve: results for k^2A_2 symmetry; short-dashed blue curve: results for k^2B_1; and dotted black curve: results for k^2B_2 symmetry.

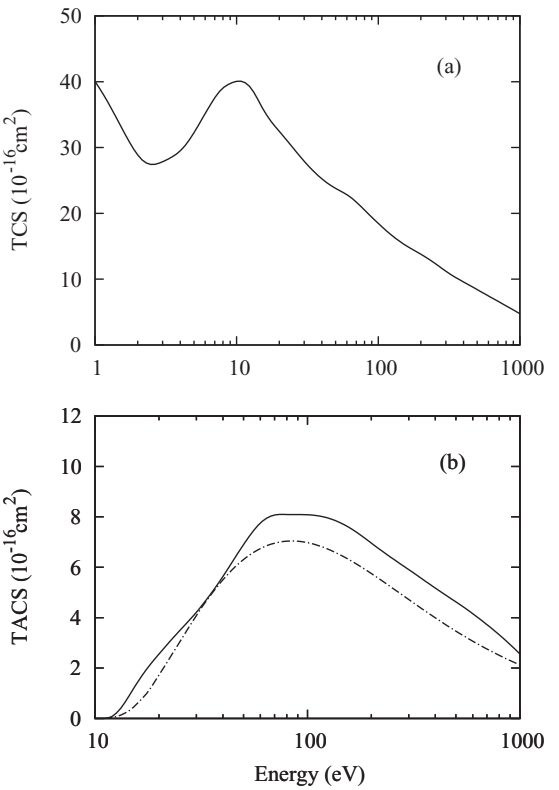

FIG. 11. (a) TCS and (b) TACS for e^--DME scattering in the 1–1000 eV range. Full curve: present calculated results; long-dashed curve: present TICS for ethanol calculated using the BEB model [34].

Finally, in Figs. 11(a) and 11(b), we show our calculated TCS and TACS, respectively, for electron scattering by DME in the 1–1000 eV range. Unfortunately, neither experimental nor other calculated results are available in the literature for comparison. On the other hand, TACS provide an upper limit for total ionization cross sections (TICS), since they account for all inelastic-scattering processes including excitation and ionization, whereas only ionization processes are accounted for in TICS. In this sense, we have also calculated electron-impact TICS of DME using the well-known binary-encounter Bethe (BEB) model [34]. The calculated BEB TICS are also shown in Fig. 11(b). It is seen that the present TACS agree qualitatively with the BEB TICS. Quantitatively, our TACS lie systematically above the TICS, which is physically consistent.

In summary, in this study we report a joint theoretical-experimental investigation of electron collision on DME in a wide energy range. More precisely, absolute DCS, ICS, and MTCS for elastic e^--DME scattering are measured in the 100–1000 eV range, whereas theoretical cross sections including TCS and TACS were reported from 1–1000 eV. In general, the results calculated with absorption effects taken into account agree better with the present measured data, which clearly illustrates the relevant influence of the inelastic-scattering processes on the elastic channel. Moreover, although the physical and chemical properties of the isomers DME and ethanol are quite different, the measured and/or calculated electron-scattering cross sections for these targets present a remarkable similarity for energies above 15 eV. This fact is in accordance with previous experimental studies [6–8]. Only at very low incident energies does the molecular character dominate the scattering processes. In addition, the present study provides evidence that the formation of molecular clusters in ethanol vapor is negligibly small, since the DCS of electron scattering by molecular clusters are expected to be very different from those of a monomer.

ACKNOWLEDGMENTS

This research was partially supported by the Brazilian agencies CNPq, FAPESP, and CAPES.

[1] E. L. M. Rabé (unpublished).
[2] R. Verbeek and J. Van der Weide, SAE Technical Paper 971607 (1997).
[3] G. Mittal, M. Chaos, C. J. Sung, and F. L. Dryer, Fuel Process. Technol. **89**, 1244 (2008).
[4] N. Hansen, T. A. Cool, P. R. Westmoreland, and K. Kohse-Höinghaus, Prog. Eng. Combust. Sci. **35**, 168 (2009).
[5] Z. Peeters, S. D. Rodgers, S. B. Charnley, L. Schriver-Mazzuoli, A. Schriver, J. V. Keane, and P. Ehrenfreund, Astronom. Astrophys. **445**, 197 (2006).
[6] Y. Nakano, M. Hoshino, M. Kitajima, H. Tanaka, and M. Kimura, Phys. Rev. A **66**, 032714 (2002).
[7] C. Szmytkowski and S. Kwitnewski, J. Phys. B **36**, 4865 (2003).
[8] C. Makochekanwa, H. Kato, M. Hoshino, H. Tanaka, H. Kubo, M. H. F. Bettega, A. R. Lopes, M. A. P. Lima, and L. G. Ferreira, J. Chem. Phys. **124**, 024323 (2006).
[9] M. H. F. Bettega, C. Winstead, and V. McKoy, Phys. Rev. A **82**, 062709 (2010).
[10] S. K. Srivastava, A. Chutjian, and S. Trajmar, J. Chem. Phys. **63**, 2659 (1975).
[11] M. A. Khakoo and S. Trajmar, Phys. Rev. A **34**, 138 (1986).
[12] H. Tanaka, T. Ishikawa, T. Masai, T. Sagara, L. Boesten, M. Takekawa, Y. Itikawa, and M. Kimura, Phys. Rev. A **57**, 1798 (1998).
[13] I. Iga, M. T. Lee, M. G. P. Homem, L. E. Machado, and L. M. Brescansin, Phys. Rev. A **61**, 022708 (2000).
[14] P. Rawat, I. Iga, M. T. Lee, L. M. Brescansin, M. G. P. Homem, and L. E. Machado, Phys. Rev. A **68**, 052711 (2003).
[15] M. B. Robin, *Higher Excited States of Polyatomic Molecules* (Academic, New York, 1974).
[16] M. G. P. Homem, I. Iga, R. T. Sugohara, I. P. Sanches, and M. T. Lee, Rev. Sci. Instrum. **82**, 013109 (2011).
[17] R. T. Sugohara, M. G. P. Homem, I. P. Sanches, A. F. de Moura, M. T. Lee, and I. Iga, Phys. Rev. A **83**, 032708 (2011).
[18] M.-T. Lee, G. L. C. de Souza, L. E. Machado, L. M. Brescansin, A. S. dos Santos, R. R. Lucchese, R. T. Sugohara, M. G. P. Homem, I. P. Sanches, and I. Iga, J. Chem. Phys. **136**, 114311 (2012).
[19] R. H. J. Jansen, F. J. de Heer, H. J. Luyken, B. van Wingerden, and H. J. Blaauw, J. Phys. B **9**, 185 (1976).
[20] P. Rawat, M. G. P. Homem, R. T. Sugohara, I. P. Sanches, I. Iga, G. L. C. de Souza, A. S. dos Santos, R. R. Lucchese, L. E. Machado, L. M. Brescansin, and M.-T. Lee, J. Phys. B **43**, 225202 (2010).
[21] G. L. C. de Souza, M.-T. Lee, I. P. Sanches, P. Rawat, I. Iga, A. S. dos Santos, L. E. Machado, R. T. Sugohara, L. M. Brescansin, M. G. P. Homem, and R. R. Lucchese, Phys. Rev. A **82**, 012709 (2010).
[22] J. R. Ferraz, A. S. dos Santos, G. L. C. de Souza, A. I. Zanelato, T. R. M. Alves, M.-T. Lee, L. M. Brescansin, R. R. Lucchese, and L. E. Machado, Phys. Rev. A **87**, 032717 (2013).
[23] F. A. Gianturco, R. R. Lucchese, and N. Sanna, J. Chem. Phys. **102**, 5743 (1995).
[24] N. T. Padial and D. W. Norcross, Phys. Rev. A **29**, 1742 (1984).
[25] M.-T. Lee, I. Iga, L. E. Machado, L. M. Brescansin, E. A. y Castro, I. P. Sanches, and G. L. C. de Souza, J. Electron Spectrosc. Relat. Phenom. **155**, 14 (2007).
[26] G. Staszewska, D. W. Schwenke, and D. G. Truhlar, Phys. Rev. A **29**, 3078 (1984).
[27] S. Hara, J. Phys. Soc. Jpn. **22**, 710 (1967).
[28] M. W. Schmidt, K. K. Baldridge, J. A. Boatz, S. T. Elbert, M. S. Gordon, J. H. Jensen, S. Koseki, N. Matsunaga, K. A. Nguyen, S. Su, T. L. Windus, M. Dupuis, and J. A. Montgomery, J. Comput. Chem. **14**, 1347 (1993).
[29] http://cccbdb.nist.gov

[30] P. G. Burke, N. Chandra, and F. A. Gianturco, J. Phys. B **5**, 2212 (1972).

[31] L. E. Machado, L. M. Brescansin, I. Iga, and M.-T. Lee, Eur. Phys. J. D **33**, 193 (2005).

[32] L. M. Brescansin, L. E. Machado, M.-T. Lee, H. Cho, and Y. S. Park, J. Phys. B: At. Mol. Opt. Phys. **41**, 185201 (2008).

[33] M. A. Khakoo, J. Blumer, K. Keane, C. Campbell, H. Silva, M. C. A. Lopes, C. Winstead, V. McKoy, R. F. da Costa, L. G. Ferreira, M. A. P. Lima, and M. H. F. Bettega, Phys. Rev. A **77**, 042705 (2008).

[34] Y.-K. Kim and M. E. Rudd, Phys. Rev. A **50**, 3954 (1994).

Journal of Electron Spectroscopy and Related Phenomena 193 (2014) 16–20

Contents lists available at ScienceDirect

Journal of Electron Spectroscopy and Related Phenomena

journal homepage: www.elsevier.com/locate/elspec

Cross sections for electron scattering by methylfluoride (CH_3F) in the low- and intermediate-energy ranges

J.R. Ferraz[a], A.S. dos Santos[a], G.L.C. de Souza[b,1], M.-T. Lee[b], L.M. Brescansin[c], R.R. Lucchese[d], L.E. Machado[a,*]

[a] Departamento de Física, UFSCar, 13565-905 São Carlos, SP, Brazil
[b] Departamento de Química, UFSCar, 13565-905 São Carlos, SP, Brazil
[c] Instituto de Física "Gleb Wataghin", UNICAMP, 13083-970 Campinas, SP, Brazil
[d] Department of Chemistry, Texas A&M University, College Station, TX 7784-3255, USA

ARTICLE INFO

Article history:
Received 15 December 2013
Received in revised form 3 February 2014
Accepted 5 February 2014
Available online 14 February 2014

Keywords:
Cross sections
Electron scattering
Absorption effects
Methylfluoride

PACS:
34.80.Bm

ABSTRACT

We report a theoretical study on electron scattering by methylfluoride (CH_3F) in the intermediate-energy range. Calculated elastic differential, integral, and momentum-transfer, as well as grand-total (elastic + inelastic) and total absorption cross sections are reported for impact energies ranging from 15 to 500 eV. A complex optical potential is used to represent the electron–molecule interaction dynamics. A theoretical method based on the single-center-expansion close-coupling framework and corrected by the Padé approximant technique is used to solve the scattering equations. The comparison of our calculated results with experimental and other available theoretical data is encouraging.

1. Introduction

Studies on electron scattering from fluoromethanes (CH_xF_{4-x}, $x = 1-3$) have become increasingly interesting and have attracted a major research effort in recent years. Electron-impact cross sections for these molecules are important in plasma processing, material science, and earth and environmental sciences [1,2]. Although such species also contribute to the globe-warming process, however, due to their shorter lifetime than that of CF_4 in earth's atmosphere, they were pointed as "environmentally acceptable, next-generation plasma-processing gases" [3] and are considered as possible substitutes of CF_4 in plasma processing. Particularly in this work, we are interested in the investigation on electron interactions with the simplest member of this series, namely methylfluoride (CH_3F).

Earlier experimental e^-–CH_3F studies comprise that reported by Tanaka et al. [1], who measured absolute elastic differential cross sections (DCS) at incident energies of 1.5, 30 and 100 eV. Lately, elastic e^-–CH_3F scattering was reinvestigated both experimentally and theoretically by Varella et al. [4] in the 1.5–30 eV incident energy range. Experimental values of electron-impact total ionization cross sections (TICS) were reported by Beran and Kevan [5] at incident energies of 20, 35 and 70 eV, and by Vallance et al. [6] in the 15–200 eV range. Grand-total cross sections (TCS) for this species were measured by Benitez et al. [7] in the 0.1–10 eV range and also by Krzysztofowicz and Szmytkowski [8] in the 0.1–250 eV range.

Besides the work of Varella et al. [4], who reported theoretical DCS, integral cross sections (ICS), and momentum-transfer cross sections (MTCS) obtained at the static-exchange-polarization (SEP) level of approximation, some other theoretical studies on electron scattering by CH_3F are also available in the literature. For instance, DCS and MTCS for elastic electron scattering by fluoromethanes, chloromethanes and chlorofluoromethanes, including CH_3F, were calculated by Natalense et al. [9] at the static-exchange (SE) level of approximation in the 10–30 eV energy region. The Single-Center Modified Additivity Rule (MAR-SC) was used by Joshipura and Vinodkumar [10] to calculate TCS, TICS and total absorption cross sections (TACS) at the static–exchange–polarization–absorption (SEPA) level of approximation for electron scattering by this target among various other polyatomic targets at energies ranging from

* Corresponding author. Tel.: +55 16 34127951; fax: +55 16 33614835.
E-mail address: dlem@df.ufscar.br (L.E. Machado).
[1] Present address: Departamento de Química, UFMT, 78060-900 Cuiabá, MT, Brazil.

http://dx.doi.org/10.1016/j.elspec.2014.02.001
0368-2048/

50 to 5000 eV. Manero et al. [11] used the Independent Atom Model (IAM) to calculate TCS, TACS, and ICS for electron-fluoromethanes scattering for energies ranging from 0.1 to 10 keV. More recently, Shi et al. [12] reported calculated TCS for electron scattering by fluoromethanes and chloromethanes, in the 30–5000 eV energy range, using a version of the additivity rule (AR) that includes a correction based on a geometric shielding factor, and very recently Xiao-Ming and Gang [13] also reported calculated TCS for electron scattering by fluoromethanes, using a revised AR method.

It is known that at energies above the ionization threshold, a number of inelastic scattering channels (electronic excitation, ionization, etc.) are open, leading to a reduction in the electronic flux of the elastic scattering channel. To appropriately take such effects (known as absorption effects) into account in the calculations in an *ab initio* framework is computationally prohibitive for most atomic and molecular targets. In order to overcome this difficulty, several model absorption potentials were proposed and applied within the single-channel framework [14,15]. In particular, the version 3 of the quasi-free scattering model (QFSM3) of Staszewska et al. [14] has been widely used in e^-–molecule collision calculations and applied, for instance, to electron–methylfluoride collisions by both Joshipura and Vinodkumar [10] and Shi et al. [12] whereas a modified version [16] of this absorption potential was used by Xiao-Ming and Gang [13]. Although this model-potential method is able to provide, in general, quite accurate DCS, ICS, and MTCS, most of the calculations have systematically underestimated the values of TCS and TACS [17].

In a paper published a few years ago [18], our group proposed a modified version of the QFSM3 absorption potential, referred as scaled quasi-free scattering model (SQFSM), in which an energy-dependent scaling factor is applied to the original QFSM3. Using the SQFSM, the agreement of TCS and TACS and the corresponding experimental values is significantly improved for a variety of atomic and molecular targets [19–21]. More recently, a benchmark study by Staszewska et al. [22] confirmed that the use of the scaling factor can improve the reliability of the calculated cross sections for electron–atom collisions.

In the present work, we report a theoretical study on e^-–CH_3F scattering in the intermediate-energy range. Specifically, calculated DCS, ICS, and MTCS, as well as TCS and TACS are reported for incident energies ranging from 15 to 500 eV. We hope that the comparison between our data, calculated both with and without the absorption model potential, can help clarify the role played by absorption effects in halogen-hydrocarbon compounds.

The organization of this paper is as follows: In Section 2, the theory is briefly described and some details of the calculations are given. The comparison of our calculated results with available experimental data, as well as with other theoretical results, is presented in Section 3, where we also summarize our conclusions.

2. Theory and calculation

We use a complex optical potential given by:

$$V_{opt} = V_{st} + V_{ex} + V_{cp} + iV_{ab} \tag{1}$$

to represent the e^-–CH_3F interaction dynamics. In the above equation, V_{st} and V_{ex} are the static and the exchange components, respectively, V_{cp} is the correlation–polarization contribution and V_{ab} is an absorption potential. Thus, the scattering problem is solved using the numerical solution of the Lippmann–Schwinger (LS) integral equation within the single-center-expansion close-coupling framework and further corrected using the Padé approximant technique. The basic theory of this method was already presented elsewhere [21] and will only be briefly outlined here.

Using the two-potential formalism, the reduced complex optical potential $U_{opt} = 2V_{opt}$ can be written as

$$U_{opt} = U_1 + U_2, \tag{2}$$

where the partition in U_1 and U_2 is arbitrary. Then the T matrix can also be written as

$$T_{fi} = T_1 + T_2, \tag{3}$$

where

$$T_1 = \langle \phi(\vec{k}_f)|U_1|\psi_1^+(\vec{k}_i)\rangle \tag{4}$$

and

$$T_2 = \langle \psi_1^-(\vec{k}_f)|U_2|\psi^+(\vec{k}_i)\rangle. \tag{5}$$

In Eq. (4), ϕ is the unperturbed plane wave function, ψ_1 is the distorted-wave solution of the scattering equation for the U_1 potential, whereas ψ seen in Eq. (5) is the solution of the LS scattering equation with complete interaction potential U. Moreover, the superscripts − and + appearing in Eqs. (4) and (5) denote the incoming- and outgoing-boundary conditions of the scattering waves, respectively.

In our calculations, U_1 and U_2 are chosen as

$$U_1 = U_{st} + U_{ex}^{loc} + U_{cp}, \tag{6}$$

and

$$U_2 = U_{ex} - U_{ex}^{loc} + iU_{ab}, \tag{7}$$

where U_{ex}^{loc} is a reduced local exchange potential. In the present work, U_{st} and U_{ex} are derived exactly from a near-Hartree–Fock self-consistent-field (SCF) target wave function, whereas U_{cp} is obtained in the framework of the free-electron-gas model, derived from a parameter-free local density, as prescribed by Padial and Norcross [23]. The Hara free-electron-gas exchange potential [24] is used to generate U_{ex}^{loc}. In Eq. (7), U_{ab} is the reduced SQFSM absorption potential of Lee et al. [18].

Since the potential U_1 chosen in our work is fully local, the LS equation for $\psi_1(\vec{k}_i)$ can be solved exactly, using standard numerical integration procedures. For that, both the scattering wave function and the interaction potential are single-center expanded in terms of the symmetry-adapted functions [25] as done, for example, in [21].

In order to evaluate T_2, we start with the LS equation for the total scattering wave function, written as:

$$\psi^{\pm}(\vec{r}) = \psi_1^{\pm}(\vec{r}) + \int G_1^{\pm}(\vec{r},\vec{r}')U_2(\vec{r}')\psi^{\pm}(\vec{r}')d\vec{r}', \tag{8}$$

where G_1 is the distorted-wave Green's function, which satisfies the following condition:

$$(\nabla^2 + k^2 - U_1)G_1^{\pm}(\vec{r},\vec{r}') = \delta(\vec{r},\vec{r}'). \tag{9}$$

Then the T_2 matrix is evaluated by making use of the Padé approximant in a similar way to that developed by Lucchese and McKoy [26] for linear molecules. The approach starts from some arbitrary function ϕ defined as

$$\phi^{(i)} = (G_1^+U_2)^i\psi_1, \tag{10}$$

with $\phi^{(0)} = \psi_1$. The $[N/N]$ Padé approximant of T_2 can be obtained from Eq. (22) of Gianturco et al. [27], *viz.*,

$$T_2[N/N] = -\sum_{i,j=1,N-1} \langle \psi_1^-|U_2|\phi^{(i)+}\rangle (D^{-1})_{ij} \langle \phi^{(j)-}|U_2|\psi_1^+\rangle, \tag{11}$$

where

$$D_{ij} = \langle \phi^{(i)-}|U_2 - U_2G_1^+U_2|\phi^{(j)+}\rangle. \tag{12}$$

The scattering process is studied within the fixed-nuclei framework [28], in which the DCS averaged over the molecular orientations are written as:

$$\frac{d\sigma}{d\Omega} = \frac{1}{8\pi^2}\int d\alpha \sin\beta d\beta d\gamma |f(\hat{k}'_i, \hat{k}'_f)|^2, \quad (13)$$

where $f(\hat{k}'_i, \hat{k}'_f)$ is the laboratory-frame scattering amplitude, $\hat{k}'_i$ and $\hat{k}'_f$ are the directions of incident- and scattered-electron linear momenta, respectively, and (α, β, γ) are the Euler angles which define the orientation of the principal axis of the molecule.

The quantity $f(\hat{k}'_i, \hat{k}'_f)$ is related to the T matrix elements by:

$$f(\hat{k}'_i, \hat{k}'_f) = -2\pi^2 T \quad (14)$$

Moreover, the TCS for electron–molecule scattering are obtained using the optical theorem:

$$\sigma_{tot} = \frac{4\pi}{k} Im(f(\theta = 0^\circ)) \quad (15)$$

The SCF wave function for the ground-state target used in the static-exchange calculation was obtained from an aug-cc-pVTZ gaussian basis set available in the Gaussian 03 code [29]. At the experimental equilibrium geometry of $R_{(C-F)}$ = 2.6135 a.u., $R_{(C-H)}$ = 2.0542 a.u., $\theta_{(F-C-H)}$ = 108.73° and $\theta_{(H-C-H)}$ = 110.20° [30], this basis set gives an SCF energy of −139.09837 a.u., and a permanent dipole moment of 2.044 D, in reasonable agreement with the experimental value of 1.85 D [31]. The calculated dipole polarizabilities α_{xx} = α_{yy} = 15.23 a.u., and α_{zz} = 16.16 a.u., were used to calculate the asymptotic form of V_{cp}.

In our calculations, the expansions of wave functions, interaction potentials and related matrices were all truncated at l_c = 30, for the entire energy range. Due to the strong polar nature of the target, these expansions were completed to infinity by using the well known Born Closure (BC) procedure, as used in some of our previous works [32–34].

All the calculated cross sections were converged within 5 iterations. Such iterative procedure via Padé approximant technique aims to evaluate the contribution of the absorption effects, as well as of the difference between the exact and local exchange effects to T-matrix. These contributions are highly energy-dependent. We noticed that the differences between the ICS calculated with and without Padé correction, both without BC correction, vary from +2.5% at 15 eV to −11% at 500 eV. At lower energies, this contribution is mainly due to exchange effects, whereas at higher energies it reflects mainly the absorption effects.

3. Results and discussion

Since absorption effects appear only at incident energies above excitation threshold, which is about 13.07 eV [35] for CH_3F, our results are then presented for incident energies starting at 15 eV. In Figs. 1–4, we present our DCS, both calculated with and without inclusion of the absorption effects in the 15–500 eV incident energy range. At 15 eV and 200 eV, we also present DCS data calculated with the inclusion of the absorption effects but without the BC correction. Moreover, the calculated DCS at the SEP level of approximation, as well as the experimental data of Varella et al. [4] in the 15–30 eV range, the measured data of Tanaka et al. [1] at 100 eV, and the theoretical data of Natalense et al. [9] at 30 eV, obtained at the SE level of approximation, are also shown for comparison. In contrast to those non-BC corrected data, the present calculated data with BC correction are strongly peaked in the forward direction, reflecting the polar nature of the target. The same behavior was also observed in the calculated results of Varella et al. due to the BC procedure used by them. Moreover, at incident energies of 15 and 20 eV, our results calculated with and without accounting for the

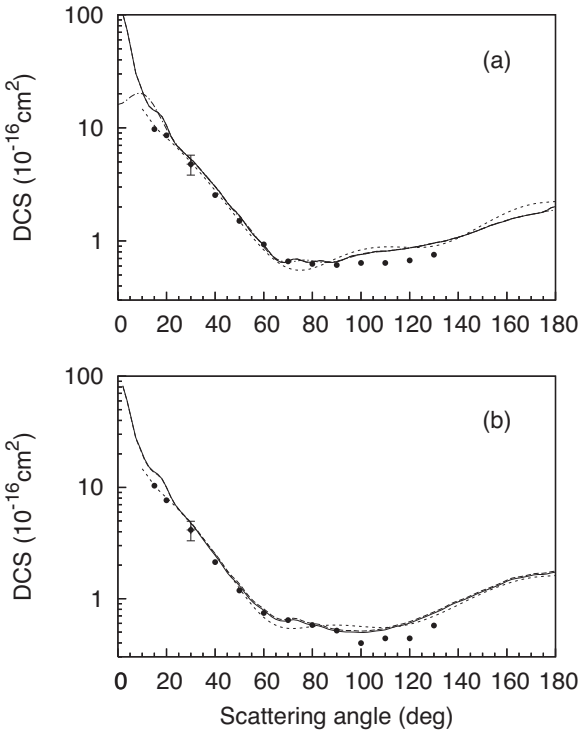

Fig. 1. DCS for elastic e^-–CH_3F scattering at (a) 15 eV and (b) 20 eV. Solid line, present results with absorption effects included in the calculation; dashed line, present results calculated without the inclusion of absorption effects; dotted-dashed line, present results calculated with absorption effects, but without the inclusion of the BC correction; short-dashed line, calculated data of Varella et al. [4]; full circles, experimental data of Varella et al. [4].

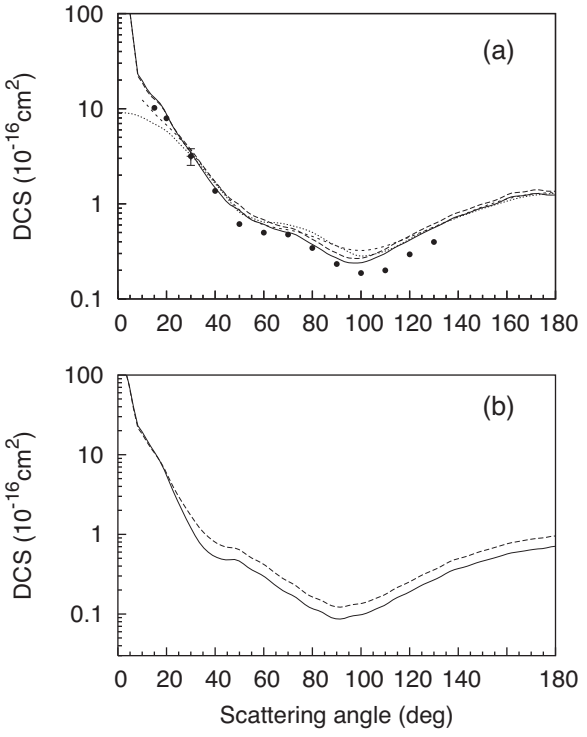

Fig. 2. Same as in Fig. 1, but for (a) 30 eV and (b) 60 eV. Symbols are the same as in Fig. 1, except: dotted line, theoretical results of Natalense et al. [9].

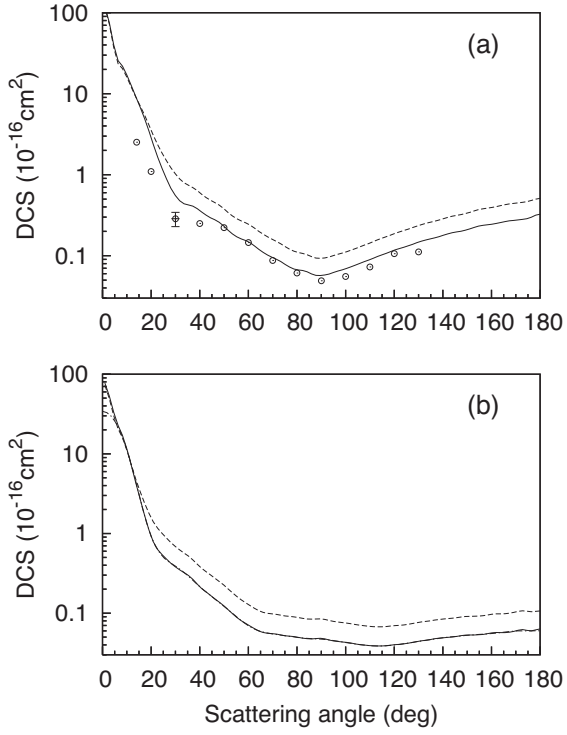

Fig. 3. Same as in Fig. 1, but for (a) 100 eV and (b) 200 eV. Symbols are the same as in Fig. 1, except: open circles, experimental data of Tanaka et al. [1].

absorption are almost indistinguishable, due to the weakness of the absorption effects at energies near the threshold. Nevertheless, the influence of such effects increases rapidly with increasing incident energies. Actually, at 60 eV and above, the DCS calculated without inclusion of V_{abs} lye significantly above those with V_{abs} included,

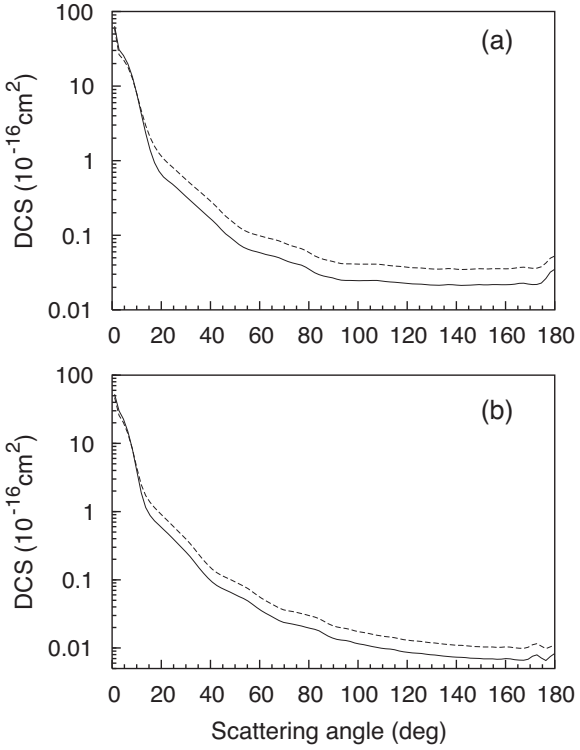

Fig. 4. Same as in Fig. 1, but for (a) 300 eV and (b) 500 eV.

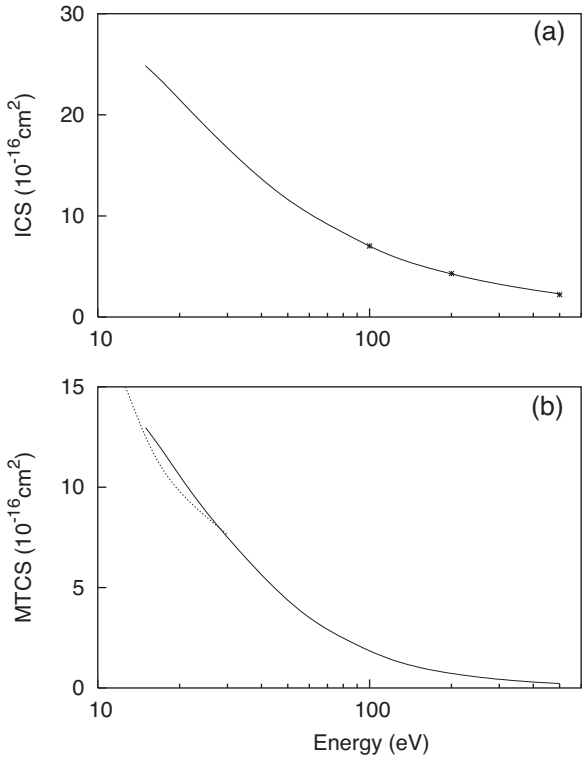

Fig. 5. (a) ICS and (b) MTCS for elastic e^-–CH_3F scattering. Solid line, present theoretical results including absorption effects; asterisks, theoretical IAM results of Manero et al. [11]; dotted line, theoretical results of Natalense et al. [9] calculated at the SE level of approximation.

mainly at intermediate and large scattering angles. This fact is due to the loss of electron flux in the elastic scattering channel as a consequence of the opening of inelastic channels.

The comparison with experimental and other theoretical results shows a generally good agreement among them. In particular, our data obtained with absorption effects are in better agreement with the experimental data than those without such effects. The small oscillations seen in our calculated results near backward scattering at 300 and 500 eV are unphysical and are due to the lack of the convergence in the single-center expansion procedure.

In Fig. 5(a) and (b) we show our ICS and MTCS, respectively, for elastic e^-–CH_3F scattering in the 15–500 eV energy range, both calculated with the inclusion of absorption effects. Our results are compared with the IAM ICS of Manero et al. [11] in the 100–500 eV energy range and with the SE MTCS of Natalense et al. [9] in the 10–30 eV range. Our calculated ICS are in very good agreement with those of Manero et al. [11] in the overlapping energies whereas our MTCS in the 15–30 eV range are in good agreement with the theoretical data of Natalense et al. This good agreement is quite interesting because it clearly indicates that the dipolar nature of the target does not affect significantly the calculated MTCS, since no BC procedure was taken into account in the calculations of Natalense et al.

In Fig. 6(a) and (b) we present our TCS and TACS, respectively, calculated using the SQFSM absorption potential at incident energies up to 500 eV. The comparison is made with the experimental TCS of Krzysztofowicz and Szmytkowski [8], as well as with the experimental TICS of Beran and Kevan [5] and of Vallance et al. [6]. The theoretical IAM TCS of Manero et al. [11], the AR TCS of Shi et al. [12], and of Xiao-Ming and Gang [13], the MAR-SC TACS of Joshipura and Vinodkumar [10] and the BEB TICS of Vallance

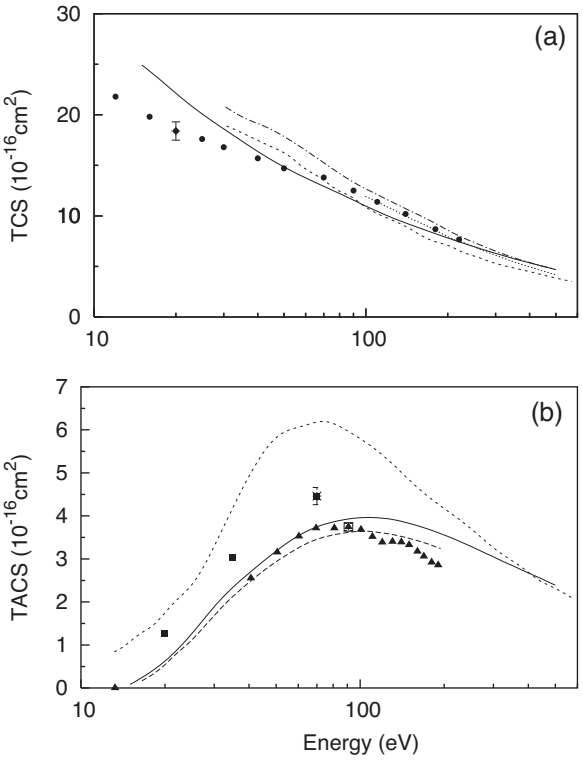

Fig. 6. (a) TCS for e^-–CH_3F scattering. Solid line, present theoretical results calculated including absorption effects; short-dashed line, calculated MAR-SC data of Joshipura and Vinodkumar [10]; dotted line, corrected AR data of Xiao-Ming and Gang [13]; dash-dotted line, revised AR data of Shi et al. [12]; full circles, experimental results of Krzysztofowicz and Szmytkowski [8]; (b) TACS for e^-–CH_3F scattering. Solid line, present theoretical results; short-dashed line, calculated MAR-SC data of Joshipura and Vinodkumar [10]; dashed line, theoretical BEB TICS of Vallance et al. [6]; full squares, experimental TICS of Beran and Kevan [5]; full triangles, experimental TICS of Vallance et al. [6].

et al. [6] are also shown for comparison. In general, all calculated TCS and TACS are in qualitative agreement among each other, but quantitatively, the MAR-SC TACS are significantly larger than other corresponding data. In general, our TACS results are in good agreement with the experimental and the BEB TICS data of Vallance et al. [6], mainly at energies up to 70 eV. Above that energy, our TACS are slightly larger than those of Vallance et al. On the other hand, the experimental TICS data of Beran and Kevan [5] are systematically higher than ours.

In summary, we report a theoretical study on e^-–CH_3F scattering in the intermediate-energy range. Our method was able to provide values of various cross sections in good agreement with the experimental results available in the literature, as well as with other theoretical data. In particular, the differences seen between the present calculated cross sections with and without inclusion of absorption effects in the 60–500 eV range has confirmed the relevance of such effects on the elastic scattering channel at these energies. We hope our data can stimulate further theoretical and/or experimental investigation on e^-–halogenomethane collisions, mainly in the intermediate-energy region.

Acknowledgements

This research was partially supported by the Brazilian agencies CNPq and FAPESP.

References

[1] H. Tanaka, T. Masai, M. Kimura, T. Nishimura, Y. Itikawa, Phys. Rev. A 56 (1997) R3338.
[2] L.G. Christophorou, J.K. Olthoff, M.V.V.S. Rao, Phys. Chem. Ref. Data 25 (1996) 1341.
[3] L.G. Christophorou, J.K. Olthoff, M.V.V.S. Rao, Phys. Chem. Ref. Data 26 (1997) 1.
[4] M.T. do N. Varella, C. Winstead, V. McKoy, M. Kitajima, H. Tanaka, Phys. Rev. A 65 (2002) 022702.
[5] J.A. Beran, L. Kevan, J. Phys. Chem. 73 (1969) 3886.
[6] C. Vallance, S.A. Harris, J.E. Hudson, P.W. Harland, J. Phys. B 30 (1997) 2465.
[7] A. Benitez, J.H. Moore, J.A. Tossell, J. Chem. Phys. 88 (1988) 6691.
[8] A.M. Krzysztofowicz, C. Szmytkowski, J. Phys. B 28 (1995) 1593.
[9] A.P.P. Natalense, M.H.F. Bettega, L.G. Ferreira, M.A.P. Lima, Phys. Rev. A 59 (1999) 879.
[10] K.N. Joshipura, M. Vinodkumar, Eur. Phys. J. D 5 (1999) 229.
[11] F. Manero, F. Blanco, G. García, Phys. Rev. A 66 (2002) 032713.
[12] D. Shi, Y. Liu, J. Sun, H. Ma, Z. Zhu, Rad. Phys. Chem. 77 (2008) 528.
[13] T. Xiao-Ming, Z. Gang, Chin. Phys. B 21 (2012) 063402.
[14] G. Staszewska, D.W. Schwenke, D.G. Truhlar, Phys. Rev. A 29 (1984) 3078.
[15] F. Blanco, G. García, Phys. Lett. A 255 (1999) 147.
[16] Y.H. Jiang, J.F. Sun, L.D. Wan, Chin. J. At. Mol. Phys. 11 (1994) 418.
[17] M.-T. Lee, I. Iga, M.G.P. Homem, L.E. Machado, L.M. Brescansin, Phys. Rev. A 65 (2002) 062702.
[18] M.-T. Lee, I. Iga, L.E. Machado, L.M. Brescansin, E.A. y Castro, I.P. Sanches, G.L.C. de Souza, J. Electron Spectrosc. Relat. Phenom. 155 (2007) 14.
[19] E.A. y Castro, G.L.C. de Souza, I. Iga, L.E. Machado, L.M. Brescansin, M.-T. Lee, J. Electron Spectrosc. Relat. Phenom. 159 (2007) 30.
[20] P. Rawat, M.G.P. Homem, R.T. Sugohara, I.P. Sanches, I. Iga, G.L.C. de Souza, A.S. dos Santos, R.R. Lucchese, L.E. Machado, L.M. Brescansin, M.-T. Lee, J. Phys. B 43 (2010) 225202.
[21] G.L.C. de Souza, M.-T. Lee, I.P. Sanches, P. Rawat, I. Iga, A.S. dos Santos, L.E. Machado, R.T. Sugohara, L.M. Brescansin, M.G.P. Homem, R.R. Lucchese, Phys. Rev. A 82 (2010) 012709.
[22] G. Staszewska, P. Staszewski, K. Zebrowski, J. Electron Spectrosc. Rel. Phenom. 168 (2008) 40.
[23] N.T. Padial, D.W. Norcross, Phys. Rev. A 29 (1984) 1742.
[24] S. Hara, J. Phys. Soc. Japan. 22 (1967) 710.
[25] P.G. Burke, N. Chandra, F.A. Gianturco, J. Phys. B 5 (1972) 2212.
[26] R.R. Lucchese, V. McKoy, Phys. Rev. A 28 (1983) 1382.
[27] F.A. Gianturco, R.R. Lucchese, N. Sanna, J. Chem. Phys. 102 (1995) 5743.
[28] See e.g., M.A. Brandt, D.G. Truhlar, Chem. Phys. Lett. 23 (1973) 48, and references therein.
[29] M.J. Frisch, G.W. Trucks, H.B. Schlegel, G.E. Scuseria, M.A. Robb, J.R. Cheeseman, J.A. Montgomery Jr., T. Vreven, K.N. Kudin, J.C. Burant, J.M. Millam, S.S. Iyengar, J. Tomasi, V. Barone, B. Mennucci, M. Cossi, G. Scalmani, N. Rega, G.A. Petersson, H. Nakatsuji, M. Hada, M. Ehara, K. Toyota, R. Fukuda, J. Hasegawa, M. Ishida, T. Nakajima, Y. Honda, O. Kitao, H. Nakai, M. Klene, X. Li, J.E. Knox, H.P. Hratchian, J.B. Cross, V. Bakken, C. Adamo, J. Jaramillo, R. Gomperts, R.E. Stratmann, O. Yazyev, A.J. Austin, R. Cammi, C. Pomelli, J.W. Ochterski, P.Y. Ayala, K. Morokuma, G.A. Voth, P. Salvador, J.J. Dannenberg, V.G. Zakrzewski, S. Dapprich, A.D. Daniels, M.C. Strain, O. Farkas, D.K. Malick, A.D. Rabuck, K. Raghavachari, J.B. Foresman, J.V. Ortiz, Q. Cui, A.G. Baboul, S. Clifford, J. Cioslowski, B.B. Stefanov, G. Liu, A. Liashenko, P. Piskorz, I. Komaromi, R.L. Martin, D.J. Fox, T. Keith, M.A. Al-Laham, C.Y. Peng, A. Nanayakkara, M. Challacombe, P.M.W. Gill, B. Johnson, W. Chen, M.W. Wong, C. Gonzalez, J.A. Pople, Gaussian 03, Revision C. 02, Gaussian Inc., Wallingford, CT, 2004.
[30] J. Demaison, J. Breidung, W. Thiel, D. Papousek, Struct. Chem. 10 (1999) 129.
[31] J.N. Shoolery, A.H. Sharbaugh, Phys. Rev. 82 (1951) 95.
[32] L.E. Machado, L.M. Brescansin, I. Iga, M.-T. Lee, Eur. Phys. J. D 33 (2005) 193.
[33] L.M. Brescansin, L.E. Machado, M.-T. Lee, H. Cho, Y.S. Park, J. Phys. B 41 (2008) 185201.
[34] M.-T. Lee, G.L.C. de Souza, L.E. Machado, L.M. Brescansin, A.S. dos Santos, R.R. Lucchese, R.T. Sugohara, M.G.P. Homem, I.P. Sanches, I. Iga, J. Chem. Phys. 136 (2012) 114311.
[35] B.P. Pullen, T.A. Carlson, W.E. Moddeman, G.K. Schweitzer, W.E. Bull, F.A. Grimm, J. Chem. Phys. 53 (1970) 768.

Electron collisions with ammonia and formamide in the low- and intermediate-energy ranges

M. G. P. Homem,[1] I. Iga,[1] G. L. C. de Souza,[2] A. I. Zanelato,[3] L. E. Machado,[4] J. R. Ferraz,[4] A. S. dos Santos,[4] L. M. Brescansin,[5] R. R. Lucchese,[6] and M.-T. Lee[1]

[1]*Departamento de Química, UFSCar, 13565-905 São Carlos, SP, Brazil*
[2]*Departamento de Química, UFMT, 78060-900 Cuiabá, MT, Brazil*
[3]*Instituto de Ciências Exatas e Tecnologia, UFAM, 69100-000 Itacoatiara, AM, Brazil*
[4]*Departamento de Física, UFSCar, 13565-905 São Carlos, SP, Brazil*
[5]*Instituto de Física Gleb Wataghin, UNICAMP, 13083-970 Campinas, SP, Brazil*
[6]*Chemistry Department, Texas A&M University, College Station, Texas 77842-3012, USA*

(Received 27 October 2014; revised manuscript received 16 November 2014; published 2 December 2014)

We report an investigation on electron collisions with two nitrogen-containing compounds, namely ammonia (NH_3) and formamide (NH_2CHO). For ammonia, both theoretical and experimental differential, integral, and momentum-transfer cross sections, as well as calculated grand-total and total absorption cross sections, are reported in the 50–500 eV incident energy range. Calculated results of various cross sections are also reported for energies below 50 eV. Experimentally, angular distributions of the scattered electrons were measured using a crossed electron beam-molecular beam geometry and then converted to absolute differential cross sections using the relative flow technique. Absolute integral and momentum-transfer cross sections for elastic e^--ammonia scattering were also derived from the measured differential cross sections. For formamide, only theoretical cross sections are presented in the 1–500 eV incident energy range. A single-center-expansion technique combined with the method of Padé was used in our calculations. For both targets, our calculated cross sections are compared with the present measured data and with the theoretical and experimental data available in the literature and show generally good agreement. Moreover, for formamide, two shape resonances located at 3.5 eV and 15 eV which correspond to the continuum $^2A''$ and $^2A'$ scattering symmetries, respectively, are identified. The former can be associated to the $^2B_1$ shape resonance in formaldehyde located at around 2.5 eV, whereas the latter can be related to the ^2E resonance in ammonia at about 10 eV. Such correspondence is very interesting and so supports the investigation on electron interaction with small building blocks, instead of with larger biomolecules.

DOI: 10.1103/PhysRevA.90.062704 PACS number(s): 34.80.Bm

I. INTRODUCTION

Without any doubt, nitrogen-containing compounds constitute a class of most abundant and important materials in universe. These molecules have played an important role in the evolution of life on Earth. Recently, it has been discovered that significant damage to DNA and RNA, such as single or double strand breaks, can be caused by their interaction with low-energy electrons [1]. Large biomolecules are built from smaller components, most of them containing nitrogen. Thus electron interaction with such molecules which form building blocks of large biomolecules has attracted considerable attention in recent years [1,2]. In the near past, several small biomolecules such as methanol [3], ethanol [4], propane [5], and dimethylether [6] were investigated both theoretically and experimentally by our group. In this work, we present a study of electron collisions with two nitrogen-containing compounds, namely ammonia (NH_3) and formamide (NH_2CHO).

Electron scattering by ammonia has many practical applications in fields such as space physics, modeling of planetary atmospheres, gas-discharge lasers, switching devices, and plasma chemistry, where NH_3 is a source of nitrogen atoms for the fabrication of nitride films and other nitrogen-containing compounds [7]. In addition, due to the ozone-layer destruction by the chlorofluorocarbon compounds, ammonia has been reintroduced as a cooling gas, replacing the freons. Thus e^--NH_3 interaction is also important in atmospheric studies, since the concentration of ammonia is expected to increase in Earth's atmosphere due to this replacement.

Previous experimental investigation on e^--NH_3 scattering is limited. The very first experimental grand-total cross sections (TCS) were reported in the 1–20 eV energy range by Brüche [8] in 1929. Lately, TCS were also measured by Sueoka *et al.* [9] using a time-of-flight technique and by Szmytkowski *et al.* [10], Zecca *et al.* [11], and García and Manero [12] using a linear transmission technique. More recently, experimental TCS were reported by Ariyasingue *et al.* [13] in the 400–4000 eV range and by Jones *et al.* [14] in the 0.02–10 eV range. Also, experimental total ionization cross sections (TICS) were reported by Rao and Srivastava [15]. In addition, Hayashi [16] reported momentum-transfer cross sections (MTCS) which are based on the drift velocity measurements of Pack *et al.* [17] and the calculations of Altshuler [18]. Absolute elastic differential cross sections (DCS) at 7.5 eV energy were reported by Ben Arfa and Tronc [19] and also relative DCS were reported by Furlan *et al.* [20] in the 12–50 eV range. The most complete experimental DCS determination for this target was probably that performed by Alle *et al.* [21]. In that work, absolute DCS were reported in the 2–30 eV energy range and in the 10°–125° angular range. Above 30 eV, the only set of experimental DCS in absolute scale were those of Bromberg measured in the 2°–10° angular range and at incident energies of 300, 400, and 500 eV, reported in the article of Harshbarger *et al.* [22]. Relative DCS, measured in the same energy and angular ranges but normalized to those of Bromberg, were also reported by Harshbarger *et al.* [22]. Finally, absolute measurements of DCS for the electron impact excitation of the $\nu_{1,3}$ vibrational

modes of e^--NH_3 at incident energies of 5, 7.5, and 15 eV were reported by Gulley *et al.* [23].

From the theoretical point of view, the literature for the elastic scattering of electrons by NH_3 is quite abundant. Some earlier DCS calculations include those reported by Gianturco and Jain [24], Pritchard *et al.* [25], Gianturco [26], and Rescigno *et al.* [27]. More recently, calculations were also reported by Ribeiro *et al.* [28] and by Munjal and Baluja [29]. In all these calculations, the framework of the fixed-nuclei approximation combined with the single-center expansion technique was employed. This procedure may cause severe convergence problems in the calculation of electron-polar molecule cross sections due to truncations in partial-wave expansions [25]. Because of that, Pritchard *et al.* reported DCS only at intermediate and backward angles where the first few partial waves dominate the description of the interaction dynamics. On the other hand, Gianturco [26], Rescigno *et al.* [27], and Munjal and Baluja [29] applied the Born-closure method to overcome this difficulty. Nevertheless, these calculations were limited to incident energies up to 20 eV. At higher energies, elastic DCS in the 0.1–1.0 keV range were calculated by Jain *et al.* using a parameter-free spherical optical potential at the static-exchange-polarization (SEP) level of approximation. In addition, calculations of TCS [31–33] and TICS [31] are also available in the literature.

Formamide, a derivative of ammonia, constitutes the simplest molecular system containing the peptide bond. Since the peptide type of chemical bonds are essential in the structure of proteins, the investigation on electron interaction with formamide can be useful to understand processes of electron-protein interactions and modeling of energy deposition upon high-energy irradiation of biomaterials [34]. Moreover, formamide is also considered as a prebiotic molecule. The identification of this system in the interestellar regions [35] has stimulated considerable studies in the astrobiological research in recent years. Despite that, the investigation on e^--formamide interaction reported in the literature is very limited, both theoretically and experimentally.

Theoretical integral cross sections (ICS) and MTCS for elastic scattering of low-energy electrons (1–12 eV) by this target were calculated by Bettega [36] using the Schwinger multichannel method (SMC). The elastic DCS, ICS, and MTCS and the excitation cross sections from the ground state to the first four low-lying electron excited states at incident energies up to 10 eV were recently calculated by Wang and Tian [37] using the *R*-matrix method. In addition, TICS in the 10–2000 eV range were calculated by Gupta *et al.* [38] using the spherical complex optical potential (SCOP) approach.

Experimentally, absolute DCS for elastic e^--NH_2CHO scattering were measured and reported by Maljković *et al.* [34] at 100, 150, and 300 eV energies and in the 20°–110° angular range. To our knowledge, no other theoretical and/or experimental determinations of cross sections for this system were reported.

In this work, we present a joint theoretical-experimental study of electron scattering by ammonia in the low- and intermediate-energy ranges. Also, a theoretical investigation on e^--NH_2CHO collisions is reported. Specifically, experimental absolute DCS for electrons elastically scattered from NH_3 are determined using the relative flow technique (RFT) [39] in the 50–500 eV range and in the 10°–130° angular range. ICS and MTCS are also derived from the experimental DCS. Theoretically, DCS, ICS, MTCS, TCS, and total absorption cross sections (TACS) are also reported in 1–500 eV energy range for both ammonia and formamide. Thus the present study represents an attempt to partially fill the lack of both theoretical and experimental results for e^--NH_3 and e^--NH_2CHO collisions.

The organization of this work is as follows. In Sec. II, we present some details of our experimental procedure. In Sec. III, the theory is briefly described. In Sec. IV, some computational details are presented and our calculated results for ammonia and formamide are compared with the present measured results, as well as with existing experimental and theoretical data. Some concluding remarks are also presented in Sec. V.

II. EXPERIMENTAL PROCEDURE

The experimental setup and procedure used in the present measurement are given in detail in some of our previous works [40,41]. Briefly, the relative angular distribution of the scattered electrons at a given incident electron energy is measured using a crossed electron beam-molecular beam geometry. The scattered electrons are energy filtered by a retarding-field energy selector with a resolution of about 1.5 eV. This resolution allows the discrimination of inelastically scattered electrons that resulted from electronic excitation, whereas those from vibrational excitation processes remain unresolved. Thus our measured DCS are indeed vibrationally summed.

The sample of ammonia used in the measurements is prepared in our laboratory from a commercial ammonia solution with concentration of 36% in weight. For each measurement, a sample of ammonia solution is put into a glass balloon attached to a gas handling manifold and then undergoes a pretreatment for elimination of atmospheric air, through several freeze-thaw cycles using liquid nitrogen as the cooling agent. After these steps, the balloon with the liquid sample is then immerged into a Dewar frask filled with ice and salt. The temperature of this system is around $-20\,^{\circ}$C. At such low temperature, the vapor pressure of water is negligible compared to that of ammonia. In fact, the purity of the gaseous ammonia so generated was constantly checked using both a quadrupole mass spectrometer and a time-of-flight mass spectrometer [42], and was shown to be better than 99%. During the measurements, the working pressure in the vacuum chamber was around 5×10^{-7} torr.

The recorded scattering intensities were converted into absolute elastic DCS using the RFT [39]. Accordingly, the DCS for a gas under determination (x) can be related with the known DCS of a secondary standard (std) as

$$\left(\frac{d\sigma}{d\Omega}\right)_x = \left(\frac{d\sigma}{d\Omega}\right)_{std} \frac{I_x}{I_{std}} \frac{R_{std}}{R_x} \left(\frac{M_{std}}{M_x}\right)^{\frac{1}{2}}, \qquad (1)$$

where I is the scattered electron intensity, R is the relative flow rate, and M is the molecular weight. The application of RFT requires precise measurements of R for both gases, x and std. They were determined according to the procedure described in our previous studies [3,4,43].

In the present study, the absolute DCS of Ar and N_2 reported by Jansen *et al.* [44] and Dubois and Rudd [45] were used as secondary standards. Details of the analysis of the experimental uncertainties have also been given elsewhere [40,41]. They were briefly estimated as follows. Uncertainties of random nature such as pressure fluctuations, electron-beam current readings, background scattering, etc., were estimated to be less than 2%. These contributions combined with the estimated statistical errors gave an overall uncertainty of 4% in the relative DCS for each gas. Also, the experimental uncertainty associated with the normalization procedure was estimated to be 5.7%. These errors combined with the quoted errors [45] in the absolute DCS of the secondary standard provided an overall experimental uncertainty of 15% in our absolute DCS. Absolute DCS were determined in the 10°–130° angular range. In order to obtain ICS and MTCS, a manual extrapolation procedure was adopted to estimate DCS at scattering angles out of the angular range covered experimentally. The overall uncertainties on the ICS and MTCS were estimated to be 24%.

III. THEORY

The theory used in this work is essentially the same as in several previous works [5,46,47]. Briefly, a complex optical potential given by

$$V_{opt} = V_{st} + V_{ex} + V_{cp} + i\,V_{ab} \tag{2}$$

was used to represent the electron-target interaction. Using this optical potential, the many-body nature of the electron-molecule interaction is reduced to a one-particle scattering problem which can be solved exactly using the numerical solution of the close-coupling Lippmann-Schwinger (LS) integral equation. In the above equation, V_{st} and V_{ex} are the static and the exchange components, respectively, and V_{cp} is the correlation-polarization contribution. In addition, V_{ab} is an absorption potential which describes the reduction of the flux of elastically scattered electrons due to opening of inelastic scattering channels.

The reduced form of the optical potential $U_{opt} = 2V_{opt}$ can be partitioned as a sum of two components:

$$U_{opt} = U_1 + U_2, \tag{3}$$

with

$$U_1 = U_{st} + U_{ex}^{loc} + U_{cp} \tag{4}$$

and

$$U_2 = U_{ex} - U_{ex}^{loc} + i\,U_{ab}, \tag{5}$$

where U_{ex}^{loc} is a reduced local exchange potential. According to the two-potential formalism, the full transition T matrix, given as

$$T_{fi} = \langle \phi(\vec{k}_f)|U_{opt}|\psi^+(\vec{k}_i)\rangle, \tag{6}$$

is also composed of two parts:

$$T_{fi} = T_1 + T_2, \tag{7}$$

where

$$T_1 = \langle \phi(\vec{k}_f)|U_1|\psi_1^+(\vec{k}_i)\rangle \tag{8}$$

and

$$T_2 = \langle \psi_1^-(\vec{k}_f)|U_2|\psi^+(\vec{k}_i)\rangle. \tag{9}$$

In Eqs. (6) and (8), ϕ is the unperturbed plane wave, ψ is the solution of the LS equation for the full optical potential U_{opt}, ψ_1 is the solution of the distorted-wave LS equation for potential U_1, and k is the magnitude of the electron linear momentum.

Further, T_2 can be obtained iteratively using the $[N/N]$ technique of Padé [48]:

$$T_2[N/N] = -\sum_{i,j=1,N-1} \langle \psi_1^-|U_2|\phi^{(i)+}\rangle (D^{-1})_{ij} \langle \phi^{(j)-}|U_2|\psi_1^+\rangle, \tag{10}$$

where

$$D_{ij} = \langle \phi^{(i)-}|U_2 - U_2 G_1^+ U_2|\phi^{(j)+}\rangle, \tag{11}$$

and G_1 is the distorted-wave Green's function, which satisfies the following condition:

$$(\nabla^2 + k^2 - U_1)G_1^{\pm}(\vec{r},\vec{r}') = \delta(\vec{r},\vec{r}'). \tag{12}$$

The superscripts $-$ and $+$ appearing in the above equations denote the incoming- and outgoing-boundary conditions of the scattering waves, respectively. In our calculation, the truncation parameter N is iteratively increased until convergence is achieved. The converged body-frame (BF) T matrix (or equivalently the BF scattering amplitude f) can then be expressed in the laboratory frame (LF) by the usual frame transformation [49]. Additionally, the TCS for electron-molecule scattering are obtained using the optical theorem:

$$\sigma_{tot} = \frac{4\pi}{k}\mathrm{Im}[f(\theta = 0^\circ)]. \tag{13}$$

In the present work, U_{st} and U_{ex} were derived exactly from a near-Hartree-Fock self-consistent-field (HF-SCF) target wave function, whereas U_{cp} was obtained in the framework of the free-electron-gas model, derived from a parameter-free local density, as prescribed by Padial and Norcross [50], and the absorption potential U_{ab} in Eq. (5) was the reduced scaled quasifree scattering model (SQFSM) absorption potential of Lee *et al.* [51], which is an improvement of the version 3 of the model absorption potential originally proposed by Staszewska *et al.* [52]. The Hara free-electron-gas-exchange potential [53] was used to generate the local exchange potential U_{ex}^{loc}.

IV. COMPUTATIONAL DETAILS AND RESULTS

A. Ammonia

The HF-SCF wave function of ammonia was obtained using the aug-cc-pVTZ (6D,10F) basis set of the GAUSSIAN 03 package [54]. At the experimental ground-state molecular geometry [55], this basis provided a total energy of −56.221 023 hartrees. The calculated electric dipole moment was 1.4682 D, in good agreement with the experimental value of 1.470 D [55]. Moreover, the asymptotic form of U_{cp} was generated with the dipole polarizabilities [55] calculated at the HF-SCF level using the same basis set. The obtained values were $\alpha_{xx} =$ 12.31 a.u., $\alpha_{yy} = 12.31$ a.u., and $\alpha_{zz} = 12.80$ a.u., resulting

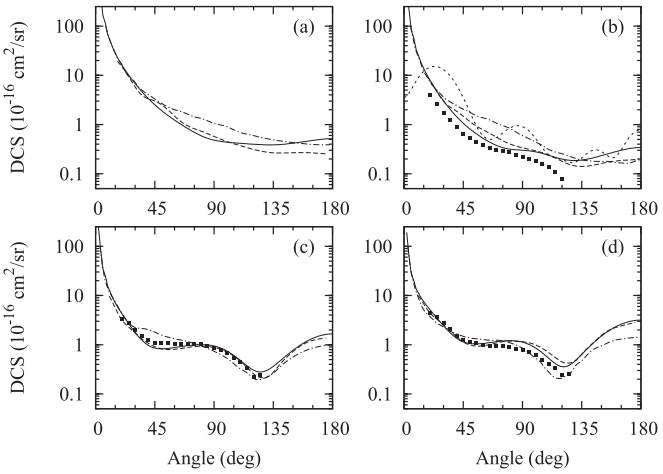

FIG. 1. DCS for elastic e^--ammonia scattering at (a) 1 eV, (b) 2 eV, (c) 5 eV, and (d) 7.5 eV. Full curve, present theoretical results calculated with Born-closure procedure; dashed curve, calculated data of Rescigno *et al.* [27]; dashed-dotted curve, calculated data of Munjal and Baluja [29]; short-dashed curve, present theoretical results calculated without Born-closure procedure; solid squares, measured data of Alle *et al.* [21].

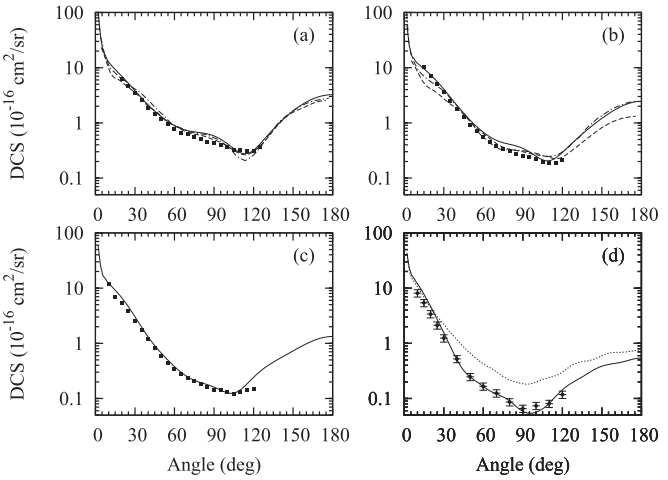

FIG. 2. Same as Fig. 1 but at (a) 15 eV, (b) 20 eV, (c) 30 eV, and (d) 50 eV except: dotted curve, present theoretical results calculated without inclusion of absorption effects; solid circles with error bars, present experimental data.

in an average dipole polarizability of $\alpha_0 = 12.473$ a.u., in fair agreement with the experimental value of 14.192 a.u. [55]. In our calculation, the wave functions and the interaction potentials, as well as the related matrices, were single-center expanded about the center of mass of the molecule in terms of the well known $X_{lh}^{p\mu}$ symmetry-adapted functions [56]. The truncation parameters used in these expansions were $l_c = 25$ and $h_c = 25$ for all bound and continuum orbitals, as well as for the T-matrix elements. The calculated cross sections were converged with $N = 7$. Since ammonia is a polar system, the partial-wave expansions converge slowly due to the long-range nature of the dipole interaction potential. In order to overcome this difficulty, a Born-closure formula was used to account for the contribution of higher partial-wave components to the scattering amplitudes. The procedure used was the same as in some of our previous studies [4,57,58].

The comparison of the present experimental and calculated DCS data with the existing theoretical [27,29] and measured [21] results is made in Figs. 1–3. In Fig. 1, our theoretical dipole-Born-corrected DCS for elastic electron scattering by ammonia in the 1–7.5 eV range are presented. Particularly, in Fig. 1(b), DCS obtained without a dipole-Born correction at 2 eV are also shown. It is seen that our DCS calculated without the dipole-Born correction present unphysical oscillations, due to the lack of convergence of the partial-wave expansion. Also, in this low-energy range, absorption effects were not included in the present study and, therefore, our calculations were performed at the same level of approximation as those of Rescigno *et al.* [27] and Munjal and Baluja [29]. From Fig. 1, it is seen that our calculated results are in good agreement with the experimental DCS of Alle *et al.* [21]. Comparing with other theoretical results, it is seen that at 5 and 7.5 eV, there is a general good agreement among all the calculated DCS. Nevertheless, at 1 and 2 eV, there are some discrepancies between these results, particularly at scattering angles larger than 40°. In general, our results are in better agreement with those of Rescigno *et al.* [27].

In Figs. 2 and 3, we present our theoretical dipole-Born-corrected DCS for elastic electron scattering by ammonia in the 15–500 eV energy range. In this range, the absorption effects were taken into account in our calculations. At 15 and 20 eV, comparison is made with the theoretical results of Rescigno *et al.* [27] and Munjal and Baluja [29]. Very good agreement is also seen among all these theoretical results which seems to indicate that the absorption effects are still weak at these energies. Nevertheless, above 30 eV inelastic scattering processes become relevant and thus affect significantly the elastic scattering processes. Such influences are clearly seen in Figs. 2(d) and 3(a), where DCS at 50 and 100 eV calculated without inclusion of absorption effects are also shown. It is seen that the DCS calculated without

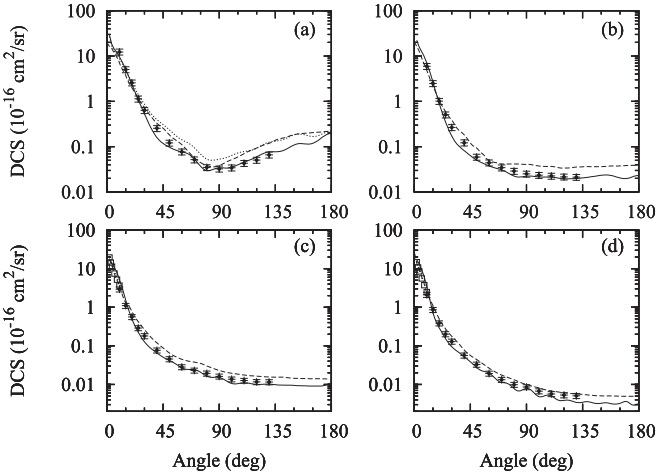

FIG. 3. Same as Fig. 2 but at (a) 100 eV, (b) 200 eV, (c) 300 eV, and (d) 500 eV, except: dashed line, calculated SHP1 results of Jain *et al.* [30] using the SCOP model; open squares, experimental DCS of Bromberg [22].

such effects lie significantly above those including them. In addition, our theoretical results are also compared with the experimental data of Alle *et al.* [21] at energies up to 30 eV and with the present measured data in the 50–500 eV range. There is a very good agreement between our theoretical data calculated with absorption effects and both experimental data. At 300 and 500 eV, the experimental DCS of Bromberg measured in the 2°–10° angular range [22] are also shown. These results seem to match very well to our measured data. At the only overlapping scattering angle, 10°, the results of Bromberg and our data agree within the experimental uncertainties at incident energies of 400 and 500 eV. However, his DCS at 10° and 300 eV is slightly out of the uncertainty margin. At these energies, our calculated results also agree well with both the present measured data and with those of Bromberg [22], although some small oscillations are seen in our theoretical DCS, particularly at scattering angles larger than 60°. Such oscillations are not clear in the experimental data and can be attributed to the lack of higher partial waves in the expansion of both the interaction potential and the T-matrix elements.

Figures 4(a) and 4(b) show our theoretical elastic ICS and MTCS, respectively, in the 1–500 eV energy range. Our ICS are compared with the calculated results of Munjal and Baluja [29] at energies up to 20 eV, with the experimental results of Alle *et al.* [21] in the 2–30 eV energy range, and with the present experimental ICS in the 50–500 eV range. Since at energies below the electronic excitation threshold the ICS and the TCS are essentially equivalent, the experimental TCS data of Jones *et al.* [14] at energies up to 10 eV are also shown. Our calculated ICS show a strong enhancement towards zero energy, which is due to the large target dipole moment. This feature is also seen in the theoretical ICS of Munjal and Baluja, and confirmed by the experimental TCS of Jones *et al.* Moreover, a broad resonance feature, centered at about 10 eV is seen, in agreement with the experimental results of Alle *et al.* [21]. Both the partial ICS and eigenphase-sum analyses indicated that the observed feature is a shape resonance in the continuum ^2E scattering channel. Quantitatively, our calculated results are in fair agreement with the TCS of Jones *et al.* at the overlapping energies. The experimental results of Alle *et al.* agree well with our calculated data in the 5–30 eV range, but lie well below our data at 2 eV. This disagreement is not surprising, since their experimental ICS were generated by integrating the DCS, which are extrapolated to the angular region where the DCS are strongly peaked, specially at such low incident energies. At energies of 50 eV and above, there is a very good agreement between our calculated and experimental ICS.

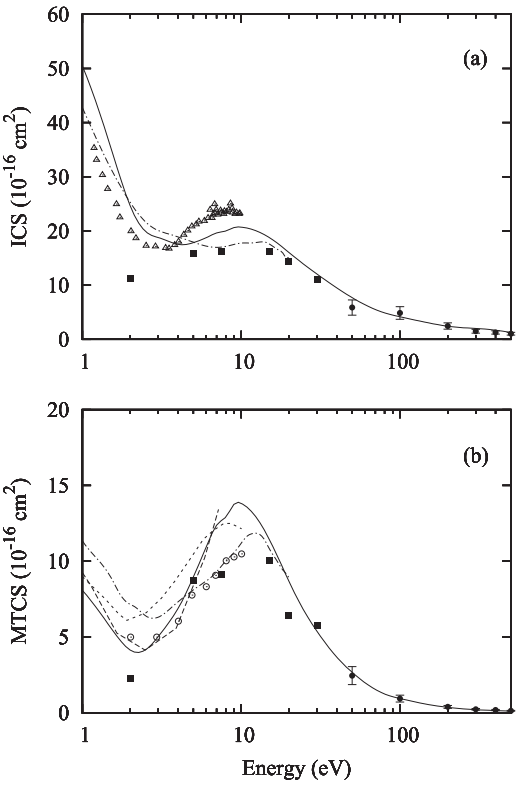

FIG. 4. (a) ICS and (b) MTCS for elastic e^--ammonia scattering in the 1–500 eV range. Full curve, present dipole-Born-corrected results; dashed-dotted curve, calculated data of Munjal and Baluja [29]; dashed curve, calculated MTCS of Rescigno *et al.* [27]; short-dashed curve, calculated MTCS of Gianturco [26]; full circles with error bars, present experimental data; solid squares, experimental data of Alle *et al.* [21]; open triangles, experimental TCS of Jones *et al.* [14]; open circles, recommended MTCS of Itikawa [59].

In Fig. 4(b), our calculated MTCS are compared with the experimental data of Alle *et al.* [21] in the 2–30 eV range, with the present experimental MTCS in the 50–500 eV range, and also with the recommended data of Itikawa [59]. The calculated MTCS of Gianturco [26], Rescigno *et al.* [27], and Munjal and Baluja [29] are also shown for comparison. Our calculated data agree very well with the present experimental data. At lower energies, our MTCS agree reasonably well with the experimental results of Alle *et al.* and with the recommended data of Itikawa. Comparison with other theoretical data also shows good agreement, particularly with those of Rescigno *et al.* [27].

In Fig. 5(a) we show our calculated TCS for electron scattering by ammonia in the 1–500 eV range. Our TCS are compared with the experimental data of Jones *et al.* [14], Szmytkowski *et al.* [10], Zecca *et al.* [11], and with the calculated data of Limbachiya *et al.* [33]. At 7 eV and above, our calculated TCS agree very well with the experimental data of Szmytkowski *et al.* and Zecca *et al.* At lower energies, our data are in reasonably good agreement with the experimental results of Jones *et al.* [14]. Although the measured data of Szmytkowski *et al.* [10] show a similar trend towards zero incident energy, they are significantly underestimated in this region. Comparison with the theoretical results of Limbachiya *et al.* [33] shows good agreement with our TCS at energies above 20 eV. At lower energies, their results are substantially underestimated. This discrepancy can be attributed to the fact that no Born-closure correction was included in their calculations. In Fig. 5(b), our TACS are compared with the experimental TICS of Rao and Srivastava [15], and with the calculated TICS of Joshipura *et al.* [31] using the SCOP model and also with the present TICS calculated using the binary-encounter Bethe (BEB) model [60]. Our TACS agree qualitatively with the experimental and calculated TICS. Quantitatively, our TACS are systematically larger than all

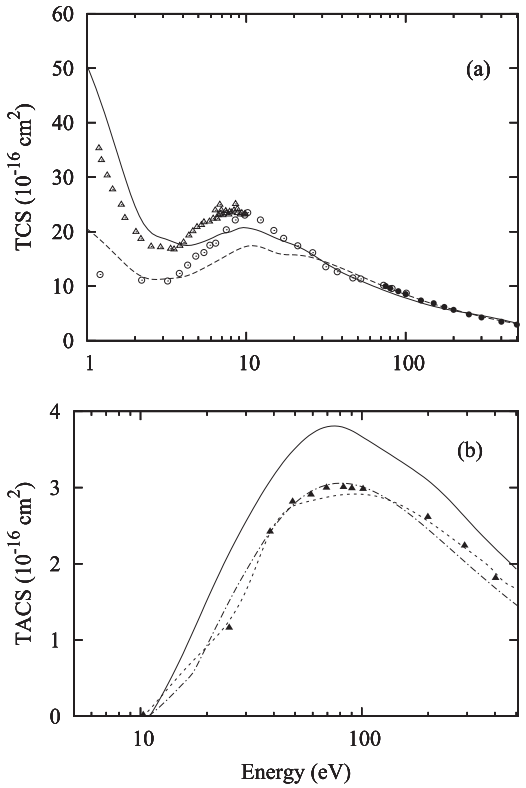

FIG. 5. (a) TCS and (b) TACS for e^--ammonia scattering. Full curves, present calculated data; dashed curve, calculated results of Limbachiya *et al.* [33]; open triangles, experimental TCS of Jones *et al.* [14]; open circles, measured data of Szmytkowski *et al.* [10]; full circles, experimental TCS of Zecca *et al.* [11]; short-dashed curve, calculated TICS of Joshipura *et al.* [31]; dashed-dotted curve, present theoretical TICS calculated using the BEB model; full triangles, experimental TICS of Rao and Srivastava [15].

the TICS. These results are expected, since TACS account for all inelastic scattering processes including excitation and ionization, whereas only ionization processes are accounted for in the TICS.

For completeness, our experimental data of DCS, ICS, and MTCS, obtained in the 50–500 eV energy range, are presented in Table I.

B. Formamide

The HF-SCF wave function of formamide was obtained using the double-zeta-valence (DZV) basis of the GAMESS package [61] and using the polarization of HONDO7. The calculation was performed at the experimental ground-state molecular geometry of this target [55]. The obtained electric dipole moment was 4.248 D, which agrees well with the calculated value of 4.28 D of Bettega *et al.* [36] and is also in fairly good agreement with the experimental value of 3.73 D [55]. The calculated dipole polarizabilities were $\alpha_{xx} = 24.940$ a.u., $\alpha_{yy} = 19.21$ a.u., and $\alpha_{zz} = 9.37$ a.u., which were used to generate the asymptotic form of U_{cp}. For this target, the truncation parameters used in the single-center expansion of the bound and scattering wave functions, the interaction potentials, and all the related matrices were $l_c = 35$ and $h_c = 35$. The calculated cross sections were converged with $N = 7$. Also for formamide, a Born-closure correction was applied to account for the contribution of higher partial-wave components to the scattering amplitudes. The procedure used is the same as for ammonia.

In Fig. 6, we compare our calculated DCS for elastic e^--NH_2CHO scattering with the theoretical data of Wang and Tian [37] in the 2–10 eV energy range. This comparison shows fair agreement between the data calculated using the different theoretical methods, particularly at 6 eV and 10 eV. Moreover, some oscillations in the calculated results might be unphysical and are probably an artifact of the Born-closure procedure [62].

TABLE I. Experimental DCS (in 10^{-16} cm^2/sr), ICS, and MTCS (in 10^{-16} cm^2) for elastic e^--ammonia scattering. Note: 1.23(1) means 1.23×10^1.

Angle	E (eV)					
(deg)	50	100	200	300	400	500
10	8.11(0)	1.23(1)	5.96(0)	2.92(0)	2.75(0)	2.11(0)
15	5.41(0)	5.03(0)	2.49(0)	1.10(0)	9.88(−1)	8.59(−1)
20	3.39(0)	2.57(0)	1.01(0)	5.61(−1)	4.87(−1)	3.86(−1)
25	2.12(0)	1.13(0)	5.09(−1)	2.89(−1)	2.44(−1)	2.02(−1)
30	1.24(0)	6.33(−1)	2.66(−1)	1.80(−1)	1.62(−1)	1.29(−1)
40	5.22(−1)	2.53(−1)	1.22(−1)	7.64(−2)	6.90(−2)	5.66(−2)
50	2.47(−1)	1.21(−1)	5.92(−2)	4.55(−2)	4.08(−2)	3.28(−2)
60	1.66(−1)	7.73(−2)	4.42(−2)	2.82(−2)	2.52(−2)	1.92(−2)
70	1.25(−1)	5.18(−2)	3.44(−2)	2.30(−2)	1.89(−2)	1.33(−2)
80	8.63(−2)	3.49(−2)	2.90(−2)	1.93(−2)	1.36(−2)	9.86(−3)
90	6.59(−2)	3.24(−2)	2.51(−2)	1.61(−2)	1.11(−2)	8.57(−3)
100	7.39(−2)	3.42(−2)	2.35(−2)	1.36(−2)	9.62(−3)	6.70(−3)
110	8.09(−2)	4.32(−2)	2.26(−2)	1.25(−2)	9.12(−3)	5.66(−3)
120	1.18(−1)	5.06(−2)	2.16(−2)	1.15(−2)	8.71(−3)	5.28(−3)
130		6.62(−2)	2.12(−2)	1.14(−2)	8.13(−3)	5.06(−3)
ICS	5.87(0)	4.86(0)	2.46(0)	1.50(0)	1.26(0)	1.05(0)
MTCS	2.45(0)	9.90(−1)	3.87(−1)	2.26(−1)	1.77(−1)	1.27(−1)

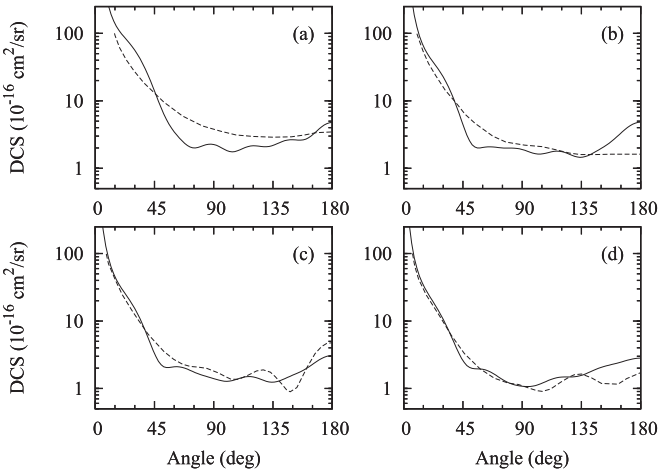

FIG. 6. Theoretical DCS for elastic e^--NH_2CHO scattering at (a) 2 eV, (b) 4 eV (c) 6 eV, and (d) 10 eV. Full curve, present results; dashed curve, calculated data of Wang and Tian [37] using the R-matrix method.

In Fig. 7, the calculated data in the 100–300 eV range are presented. The experimental DCS of Maljković *et al.* [34] measured at 100, 150, and 300 eV are also presented for comparison. It is seen that there is a good agreement between theory and experiment, except that some small oscillations seen in the theoretical results are not clear in the measured data. Nevertheless, we believe that those oscillations are physical and can be attributed to electron-diffraction effects.

In Figs. 8(a) and 8(b) we present the calculated ICS and MTCS, respectively, for this system. We have identified two shape resonances: the one located at about 3.5 eV is a resonance in the $^2A''$ scattering channel, whereas that located at about 15 eV belongs to the $^2A'$ scattering channel. Our calculated position and assignment of the shape resonances agree very well with those observed by Goumans *et al.* [63] in their investigation of the dissociative electron attachment

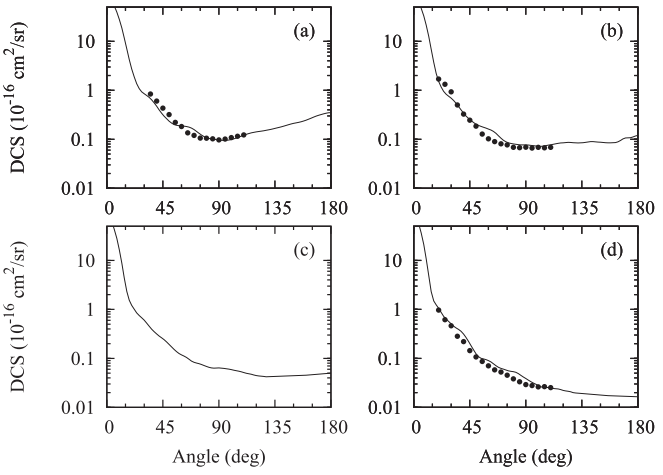

FIG. 7. DCS for elastic e^--NH_2CHO scattering at (a) 100 eV, (b) 150 eV, (c) 200 eV, and (d) 300 eV. Full curve, present dipole-Born-corrected data calculated including absorption effects; full circles, experimental data of Maljković *et al.* [34].

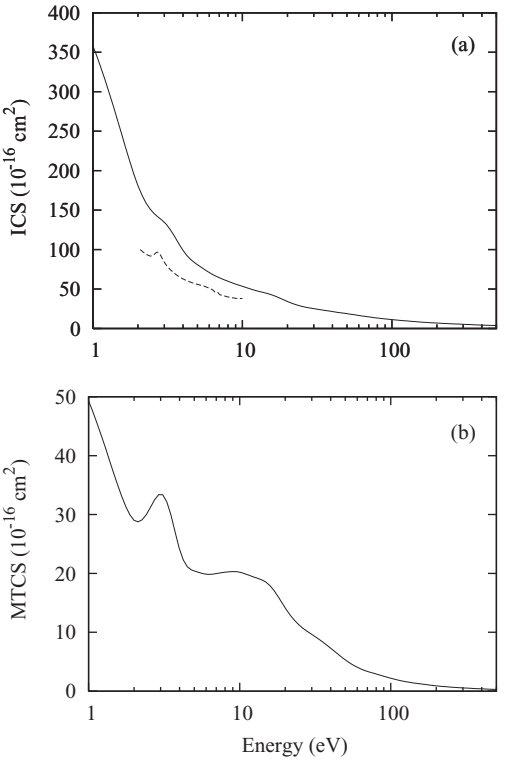

FIG. 8. (a) ICS and (b) MTCS for elastic e^--NH_2CHO scattering in the 1–500 eV range. Full curve, present dipole-Born-corrected results; dashed curve, calculated data of Wang and Tian [37] using the R-matrix method.

to formamide. By searching the poles of the S matrix in the complex plane at the equilibrium geometry, these authors found a π^* shape resonance belonging to the A'' symmetry located at 3.77 eV, and a σ^* shape resonance belonging to the A' symmetry located at 14.9 eV. On the other hand, the $^2A''$ shape resonance was also identified in some more recent investigations, but at lower energies: it occurs at 2.50 eV in the investigation of Bettega [36], at 2.25 eV in the study of Wang and Tian [37], and at 2.12 eV as reported by Gallup [64]. Different ways to treat the polarization effects may be the origin of these discrepancies. Moreover, the ICS calculated by Wang and Tian using the R-matrix approach [37] are also shown in Fig. 8(a) to compare with our data. In the overlapping energy range, their results lie about 30% below ours. This discrepancy may be due to the fact that only 57% of the Born correction is included in their results as stated by those authors.

It is interesting to note that formamide can roughly be considered as a union of a formaldehyde molecule with an ammonia molecule. Similar to formaldehyde, formamide is also strongly polar and has an empty π^* orbital and therefore supports a shape resonance. Probably, the feature located at about 3.5 eV corresponds to the one seen in the $^2B_1$ continuum channel of formaldehyde [47], whereas the broad resonance feature at about 15 eV corresponds to that ^2E shape resonance seen in ammonia.

In Figs. 9(a) and 9(b) we present our calculated TCS and TACS, respectively, for formamide. The TICS of Gupta *et al.* [38] calculated using the SCOP model, and the present

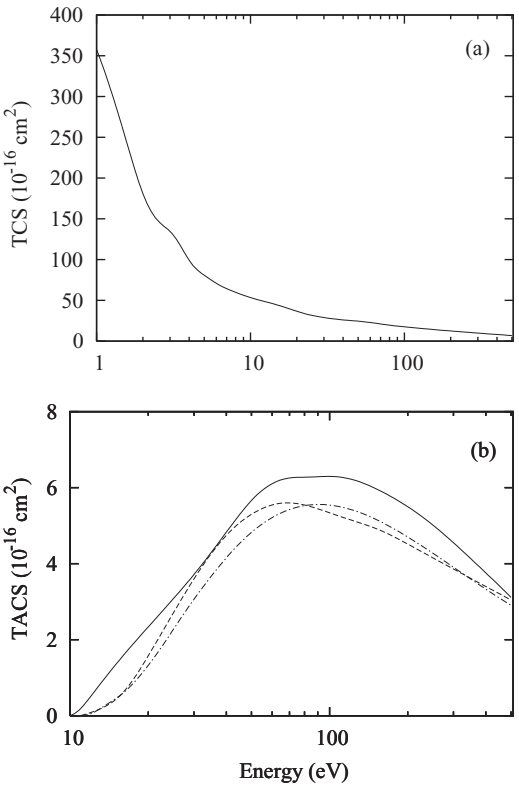

FIG. 9. (a) TCS and (b) TACS for e^--NH_2CHO scattering in the 1–500 eV range. Full curve, present calculated results; dashed-dotted curve, present calculated TICS using the BEB model [60]; dashed curve, calculated TICS of Gupta *et al.* [38].

calculated TICS using the BEB model [60] are also shown for comparison. It is interesting to note that although the present TACS and both results of TICS show qualitative agreement, the TACS are systematically larger than the TICS, as expected.

V. CONCLUSIONS

In this study we report a joint theoretical-experimental investigation on electron collisions with ammonia in a wide energy range. More precisely, absolute DCS, ICS, and MTCS for elastic e^--NH_3 scattering are measured in the 50–500 eV range, whereas theoretical cross sections including the TCS and TACS are reported from 1 to 500 eV. In the 1–30 eV range, our theoretical data calculated including the Born-closure correction agree very well with the experimental results of Alle *et al.* [21] and also with some recent theoretical data [27,29]. At energies above 30 eV, the results calculated with inclusion of absorption effects agree better with the present measured data, which clearly illustrate the influence of the inelastic scattering processes on the elastic channel. For this target, a shape resonance in the ^2E scattering channel was identified, which was also confirmed by the existing experimental data [21].

For formamide, our calculated DCS in the 100–300 eV energy range are compared with the experimental data of Maljković *et al.* [34] and show a general good agreement. Unfortunately, no other experimental results, particularly at lower incident energies, are available to compare with our data. Moreover, two shape resonances, centered at 3.5 eV and 15 eV, respectively, were identified. The one located at 3.5 eV is a $^2A''$ resonance corresponding to the $^2B_1$ shape resonance in formaldehyde [47], whereas the broad structure located at about 15 eV is a $^2A'$ resonance which corresponds to the ^2E resonance in ammonia. Considering that the formamide molecule is roughly a union of formaldehyde and ammonia, the observed correspondence is very interesting and clearly indicates that the recent investigation on electron interaction with small building blocks, instead of with larger biomolecules itself, is relevant.

ACKNOWLEDGMENT

This research was partially supported by the Brazilian agencies CNPq, FAPESP, and CAPES.

[1] B. Boudaïffa, P. Cloutier, D. Hunting, M. A. Huels, and L. Sanche, Science **287**, 1658 (2000).
[2] M. A. Huels, B. Boudaïffa, P. Cloutier, D. Hunting, and L. Sanche, J. Am. Chem. Soc. **125**, 4467 (2003).
[3] R. T. Sugohara, M. G. P. Homem, I. P. Sanches, A. F. de Moura, M. T. Lee, and I. Iga, Phys. Rev. A **83**, 032708 (2011).
[4] M.-T. Lee, G. L. C. de Souza, L. E. Machado, L. M. Brescansin, A. S. dos Santos, R. R. Lucchese, R. T. Sugohara, M. G. P. Homem, I. P. Sanches, and I. Iga, J. Chem. Phys. **136**, 114311 (2012).
[5] G. L. C. de Souza, M.-T. Lee, I. P. Sanches, P. Rawat, I. Iga, A. S. dos Santos, L. E. Machado, R. T. Sugohara, L. M. Brescansin, M. G. P. Homem, and R. R. Lucchese, Phys. Rev. A **82**, 012709 (2010).
[6] R. T. Sugohara, M. G. P. Homem, I. Iga, G. L. C. de Souza, L. E. Machado, J. R. Ferraz, A. S. dos Santos, L. M. Brescansin, R. R. Lucchese, and M.-T. Lee, Phys. Rev. A **88**, 022709 (2013).
[7] T. Sato, F. Shibata, and T. Goto, Chem. Phys. **108**, 147 (1986).
[8] E. Brüche, Ann. Phys. (Leipzig) **83**, 1065 (1927).
[9] O. Sueoka and S. Mori, J. Phys. Soc. Jpn. **53**, 2491 (1984).
[10] C. Szmytkowski, K. Maciag, G. Karwarsz, and D. Filipović, J. Phys. B **22**, 525 (1989).
[11] A. Zecca, G. P. Karwasz, and R. S. Brusa, Phys. Rev. A **45**, 2777 (1992).
[12] G. García and F. Manero, J. Phys. B **29**, 4017 (1996).
[13] W. M. Ariyasinghe, T. Wijeratne, and P. Palihawadana, Nucl. Instrum. Meth. B **217**, 389 (2004).
[14] N. C. Jones, D. Field, S. L. Lunt, and J. P. Ziesel, Phys. Rev. A **78**, 042714 (2008).
[15] M. V. V. S. Rao and S. K. Srivastava, J. Phys. B **25**, 2175 (1992).
[16] H. Hayashi, Institute of Plasma Physics, Nagoya University, Japan, Report No. IPPJ-AM-19, 1981 (unpublished).
[17] J. I. Pack, R. E. Voshall, and A. V. Phelps, Phys. Rev. **127**, 2084 (1962).
[18] S. Altshuler, Phys. Rev. **107**, 114 (1957).
[19] M. Ben Arfa and M. Tronc, J. Chim. Phys. **85**, 889 (1988).
[20] M. Furlan, M.-J. Hubin-Franskin, J. Delwiche, and J. E. Collin, J. Chem. Phys. **92**, 213 (1990).

[21] D. T. Alle, R. J. Gulley, S. J. Buckman, and M. J. Brunger, J. Phys. B **25**, 1533 (1992).
[22] W. R. Harshbarger, A. Skerbele, and E. N. Lassettre, J. Chem. Phys. **54**, 3784 (1971).
[23] R. J. Gulley, M. J. Brunger, and S. J. Buckman, J. Phys. B: At. Mol. Opt. Phys. **25**, 2433 (1992).
[24] F. A. Gianturco and A. Jain, Phys. Rep. **143**, 347 (1986).
[25] H. P. Pritchard, M. A. P. Lima, and V. McKoy, Phys. Rev. A **39**, 2392 (1989).
[26] F. Gianturco, J. Phys. B: At. Mol. Opt. Phys. **24**, 4627 (1991).
[27] T. N. Rescigno, B. H. Lengsfield, C. W. McCurdy, and S. D. Parker, Phys. Rev. A **45**, 7800 (1992).
[28] E. M. S. Ribeiro, L. E. Machado, M.-T. Lee, and L. M. Brescansin, Comput. Phys. Commun. **136**, 117 (2001).
[29] H. Munjal and K. Baluja, J. Phys. B **40**, 1713 (2007).
[30] A. K. Jain, A. N. Tripathi, and A. Jain, Phys. Rev. A **39**, 1537 (1989).
[31] K. N. Joshipura, M. Vinodkumar, and U. M. Patel, J. Phys. B **34**, 509 (2001).
[32] J. Yuan and Z. Zhang, Phys. Rev. A **45**, 4565 (1992).
[33] C. Limbachiya, M. Vinodkumar, and N. Mason, Phys. Rev. A **83**, 042708 (2011).
[34] J. B. Maljković, F. Blanco, G. García, and A. R. Milosavljević, Nucl. Instrum. Methods, Phys. Res. B **279**, 124 (2012).
[35] J. M. Hollis, F. J. Lovas, A. Remijian, P. R. Jewell, V. Ilushin, and I. Kleiner, Astrophys. J. Lett. **643**, L25 (2006).
[36] M. H. F. Bettega, Phys. Rev. A **81**, 062717 (2010).
[37] Y.-F. Wang and S. X. Tian, Phys. Rev. A **85**, 012706 (2012).
[38] D. Gupta, R. Naghma, and B. Antony, Mol. Phys. **112**, 1201 (2014).
[39] S. K. Srivastava, A. Chutjian, and S. Trajmar, J. Chem. Phys. **63**, 2659 (1975).
[40] I. Iga, M. T. Lee, M. G. P. Homem, L. E. Machado, and L. M. Brescansin, Phys. Rev. A **61**, 022708 (2000).
[41] P. Rawat, I. Iga, M. T. Lee, L. M. Brescansin, M. G. P. Homem, and L. E. Machado, Phys. Rev. A **68**, 052711 (2003).
[42] I. Iga, I. P. Sanches, S. K. Srivastava, and M. Mangan, Int. J. Mass Spectrom. **208**, 159 (2001).
[43] M. G. P. Homem, I. Iga, R. T. Sugohara, I. P. Sanches, and M. T. Lee, Rev. Sci. Instrum. **82**, 013109 (2011).
[44] R. H. J. Jansen, F. J. de Heer, H. J. Luyken, B. van Wingerden, and H. J. Blaauw, J. Phys. B **9**, 185 (1976).
[45] R. D. DuBois and M. E. Rudd, J. Phys. B **9**, 2657 (1976).
[46] P. Rawat, M. G. P. Homem, R. T. Sugohara, I. P. Sanches, I. Iga, G. L. C. de Souza, A. S. dos Santos, R. R. Lucchese, L. E. Machado, L. M. Brescansin, and M.-T. Lee, J. Phys. B **43**, 225202 (2010).
[47] J. R. Ferraz, A. S. dos Santos, G. L. C. de Souza, A. I. Zanelato, T. R. M. Alves, M.-T. Lee, L. M. Brescansin, R. R. Lucchese, and L. E. Machado, Phys. Rev. A **87**, 032717 (2013).
[48] F. A. Gianturco, R. R. Lucchese, and N. Sanna, J. Chem. Phys. **102**, 5743 (1995).
[49] A. R. Edmonds, *Angular Momentum and Quantum Mechanics* (Princeton University Press, Princeton, NJ, 1960).
[50] N. T. Padial and D. W. Norcross, Phys. Rev. A **29**, 1742 (1984).
[51] M.-T. Lee, I. Iga, L. E. Machado, L. M. Brescansin, E. A. y Castro, I. P. Sanches, and G. L. C. de Souza, J. Electron Spectrosc. Relat. Phenom. **155**, 14 (2007).
[52] G. Staszewska, D. W. Schwenke, and D. G. Truhlar, Phys. Rev. A **29**, 3078 (1984).
[53] S. Hara, J. Phys. Soc. Jpn. **22**, 710 (1967).
[54] M. J. Frisch *et al.*, *Gaussian 03, Revision C. 02* (Gaussian Inc., Wallingford, CT, 2004).
[55] http://cccbdb.nist.gov
[56] P. G. Burke, N. Chandra, and F. A. Gianturco, J. Phys. B **5**, 2212 (1972).
[57] L. E. Machado, L. M. Brescansin, I. Iga, and M.-T. Lee, Eur. Phys. J. D **33**, 193 (2005).
[58] L. M. Brescansin, L. E. Machado, M.-T. Lee, H. Cho, and Y. S. Park, J. Phys. B **41**, 185201 (2008).
[59] Y. Itikawa, At. Data Nucl. Data Tables **14**, 1 (1974).
[60] Y.-K. Kim and M. E. Rudd, Phys. Rev. A **50**, 3954 (1994).
[61] M. W. Schmidt, K. K. Baldridge, J. A. Boatz, S. T. Elbert, M. S. Gordon, J. H. Jensen, S. Koseki, N. Matsunaga, K. A. Nguyen, S. Su, T. L. Windus, M. Dupuis, and J. A. Montgomery, J. Comput. Chem. **14**, 1347 (1993).
[62] M. A. Khakoo, J. Blumer, K. Keane, C. Campbell, H. Silva, M. C. A. Lopes, C. Winstead, V. McKoy, R. F. da Costa, L. G. Ferreira, M. A. P. Lima, and M. H. F. Bettega, Phys. Rev. A **77**, 042705 (2008).
[63] T. P. M. Goumans, F. A. Gianturco, F. Sebastianelli, I. Baccarelli, and J. L. Rivail, J. Chem. Theory Comput. **5**, 217 (2009).
[64] G. A. Gallup, J. Chem. Phys. **139**, 104308 (2013).

Theoretical and experimental investigation of electron collisions with dimethyl sulfide

M. G. P. Homem,[1] I. Iga,[1] J. R. Ferraz,[2] A. S. dos Santos,[2] L. E. Machado,[2] G. L. C. de Souza,[3] L. M. Brescansin,[4] R. R. Lucchese,[5] and M.-T. Lee[1]

[1]*Departamento de Química, UFSCar, 13565-905 São Carlos, São Paulo, Brazil*
[2]*Departamento de Física, UFSCar, 13565-905 São Carlos, São Paulo, Brazil*
[3]*Departamento de Química, UFMT, 78060-900 Cuiabá, Mato Grosso, Brazil*
[4]*Instituto de Física "Gleb Wataghin," UNICAMP, 13083-970 Campinas, São Paulo, Brazil*
[5]*Chemistry Department, Texas A&M University, College Station, Texas 77842-3012, USA*

(Received 16 December 2014; published 30 January 2015)

We report a joint theoretical-experimental investigation of elastic electron scattering by dimethyl sulfide in the low- and intermediate-energy regions. More specifically, experimental differential, integral, and momentum-transfer cross sections are given in the 30–800 eV and $10^\circ - 130^\circ$ ranges. Theoretical cross sections are reported in the 1–500 eV interval. The experimental differential cross sections were determined using a crossed electron-beam–molecular-beam geometry, whereas the absolute values of the cross sections were obtained using the relative-flow technique. Theoretically, a complex optical potential was used to represent the collision dynamics, and a single-center expansion method combined with the Padé approximant method was used to solve the scattering equations. Our experimental data are in good agreement with the present calculated data but strongly disagree with those reported in a previous investigation.

DOI: 10.1103/PhysRevA.91.012713 PACS number(s): 34.80.Bm

I. INTRODUCTION

From an environmental point of view, studies involving sulfur-containing compounds are relevant since many of them, such as hydrogen sulfide (H_2S), sulfur dioxide (SO_2), and sulfuric acid (H_2SO_4), are atmospheric pollutants and are responsible for the acidity of rain. In particular, one of the principal volatile sulfur-containing species, dimethyl sulfide (DMS) with the chemical formula $(CH_3)_2S$, is the major natural source of sulfur in the atmosphere [1]. It is produced in marine environments by biodegradation of organosulfur compounds and thus plays an important role in the atmospheric sulfur cycle. Probably for this reason, DMS has attracted considerable attention in both theoretical [2] and experimental investigations [3–9]. However, the only study up to now specifically concerning electron-DMS interaction is that reported by Rao *et al.* [8] in 2009. In that study, differential (DCS), integral (ICS), and momentum-transfer (MTCS) cross sections in the 30–500 eV energy range were reported for elastic electron scattering by DMS and also for dimethyl sulfoxide (DMSO). Rao *et al.* compared the experimental data only with their calculated results based on the independent-atom model (IAM) approach since there were no other experimental or theoretical cross-section determinations for these targets in the literature. It is interesting to note that double-dip structures are seen in their measured DCS for both DMS and DMSO at incident energies up to 100 eV. The authors attributed such structures to the occurrence of d-wave shape resonance during the collision processes. They justified such an occurrence based on the fact that the shape of the potential for electron interaction with both targets has a notable $3d$ character, and therefore a d-wave enhancement would increase the cross-section values through the medium angles as seen in their experiment [8]. The appearance of such double-dip structures in the measured DCS for DMS and DMSO at incident energies as high as 100 eV is, by itself, very interesting, although not confirmed by their IAM-based theory.

In order to understand the physical nature of the double-dip features, we performed a theoretical investigation of e^--DMS scattering. In our calculation, the dynamics of the projectile-target interaction is represented by a molecular complex optical potential (MCOP) at the static-exchange-polarization plus absorption (SEPA) level of approximation. This model has already been applied by our group to study electron collisions with other sulfur-containing molecules, e.g., H_2S [10] and SO_2 [11], and has successfully reproduced similar double-dip structures. For the sake of completeness, our calculations were carried out in the wide 1–500 eV energy range, thus providing cross-section data at energies below 30 eV, not covered in the Rao *et al.*'s article. Surprisingly, our DCS calculated in the 30–100 eV range do not present evidences of strong double-dip features. Quantitatively, there is also significant disagreement between our calculated results and their measured data, even at energies of hundreds of eV.

At energies above 75 eV, although their theoretical DCS calculated using the IAM agree fairly well with their experimental results, they strongly disagree with our calculation, even at 500 eV. This fact is quite surprising since it is expected that the results calculated using the IAM would converge to those calculated with more sophisticated methods at incident energies of hundreds of eV [12,13].

In order to solve such controversies, we decided to reinvestigate experimentally the elastic e^--DMS scattering. Particularly, DCS are measured in the 30–800 eV energy range. These data are compared with the DCS of Rao *et al.* and with our theoretical results obtained using both the MCOP and the IAM-based method. Experimental ICS and MTCS are generated from the measured DCS via a numerical integration procedure.

The organization of this work is as follows: In Sec. II, we present briefly the experimental procedure. In Sec. III, the theory used and details of the calculations are presented. Finally, in Sec. IV, we present our calculated and measured data and compare them with the experimental and IAM data

of Rao *et al.* Some concluding remarks are also presented in that section.

II. EXPERIMENT

The DMS used in the measurements was purchased from Sigma-Aldrich and had a purity higher than 99%. For each measurement, approximately 1 mL of the liquid sample was put into a small vial attached to the gas-handling manifold [14] and then underwent a pretreatment for elimination of atmospheric air through several freeze-thaw cycles. A gaseous DMS beam was formed by the saturated vapor above the liquid, and its purity was checked during the measurements using a residual gas analyzer attached to the electron spectrometer chamber.

The DCS was measured using the same experimental setup and procedure presented in several previous works [14–20]. Briefly, the intensities of the elastically scattered electrons were measured using a crossed electron-beam–molecular-beam geometry. The scattered electrons are energy filtered by a retarding-field energy analyzer with a resolution of about 1.5 eV. This analyzer discriminates the inelastically scattered electrons resulting from electronic excitation but not those from vibrational excitation. Therefore, our reported results are indeed vibrationally summed cross sections. Further, the scattered intensities are converted to absolute DCS using the relative-flow technique (RFT) [21] according to the procedure described in Refs. [14,17,20]. The application of RFT requires precise determination of the relative flows for both DMS and the secondary standards. They were measured according to the procedure described in Ref. [14]. In the present work, argon was used as a secondary standard. Specifically, the absolute DCS of Jansen *et al.* [22], with quoted experimental uncertainties of 6%, were used to normalize our data in the 100–500 eV range. In addition, at 50 and 800 eV, the absolute DCS of Dubois and Rudd [23] with uncertainties of 12% and the DCS reported by Williams and Willis [24] at 30 eV with quoted errors of 8% were used for normalization.

Our estimation of overall experimental uncertainties followed a procedure also given elsewhere [17–20]. Essentially, for the measured scattering intensities of each gas, the uncertainties of random nature (pressure fluctuations, electron-beam-current readings, background scattering, etc.) contributed less than 2% each; the statistical errors were estimated to be 3%. Additionally, there was still an uncertainty of 6% associated with the normalization procedure. The combination of all these contributions with the quoted uncertainties in the absolute DCS of the secondary standards [22–24] provided overall estimated uncertainties of 15% at 50 and 800 eV and 11% elsewhere.

In order to obtain ICS and MTCS, an extrapolation procedure was adopted to estimate DCS at scattering angles in the angular range not covered experimentally. In order to reduce the arbitrariness in this procedure we followed the trend of the theoretical results. The overall uncertainties on ICS and MTCS were estimated to be around 25% at 50 and 800 eV and 20% elsewhere.

III. THEORY AND NUMERICAL PROCEDURE

The theory used in this work is essentially the same as that in several previous works [25–27]. Briefly, a complex optical potential $U_{\rm opt}$ composed of static ($U_{\rm st}$), exchange ($U_{\rm ex}$), correlation-polarization ($U_{\rm cp}$), and absorption ($U_{\rm ab}$) contributions was used to represent the electron-target interaction. Using this potential, the many-body nature of the electron-molecule interaction was reduced to a one-particle scattering problem. To solve this problem, $U_{\rm opt}$ was divided in two parts, namely, U_1 and U_2. Accordingly, the transition T matrix can be written as

$$T = T_1 + T_2, \tag{1}$$

where

$$T_1 = \langle \phi(\vec{k}_f)|U_1|\psi_1^+(\vec{k}_i)\rangle \tag{2}$$

and

$$T_2 = \langle \psi_1^-(\vec{k}_f)|U_2|\psi^+(\vec{k}_i)\rangle. \tag{3}$$

In Eqs. (2) and (3), ϕ is the unperturbed plane wave, ψ is the solution of the Schrödinger scattering equation for the full optical potential $U_{\rm opt}$, ψ_1 is the solution of the distorted-wave Schrödinger equation for potential U_1, and k is the magnitude of the electron linear momentum. The partition of $U_{\rm opt}$ into U_1 and U_2 is arbitrary. In this work, we chose

$$U_1 = U_{\rm st} + U_{\rm ex}^{\rm loc} + U_{\rm cp} \tag{4}$$

and

$$U_2 = U_{\rm ex} - U_{\rm ex}^{\rm loc} + iU_{\rm ab}, \tag{5}$$

where $U_{\rm ex}^{\rm loc}$ is a reduced local exchange potential.

In the present work, $U_{\rm st}$ and $U_{\rm ex}$ were derived exactly from a near-Hartree-Fock self-consistent-field (HF-SCF) target wave function, whereas $U_{\rm cp}$ was obtained in the framework of the free-electron-gas model, derived from a parameter-free local density, as prescribed by Padial and Norcross [28]. The absorption potential $U_{\rm ab}$ is the scaled quasifree scattering model (SQFSM) absorption potential of Lee *et al.* [29], which is an improvement of version 3 of the model absorption potential originally proposed by Staszewska *et al.* [30]. The Hara free-electron-gas-exchange potential [31] was used to generate the local exchange potential $U_{\rm ex}^{\rm loc}$. Since U_1 is fully local, ψ_1 and T_1 were obtained by solving exactly the distorted-wave Schrödinger scattering equation via numerical procedures. Further, T_2 can be obtained iteratively using the $[N/N]$ Padé approximant technique [32],

$$T_2[N/N] = -\sum_{i,j=1,N-1} \langle \psi_1^-|U_2|\phi^{(i)+}\rangle (D^{-1})_{ij} \langle \phi^{(j)-}|U_2|\psi_1^+\rangle, \tag{6}$$

where

$$D_{ij} = \langle \phi^{(i)-}|U_2 - U_2 G_1^+ U_2|\phi^{(j)+}\rangle \tag{7}$$

and G_1 is the distorted wave Green's function, which satisfies the following condition:

$$(\nabla^2 + k^2 - U_1)G_1^{\pm}(\vec{r},\vec{r}') = \delta(\vec{r},\vec{r}'). \tag{8}$$

The superscripts $-$ and $+$ appearing in the above equations denote the incoming and outgoing boundary conditions of the scattering waves, respectively. In our calculation, the truncation parameter N was iteratively increased until convergence was achieved. The converged body-frame (BF) T matrix (or, equivalently, the BF scattering amplitude f) can then be

TABLE I. Experimental DCS (in 10^{-16} cm^2/sr) and ICS and MTCS (in 10^{-16} cm^2) for elastic e^--DMS scattering.

Angle	E (eV)								
(deg)	30	50	100	150	200	300	400	500	800
10	32.04	28.37	18.78	11.10	9.43	9.12	7.01	5.09	4.48
15	14.01	10.49	6.28	3.91	3.53	2.92	2.37	2.17	1.88
20	6.73	4.56	1.99	1.81	1.83	1.35	1.35	1.21	0.909
25	4.02	2.64	1.26	1.23	1.10	0.84	0.855	0.591	0.545
30	2.59	1.79	0.922	0.690	0.618	0.526	0.413	0.349	0.322
40	1.789	1.08	0.493	0.373	0.266	0.214	0.251	0.161	0.101
45	1.61	0.883	0.359	0.289	0.192	0.191	0.181	0.105	0.076
50	1.44	0.612	0.289	0.187	0.149	0.129	0.131	0.086	0.053
60	1.02	0.379	0.187	0.133	0.104	0.083	0.080	0.055	0.034
70	0.713	0.332	0.132	0.106	0.084	0.057	0.049	0.037	0.025
80	0.810	0.330	0.121	0.076	0.057	0.037	0.034	0.028	0.019
90	0.800	0.266	0.115	0.063	0.038	0.026	0.026	0.021	0.017
100	0.742	0.260	0.091	0.053	0.028	0.026	0.024	0.017	0.015
110	0.546	0.231	0.079	0.040	0.028	0.026	0.027	0.017	0.013
120	0.519	0.249	0.089	0.043	0.037	0.031	0.027	0.018	0.012
130	0.554	0.308	0.128	0.058	0.046	0.041	0.029	0.019	0.011
ICS	20.5	14.6	11.2	8.2	7.4	6.4	5.2	4.4	2.8
MTCS	9.2	5.3	2.2	1.2	0.82	0.68	0.59	0.41	0.27

expressed in the laboratory frame (LF) by the usual frame transformation [33].

The HF-SCF wave function of DMS was obtained using the triple-zeta valence (TZV-3d) basis set of the GAMESS package [34]. At the experimental ground-state molecular geometry [35], this basis provided a total energy of −476.786114 hartrees. The calculated electric dipole moment was 1.7175 D, in fairly good agreement with the experimental value of 1.50 D [35]. Moreover, the asymptotic form of $U_{\rm cp}$ was generated with the dipole polarizabilities calculated at the HF-SCF level using the same basis set. The obtained values were $\alpha_{xx} = 53.06$ a.u., $\alpha_{yy} = 52.09$ a.u., and $\alpha_{zz} = 44.02$ a.u., resulting in an average dipole polarizability of $\alpha_0 = 49.72$ a.u., in good agreement with the experimental value of 50.95 a.u. [35]. In our calculation, the wave functions and interaction potentials, as well as the related matrices, were all single-center expanded about the center of mass of the molecule in terms of the well-known symmetry-adapted functions $X_{lh}^{p\mu}$ [36]. The truncation parameters used in these expansions were $l_c = 35$ and $h_c = 35$ for all bound and continuum orbitals, as well as for the T-matrix elements. The calculated cross sections were converged at N up to 10. Since DMS is a polar system, the partial-wave expansions converged slowly due to the long-range nature of the dipole interaction potential. In order to overcome this difficulty, a Born-closure formula was used to account for the contribution of higher partial-wave components to the scattering amplitudes. The procedure used was the same as that in some of our previous studies [10,18,37].

In the IAM framework, the DCS for e^--DMS scattering is written as

$$\frac{d\sigma}{d\Omega} = \sum_{i,j}^{N_a} f_i(\theta,k) f_j^*(\theta,k) \frac{\sin(sr_{ij})}{sr_{ij}}, \tag{9}$$

where $f_i(\theta,k)$ is the complex scattering amplitude due to the ith atom in a molecule, r_{ij} is the internuclear distance between atoms i and j, and $s = 2k\sin(\frac{\theta}{2})$ is the magnitude of the transferred momentum during the collision. The sum extends over the N_a atoms of the molecule. The scattering amplitudes were obtained by solving the partial-wave radial Schödinger equation at the SEPA level of approximation:

$$\left(\frac{d^2}{dr^2} - \frac{l(l+1)}{r^2} - U_{\rm opt} + k^2\right) u_l(r) = 0. \tag{10}$$

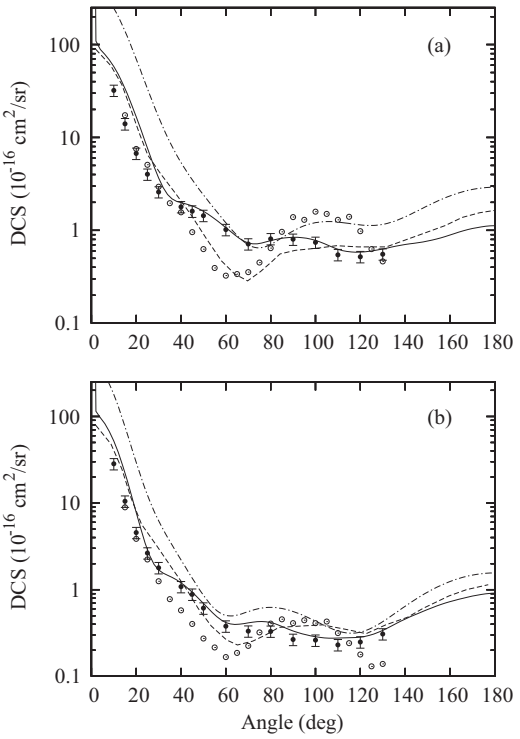

FIG. 1. DCS for elastic e^--DMS scattering at (a) 30 eV and (b) 50 eV. Solid curve, present calculated data using the MCOP; dot-dashed curve, present calculated data using the IAM; dashed curve, IAM data of Rao *et al.* [8]; solid circles with error bars, present experimental data; open circles, measured data of Rao *et al.*

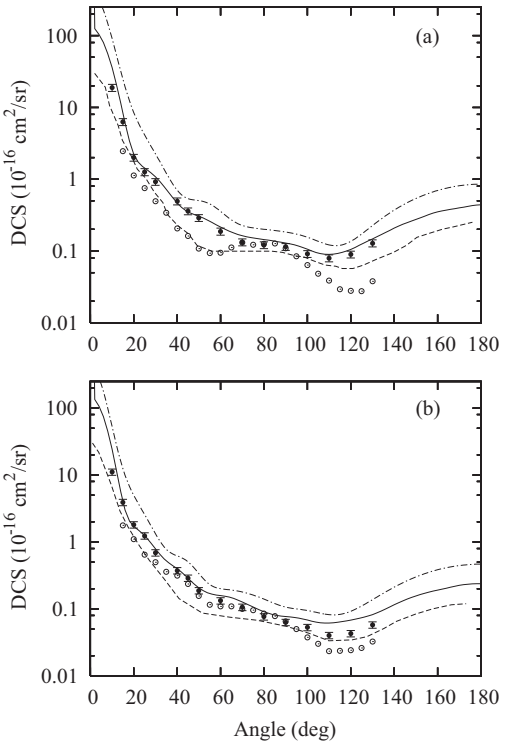

FIG. 2. Same as in Fig. 1, but at (a) 100 eV and (b) 150 eV.

The static atomic potentials were given by Salvat *et al.* [38], and a model potential proposed by Furness and McCarthy [39] was used to account for the exchange contributions.

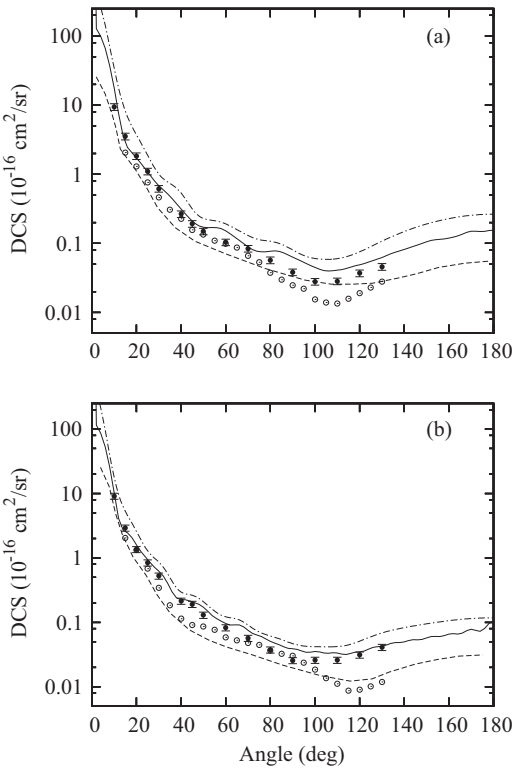

FIG. 3. Same as in Fig. 1, but at (a) 200 eV and (b) 300 eV.

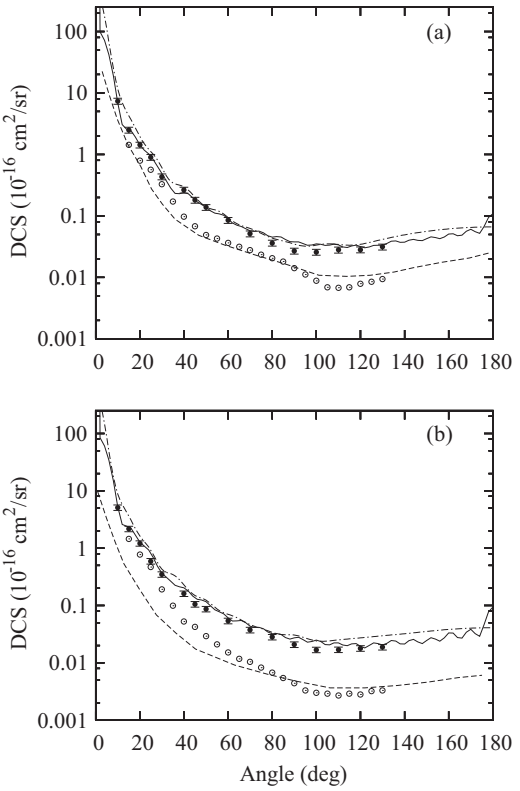

FIG. 4. Same as in Fig. 1, but at (a) 400 eV and (b) 500 eV.

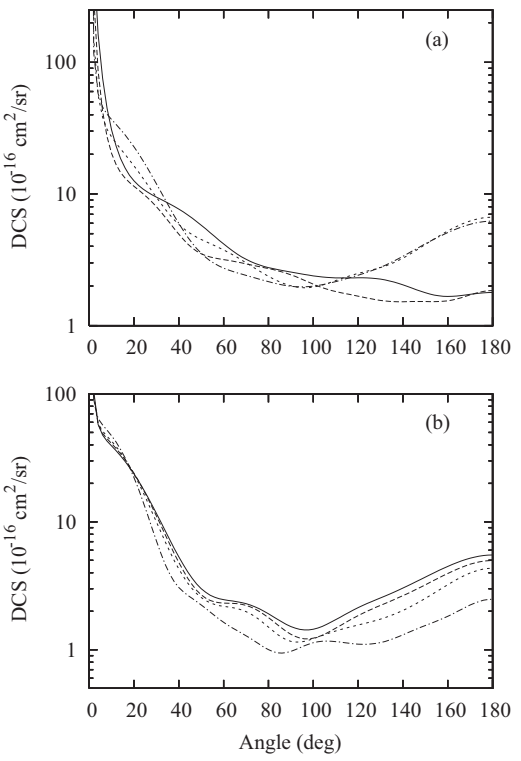

FIG. 5. Present theoretical MCOP DCS for elastic e^--DMS scattering. (a) Solid curve, at 1 eV; long-dashed curve, at 2 eV; short-dashed curve, at 5 eV; dotted-dashed curve, at 8 eV. (b) Solid curve, at 10 eV; long-dashed curve, at 12 eV; short-dashed curve at 15 eV; dotted-dashed curve, at 20 eV.

The potential of Padial and Norcross [28] and the SQFSM absorption potential of Lee *et al.* [29] were used to account for the correlation-polarization and the absorption contributions, respectively. The atomic polarizabilities, as well as the internuclear distances used in the calculation, were taken from the literature [35,40].

IV. RESULTS AND DISCUSSION

Our experimental DCS, ICS, and MTCS in the 30–800 eV range for elastic electron scattering by DMS are listed in Table I. In Figs. 1–4, we present a comparison of the present experimental and calculated MCOP DCS with the experimental data of Rao *et al.* [8] in the 30–500 eV energy range. The present calculated results using the IAM, as well as the IAM data of Rao *et al.*, are also shown. The comparison with the experimental data of Rao *et al.* is meaningful since their results are also vibrationally unresolved. It is seen that the present measured DCS disagree strongly with the experimental data of Rao *et al.*, both qualitatively and quantitatively, particularly at scattering angles larger than 40°. Moreover, no evidence of a pronounced double-dip structure is seen in our DCS in the 30–100 eV range. The best agreement between the two sets of experimental data occurs at 150 eV; however, their results are systematically lower than ours. Also at 300 eV and above, although the measured DCS of Rao *et al.* [8] agree qualitatively with our data, the magnitude of their DCS at large scattering angles lies well below. On the other hand, there is a very good qualitative agreement between our experimental data and the present calculated results using the MCOP. Quantitative agreement is also good, except at 30 and 50 eV, where our calculation overestimates the present experimental DCS at small scattering angles. At 400 and 500 eV, small oscillations are seen in our calculated data, particularly at large scattering angles. They are attributed to the lack of convergence in the partial-wave expansion of both the interaction potential and the T-matrix elements. Moreover, our calculated results using the IAM at 30 eV disagree qualitatively and quantitatively with both the present experimental data and calculated results using the MCOP. At higher energies, although there is a qualitative agreement between the results calculated using the IAM and MCOP, IAM-based calculations systematically overestimate the DCS. Nevertheless, the discrepancies between the two sets of theoretical data diminish with increasing incident energies, as expected [12,13]. Although there is an overall qualitative agreement between both IAM calculations, the magnitude of the IAM DCS reported by Rao *et al.* [8] is much smaller than the present IAM data, which is quite intriguing since the essence of the physics accounted for in both IAM calculations is quite similar. Actually, the lack of inclusion of absorption effects in their calculation would only increase the magnitude of DCS. Therefore we cannot explain the reason for such strong disagreement.

For the sake of completeness, in Fig. 5, we present some MCOP DCS in the 1–20 eV energy range. Unfortunately, there are neither experimental nor theoretical results to compare

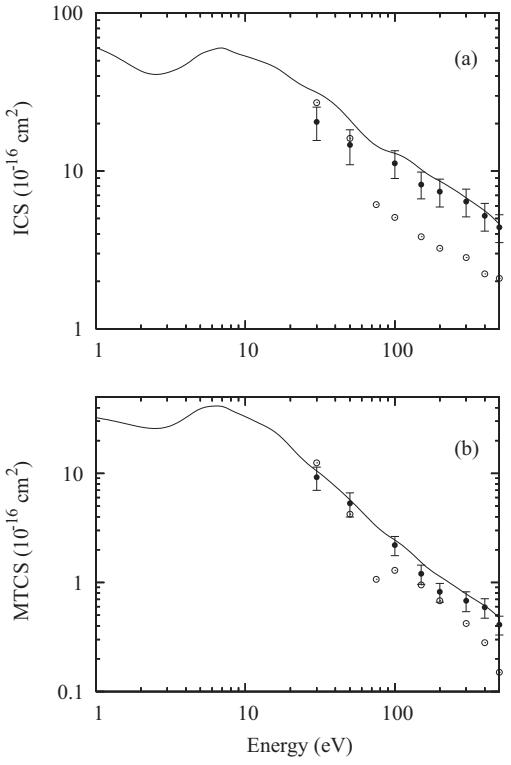

FIG. 6. (a) ICS and (b) MTCS for elastic e^--DMS scattering in the 1–500 eV range. Solid curve, present calculated data using the MCOP; solid circles with error bars, present experimental data; open circles, measured data of Rao *et al.* [8].

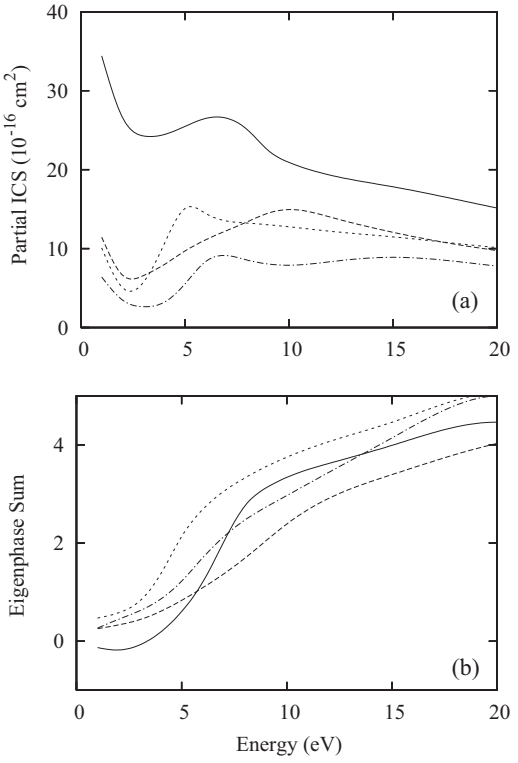

FIG. 7. Present partial-channel (a) ICS and (b) eigenphase sum calculated using the MCOP for elastic e^--DMS scattering in the 1–20 eV energy range. Solid curve, for A_1 symmetry; dot-dashed curve, for A_2 symmetry; long-dashed curve, for B_1 symmetry; short-dashed curve, for B_2 symmetry.

with our data. It is interesting to note that in the energy interval between 10 and 15 eV, the calculated DCS do show some double-dip structure evidence, indicating the possible occurrence of d-wave resonance.

In Fig. 6, we present our theoretical ICS and MTCS calculated using the MCOP for electron scattering by DMS in the 1–500 eV energy range. The present experimental results of ICS and MTCS and those reported by Rao *et al.* [8] are also shown for comparison with our theoretical results. In general, there is good agreement between our calculated and measured data at 100 eV and above. Nevertheless, our calculation overestimates slightly the experimental ICS at 30 and 50 eV. On the other hand, the experimental ICS and MTCS reported by Rao *et al.* lie well below both our calculated and experimental results, except at 30 and 50 eV, where their results agree reasonably well with ours. However, considering the significant discrepancies between their measured DCS and ours at these energies, we conclude that this apparent good agreement is probably fortuitous.

At low incident energies, our calculated ICS and MTCS show a broad resonance-like feature centered at about 7 eV and a shoulder at about 15 eV. In order to clarify the physical nature of these features, we present in Figs. 7(a) and 7(b) the partial ICS (without Born correction) and the eigenphase sums. From Fig. 7, one may conclude that the feature located at about 7 eV, seen in Fig. 6, is a combination of $^2B_2$ (at 5 eV), $^2A_2$ (at 6.5 eV), and $^2A_1$ (at 7 eV) shape resonances, whereas that seen at about 15 eV is due to a broad $^2B_1$ (at 10 eV) shape resonance. Probably, the double-dip behavior seen in our calculated DCS in the 10–15 eV range can be associated with this $^2B_1$ resonance.

In summary, in this study, we report a joint theoretical-experimental investigation of electron collision with DMS in a wide energy range. More precisely, absolute DCS, ICS, and MTCS for elastic e^--DMS scattering were reinvestigated experimentally in the 30–800 eV range. This investigation was mainly motivated by the strong disagreement between our theoretical cross sections calculated using the MCOP model and the existing experimental data [8]. As a result, it is seen that the present experimental DCS, ICS, and MTCS and those of Rao *et al.* show significant discrepancies. However, the reliability of the present measurement is supported by the MCOP calculations in the entire energy range covered herein and by the present IAM calculations at the higher end of the energies.

ACKNOWLEDGMENTS

This research was partially supported by the agencies CNPq (Brazil), FAPESP (Brazil), and CAPES (Brazil).

[1] R. J. Charlson, J. E. Lovelock, M. O. Andreae, and S. G. Warren, Nature (London) **326**, 655 (1987).
[2] M. R. Manaa and D. R. Yarkony, J. Am. Chem. Soc. **116**, 11444 (1994).
[3] J. H. Lee, R. B. Timmons, and L. J. Stief, J. Chem. Phys. **64**, 300 (1976).
[4] P. Quintana, R. F. Delmdahl, D. H. Parker, B. Martínez-Haya, F. J. Aoiz, L. Bañares, and E. Verdasco, Chem. Phys. Lett. **325**, 146 (2000).
[5] Y. Zheng, J. Rolke, G. Cooper, and C. E. Brion, J. Electron Spectrosc. Relat. Phenom. **123**, 377 (2002).
[6] B. Martínez-Haya, P. Quintana, L. Bañares, P. Samartzis, D. J. Smith, and T. N. Kitsopoulos, J. Chem. Phys. **114**, 4450 (2001).
[7] P. Limão-Vieira, S. Eden, P. A. Kendall, N. J. Mason, and S. V. Hoffmann, Chem. Phys. Lett. **366**, 343 (2002).
[8] K. C. Rao, K. G. Bhushan, R. Mukund, S. C. Gadkari, and J. V. Yakhmi, Phys. Rev. A **79**, 062714 (2009).
[9] R. B. Bernini, L. B. G. da Silva, F. N. Rodrigues, L. H. Coutinho, A. B. Rocha, and G. G. B. de Souza, J. Chem. Phys. **136**, 144307 (2012).
[10] L. M. Brescansin, L. E. Machado, M.-T. Lee, H. Cho, and Y. S. Park, J. Phys. B **41**, 185201 (2008).
[11] L. E. Machado, R. T. Sugohara, A. S. dos Santos, M.-T. Lee, I. Iga, G. L. C. de Souza, M. G. P. Homem, S. E. Michelin, and L. M. Brescansin, Phys. Rev. A **84**, 032709 (2011).
[12] A. Jain, S. S. Tayal, L. C. G. Freitas, and M.-T. Lee, J. Phys. B **16**, L99 (1983).
[13] M.-T. Lee, L. M. Brescansin, M. A. P. Lima, L. E. Machado, and E. P. Leal, J. Phys. B **23**, 4331 (1990).
[14] M. G. P. Homem, I. Iga, R. T. Sugohara, I. P. Sanches, and M. T. Lee, Rev. Sci. Instrum. **82**, 013109 (2011).
[15] I. Iga, M. T. Lee, M. G. P. Homem, L. E. Machado, and L. M. Brescansin, Phys. Rev. A **61**, 022708 (2000).
[16] P. Rawat, I. Iga, M. T. Lee, L. M. Brescansin, M. G. P. Homem, and L. E. Machado, Phys. Rev. A **68**, 052711 (2003).
[17] R. T. Sugohara, M. G. P. Homem, I. P. Sanches, A. F. de Moura, M. T. Lee, and I. Iga, Phys. Rev. A **83**, 032708 (2011).
[18] M.-T. Lee, G. L. C. de Souza, L. E. Machado, L. M. Brescansin, A. S. dos Santos, R. R. Lucchese, R. T. Sugohara, M. G. P. Homem, I. P. Sanches, and I. Iga, J. Chem. Phys. **136**, 114311 (2012).
[19] R. T. Sugohara, M. G. P. Homem, I. Iga, G. L. C. de Souza, L. E. Machado, J. R. Ferraz, A. S. dos Santos, L. M. Brescansin, R. R. Lucchese, and M.-T. Lee, Phys. Rev. A **88**, 022709 (2013).
[20] M. G. P. Homem, R. T. Sugohara, I. P. Sanches, M. T. Lee, and I. Iga, Phys. Rev. A **80**, 032705 (2009).
[21] S. K. Srivastava, A. Chutjian, and S. Trajmar, J. Chem. Phys. **63**, 2659 (1975).
[22] R. H. J. Jansen, F. J. de Heer, H. J. Luyken, B. van Wingerden, and H. J. Blaauw, J. Phys. B **9**, 185 (1976).
[23] R. D. DuBois and M. E. Rudd, J. Phys. B **9**, 2657 (1976).
[24] J. F. Williams and B. A. Willis, J. Phys. B **9**, 1670 (1975).
[25] P. Rawat, M. G. P. Homem, R. T. Sugohara, I. P. Sanches, I. Iga, G. L. C. de Souza, A. S. dos Santos, R. R. Lucchese, L. E. Machado, L. M. Brescansin, and M.-T. Lee, J. Phys. B **43**, 225202 (2010).
[26] G. L. C. de Souza, M.-T. Lee, I. P. Sanches, P. Rawat, I. Iga, A. S. dos Santos, L. E. Machado, R. T. Sugohara, L. M. Brescansin, M. G. P. Homem, and R. R. Lucchese, Phys. Rev. A **82**, 012709 (2010).
[27] J. R. Ferraz, A. S. dos Santos, G. L. C. de Souza, A. I. Zanelato, T. R. M. Alves, M.-T. Lee, L. M. Brescansin, R. R. Lucchese, and L. E. Machado, Phys. Rev. A **87**, 032717 (2013).

[28] N. T. Padial and D. W. Norcross, Phys. Rev. A **29**, 1742 (1984).
[29] M.-T. Lee, I. Iga, L. E. Machado, L. M. Brescansin, E. A. y Castro, I. P. Sanches, and G. L. C. de Souza, J. Electron Spectrosc. Relat. Phenom. **155**, 14 (2007).
[30] G. Staszewska, D. W. Schwenke, and D. G. Truhlar, Phys. Rev. A **29**, 3078 (1984).
[31] S. Hara, J. Phys. Soc. Jpn. **22**, 710 (1967).
[32] F. A. Gianturco, R. R. Lucchese, and N. Sanna, J. Chem. Phys. **102**, 5743 (1995).
[33] A. R. Edmonds, *Angular Momentum and Quantum Mechanics* (Princeton University Press, Princeton, NJ, 1960).
[34] M. W. Schmidt, K. K. Baldridge, J. A. Boatz, S. T. Elbert, M. S. Gordon, J. H. Jensen, S. Koseki, N. Matsunaga, K. A. Nguyen, S. Su, T. L. Windus, M. Dupuis, and J. A. Montgomery, J. Comput. Chem. **14**, 1347 (1993).
[35] NIST Computational Chemistry Comparison and Benchmark Database, http://cccbdb.nist.gov.
[36] P. G. Burke, N. Chandra, and F. A. Gianturco, J. Phys. B **5**, 2212 (1972).
[37] L. E. Machado, L. M. Brescansin, I. Iga, and M.-T. Lee, Eur. Phys. J. D **33**, 193 (2005).
[38] F. Salvat, J. D. Martínez, R. Mayol, and J. Parellada, Phys. Rev. A **36**, 467 (1987).
[39] J. B. Furness and I. E. McCarthy, J. Phys. B **6**, 2280 (1973).
[40] *Handbook of Chemistry and Physics*, 73rd ed., edited by D. R. Lide (CRC Press, Boca Raton, FL, 1992).

Theoretical and experimental investigation of electron collisions with acetone

M. G. P. Homem,[1] I. Iga,[1] L. A. da Silva,[1] J. R. Ferraz,[2] L. E. Machado,[2] G. L. C. de Souza,[3] V. A. S. da Mata,[3] L. M. Brescansin,[4] R. R. Lucchese,[5] and M.-T. Lee[1]

[1]*Departamento de Química, UFSCar, 13565-905 São Carlos, São Paulo, Brazil*
[2]*Departamento de Física, UFSCar, 13565-905 São Carlos, São Paulo, Brazil*
[3]*Departamento de Química, UFMT, 78060-900 Cuiabá, Mato Grosso, Brazil*
[4]*Instituto de Física "Gleb Wataghin," UNICAMP, 13083-970 Campinas, São Paulo, Brazil*
[5]*Chemistry Department, Texas A&M University, College Station, Texas 77842-3012, USA*

(Received 2 August 2015; published 21 September 2015)

We report a joint theoretical-experimental investigation on elastic electron scattering by acetone in the low- and intermediate-energy regions. More specifically, experimental differential, integral, and momentum-transfer cross sections are given in the 30–800 eV and 10°–120° ranges. Theoretical cross sections are reported in the 1–500 eV interval. The experimental differential cross sections were determined using a crossed electron-beam–molecular-beam geometry, whereas the absolute values of the cross sections were obtained using the relative-flow technique. Theoretically, a complex optical potential derived from a Hartree-Fock molecular wave function was used to represent the collision dynamics, and a single-center expansion method combined with the Padé approximant technique was used to solve the scattering equations. Our experimental cross-section data are in generally good agreement with the present calculated data. Also, our calculated grand-total and total absorption cross sections are in good agreement with the experimental results reported in the literature. Nevertheless, our calculations have revealed a strong shape resonance in the $^2B_2$ scattering channel not clearly seen in the experimental results. Possible reasons for this fact are also discussed.

DOI: 10.1103/PhysRevA.92.032711 PACS number(s): 34.80.Bm

I. INTRODUCTION

From a theoretical point of view, electron-assisted processes involving the organic molecules with the carbonyl group in their structures may support a shape resonance due to the existence of an empty π^* orbital that may trap electrons to form metastable states. Such resonances were in fact identified in the theoretical studies of low-energy electron collisions with formaldehyde [1–3], formic acid [4,5], and, more recently, acetaldehyde [6] and formamide [7]. Experimentally, such resonances were seen in studies involving electron interaction with carbonyl-containing compounds. For instance, π^* shape resonances in the vibrational excitation cross sections (VECS) for electron scattering by formaldehyde were reported by Benoit and Abouaf [8]. For acetaldehyde, such resonances in VECS were reported by Benoit *et al.* [9] and by Dressler and Alan [10]. Using the transmission technique, Van Veen *et al.* [11] and Jordan and Burrow [12] also observed the π^* resonance in electron-acetaldehyde interaction.

Recently, grand-total cross sections (TCS) for electron scattering by acetaldehyde were measured in the 0.7–400 eV range by Szmytkowski [13]. His experimental results did not show evidence of shape resonances at energies below 6 eV. More recently, Gauf *et al.* [6] reported measured elastic differential cross sections (DCS) for e^--acetaldehyde collisions in the 1–50 eV range. At energies below 20 eV, their experimental fixed-angle DCS at some selected angles also did not reveal evidence of the π^* shape resonance.

Acetone is similar to acetaldehyde. As for acetaldehyde, the experimental investigation of electron-assisted processes involving acetone is also quite intense. Normalized total ionization cross sections (TICS) at 75 eV were reported by Otvos and Stevenson [14], Harrison *et al.* [15], and Beran and Kevan [16]. Absolute TICS were measured by Bull and Harland [17] in the 15–285 eV range. The negative ion formation by electron attachment to acetone was investigated by Dorman [18], Naff *et al.* [19], and Jordan and Burrow [12]. Experimental TCS for electron-acetone scattering in the 0.8–600 eV range were reported by Kimura *et al.* [20]. More recently, absolute TCS for electron-acetone collision were measured by Szmytkowski [13] in the 0.7–400 eV range. In addition, TCS for positron-acetone scattering in the 0.2–23 eV interval were recently reported by Zecca *et al.* [21]. Nevertheless, there is no reported measurement of the DCS for elastic electron scattering by acetone in the literature.

As for acetaldehyde, TCS reported by Szmytkowski [13] for acetone also did not present evidence of the π^* shape resonance at low incident energies. One possible reason is that both acetaldehyde and acetone are strongly polar targets; therefore the π^* shape resonance feature might be masked by the intense dipole-scattering background, as seen in our previous work on formamide [7]. In order to clarify this fact, the present paper reports a theoretical investigation on e^--acetone scattering. In our calculation, the dynamics of the projectile-target interaction is represented by a molecular complex optical potential (MCOP) at the static-exchange-polarization plus absorption (SEPA) level of approximation. This model has already been applied by our group to study electron collisions with other carbonyl-containing molecules, e.g., formaldehyde [3] and formamide [7]. Also, due to the lack of experimental DCS for this target, we performed measurements of this physical quantity in the 30–800 eV range using the relative-flow technique (RFT). The experimental elastic integral (ICS) and momentum-transfer cross sections (MTCS) are generated from the measured DCS via a numerical integration procedure.

The organization of this work is as follows: In Sec. II, we present briefly the experimental procedure. In Sec. III, the theory we used and details of the calculations are presented. In Sec. IV, we compare our calculated and measured data. Comparison with the experimental TCS of Kimura *et al.* [20] and Szmytkowski [13] and TICS of Bull and Harland [17] are also presented. Finally, some concluding remarks are also presented in that section.

II. EXPERIMENT

Measurements of the scattered-electron intensities were performed using a crossed electron-beam–molecular-beam geometry with the same procedure and experimental setup presented in our previous works [22–28]. The electron source used in our setup provides a beam in the 30–1000 eV range. This beam is perpendicular to the gas beam which is generated by a molybdenum tube with inner diameter $d = 1$ mm and aspect ratio $\gamma = d/L = 0.03$. Details of our gas manifold were described previously [25].

Acetone was purchased from Merk with purity better than 99%. For the measurements, approximately 1 mL of sample was transferred into a small glass vial attached to the gas manifold and underwent a treatment in order to eliminate atmospheric air through freeze-thaw cycles. The working pressure in the scattering chamber was kept typically at 5×10^{-7} Torr, and the pressure in the gas reservoir of the gas manifold was lower than 0.5 Torr. The purity of the sample was checked with a quadrupole residual gas analyzer attached to the scattering chamber. In addition, the vial containing the sample was kept in a bath with water and ice in order to ensure the gas-beam stability during the measurements.

The electronic inelastically scattered electrons were discriminated from those scattered elastically by using a retarding-field energy analyzer with resolution around 1.5 eV. This resolution does not allow the separation of the vibrationally elastic and inelastic processes; thus the measured intensities are vibrationally summed. The scattered intensities were converted to absolute DCS using the RFT [29]. For that, precise determination of the relative flows of both acetone and the secondary standards (argon and nitrogen) is required. Such flows were measured following the procedure already described [25]. Moreover, the DCS for N_2 at 30 eV reported by Shyn and Carignan [30], with quoted errors of 14%, and the DCS for Ar of Jansen *et al.* [31] in the 100–500 eV range, with quoted experimental uncertainties of 6.5%, were used to normalize our data. The absolute DCS for N_2 at 50 eV with experimental uncertainties of 19% and those for Ar at 800 eV with uncertainties of 12%, both from DuBois and Rudd [32], were used. The uncertainties quoted for the secondary standards plus those associated with the statistical nature of the measured scattering intensities of each gas (estimated to be 3%), the uncertainties of pressure fluctuations, electron-beam current readings, background scattering (estimated to be less than 2% each), and the uncertainty associated with the normalization procedure (6%) provided overall estimated uncertainties of 16.5% at 30 eV, 21% at 50 eV, 15% at 800 eV, and 11% elsewhere. The ICS and MTCS were obtained via a numerical integration over the DCS. An extrapolation procedure was used to estimate the DCS at scattering angles not covered experimentally. The trend of the theoretical results was followed in this procedure in order to reduce the arbitrariness. The overall uncertainties on ICS and MTCS were estimated to be 30% at 30 and 50 eV and 25% elsewhere.

III. THEORY AND NUMERICAL PROCEDURE

Since the theory used in this work has already been given in detail in several previous works [3,33,34], it will be presented only briefly. Basically, a complex optical potential $U_{\rm opt}$ composed of static (U_{st}), exchange (U_{ex}), correlation-polarization (U_{cp}), and absorption (U_{ab}) contributions is used to represent the electron-target interaction. This potential is divided in two parts, namely, U_1 and U_2. Then, the transition T matrix can also be written as

$$T = T_1 + T_2, \tag{1}$$

where

$$T_1 = \langle \phi(\vec{k}_f)|U_1|\psi_1^+(\vec{k}_i)\rangle \tag{2}$$

and

$$T_2 = \langle \psi_1^-(\vec{k}_f)|U_2|\psi^+(\vec{k}_i)\rangle. \tag{3}$$

In Eqs. (2) and (3), ϕ is the unperturbed plane wave, ψ is the solution of the Schrödinger scattering equation for the full optical potential $U_{\rm opt}$, ψ_1 is the solution of the distorted-wave Schrödinger equation for potential U_1, and k is the magnitude of the electron linear momentum. The partition of $U_{\rm opt}$ into U_1 and U_2 is arbitrary. In this work, we chose

$$U_1 = U_{st} + U_{ex}^{\rm loc} + U_{cp} \tag{4}$$

and

$$U_2 = U_{ex} - U_{ex}^{\rm loc} + iU_{ab}, \tag{5}$$

where $U_{ex}^{\rm loc}$ is a reduced local exchange potential.

By solving numerically the distorted-wave Schrödinger scattering equation with potential U_1, ψ_1 and T_1 are obtained. Further, T_2 is obtained iteratively using the $[N/N]$ Padé approximant technique [35]:

$$T_2[N/N] = -\sum_{i,j=1,N-1} \langle \psi_1^-|U_2|\phi^{(i)+}\rangle (D^{-1})_{ij} \langle \phi^{(j)-}|U_2|\psi_1^+\rangle, \tag{6}$$

where

$$D_{ij} = \langle \phi^{(i)-}|U_2 - U_2 G_1^+ U_2|\phi^{(j)+}\rangle \tag{7}$$

and G_1 is the distorted-wave Green's function, which satisfies the following condition:

$$(\nabla^2 + k^2 - U_1)G_1^{\pm}(\vec{r},\vec{r}') = \delta(\vec{r},\vec{r}'). \tag{8}$$

The superscripts $-$ and $+$ appearing in the above equations denote the incoming and outgoing boundary conditions of the scattering waves, respectively. In our calculation, the truncation parameter N was iteratively increased until convergence was achieved. The converged body-frame (BF) T matrix (or, equivalently, the BF scattering amplitude f) can then be expressed in the laboratory frame (LF) by the usual frame transformation [36].

TABLE I. Experimental DCS (in 10^{-16}cm^2/sr) and ICS and MTCS (in 10^{-16}cm^2) for elastic e^--acetone scattering.

Angle (deg)	E (eV)								
	30	50	100	150	200	300	400	500	800
10	31.40	52.28	33.64	24.33	16.91	11.78	7.63	7.27	4.60
15	17.84		7.10	7.39	3.94	4.04	3.14	3.17	2.01
20	8.46	8.45	2.76	3.24	2.24	1.99	1.59	1.47	1.24
25	4.58		1.44	1.92	1.33	0.923	0.963	1.04	0.548
30	2.66	1.67	1.09	1.02	0.746	0.765	0.789	0.656	0.249
35	2.16		0.767	0.723	0.668	0.601	0.501	0.359	0.178
40	1.73	1.06	0.591	0.499	0.494	0.396	0.268	0.256	0.120
50	1.43	0.680	0.365	0.364	0.259	0.179	0.157	0.120	0.052
60	1.04	0.398	0.268	0.194	0.156	0.136	0.098	0.078	0.030
70	0.855	0.261	0.172	0.126	0.129	0.092	0.066	0.051	0.020
80	0.672	0.199	0.129	0.137	0.098	0.071	0.055	0.034	0.015
90	0.582	0.175	0.110	0.120	0.077	0.050	0.039	0.028	0.011
100	0.523	0.184	0.142	0.115	0.059	0.049	0.035	0.022	0.010
110	0.599	0.209	0.160	0.129	0.046	0.044	0.030	0.018	0.009
120	0.621	0.264	0.187	0.136	0.036	0.039	0.025	0.016	0.007
ICS	22.4	20.1	12.4	9.7	8.6	5.7	4.4	4.1	2.9
MTCS	11.0	5.2	3.1	2.1	1.4	0.86	0.62	0.47	0.21

The ground-state Hartree-Fock self-consistent-field (HF-SCF) wave function of acetone was obtained using the triple-zeta valence (TZV-3d) basis set of the GAMESS package [37]. At the experimental molecular geometry [38], this basis provided a total energy of −192.022905 hartrees. The calculated electric dipole moment is 3.2080 D, in fairly good agreement with the

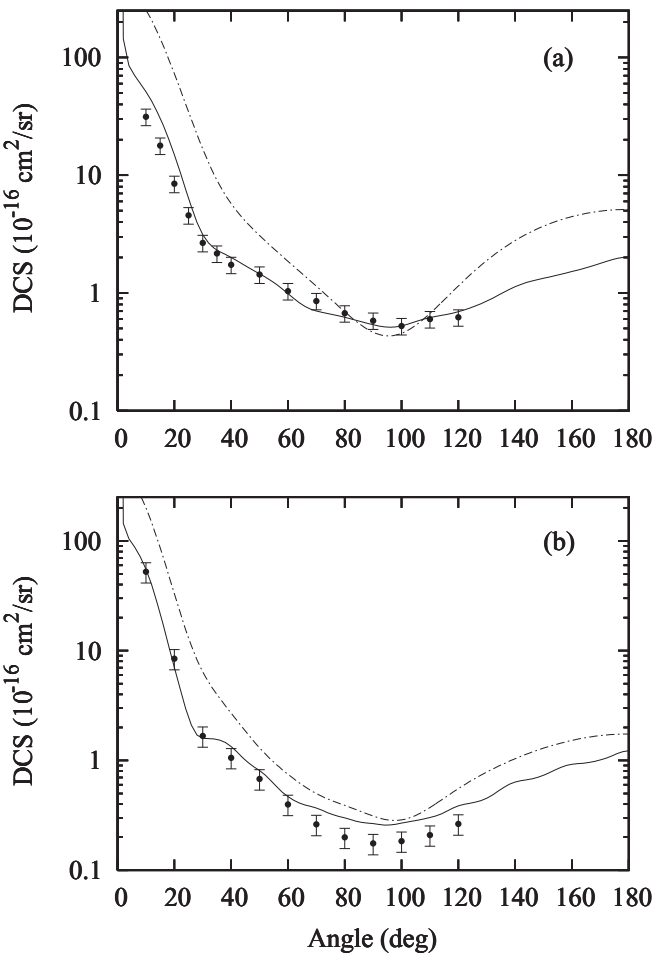

FIG. 1. DCS for elastic e^--acetone scattering at (a) 30 eV and (b) 50 eV. Solid curve, the present MCOP results; dash-dotted curve, the present IAM results; solid circles, the present experimental results.

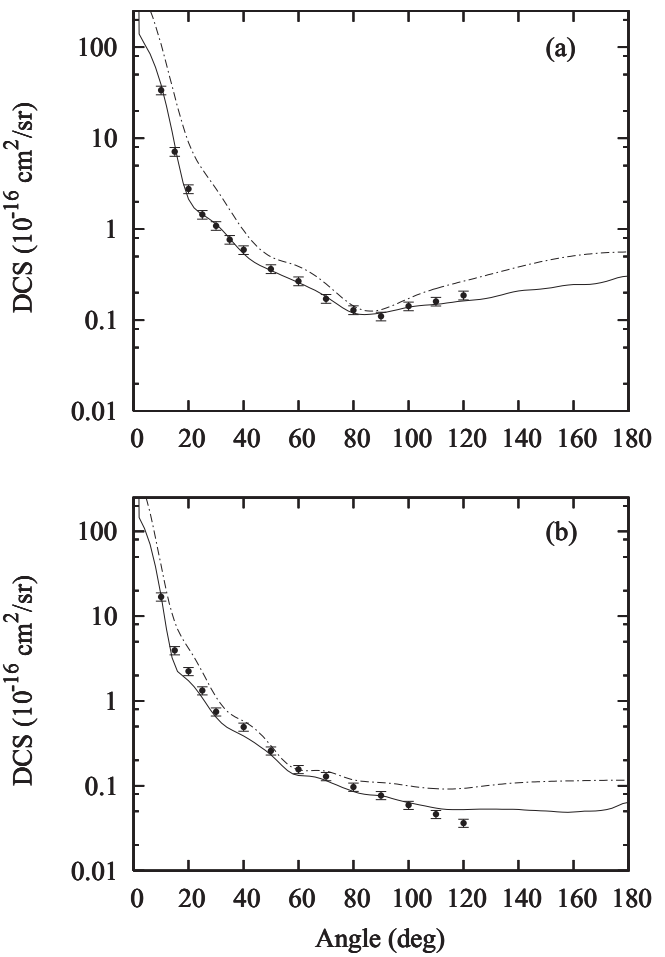

FIG. 2. Same as in Fig. 1, but at (a) 100 eV and (b) 200 eV.

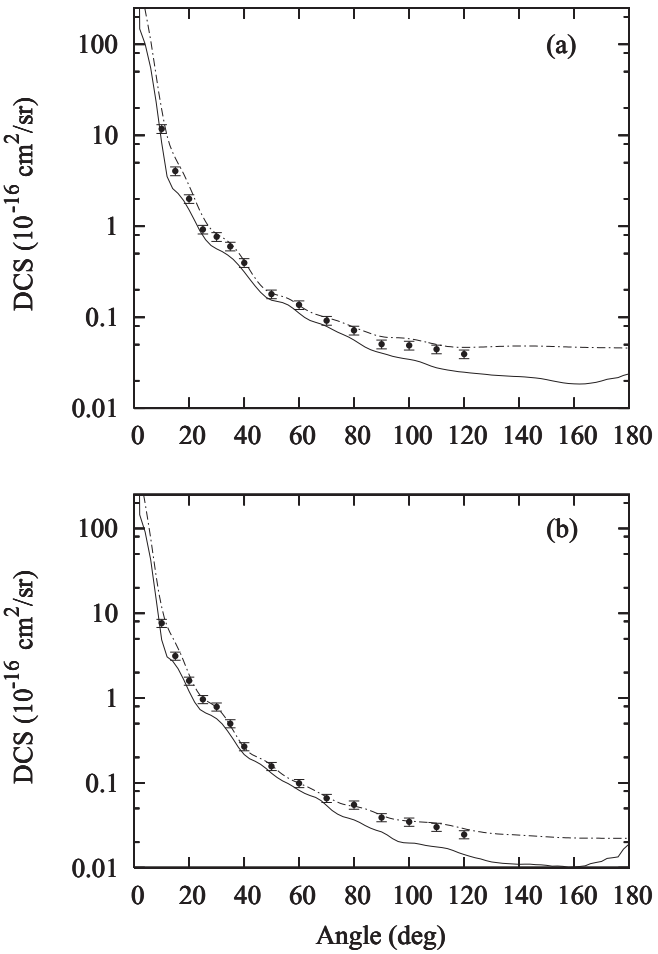

FIG. 3. Same as in Fig. 1, but at (a) 300 eV and (b) 400 eV.

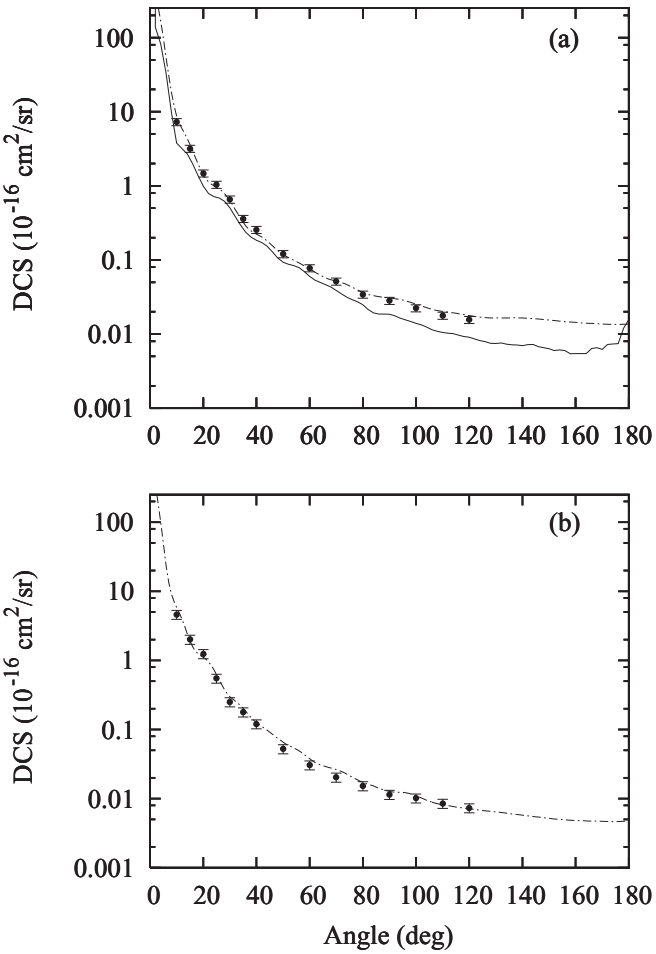

FIG. 4. Same as in Fig. 1, but at (a) 500 eV and (b) 800 eV.

experimental value of 2.88 D [38]. It is necessary to go beyond the HF level to obtain values closer to experimental data. The dipole polarizabilities calculated at the HF-SCF level using the same basis set are $\alpha_{xx} = 31.98$ a.u., $\alpha_{yy} = 41.10$ a.u., and $\alpha_{zz} = 42.60$ a.u., resulting in an average dipole polarizability of $\alpha_0 = 38.56$ a.u., in good agreement with the experimental value of 41.14 a.u. [38].

In the present work, U_{st} and U_{ex} were derived exactly from the target wave function, whereas U_{cp} was obtained in the framework of the free-electron-gas model, derived from a parameter-free local density, as prescribed by Padial and Norcross [39]. Our calculated polarizabilities are used to generate the asymptotic form of U_{cp}.

The absorption potential U_{ab} is the scaled quasifree scattering model (SQFSM) absorption potential of Lee *et al.* [40], which is an improvement of version 3 of the model absorption potential originally proposed by Staszewska *et al.* [41]. The Hara free-electron-gas-exchange potential [42] was used to generate the local exchange potential U_{ex}^{loc}.

In our calculation, the wave functions and interaction potentials, as well as the related matrices, are single-center expanded about the center of mass of the molecule in terms of the symmetry-adapted functions $X_{lh}^{p\mu}$ [43]. The truncation parameters used in these expansions were $l_c = 30$ and $h_c = 30$ for all bound and continuum orbitals, whereas the T-matrix elements were truncated at $l_c = 25$ and $h_c = 25$ for energies up to 50 eV and at $l_c = 30$ and $h_c = 30$ for higher energies. The calculated cross sections were converged at N up to 10.

Also, a Born-closure formula is used to account for the contribution of higher partial-wave components of the scattering amplitudes. This procedure is necessary due to the strongly polar nature of the target, as used in some of our previous studies [27,44,45].

IV. RESULTS AND DISCUSSION

Our experimental DCS, ICS, and MTCS for elastic electron scattering by acetone in the 30–800 eV range are listed in Table I. In Figs. 1–4, we present the comparison of the present experimental DCS with our calculated results in the 30–800 eV range. The present results calculated using the independent-atom model (IAM) [24] are also shown. In general there is good agreement between the present measured results and calculated MCOP data using the Padé approximant method, particularly at energies up to 300 eV. At higher energies, the theoretical MCOP results underestimate the DCS at large scattering angles. This discrepancy is mainly due to the lack of convergence in the single-center expansion of the nuclear part of the interacting potential for atoms a few angstroms away from the origin. Particularly at high incident energies,

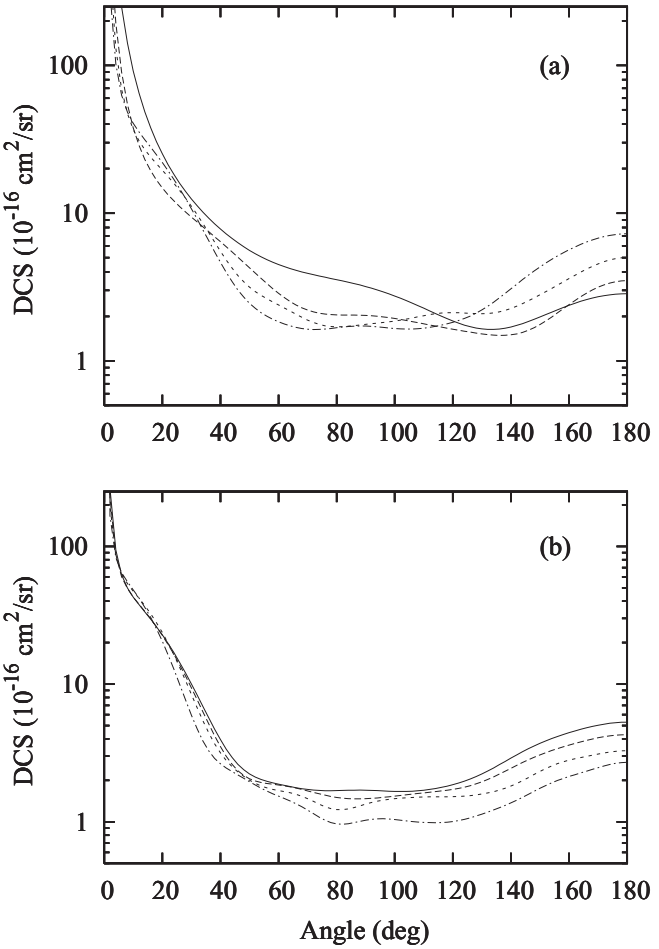

FIG. 5. Present MCOP DCS for elastic e^--acetone scattering. (a) Solid curve, at 1 eV; long-dashed curve, at 3 eV; short-dashed curve, at 5 eV; dash-dotted curve, at 8 eV. (b) Solid curve, at 10 eV; dashed curve, at 12 eV; short-dashed curve, at 15 eV; dash-dotted curve, at 20 eV.

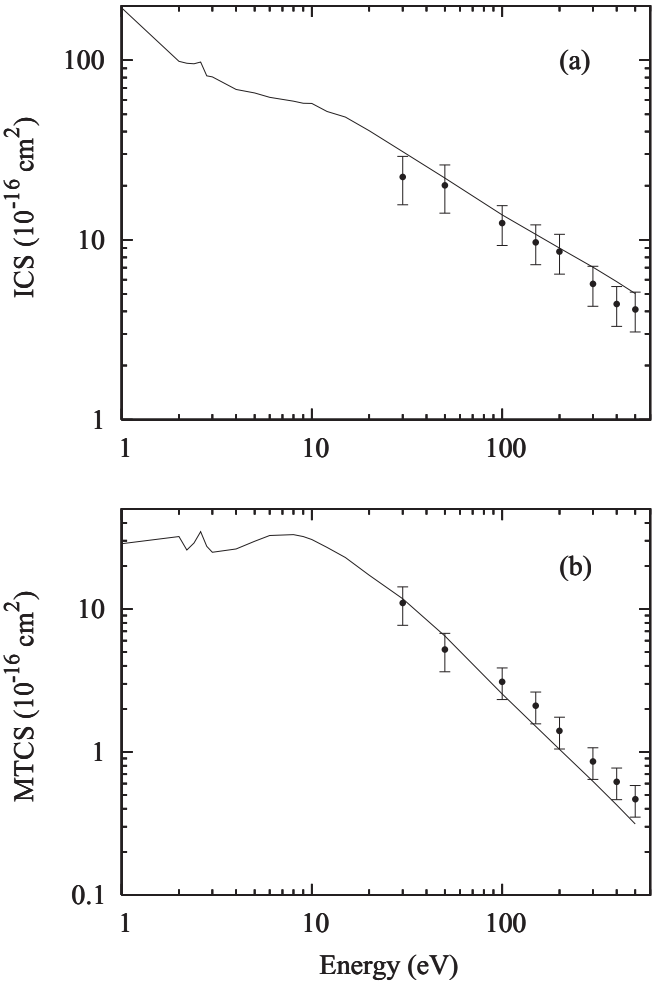

FIG. 6. (a) ICS and (b) MTCS for elastic e^--acetone scattering in the 1–500 eV range. Solid curve, present calculated data using the MCOP; solid circles, present experimental data.

the scattering electron penetrates deeply into the molecule and then would be more affected by that part of the potential. For a target like acetone, such convergence would be achieved only with very large values of l_c. The calculated results using the IAM lie systematically above the theoretical MCOP data. Nevertheless, the discrepancies diminish with increasing incident energies. At 100 eV and below, the IAM calculations also strongly overestimate the experimental DCS. However, it is interesting to note that for energies higher than 300 eV, the theoretical results calculated using the IAM are in better agreement with the measured data at large scattering angles due to the multicentric nature of the interaction potential used in these calculations [46]. Moreover, shallow oscillations seen in the experimental and in the theoretical DCS are due to the electron diffraction effects.

For the sake of completeness, in Fig. 5, we present some MCOP DCS in the 1–20 eV range. Unfortunately, there are no other results to compare with our data in this energy range. It is noted that the calculated DCS between 8 and 10 eV show some evidence of weak double-dip structure, indicating the possible occurrence of d-wave resonances.

In Fig. 6, we present our theoretical ICS and MTCS calculated using the MCOP for electron scattering by acetone in the 1–500 eV range. The present experimental results of ICS and MTCS in the 30–500 eV range are also shown for comparison. In general, there is reasonable agreement between our calculated and measured data in the entire energy range where comparison is made. At low incident energies, our calculated ICS and MTCS show a small peak at incident energy around 2.6 eV and a broad resonance-like feature centered at about 8 eV. These features are more visible in the calculated MTCS than in ICS. In order to clarify the physical nature of these features, we present in Figs. 7(a) and 7(b) the partial ICS (without Born correction) and the eigenphase sums. From these figures, it is clearly seen that the peak located at 2.6 eV is due to a strong $^2B_2$ ($^2\pi^*$) resonance, whereas the broad feature located at about 8 eV is a combination of weak $^2B_1$ and $^2A_2$ resonances (both at around 8 eV) and a weak $^2A_1$ shape resonance at around 10 eV. Probably, the double-dip behavior seen in our calculated DCS in the 8–10 eV range can be associated with these resonances. Unfortunately, our measurement does not cover incident energies below 30 eV,

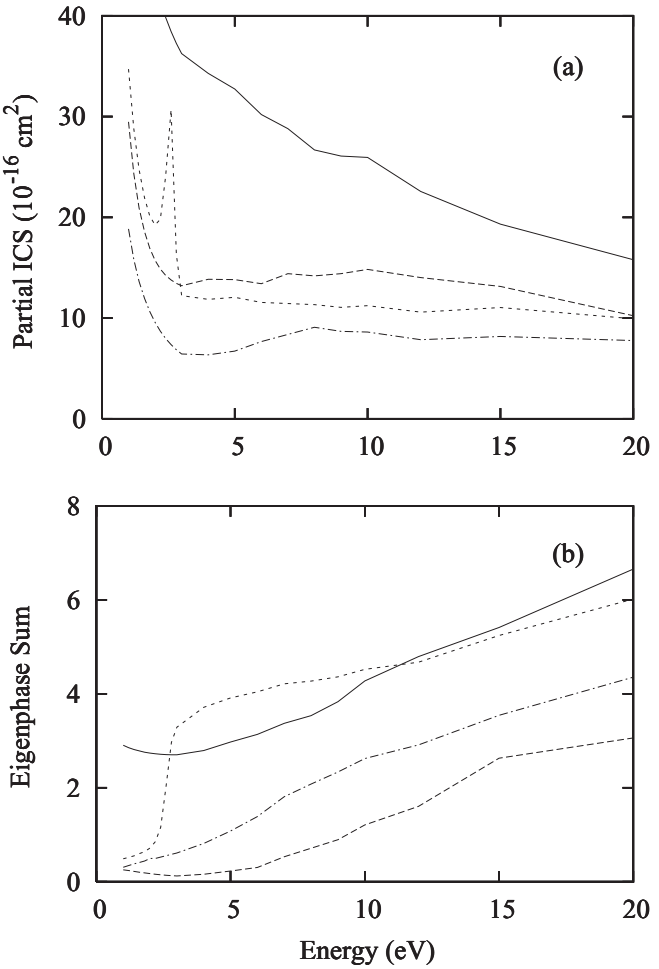

FIG. 7. Present partial-channel (a) ICS and (b) eigenphase sums calculated using the MCOP for elastic e^--acetone scattering in the 1–20 eV energy range. Solid curve, A_1 symmetry; dash-dotted curve, A_2 symmetry; long-dashed curve, B_1 symmetry; short-dashed curve, B_2 symmetry.

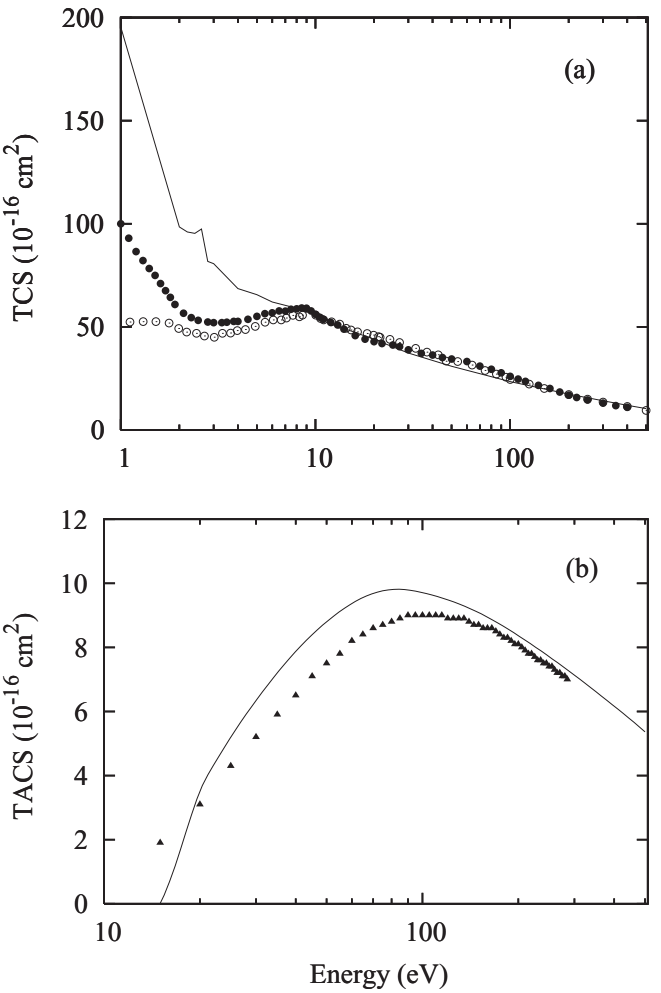

FIG. 8. (a) TCS and (b) TACS for e^--acetone scattering in the 1–500 eV range. Solid curve, present data calculated using the MCOP; solid circles, experimental data of Szmytkowski [13]; open circles, experimental data of Kimura *et al.* [20]; triangles, experimental data for TICS of Bull and Harland [17].

and also there are no other experimental data in the literature to compare with our calculations.

In Fig. 8(a), we present our theoretical TCS for electron scattering by acetone in the 1–500 eV range. The experimental TCS of Kimura *et al.* [20] in the 1–500 eV range and of Szmytkowski [13] in the 1–400 eV range are also shown for comparison to our data. Both experimental results show a bump at around 8 eV, which agrees with our theoretical prediction. This resonance was also seen in electron scattering by hydrocarbon experiments and is of a $k\sigma^*$ nature, as already discussed by Kimura *et al.* [20]. Quantitatively, there is also good agreement between our calculated results and the measured data at 10 eV and above. Nevertheless, the $^2B_2$ resonance located at about 2.6 eV predicted by our calculation is not seen in the TCS measured by Szmytkowski [13]. The TCS of Kimura *et al.* has shown a small shoulder at about 1.5 eV which may be due to the $^2B_2$ ($^2\pi^*$) resonance but shifted to lower incident energies. Moreover, our calculation overestimates both experimental TCS, particularly at energies below 3 eV. There is also a strong disagreement between the two sets of experimental data in this energy region. Such discrepancies are somewhat expected due to the difficulties associated with the measurements of TCS for strongly polar targets at low incident energies.

In Fig. 8(b), the present total absorption cross sections (TACS) are compared with the experimental TICS of Bull and Harland [17] in the 15–285 eV energy range. In general, there is very good qualitative agreement between the calculated TACS and experimental TICS. Quantitatively, our TACS lie above the TICS in the entire energy range, except at 15 eV. Since TACS account for both excitation and ionization processes, whereas only ionization processes are accounted for in TICS, the above behavior is then expected.

In summary, in this study, we reported a joint theoretical-experimental investigation of electron collisions with acetone in a wide energy range. More precisely, absolute DCS, ICS, and MTCS for elastic e^--acetone scattering were investigated experimentally in the 30–800 eV range. The present study was mainly motivated by the lack of experimental cross-section data for this target in the literature. Our measured data are in generally good agreement with our theoretical

data calculated using the MCOP model. Moreover, although a sharp resonance in the $^2B_2$ scattering channel at about 2.6 eV was revealed in our calculations, as seen in Fig. 7(a), it becomes a small peak in the calculated ICS and MTCS curves. The main reason for this fact is the strong contribution of the structureless dipole interaction in the calculated ICS and MTCS at low incident energies, which has masked the resonance peak. Also, the absence of clear evidence of the occurrence of this resonance in the experimental TCS of Kimura *et al.* [20] and Szmytkowski [13] may also be caused by the vibrational motion of the target. In fact, we have performed a simulation of the vibrational effects of the carbonyl group on this resonance. In this simulation, we have fixed the equilibrium geometry of the target except for the C=O bond, which is allowed to vary. The $^2B_2$ resonances are calculated at five C=O internuclear distances ($r = r_{eq} + \Delta r$, with $\Delta r = -0.12, -0.06, 0.0, 0.06$, and 0.12 Å). It was seen that both the height and the width of the resonance changed with the bond length. Nevertheless, the vibrational-averaged ICS calculated using harmonic-oscillator vibrational wave functions showed only a very small broadening of the resonant peak.

ACKNOWLEDGMENTS

The authors would like to thank Dr. A. S. dos Santos, L. M. F. de Oliveira, and G. E. O. Camargo for their valuable help. This research was partially supported by the agencies CNPq (Brazil), FAPESP (Brazil), and CAPES (Brazil).

[1] T. N. Rescigno, C. W. McCurdy, and B. I. Schneider, Phys. Rev. Lett. **63**, 248 (1989).
[2] S. Kaur and K. L. Baluja, J. Phys. B **38**, 3917 (2005).
[3] J. R. Ferraz, A. S. dos Santos, G. L. C. de Souza, A. I. Zanelato, T. R. M. Alves, M.-T. Lee, L. M. Brescansin, R. R. Lucchese, and L. E. Machado, Phys. Rev. A **87**, 032717 (2013).
[4] M. H. F. Bettega, Phys. Rev. A **74**, 054701 (2006).
[5] C. S. Trevisan, A. E. Orel, and T. N. Rescigno, Phys. Rev. A **74**, 042716 (2006).
[6] A. Gauf, C. Navarro, G. Balch, L. R. Hargreaves, M. A. Khakoo, C. Winstead, and V. McKoy, Phys. Rev. A **89**, 022708 (2014).
[7] M. G. P. Homem, I. Iga, G. L. C. de Souza, A. I. Zanelato, L. E. Machado, J. R. Ferraz, A. S. dos Santos, L. M. Brescansin, R. R. Lucchese, and M.-T. Lee, Phys. Rev. A **90**, 062704 (2014).
[8] C. Benoit and R. Abouaf, Chem. Phys. Lett. **123**, 134 (1986).
[9] C. Benoit, R. Abouaf, and S. Cvejanovic, Chem. Phys. **117**, 295 (1987).
[10] R. Dressler and M. Allan, J. Electron Spectrosc. Relat. Phenom. **41**, 275 (1986).
[11] E. H. van Veen, W. L. van Dijik, and H. H. Brongersma, Chem. Phys. **16**, 337 (1976).
[12] K. D. Jordan and P. D. Burrow, Acc. Chem. Res. **11**, 341 (1978).
[13] C. Szmytkowski, J. Phys. B **43**, 055201 (2010).
[14] J. W. Otvos and D. P. Stevenson, J. Am. Chem. Soc. **78**, 546 (1956).
[15] A. G. Harrison, E. G. Jones, S. K. Gupta, and G. P Nagy, Can. J. Chem. **44**, 1967 (1966).
[16] J. A. Beran and L. Kevan, J. Phys. Chem. **73**, 3866 (1969).
[17] J. N. Bull and P. W. Harland, Int. J. Mass Spectrom. **273**, 53 (2008).
[18] F. H. Dorman, J. Chem. Phys. **44**, 3856 (1966).
[19] W. T. Naff, R. N. Compton, and C. D. Cooper, J. Chem. Phys. **57**, 1303 (1972).
[20] M. Kimura, O. Sueoka, A. Hamada, and Y. Itikawa, Adv. Chem. Phys. **111**, 537 (2007).
[21] A. Zecca, L. Chiari, E. Trainotti, A. Sarkar, and M. J. Brunger, PMC Phys. B **3**, 4 (2010).
[22] I. Iga, M. T. Lee, M. G. P. Homem, L. E. Machado, and L. M. Brescansin, Phys. Rev. A **61**, 022708 (2000).
[23] P. Rawat, I. Iga, M. T. Lee, L. M. Brescansin, M. G. P. Homem, and L. E. Machado, Phys. Rev. A **68**, 052711 (2003).
[24] M. G. P. Homem, R. T. Sugohara, I. P. Sanches, M. T. Lee, and I. Iga, Phys. Rev. A **80**, 032705 (2009).
[25] M. G. P. Homem, I. Iga, R. T. Sugohara, I. P. Sanches, and M. T. Lee, Rev. Sci. Instrum. **82**, 013109 (2011).
[26] R. T. Sugohara, M. G. P. Homem, I. P. Sanches, A. F. de Moura, M. T. Lee, and I. Iga, Phys. Rev. A **83**, 032708 (2011).
[27] M.-T. Lee, G. L. C. de Souza, L. E. Machado, L. M. Brescansin, A. S. dos Santos, R. R. Lucchese, R. T. Sugohara, M. G. P. Homem, I. P. Sanches, and I. Iga, J. Chem. Phys. **136**, 114311 (2012).
[28] R. T. Sugohara, M. G. P. Homem, I. Iga, G. L. C. de Souza, L. E. Machado, J. R. Ferraz, A. S. dos Santos, L. M. Brescansin, R. R. Lucchese, and M.-T. Lee, Phys. Rev. A **88**, 022709 (2013).
[29] S. K. Srivastava, A. Chutjian, and S. Trajmar, J. Chem. Phys. **63**, 2659 (1975).
[30] T. W. Shyn and G. R. Carignan, Phys. Rev. A **22**, 923 (1980).
[31] R. H. J. Jansen, F. J. de Heer, H. J. Luyken, B. van Wingerden, and H. J. Blaauw, J. Phys. B **9**, 185 (1976).
[32] R. D. DuBois and M. E. Rudd, J. Phys. B **9**, 2657 (1976).
[33] P. Rawat, M. G. P. Homem, R. T. Sugohara, I. P. Sanches, I. Iga, G. L. C. de Souza, A. S. dos Santos, R. R. Lucchese, L. E. Machado, L. M. Brescansin, and M.-T. Lee, J. Phys. B **43**, 225202 (2010).
[34] G. L. C. de Souza, M.-T. Lee, I. P. Sanches, P. Rawat, I. Iga, A. S. dos Santos, L. E. Machado, R. T. Sugohara, L. M. Brescansin, M. G. P. Homem, and R. R. Lucchese, Phys. Rev. A **82**, 012709 (2010).
[35] F. A. Gianturco, R. R. Lucchese, and N. Sanna, J. Chem. Phys. **102**, 5743 (1995).
[36] A. R. Edmonds, *Angular Momentum and Quantum Mechanics* (Princeton University Press, Princeton, NJ, 1960).
[37] M. W. Schmidt, K. K. Baldridge, J. A. Boatz, S. T. Elbert, M. S. Gordon, J. H. Jensen, S. Koseki, N. Matsunaga, K. A. Nguyen, S. Su, T. L. Windus, M. Dupuis, and J. A. Montgomery, J. Comput. Chem. **14**, 1347 (1993).
[38] Computational Chemistry Comparison and Benchmark DataBase, http://cccbdb.nist.gov.

[39] N. T. Padial and D. W. Norcross, Phys. Rev. A **29**, 1742 (1984).
[40] M.-T. Lee, I. Iga, L. E. Machado, L. M. Brescansin, E. A. y Castro, I. P. Sanches, and G. L. C. de Souza, J. Electron Spectrosc. Relat. Phenom. **155**, 14 (2007).
[41] G. Staszewska, D. W. Schwenke, and D. G. Truhlar, Phys. Rev. A **29**, 3078 (1984).
[42] S. Hara, J. Phys. Soc. Jpn. **22**, 710 (1967).
[43] P. G. Burke, N. Chandra, and F. A. Gianturco, J. Phys. B **5**, 2212 (1972).
[44] L. M. Brescansin, L. E. Machado, M.-T. Lee, H. Cho, and Y. S. Park, J. Phys. B **41**, 185201 (2008).
[45] L. E. Machado, L. M. Brescansin, I. Iga, and M.-T. Lee, Eur. Phys. J. D **33**, 193 (2005).
[46] M.-T. Lee and L. C. G. Freitas, J. Phys. B **13**, 233 (1983).